Understand and overcome the limitations of silicon/amorphous silicon (a-Si H) nanowire solar cells

Tiphaine Mathieu-Pennober

université PARIS-SACLAY

Understand and overcome the limitations of silicon/amorphous silicon (a-Si:H) nanowire solar cells

Comprendre et dépasser les limitations induites par l'utilisation de nanofils de silicium/silicium amorphe (a-Si:H) dans les cellules solaires

Thèse de doctorat de l'université Paris-Saclay

École doctorale n° 575,
Physique et ingénierie : Electrons, Photons, Sciences du vivant (EOBE)
Spécialité de doctorat : Électronique et Optoélectronique,
Nano- et Microtechnologies
Graduate School : Sciences de l'ingénierie et des systèmes
Référent : Faculté des sciences d'Orsay

Thèse préparée dans l'unité de recherche C2N (Université Paris-Saclay, CNRS)
sous la direction de **Maria TCHERNYCHEVA**, directrice de recherche

Thèse soutenue à Paris-Saclay, le 13 juillet 2022, par

Tiphaine MATHIEU-PENNOBER

Composition du jury

Jean-François GUILLEMOLES Directeur de recherche, Insitut Polytechnique de Paris, laboratoire IPVF	Président
Anna FONTCUBERTA-I-MORRAL Professeure, Ecole Polytechnique Fédérale de Lausanne (EPFL)	Rapportrice & Examinatrice
Erwann FOURMOND Maître de conférences, HDR, INSA Lyon	Rapporteur & Examinateur
José ALVAREZ Chargé de recherche, Université Paris-Saclay, GEEPS	Examinateur
Maria TCHERNYCHEVA Directrice de recherche, Université Paris-Saclay, C2N	Directrice de thèse

THESE DE DOCTORAT

NNT : 2022UPAST101

université PARIS-SACLAY

ÉCOLE DOCTORALE
Physique et ingénierie : Electrons, Photons, Sciences du vivant (EOBE)

Titre: Comprendre et dépasser les limitations induites par l'utilisation de nanofils de silicium et silicium amorphe (a-Si:H) dans les cellules solaires

Mots clés: Photovoltaïque, Nanofils, Electrode transparente, EBIC, Silicium amorphe, Flexibilité

Résumé: Le potentiel utilisable de l'énergie solaire représente plus du double de la consommation finale humaine en 2019. Néanmoins, seulement 0.2 % du potentiel est aujourd'hui utilisé par la technologie photovoltaïque. Le silicium cristallin (95 % du marché actuel) est très avancé, puisque les modules actuellement produits ont une efficacité autour de 20 %. Néanmoins, l'efficacité de conversion n'est pas le seul facteur pour choisir une technologie photovoltaïque. En particulier, son impact environnemental, sa résistance aux conditions extérieures ou son adéquation à l'application choisie sont également déterminants. Des technologies alternatives ont donc leur place dans le mix photovoltaïque.

En particulier, le silicium amorphe constitue un matériau abondant qui ne nécessite pas une purification coûteuse en énergie. De plus, il est non toxique, aux excellentes propriétés optiques. Il présente des limitations électriques, mais l'utilisation de nanofils cœur-coquille remédie à ce problème en séparant les directions de propagation de la lumière et de collection des porteurs de charge. La croissance peut se faire sur tout type de substrat (typiquement du verre), à faible température. Ainsi, on peut obtenir des performances correctes sur de larges surfaces et à faible coût.

J'ai montré que les cellules à base de nanofils cœur-coquille silicium/silicium amorphe (Si NW/a-Si:H) sont d'abord limitées par leur contact supérieur, qui doit être à la fois conducteur et transparent. J'ai développé une électrode hybride, faite d'ITO, capable de connecter les nanofils Si NW/a-Si:H, et de nanofils d'argent (Ag NWs), qui forment un maillage conducteur. Une optimisation directement sur la cellule est nécessaire et a permis une augmentation de l'efficacité de conversion de 4.3 % à 6.6 %.

L'un des inconvénients principaux des nanofils d'argent est leur dégradation dans le temps. Nous les avons encapsulés dans une couche de ZnO dopé au titane pour les protéger. J'ai suivi la dégradation des nanofils par l'observation en microscopie électronique à balayage, et par des mesures de transmittance et réflectance totales et de résistance de couche. Cette étude a montré que les propriétés des nanofils d'argent, même nus, sont stables sur une échelle supérieure à un an. Néanmoins, ils n'ont pas été exposés à d'importants niveaux de courant ou d'illumination. Or, la lumière et le courant peuvent accélérer la dégradation et seront nécessairement présents lors de l'utilisation d'Ag NWs sur des cellules solaires. La même étude sous illumination et/ou courant serait donc utile.

Les cellules faites de Si NW/a-Si:H avec le contact hybride devraient être flexibles. Néanmoins, l'observation au MEB a montré des fissures dans les cellules à nanofils. Ceux-ci étant denses, ils ont un comportement qui s'approche des couches minces et perdent leur flexibilité.

Nous avons aussi voulu comprendre le changement de performance sous forte illumination. La comparaison des courbes I-V pour une cellule Si NW/a-Si:H, une cellule planaire de silicium amorphe et une cellule de référence en silicium cristallin a montré plusieurs phénomènes, réversibles ou non. En particulier, cela a mis en évidence l'effet Staebler-Wronski, caractéristique de a-Si:H, et les conséquences du substrat de verre sur l'élévation de la température et la baisse drastique d'efficacité.

Par ailleurs, j'ai pu utiliser la technique EBIC (courant induit par faisceau électronique) sur de nombreuses structures. J'ai observé les cellules à base de Si NW/a-Si:H en vue de dessus. J'ai également caractérisé des cellules solaires à nanofils III-V sur silicium pour tandem. Enfin, j'ai aussi caractérisé des nanofils GaN/InGaN, destinés à la fabrication de diodes électro-luminescentes.

université PARIS-SACLAY

ÉCOLE DOCTORALE
Physique et ingénierie : Electrons, Photons, Sciences du vivant (EOBE)

Title: Understand and overcome the limitations of silicon/amorphous silicon (a-Si:H) nanowire solar cells

Keywords: Solar cell, Nanowires, Transparent electrode, EBIC, Amorphous silicon, Flexibility

Abstract: The exploitable solar potential corresponds to more than twice the final human consumption of energy in 2019. Yet, only 0.2 % of this potential is used today for photovoltaic conversion. Crystalline silicon, which holds 95 % of the market, is an advanced technology, with currently made modules showing a power conversion efficiency around 20 %. However, the power conversion efficiency is not the only parameter to consider when choosing a photovoltaic technology. Its environmental impact, the dependence of its power conversion efficiency on the illumination and temperature conditions, and the match between the PV technology characteristics and the application are also key factors. Consequently, there is room for other technologies than c-Si, including less efficient ones.

In particular, amorphous silicon is an abundant material with no need for an energy-costly purification process. Besides, it is non-toxic and displays excellent optical properties. The main drawback is its poor material quality, limiting the transport distance of the minority charge carriers. This issue can be solved in core-shell nanowires, where the direction for the absorption of the light and for the collection of charge carriers are separated. Moreover, these cells can be grown on various substrates (usually glass) at low temperatures. Low-cost, large-area working solar cells can hence be obtained.

I showed that the solar cells made of silicon/amorphous silicon (a-Si:H) core-shell nanowires are first limited by the top contact. It has to be both transparent and conductive. I developed a hybrid electrode, made of ITO (able to connect every single Si nanowire) and silver nanowires (able to make a conductive network on top of the Si NW/a-Si:H). I optimized the electrode properties directly on the device and increased the power conversion efficiency from 4.3 % to 6.6 %.

One of the main shortcomings of the silver nanowires (Ag NWs) is their degradation with time. We encapsulated them in a titanium-doped ZnO layer to protect them. I monitored their degradation with scanning electron microscopy, measurements of total transmittance and reflectance, and measurements of the sheet resistance. This study showed that the properties of bare silver nanowires are not degraded over more than a year. Yet, they had not been exposed to light or current stress. Light and current would nonetheless be present in the use of the solar cell. The same study under illumination or with current would be needed.

The cells made of Si NW/a-Si:H with the hybrid contact are expected to be flexible. However, SEM observations showed cracks in the Si NW array. Because they are dense, Si NWs behave almost as a thin film and lose their flexible feature.

We also wanted to understand the change in performance under strong illumination. Comparing I-V curves of a Si NW/a-Si:H with a planar a-Si:H and a crystalline silicon solar cells evidenced different phenomena, reversible or not. In particular, it showed the Staebler-Wronski effect, typical of a-Si:H, and the consequences of the glass substrate on the increase of temperature and the drastic loss in performance.

In addition, I used the EBIC technique (electron beam induced current) on various structures. I observed the Si NW/a-Si:H in plane-view. I also characterized III-V nanowires on silicon for tandem solar cells. Finally, I also characterized GaN/InGaN nanowires for electroluminescent diodes.

Remerciements

Je souhaite remercier tous les membres du jury pour avoir pris le temps de lire et comprendre mon travail. Merci aux rapporteurs, Erwann Fourmond et Anna Fontcuberta-i-Morral, pour vos commentaires sur le manuscrit. Merci tout particulièrement Anna pour m'avoir fait découvrir les nanofils, donné envie de faire une thèse et régulièrement encouragée. Merci également à Jean-François Guillemoles et José Alvarez pour avoir accepté de prendre part à ce jury.

J'aimerais aussi remercier les personnes avec qui j'ai échangé sur mon travail. Merci Maria de m'avoir accompagnée pendant ces années. Tu as toujours été disponible pour un échange, que je vienne pour des détails techniques ou pour une remise en question complète des objectifs actuels. Ensemble, on a navigué entre nanofils d'argent et nanofils de silicium, entre cellules tandem à nanofils, LEDs et cellules à bas coût, entre III-V et silicium amorphe, entre dispositifs et nanofil unique, entre salle blanche et EBIC. On a même approché les rivages du water splitting. Que tu décides ou non de continuer ta collaboration avec les nanofils de silicium, j'espère que ma thèse t'aura permis de mieux les apprivoiser. Merci Martin d'avoir partagé ton expérience des cellules solaires en silicium amorphe et pour la rigueur dont tu faisais preuve face à chaque nouveau résultat. Je ressortais souvent de ces discussions avec des perspectives complètement changées (et l'estomac creux). La fatigue associée à ces longs échanges était compensée par ton enthousiasme. Merci Shan-Ting pour notre collaboration, j'ai beaucoup aimé travailler avec toi. Tu es la preuve qu'un bon chercheur n'est pas qu'un réservoir de connaissances mais sait également s'organiser et communiquer. J'espère que tu as trouvé à Shanghai ce qu'il te manquait ici. Merci François pour les discussions occasionnelles qui permettaient de prendre un peu de recul et pour les répétitions et relectures diverses. Et bien sûr pour la caméra ! Et enfin, merci Fabien pour toute ton aide pour l'EBIC. Tu étais toujours prêt à répondre à mes dernières questions et toujours intéressé par les mesures en cours. C'est aussi grâce à toi que je suis allée à la rencontre du reptile de Monty, ce qui a eu un effet monstre sur mon travail de thèse.

Mais au quotidien, c'est le E114 que je dois remercier, à qui je pouvais tout demander, un moment de divertissement, des connaissances pointues, ou une discussion plus philosophique. Alors, φ ou ϕ ? q ou e ? (en écrivant ça, j'ai découvert $\backslash varpi$, ϖ, c'est cadeau). Le début de cette thèse me paraît d'autant plus loin que je ne vous connaissais pas encore. Enfin presque pas, j'avais déjà entendu Paul chanter à travers la vitre et décidé que ce personnage était fort malpoli. Mais une fois la barrière de potentiel franchie, j'ai compris que je pouvais compter sur toi. Aujourd'hui, tu ne parviens (presque) plus à me choquer, et je me doute que ça t'attriste. Mathieu, je t'ai d'abord vu comme un rival pour le E114, mais était-ce vraiment le E114 sans toi ? Merci pour les discussions, dans le RER, pendant les pauses café, dans le tram, pendant les pauses thé, dans les escaliers, ou pendant le déjeuner (surtout côte à côte). Je sais que si la police de la gentillesse cherche un coupable, aucun alibi ne te sauvera face à l'ensemble des témoignages t'incriminant. De mon côté, je leur raconterai notamment les pains aux raisins et la métamorphose d'un frigo. Très honorée d'avoir fait partie des Mathieux. Oussama, merci pour tes pointes d'humour, l'air de rien, toujours parfaitement dosées. Grâce à toi, j'ai enfin vu *Grave* (même si je n'ai pas suffisamment prêté attention à la B.O.).

Merci à mes coéquipiers si divers, les nouveaux et les anciens, Amaury, Jules, Nuño, Arup, Omar, Valerio, Lu, Nan, Ahmed. Aucun n'a eu la chance de découvrir le silicium amorphe, peu ont goûté le plaisir des cellules solaires, mais la plupart ont connu la joie des nanofils et quelques privilégiés le régal de l'EBIC. Nuño, merci d'être *noisy* et en même temps attentif aux autres. Je n'aurais pas gardé le même souvenir de Pise si tu n'avais pas été là. Merci Jules pour toutes ces barres de cacahuètes, elles m'ont réchauffé le cœur, l'estomac et le cerveau.

Merci aux autres photovoltaïciennes et photovoltaïciens du C2N d'avoir partagé certaines de mes préoccupations, en particulier Amaury, Stéphane, Andrea. Bérengère et Capucine, nos débuts ont été ralentis par le covid mais nous avons tenu bon ! J'ai découvert avec vous le plaisir de discuter de *window layer* entre la poire et le fromage (mais pas au déjeuner tout de même, j'ai retenu les fondamentaux). Nos pérégrinations nous ont emmenées aux Houches, à Strasbourg et même à Dourdan. Berlin sera peut-être la prochaine étape ? Si ce n'est pas le vin chaud qui nous motive, ce sera sûrement une Currywurst végétarienne. *(To Be Continued.)* Salim, je suis étonnée de ne pas avoir entendu ton rire avant les Houches. Mais je suis aussi ravie de l'avoir finalement découvert et j'espère l'entendre encore même si les prochains mois seront plus compliqués ! Carlos, je suis désolée pour les nombreuses irruptions et interruptions dans votre bureau, mais tu as su rester imperturbable, probablement grâce au café. Merci Guillaume d'avoir créé du lien entre les équipes (coucou Cléophanie !) et entre les labos. Peu importe ton humeur réelle, tu sais donner le sourire aux gens que tu rencontres.

Merci aux ODINers, notamment Mario, Raffaele, Sophie, Stefano. Tanbir, j'espère qu'on se rattrapera et que, si ce n'est pas pour Whistler, on trouvera tout de même une expo au Musée d'Orsay. Merci Marina d'être une source infinie de bonne humeur, de connaissances et d'anecdotes. Jean-Michel, je ne savais pas sur quel pied danser au début, mais plusieurs années et un karaoké plus tard, je me suis enfin souvenue qu'un Breton avait forcément bon fond. Merci Linh pour les discussions sportives ! Et merci Quentin pour m'avoir conté l'histoire du laboratoire et dépeint le paysage actuel de la recherche.

Merci à celles et ceux que j'ai côtoyé·e·s pour l'enseignement, notamment Adel et Guillaume. Merci Marie, Francesca et Kevin pour m'avoir fait autant confiance et révélé les coulisses de l'enseignement associé à la recherche. Dommage que le covid soit passé par là et ait limité les échanges, même si ça a été l'occasion de réfléchir à l'enseignement à distance.

Merci aussi aux personnes que j'ai croisées en salle blanche, en particulier David, Jean-Luc, Christophe, Cédric, Téo, Nathalie. Vous m'avez beaucoup aidée alors que mes premiers pas coïncidaient avec ceux du labo.

Merci à ceux et celles du PICM et de Platine, Mutaz, Weixi, Eric, Junkang, Letian, Chaoqi, Jérôme, Maria, Dmitri, Gaël, Hindia, Boris, Robert, Nicolas, Gookbin... Vous m'avez accueillie, ouvert des portes (au sens propre), formée. J'ai toujours trouvé quelqu'un pour répondre à mes questions, même s'il fallait parfois marcher un peu (il me semble bien avoir visité tous les bâtiments dans lesquels le PICM a essaimé).

Valérie, merci d'avoir trouvé des moments pour nos discussions dans ton emploi du temps plus que chargé. Tes engagements et l'évidence avec laquelle tu les réalises m'impressionnent. Qu'il s'agisse de sciences, de participation à la société, de carrière, tous nos échanges m'ont fait réfléchir. C'est aussi grâce à toi que j'ai réalisé que l'absence de résultats pouvait être un résultat.

Un grand merci à Nina Kraften[1], pour être toujours là après tant d'années. J'ai hâte de fêter nos 10 ans ! Merci Emeline d'avoir accepté de suivre le feuilleton *Vingt-quatre heures de la vie d'une thésarde* et ses 1258 épisodes et d'avoir toujours pris le temps de répondre à chaque point, aussi futile fût-il. Antoine, j'aurais dû te laisser écrire ces remerciements, on se serait bien moins ennuyés. Tu ne t'en doutais pas nécessairement, mais tu étais le modèle du doctorant qui est capable de voir au delà de son quotidien et sait ce qu'il veut (oui, oui). Si ce modèle me paraissait hors d'atteinte, il restait l'idéal vers lequel tendre. Et, forcément, merci pour ton enthousiasme sans failles. Merci Rémi pour ton soutien et tes jeux de mots bien plus mauvais que les miens. Merci Nico de toujours nous accorder du temps, malgré ton agenda de ministre. Claire et Elodie, je ne suis pas certaine de faire partie de la mafia un jour, mais je suis très contente d'en apprendre toujours plus sur son fonctionnement et l'absence de fenêtres ! Merci Mog et Paul de revenir nous voir régulièrement, sans jamais oublier de prendre votre sympathie dans vos bagages.

Camille, Laura, Marie-Alix, j'ai fait ce que j'ai pu, mais j'ai échoué. Malgré ce titre durement gagné, je ne sais toujours pas ce qu'est un angiosarcome de Kaposi, l'amélogénine ou une schizophrénie hébéphrénique. Rassurez-vous, je l'ai désormais accepté et suis tout de même prête à signer un renouvellement de contrat (incluant week-ends à la mer, jeux de société variés, dîners de desserts, films, etc). Merci Marion, ma grande sœur de thèse (mais d'une famille recomposée) et mon aide à l'introspection. Je profite à chaque fois de ta science, de ton recul, et de ton don pour raconter les histoires. Je suis très heureuse qu'on se soit accompagnées ces dernières années. Merci Neige pour toutes ces longues promenades parisiennes. Elles illustrent les nombreux commentaires de philosophes sur les bienfaits de la marche sur l'esprit. J'espère qu'elles continueront à balle. Merci Ting, d'être présente malgré le peu de temps que tu as en ce moment. J'espère que tu pourras bientôt en profiter davantage. Merci Juliette et Meriel de m'avoir encouragée sur la dernière ligne droite. Merci Freddie d'être toujours si élégant, à toute heure de la journée et de la nuit. Merci Prima pour l'ambiance sonore de bord de mer dans un appartement parisien.

Merci Aurélie, Tatung, Jérémy et Célia d'avoir suivi l'avancée de ma thèse. On ne choisit pas sa (belle) famille, mais j'ai été chanceuse au tirage.

Enfin, en derniers auteurs, merci à ma grand-mère et à mes parents pour la mise en place et le suivi du projet, je crois que vous avez géré. Merci frérot pour les fous-rires, les commentaires Top Chef, les compliments cash (et le gilet, c'est important un gilet). Et tout le reste.

Kevin, je ne vais pas faire la liste des duos célèbres auxquels s'identifier (n'est-ce pas John ?) mais tu n'en restes pas moins mon acolyte, mon complice, mon allié, mon compagnon, mon associé, mon camarade, mon ami, mon binôme. Tous ces jours de thèse, tu m'as fait rire et sourire. Malgré nos cadres de travail si différents pour la gestion du temps et l'encadrement, tu as su m'écouter, m'encourager et me faire profiter de ton expérience. Ça ne s'arrêtait déjà pas à la thèse, et ça ne s'arrêtera pas avec la thèse.

[1] Le saviez-vous ?

Contents

List of Acronyms and Symbols

Acronyms

Symbols

FF	Fill-factor
I_{sc}	Short-circuit current
J_{sc}	Short-circuit current density
R_{se}	Series resistance
$R_{\square}$	Sheet resistance
R_{shunt}	Shunt resistance
V_{oc}	Open-circuit voltage

Synthèse en français

Une alternative aux énergies fossiles est désormais nécessaire. Parmi les sources possibles d'énergies renouvelables, l'énergie solaire est particulièrement prometteuse, puisque son potentiel utilisable représente plus du double de la consommation finale humaine en 2019. Néanmoins, elle reste relativement peu exploitée : seulement 0.2 % du potentiel est aujourd'hui utilisé par la technologie photovoltaïque (le solaire thermique est négligeable en comparaison), ce qui correspond à ∼0.6 % de la consommation énergétique (Figure 1 **(a)**). Le silicium cristallin représente 95 % du marché actuel avec des modules actuellement produits d'une efficacité supérieure à 20 %. Néanmoins, l'efficacité de conversion n'est pas le seul facteur pour choisir une technologie photovoltaïque (PV). En particulier, son impact environnemental, sa résistance aux conditions extérieures (niveau d'illumination, température...) ou son adéquation avec l'application choisie (flexibilité...) sont également déterminants. Des technologies alternatives ont donc leur place dans le mix photovoltaïque.

En particulier, le silicium amorphe constitue un matériau abondant, non toxique, aux excellentes propriétés optiques. Il présente des limitations électriques, mais l'utilisation de nanofils permet de remédier à ce problème. Les nanofils sont des structures de fort rapport d'aspect avec un diamètre inférieur à un micron. Ils peuvent être constitués de différents matériaux et permettent notamment une meilleure absorption de la lumière. De plus, l'emploi d'une structure radiale, ou cœur-coquille, permet de séparer les directions de propagation de la lumière et de collection des porteurs de charge. Ainsi, la distance à parcourir pour les porteurs de charge est diminuée, ce qui est particulièrement bénéfique pour les matériaux dont les porteurs présentent de faibles mobilités.

Les nanofils utilisés sont schématisés sur la Figure 1 **(b)**, avec leurs dimensions. Ils sont composés d'un cœur de silicium cristallin dopé p, élaboré par PECVD (dépôt chimique en phase vapeur assisté par plasma) avec un catalyseur d'étain, et d'une jonction p-i-n en silicium amorphe (a-Si:H), déposée par PECVD. Le contact arrière est constitué de FTO (oxyde d'étain dopé au fluor) ou d'un ensemble argent/AZO (oxyde de zinc dopé à l'aluminium). La croissance des nanofils peut se faire sur tout type de substrat (typiquement du verre), à faible température (<400 °C pour le cœur, 180 °C pour la coquille). Ainsi on peut obtenir des performances correctes sur de larges surfaces et à faible coût en limitant l'utilisation de matériau. Le record d'efficacité pour ces cellules est aujourd'hui de 9.2 % [Misra 2015b].

Dans ce travail, j'ai montré que les cellules à base de nanofils cœur-coquille silicium et silicium amorphe (Si NW/a-Si:H) sont d'abord limitées par leur contact supérieur. Comme celui-ci est situé du côté de la lumière, il doit être à la fois conducteur et transparent. Même sur une structure planaire, il y a un compromis à trouver entre ces propriétés, puisque les porteurs de charge responsables de la conduction réfléchissent et absorbent la lumière. Des matériaux efficaces ont été développés pour les surfaces planaires, notamment les oxydes transparents conducteurs (TCOs) comme l'ITO, mais leur dépôt est modifié lorsque le substrat est nanostructuré. Ainsi, sur les nanofils Si NW/a-Si:H, la couche d'ITO déposée par pulvérisation cathodique n'est pas du tout

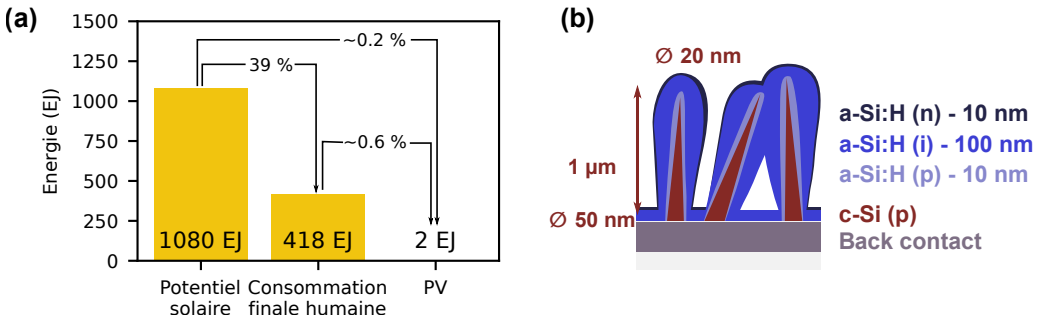

Figure 1: **(a)** Potentiel solaire exploitable comparé à la consommation humaine finale et à l'énergie consommée provenant du photovoltaïque. L'énergie est en exajoule (10^{18} J). **(b)** Schéma en coupe des nanofils Si NW/a-Si:H.

conforme. Même avec l'épaisseur optimale, la couche est très épaisse sur le dessus du nanofil et de plus en plus fine sur ses flancs. Cela induit des pertes optiques pour une conduction latérale qui reste médiocre. De plus, un seul matériau ne peut suffire à assurer le transport des porteurs de charge sur les échelles très différentes présentes (du nanofil individuel, 300 nm, à la cellule complète, 4 mm). Pour cette raison, le recours à un hybride est bénéfique. Dans notre cas, nous avons choisi d'allier l'ITO aux nanofils d'argent (Ag NWs), qui sont de très bon conducteurs. L'ITO est capable de connecter les nanofils Si NW/a-Si:H, tandis que le réseau de nanofils d'argent permet un maillage, ce qui assure une collecte du courant sur l'ensemble de la cellule. La Figure 2 **(a)** présente une coupe en microscopie électronique à balayage (MEB) d'une cellule solaire avec un contact hybride fait d'ITO et de nanofils d'argent. L'utilisation d'un hybride augmente le nombre de degrés de liberté accessibles pour l'optimisation et permet de décomposer l'optimisation en plusieurs étapes. Comme la nanostructuration de la cellule modifie les dépôts normalement prévus pour des substrats planaires, une optimisation directement sur la cellule est nécessaire. Cela empêche la mesure directe de la transparence et de la résistance de l'électrode.

Dans un premier temps, j'ai optimisé la transparence de la couche d'ITO. Pour la caractériser, j'ai utilisé des mesures EQE (efficacité quantique externe). La mesure du courant généré dans la cellule à très faible illumination permet de se défaire des problèmes de conduction. Comme le reste de la structure de la cellule est identique, nous avons pu comparer les électrodes. Parmi les épaisseurs testées (correspondant à 40 nm, 80 nm, 240 nm sur un substrat planaire), 80 nm a montré la plus grande transparence, grâce à une faible absorption et un effet d'anti-réflexion. Un revêtement plus conforme pourrait permettre une amélioration supplémentaire. Pour tester cette hypothèse, j'ai remplacé l'ITO par du TZO (oxyde de zinc dopé au titane) déposé par ALD (dépôt par couche atomique). Les mesures I-V ont montré que cela mène à de faibles résistances parallèles, car l'oxyde peut contacter électriquement la cellule planaire parasite, de mauvaise qualité, et les possibles défauts. J'ai donc conservé l'ITO déposé par pulvérisation pour l'oxyde transparent et conducteur. J'ai ensuite déterminé la densité optimale de nanofils d'argent en comparant les performances des cellules solaires avec un contact hybride {ITO 80 nm / Ag NWs} sous illumination AM1.5G. Comme attendu, les nanofils d'argent diminuent la résistance de série. Avec une faible densité, ils mènent aussi à une augmentation du courant de court-circuit J_{sc}. En effet, malgré les pertes optiques

induites, ils permettent une meilleure collection des (moindres) charges générées. Au delà de 9 µg/cm^2, les pertes optiques sont prédominantes et J_{sc} diminue. La densité optimale (16 µg/cm^2) correspond à une faible résistance de série R_{se} et à un J_{sc} qui reste élevé. Grâce au contact hybride, l'efficacité de conversion de la cellule est augmentée de 4.3 % à 6.6 % (Figure 2 **(b)**). Cette amélioration provient de l'augmentation de J_{sc} (amélioration de la transparence et de la conduction) et du facteur de remplissage, ou fill-factor (amélioration de la conduction).

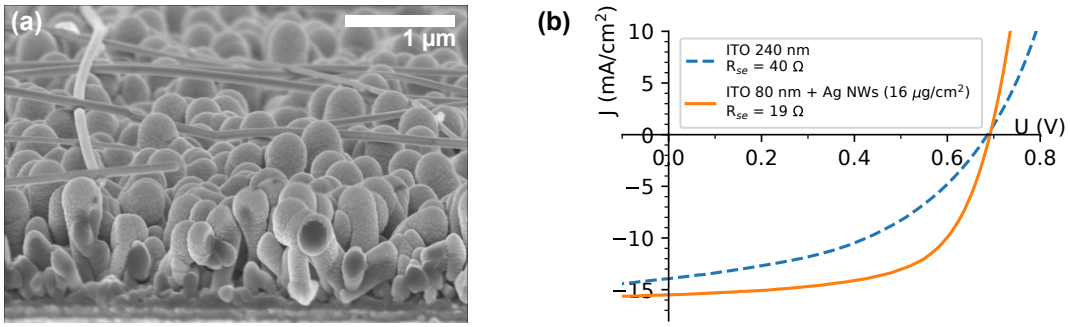

Figure 2: **(a)** Image MEB en coupe de nanofils Si NW/a-Si:H avec un contact hybride {ITO 80 nm / Ag NWs}. **(b)** Courbes J-V d'une cellule avec le contact optimal pour de l'ITO seul (bleu) et avec un contact hybride (orange).

L'un des inconvénients principaux des nanofils d'argent est leur dégradation dans le temps. De nombreuses études ont mis en avant cette dégradation, qui survient parfois en quelques semaines. Il y a deux causes principales : la corrosion de l'argent par le soufre présent dans l'atmosphère, fortement accélérée par l'humidité ambiante, et l'instabilité thermodynamique des fils. Cette dégradation se traduit d'abord par des nanoparticules, qui peuvent d'abord être observées au MEB (Figure 3 **(a)**). Les fils sont finalement hachés et la conduction électrique est perdue.

Pour empêcher cette dégradation, les nanofils ont souvent été encapsulés dans des matériaux devant les protéger. Nous avons choisi d'utiliser le TZO déposé par ALD. Grâce aux bonnes propriétés optiques et électriques du TZO, cette couche permet la protection des nanofils tout en faisant partie de l'électrode finale. Pour suivre la dégradation des nanofils d'argent, j'ai réalisé un dépôt de nanofils sur du verre et sur des substrats verre/ITO (chimiquement proche de l'environnement en cellule). Un échantillon témoin n'a pas été protégé. Sur les autres, ces différentes couches de protection ont été ajoutées : 5 nm, 10 nm, 20 nm de TZO déposé par ALD ou 20 nm d'ITO par pulvérisation cathodique. A cause de l'inertie chimique de l'argent, les dépôts de 5 nm et 10 nm de TZO n'ont pas suffi à recouvrir les fils. J'ai aussi observé un dépôt différent sur les nanofils d'argent en fonction du substrat sur lequel ces derniers étaient déposés.

J'ai suivi la dégradation des nanofils par l'observation en microscopie électronique à balayage, et par des mesures de transmittance et réflectance totales et de résistance de couche $R_{\square}$. Ce suivi régulier s'est déroulé sur 20 mois. Je n'ai pas observé de changement significatif dans les propriétés optiques (Figure 3 **(b)**). La résistance de couche R_{sheet} est assez stable, et reste bien inférieure à celle de 80 nm d'ITO (47 Ω/□), mais les mesures étant très dispersées, il n'y a pas de conclusion plus précise (Figure 3 **(c)**).

L'observation au microscope a montré des nanoparticules typiques de la corrosion des nanofils d'argent, mais leur nombre et leur taille restent limités. Ces particules n'ont été observées que sur les fils nus, car il n'est pas possible de les distinguer du TCO en microscopie pure. Cette étude montre que les nanofils d'argent sont stables sur une échelle de plus d'un an. Néanmoins, ils n'ont pas été exposés à d'importants niveaux de courant ou d'illumination. Or, la lumière et le courant peuvent accélérer la dégradation et seront nécessairement présents lors de l'utilisation d'Ag NWs sur des cellules solaires. La même étude sous illumination et/ou courant serait donc utile.

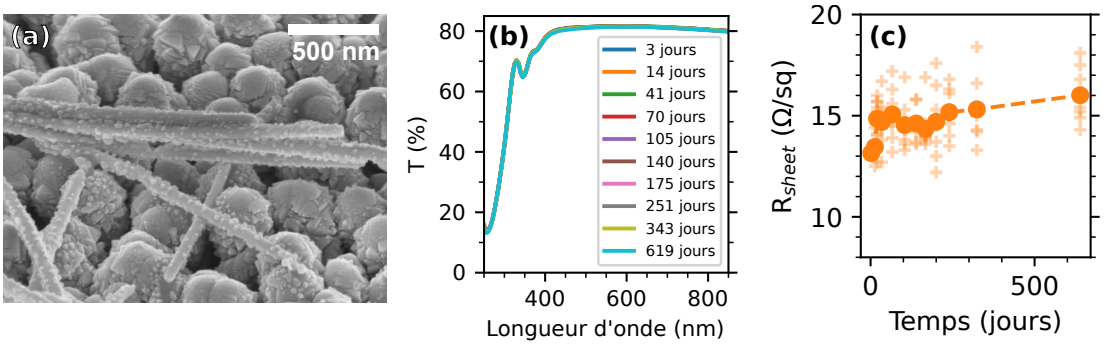

Figure 3: **(a)** Image MEB de nanofils d'argent dégradés. De petites nanoparticules (∼10 nm de diamètre) sont visibles à la surface. **(b)** Mesures répétées sur 20 mois de la transmittance totale d'un échantillon verre/Ag NWs sans couche de protection. **(c)** Évolution temporelle de la résistance de couche $R_{\square}$ pour le même échantillon.

Les cellules solaires majoritaires sont constituées de matériau inorganiques, peu flexibles. Or, la flexibilité est nécessaire pour certaines applications (bâtiment, procédure rouleau à rouleau (roll-to-roll process)). Pour un matériau donné, un changement de structure peut limiter la contrainte et améliorer la flexibilité de l'ensemble. En particulier, les ensembles de nanofils verticaux sont intrinsèquement flexibles, car le rayon de courbure typique est bien plus grand que le diamètre d'un nanofil (>mm contre < µm). Cependant, le contact supérieur nécessaire pour connecter tous les fils est également soumis à des contraintes mécaniques et peut limiter l'efficacité de la cellule. Le contact hybride devrait être moins sensible à la flexion. Le réseau de nanofils d'argent peut en effet se déformer pour s'adapter à la flexion. L'oxyde conducteur peut potentiellement rompre, mais le maillage de nanofils d'argent fera la jonction électrique entre les morceaux.

Nous avons donc fabriqué des cellules faites de Si NW/a-Si:H sur du verre flexible (70 um d'épaisseur) et testé leur performance sous illumination AM1.5G, avec différentes flexions. J'ai testé 29 cellules au total avec des rayons de courbure allant jusqu'à ∼2 cm. Les résultats sont résumés dans la Figure 4 **(a)**. La Figure 4 **(b)** est une photographie d'un échantillon sous flexion. 5 cellules ont montré une forte dégradation, principalement due à une résistance de shunt plus faible, même si certaines ont été complètement court-circuitées. 18 cellules n'ont montré aucune dégradation. Il semble que le contact n'était pas limitant, qu'il soit d'ITO uniquement (risque de rupture) ou hybride (risque de court-circuit par Ag NWs). Les mesures ont souvent été limitées par la fracture du verre.

Afin de mieux comprendre les mécanismes possibles de dégradation, j'ai utilisé la technique d'EBIC (courant induit par faisceau électronique). Celle-ci consiste à exposer une structure faite de semi-conducteurs à un faisceau électronique qui excite des paires électron-trou dans le matériau. En présence d'une jonction, et d'un contact aux bornes du dispositif, un courant est mesuré. Cela permet de réaliser une carte du courant généré et collecté en tout point avec une très bonne résolution spatiale (celle-ci est limitée par la poire d'interaction, i.e. volume dans lequel sont générées les paires). De plus, cette carte peut être comparée à la morphologie de l'échantillon obtenue par la microscopie électronique. La comparaison de cellules dégradées et non-dégradées après flexion n'a pas mis en évidence de différence claire. J'ai donc décidé de réaliser des observations EBIC directement sur une cellule en flexion. Pour cela, j'ai utilisé des feuillets métalliques (Al et Cu) comme substrats. Malheureusement, la plupart des cellules avec des nanofils Si NW/a-Si:H étaient court-circuitées (de nouvelles croissances devraient résoudre ce problème). Néanmoins, l'observation au MEB a montré des fissures dans les cellules à nanofils (Figure 4 **(c)**). Ceux-ci étant denses, ils ont un comportement qui s'approche des couches minces et perdent leur flexibilité. De plus, des observations EBIC sur des cellules planaires de silicium amorphe ont confirmé que les cartes EBIC permettent d'accéder à des défauts électriques qu'on ne peut obtenir avec la microscopie uniquement. Malgré cela, nous n'avons pu remonter à l'origine de la dégradation responsable de la baisse de R_{shunt}.

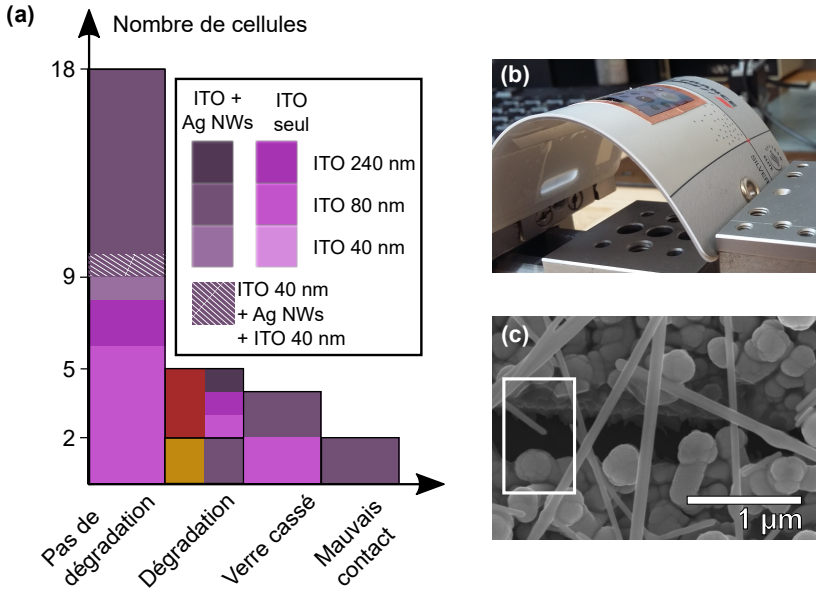

Figure 4: **(a)** Résultats des tests de flexion sous illumination. La légende indique les différents contacts supérieurs utilisés. Je fais la distinction entre deux types de dégradation : partielle (diminution de V_{oc}, du facteur de remplissage et de R_{shunt}, en jaune) et complète (diminution de I_{sc}, V_{oc}, du facteur de remplissage et de R_{shunt}, en rouge). **(b)** Photographie d'un échantillon sur verre flexible lors d'une mesure sous flexion. **(c)** Image MEB (vue de dessus) d'une cellule de Si NW/a-Si:H avec un contact hybride après flexion. On peut observer une fissure centrale, qui passe entre les nanofils de silicium (cadre blanc). Les nanofils d'argent sur le dessus joignent les deux parties.

En raison des problèmes de collecte des charges dans le silicium amorphe, l'utilisation de ce matériau dans les cellules solaires se limite à de faibles illuminations. De plus, ses propriétés électriques se dégradent sous l'exposition à la lumière (effet Staebler-Wronski). Pour ces raisons, on considère souvent le silicium amorphe comme un matériau ne pouvant résister à de fortes illuminations et peu d'études à ce sujet existent. Nous avons voulu comprendre le changement dans les performances sous illumination monochromatique à 532 nm (longueur d'onde adaptée à a-Si:H) et comparer le changement en fonction de la structure (Si NW/a-Si:H ou a-Si:H planaire). La majorité des mesures présentées sont faites sur une cellule avec un contact épais d'ITO. La cellule a un diamètre de 2 mm et la surface éclairée de 0.57 mm (utilisation d'un diaphragme de 800 µm). Pour différentes illuminations jusqu'à 330 W/cm^2, j'ai enregistré des courbes I-V pour une cellule Si NW/a-Si:H, une cellule planaire de silicium amorphe et une cellule de référence en silicium cristallin. A partir des courbes I-V, j'ai extrait les paramètres suivants : courant de court-circuit (I_{sc}), tension de circuit ouvert (V_{oc}), facteur de remplissage (FF), efficacité, résistances de série (R_{se}) et de shunt (R_{shunt}). De plus, j'ai répété des mesures pour certaines illuminations après exposition à différentes puissances. Cela permet de déterminer quels sont les changements réversibles ou irréversibles dans ceux observés. J'ai distingué différents effets.

Dès les premières puissances (1.7 W/cm^2), le facteur de remplissage diminue quand l'illumination augmente (réversible). Cela s'explique notamment par la forte résistance du contact supérieur et la faible mobilité des porteurs dans le silicium amorphe. J'ai aussi observé une diminution du courant I_{sc}. Elle correspond à un changement du matériau, car elle irréversible dans le temps. Après exposition à des puissances plus importantes ($\sim$100 W/cm^2), le niveau de courant initial est obtenu. L'effet Staebler-Wronski, caractéristique de a-Si:H, en est la raison. Quand le matériau est exposé à la lumière, des défauts sont créés. Ces défauts sont propices aux recombinaisons des porteurs de charge et limitent le parcours de ceux-ci. Cet effet est réversible lorsque le matériau est recuit. Dans notre situation, la température dans les fils augmente avec l'illumination et un recuit in-situ se produit.

Dans un second temps ($\sim$30 W/cm^2), nous avons observé une très forte diminution de V_{oc} (réversible), qui se produit également pour la cellule a-Si:H planaire, mais pas pour c-Si (Figure 5 **(a)**). Des mesures sous lumière pulsée (illumination de 1 ms à une fréquence de 10 Hz) ne montrent pas ce changement, alors qu'une illumination continue avec le même dispositif le montre. Cette diminution de V_{oc} provient donc d'un phénomène assez lent, probablement l'élévation de la température. Une mesure de l'évolution de V_{oc} en fonction du temps au moment de l'illumination confirme le temps important nécessaire à cette décroissance (Figure 5 **(b)**). En parallèle, j'ai mesuré l'évolution temporelle de la température de surface avec une caméra thermique. Celle-ci coïncide avec la décroissance de V_{oc}. Enfin, j'ai répété ces séries de mesure pour différentes surfaces d'illumination (diaphragmes de 400 µm, 800 µm, et 1400 µm). La décroissance de V_{oc} dépend majoritairement de la puissance totale, ce qui est en accord avec des effets thermiques. Ceux-ci peuvent provenir de la faible conductivité thermique du silicium amorphe comparé au silicium cristallin, ou du substrat (verre pour a-Si:H, c-Si pour c-Si). Des mesures de la température de surface pour une cellule de nanofils Si NW/a-Si:H avec du silicium cristallin comme substrat ont montré que l'augmentation de la température était principalement due au verre. Malheureusement, je n'ai pas pu réaliser les mesures I-V sur la cellule de nanofils Si NW/a-Si:H sur c-Si.

Pour des illuminations encore supérieures (∼60 W/cm^2), j'ai aussi observé une diminution (réversible) du courant I_{sc}. J'ai montré qu'elle était vraisemblablement causée par l'augmentation des recombinaisons (due à la température) associée à un faible facteur de remplissage.

Enfin, au-delà de ∼160 W/cm^2, les performances de la cellule ont été fortement dégradées (I_{sc}, V_{oc}, FF). Ce changement irréversible est probablement la conséquence d'une seconde dégradation du matériau par la création de défauts sous illumination (effet Staebler-Wronski). Néanmoins, d'autres phénomènes sont possibles. En particulier, les mesures avec le diaphragme de 400 µm ont conduit à une cristallisation partielle du silicium amorphe en silicium cristallin, ainsi qu'à des fissures dues à la température. Cela n'a pas été observé pour les autres illuminations, pour lesquelles les densités de puissance étaient plus faibles. Toutefois, on ne peut exclure ce phénomène à une plus petite échelle, indiscernable au microscope électronique à balayage.

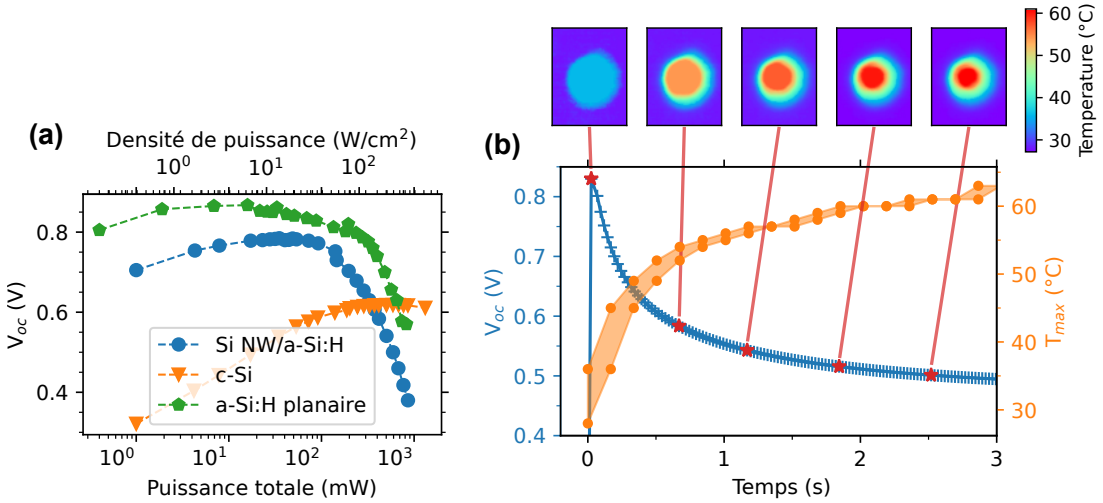

Figure 5: **(a)** Tension de circuit-ouvert V_{oc} en fonction de la puissance d'illumination pour une cellule à nanofils (Si NW/a-Si:H), une cellule de silicium cristallin (c-Si) et une cellule planaire de silicium amorphe. **(b)** Evolution temporelle de V_{oc} (bleu, gauche) et de la température maximale mesurée en surface (orange, droite). Le laser est allumé à t = 0 s. Des cartes de température montrent la répartition spatiale de la température.

Par ailleurs, j'ai pu utiliser la technique EBIC sur de nombreuses structures, détaillées en annexe. J'ai observé les cellules à base de Si NW/a-Si:H en vue de dessus. En particulier, j'ai mis en évidence la dégradation des propriétés électriques de a-Si:H sous le faisceau électronique. La tension d'accélération utilisée pour une mesure EBIC est un paramètre déterminant. J'ai montré que pour les nanofils Si NW/a-Si:H avec un contact épais d'ITO (240 nm), celle-ci devait dépasser 15 kV.

J'ai également caractérisé des cellules solaires à nanofils III-V sur silicium pour tandem, élaborées par gravure ou par croissance de nanofils. Lorsqu'un contact supérieur est déposé sur les nanofils, l'observation EBIC permet de comparer les propriétés entre les fils et de déterminer l'homogénéité de l'ensemble (Figure 6 **(a)**). De plus, l'utilisation de l'EBIC permet de vérifier la présence des différentes jonctions : la jonction principale

présente dans les nanofils (Figure 6 **(b)**, gauche) et la jonction tunnel qui fait la connexion électrique entre les deux cellules (Figure 6 **(b)**, droite). Je n'ai pas pu mettre en évidence la jonction de la cellule silicium. L'illumination avec le faisceau électronique est ponctuelle. Or, une cellule tandem à deux bornes nécessite qu'un même courant passe dans les deux cellules. Si une des cellules n'est pas éclairée, elle limite le courant qui peut être collecté aux bornes de la cellule tandem.

Finalement, j'ai aussi caractérisé des nanofils GaN/InGaN, à jonction axiale ou radiale, destinés à la fabrication de diodes électro-luminescentes. La caractérisation des fils axiaux a notamment permis de mettre en évidence une inhomogénéité dans la croissance. Seuls les fils correspondant à la structure attendue ont été électriquement contactés et un dispositif luminescent a pu être fabriqué.

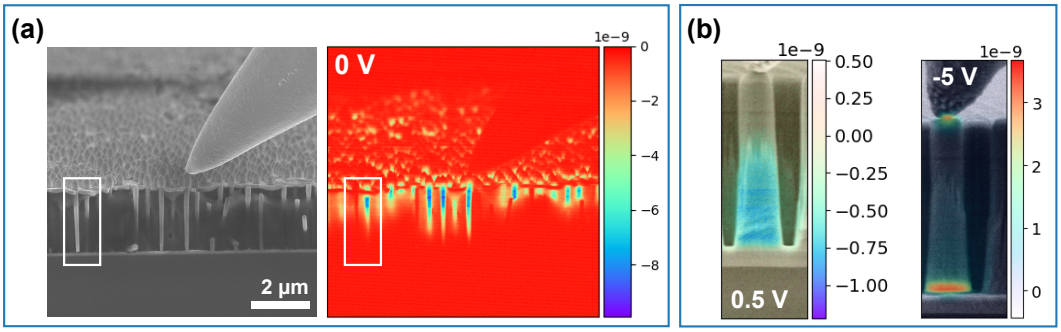

Figure 6: **(a)** Image MEB (gauche) et carte EBIC associée (droite) d'une cellule tandem composée d'un ensemble de nanofils cœur-coquille GaAs/InGaAs sur silicium. La jonction radiale des nanofils est visible. Un contact supérieur d'ITO permet de collecter le courant provenant de nombreux nanofils. **(b)** Superposition de carte EBIC et d'image MEB d'un nanofil InGaP sur silicium. Le courant associé à la jonction p-i-n axiale est collecté lorsqu'une polarisation inverse (ici $V > 0$) lui est appliquée (gauche). Lorsqu'une polarisation directe est appliquée, d'autres jonctions, de polarité opposée, peuvent être observées (droite). Ici, il s'agit un contact Schottky entre le semi-conducteur et la pointe (haut du nanofil) et de la jonction tunnel (pied du nanofil).

General introduction

In 2021-2022, the Intergovernmental Panel on Climate Change (IPCC) has issued its sixth assessment report[2]. It confirmed the modification of climate caused by greenhouse gases from anthropogenic origin. Although the alteration is irreversible, different mitigation and adaptation scenarios are still possible depending on the actions carried out worldwide. In particular, the third part of the report deals with the mitigation of climate change and recalls the necessity of low-to-no-carbon energy sources to reach a zero net greenhouse gases society. In scenarios that limit the global warming below 2 °C, low-carbon sources would produce more than 93% of global electricity by 2050 [Clarke 2022]. As an indication the final energy consumption in 2019 was 418 EJ (418×10^{18} J). Figure 7 shows the share of electricity in this consumption and the distribution of today's low carbon energy sources in electricity. It evidences that the shares of the recent renewable energies, photovoltaics (PV) and wind energy, are still small.

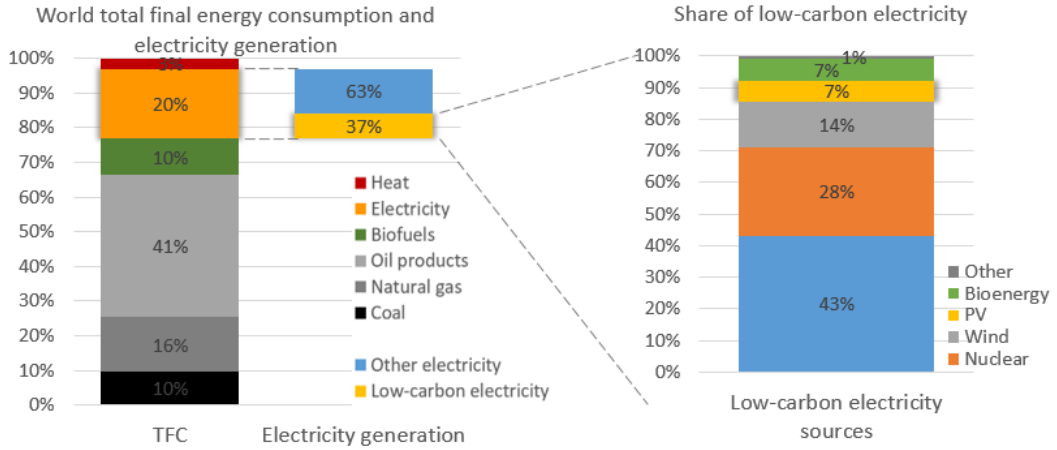

Figure 7: **(a)** Distribution of energy sources in the total final consumption (TFC), **(b)** share of low-carbon electricity in the electricity generation and **(c)** distribution of energy sources in the low-carbon electricity mix. *PV* stands for photovoltaics, *Other* comprises geothermal, thermal solar (1 % of all solar) and marine energy. With data from [Clarke 2022]. All values correspond to 2019.

PV relies on the conversion of solar energy to electricity. Its potential is tremendous, as it corresponds to more than twice the final consumption of energy by humanity in 2019. Even after subtracting the part needed for land-use, the energy reaching the Earth's surface amounts to 300 PWh (300×10^{15} Wh) per year (1080 EJ/yr) [Dupont 2020]. Still, as is clear in Figure 8, only a small percentage is used. Nonetheless, thanks to the development of technologies (and the resulting lower cost) and policies, the PV installation is increasing rapidly (+170 % increase in the share of consumed energy between 2015 and 2019).

In 2020, 95 % of solar PV is made of crystalline silicon, and good-efficiency modules give a ∼20.4 % power conversion efficiency [Fraunhofer ISE 2022]. Nonetheless, although

[2] https://www.ipcc.ch/reports/?rp=ar6

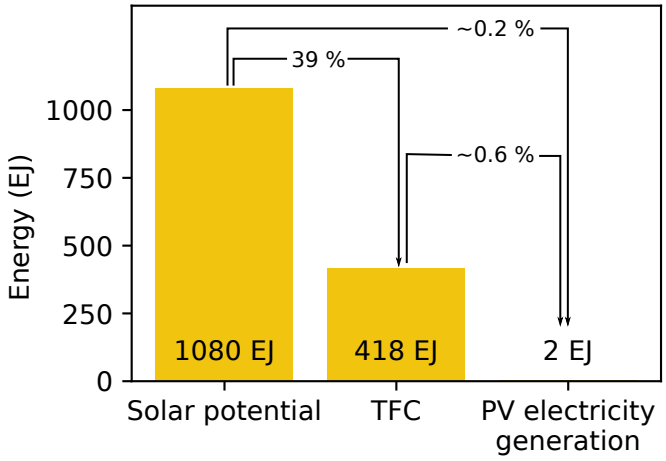

Figure 8: Exploitable solar potential, compared to the total final consumption (TFC) and to the actual energy generated by PV in 2019. With data from [Clarke 2022].

crystalline silicon performs better (today) than most PV technologies, especially on the scale of panels, the power conversion efficiency is not the only parameter for choosing a PV technology. In particular, the following factors are also important for a widespread and low-carbon PV:

- the environmental impact of the system,
- the dependence of the power conversion efficiency on the illumination and temperature conditions,
- the match between the PV technology characteristics and the application.

The environmental impact of the system can be estimated through life cycle assessments. The common criteria for comparison are the energy payback time EPBT (time required to produce the energy needed for the fabrication), or the energy return on investment EROI (amount of energy produced over the lifetime of a panel compared to the energy needed for the fabrication) and the emission of greenhouse gases per kWh (given in g CO_2-eq./kWh). Other environmental effects, such as the land use and the impact on biodiversity, should be assessed as well [Hertwich 2015]. They are however less dependent on the technology. From several studies, it appears that thin-film PV performs much better environmentally than Crystalline silicon (c-Si), due to the huge amount of energy and the acid needed for the silicon purification (1.6 kg HCl at 30 % for 1 kg solar-grade Si) [Frischknecht 2020, Liu 2020, Louwen 2017]. Cadmium Telluride (CdTe) shows a particularly low impact in terms of energy and greenhouse gase emissions, while Hydrogenated amorphous silicon (a-Si:H) remains behind due to its lower efficiency. However, CdTe or Copper Indium Gallium Sulfide (CIGS) require materials that are less abundant than silicon, and even highly toxic for cadmium. In addition, whereas the standard test conditions (1 Sun illumination, 25 °C) allow for comparison between technologies, the change in the performance of different technologies with illumination (direct or diffuse, illumination power and angle) or with temperature is not taken into account. Yet, it can affect their actual conversion efficiency depending on the location of

the panels. Finally, different applications, for instance a utility-scale PV central, rooftop PV or small on-device solar cells, have different requirements. While they may be less efficient, smaller installations allow for a distributed production of PV and reduce losses due to transport. Consequently, there is room for other technologies than c-Si, including less efficient ones.

Amorphous silicon, that is studied in this thesis, is an abundant material, which does not require a high energy for fabrication, and better sustains moderate to high temperatures. However, it is limited by the low mobility of its charge carriers. The transition from thin films to radial-junction nanowires (NWs) helps to overcome this issue. In addition, they could result in flexible solar cells that are low-cost and made of inorganic materials. a-Si:H NW solar cells have been demonstrated already in 2010. During my phD, I have analyzed different aspects related to their morphology and material. The manuscript is organized as follows.

In chapter 1, I present the Si NW/a-Si:H solar cells. First, I recall some principle of photovoltaics and the present status of PV technology, then I explain what nanowires are and how they are beneficial for solar cells. I also give a detailed description of the structure studied, made of arrays of Si NW/a-Si:H. Finally, I focus on the impact of resistances in solar cells.

Indeed, the use of NWs affects the collection of current at the scale of the cell because of a high series resistance. In chapter 2, I explain why the collection of current is difficult in the Si NW/a-Si:H solar cells and evidence the advantage of using a hybrid electrode (made of two materials). This electrode consists in Indium Tin Oxide (SnO_2-In_2O_3) (ITO) and silver nanowires (Ag NWs). I describe how I optimized its optical and electrical properties directly on the array of nanowires. Furthermore, I studied the consequences of replacing ITO by Ti-doped ZnO deposited by Atomic-Layer Deposition (ALD) and reported the conclusions.

On solar cells with a hybrid electrode, we observed the degradation of Ag NWs. To prevent it, we used an encapsulation layer made of a conductive and transparent oxide. I assessed the change in the morphology and optical and electrical properties over more than a year. All details are given in chapter 3.

Thanks to the standing NWs and to the hybrid electrode, we expect the resulting solar cell to be flexible. In chapter 4, I report the bending tests carried out under illumination and the observation of bent cells in a SEM chamber and with EBIC.

Finally, in chapter 5, I focus on the properties of amorphous silicon in order to understand the actual limitations of the material and how they are affected by the NW architecture. To this end, I compared the performance of solar cells made of Si NW/a-Si:H, c-Si and planar a-Si:H under high illumination with monochromatic light at 532 nm. I observed multiple changes and disentangled the different causes.

In addition, I describe Electron-Beam Induced Current (EBIC), a characterization tool that gives access to the microscopic electrical properties of solar cells. I carried out EBIC observations of various structures. Although they are not directly related to the main topic of the thesis, they show the assets of this tool for the understanding of semiconductor junctions. They are reported in Appendix A.

Chapter 1

Introduction

Contents

1.1 Solar cells

1.1.1 Principle

A solar cell is a device which absorbs light and generates an electrical power from it. Its Power Conversion Efficiency (PCE) can be determined by comparing the two powers, the maximal electrical one $P^{\text{el}}_{\text{max}}$ and the incoming light power P^{light},

$$PCE = \frac{P^{\text{el}}_{\text{max}}}{P^{\text{light}}}. \tag{1.1}$$

To obtain a solar cell, a semiconductor is needed, as it enables the transformation of the light to electrochemical power. As is displayed in Figure 1.1 **(a)**, photons from the incoming light can be absorbed by the semiconducting material with their energy transferred to the material, which creates electron/hole (e^-/h^+) pairs. For an efficient solar cell, the photogenerated charge carriers must be extracted. It requires a separation of the charge carriers to be collected at opposite contacts. Asymmetric structures are used to this end, such as the p-n junction.

A semiconductor material is characterized by its band gap energy E_g. As displayed in Figure 1.1 **(b)**, only photons of a higher energy (i.e. shorter wavelength) are absorbed.

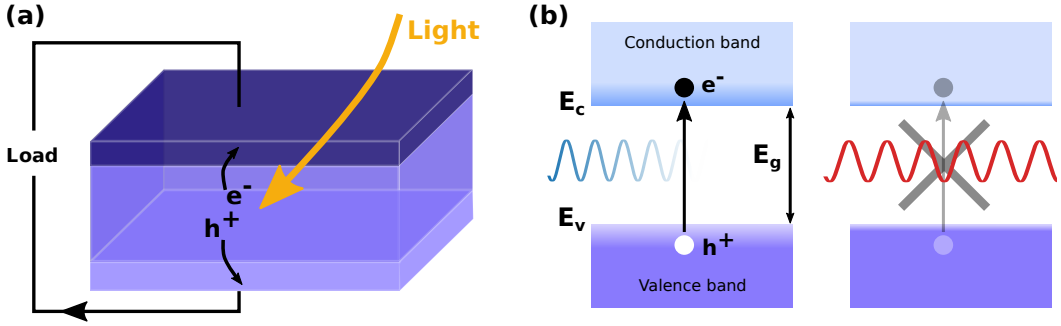

Figure 1.1: **(a)** Sketch of a solar cell in use. The asymmetric structure is shown through the colors used for the different layers. The use of different materials or doping types ensures the collection of carriers. **(b)** Schematic band diagram of a semiconductor with band gap energy E_g with incoming blue or red light.

The power conversion efficiency of solar cells has intrinsic, physical limitations, described and modeled by Shockley and Queissler [Shockley 1961, Guillemoles 2019], which are imposed by the balance between the absorption losses and thermalization losses. With the optimal band gap energy (1.34 eV), the highest power conversion efficiency that can be reached is 33 %. New structures and setups, such as multi-junction solar cells and Concentration Photovoltaics (CPV), have been developed to overcome these limitations, with an ultimate record of 47.1 % for a multijunction cell under concentration [Geisz 2020].

1.1.2 I-V characteristics

I-V curves I-V curves are the most important characterization of solar cells. A voltage is applied and the current is measured. Figure 1.2 shows an example of a J-V curve

(I-V curve where the current density J is displayed) under illumination. The maximal power that the solar cell can generate per unit area, $P_{\max}$, can be determined as well as the corresponding maximal power point (mpp). From this value, the performance of the solar cell under a given illumination is obtained and different solar cells can be compared.

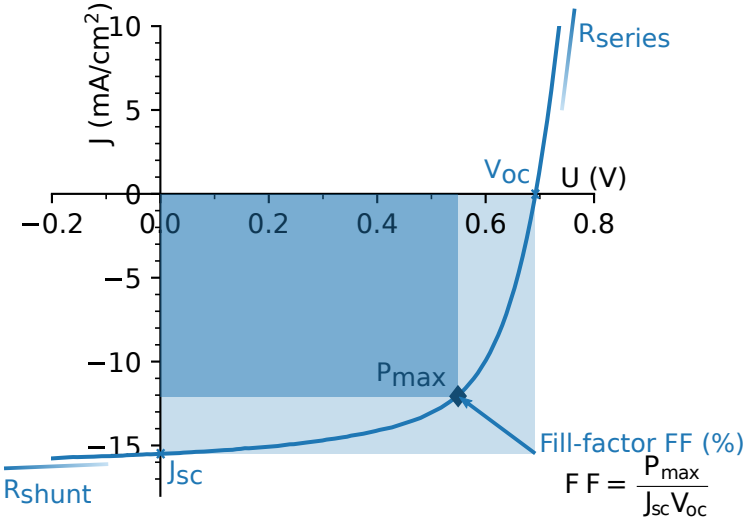

Figure 1.2: J-V curve of a solar cell. The maximal power per unit area $P_{\max}$ is shown with ♦.

Other parameters can be extracted that also describe the performance of the device, they are shown in Figure 1.2. In particular, the short-circuit current density J_{sc}, the open-circuit voltage V_{oc} and the fill-factor FF help to understand the limitations of the device.

J_{sc}, V_{oc}, FF The short-circuit current density corresponds to the highest current density that could be extracted from the cell (however, without power since $V = 0\,\mathrm{V}$). It strongly depends on the absorption of light by the device. Conversely, the open-circuit voltage corresponds to the highest voltage that could be obtained from the cell (however, without power since $I = 0\,\mathrm{A}$). It is mostly determined by the energy of the collected carriers (via the band gap energy and the contacts). The fill-factor FF compares the obtained power per unit area to the upper limit set by J_{sc} and V_{oc},

$$FF = \frac{P_{\max}}{J_{sc} V_{oc}}. \tag{1.2}$$

The fill-factor describes the good collection of carriers: ideally all carriers should be collected, without losing any energy. In Figure 1.2, the fill-factor corresponds to the ratio of the dark blue area to the light blue one. It can also be understood as the squareness of the I-V line. It is a complex parameter that depends on various parameters in the device. High fill-factors are above 75 % up to 85 % for the record cells [Yoshikawa 2017, Peng 2021]. More information can be found in I-V curves, but it requires a more thorough analysis.

Standard illumination Standard conditions (temperature and illumination) have been stated to compare different PV technologies. The standard illumination for flat panels is called AM1.5G and is shown in Figure 1.3. It was initially determined from sunny sites of measurements in the US. It corresponds to a total power density of $1000\,\mathrm{W/m^2}$ (or $100\,\mathrm{mW/cm^2}$) and to a wavelength distribution close to the sunlight reaching the earth surface. AM1.5 stands for *Air Mass 1.5*, because the sunlight has gone through 1.5 atmosphere (due to the angle). This lowers the overall power density and add specific features. G stands for *global* and takes into account both the direct and diffuse light. Other standards are used for concentration Photovoltaics (PV) (direct + circumsolar air mass 1.5, AM1.5D) or spatial PV (extraterrestrial spectrum, AM0).

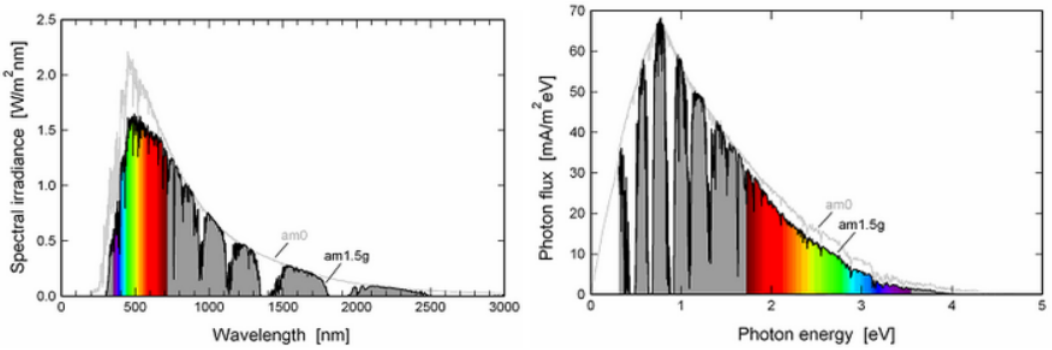

Figure 1.3: AM0 and AM1.5G standard spectra. The absorption due to the atmosphere (UV light and molecular bands in the IR) is clear. The visible part of the spectrum is shown with colors. From PV Lighthouse website.

1.1.3 p(i)n junctions

Principle A fundamental structure in today's solar cells is the *p-n junction*. A p-doped and an n-doped materials are combined.[1] Because the electrons have different potentials in the p-doped and n-doped materials, they move, until the potential, called the *Fermi level*, is the same everywhere. The junction is at thermal equilibrium. It results in the situation depicted in Figure 1.4 **(a)**. A gradient in the electron concentration (n) is obtained, as well as in the hole concentration (p). At the junction, the concentration of carriers is very low. It is the *depletion region*. In addition, the opposite charges create a built-in potential V_{bi} and an electric field.

p-n vs. p-i-n junctions A structure close to the p-n junction is the p-i-n junction, where an intrinsic (non-doped) layer is inserted between the doped regions. Figure 1.4 shows the features of a p-n and a p-i-n homojunctions at thermal equilibrium. In a p-n junction, the electric field is localized at the junction. Only carriers generated generated in the depletion region or able to reach it through diffusion will take advantage of the field. It is an issue for materials with short diffusion lengths, since the collected current will be generated only over a very thin layer. In a p-i-n junction, the equilibration between electrochemical potentials from the p- and n-doped regions results in charged

[1] If the same material is used, it is a homojunction, if not a heterojunction.

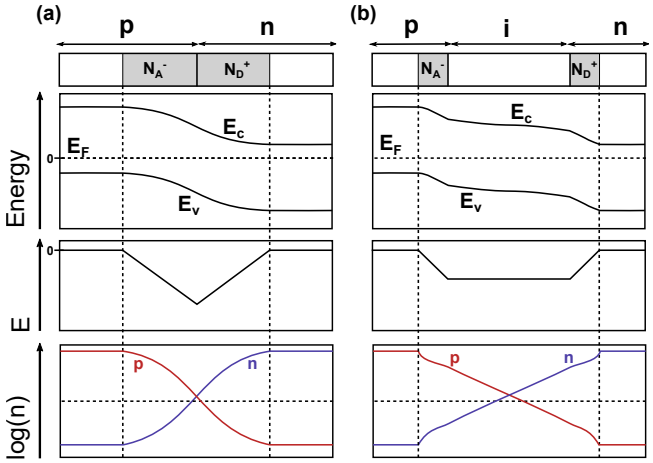

Figure 1.4: Schematic energy band diagram with the valence and conduction band edges (E_v and E_c) and the Fermi level E_F (top), electric field (middle) and logarithmic concentration of carriers (bottom) in **(a)** a p-n junction and **(b)** a p-i-n junction at thermal equilibrium (dark, no applied voltage). N_{A}^- is the concentration of ionized acceptors and N_{D}^+ is the concentration of ionized donors.

regions at the p/i and i/n interfaces. The electric field spans across the whole intrinsic layer, which makes the collection of carriers generated in this region easier. For the same doping of the p and n regions, the magnitude of the electric field is lower in a p-i-n junction than in a p-n one. In addition, the actual depletion width (shaded region) is smaller. As detailed in [De Lépinau 2020], it can be highly beneficial for core-shell nanowires, where (thin) doped regions can be fully depleted if the doping is too low.

1.1.4 Out of equilibrium

Figure 1.4 displays the features of p-n and p-i-n junctions at thermal equilibrium. All carriers share the same electrochemical potential and there is no current. Yet, a solar cell is used out of equilibrium. When carriers are injected, either from external light or under bias, the cell is out of thermal equilibrium[2] and currents are created. A steady-state can be reached (no change in the carrier-density at a given position with time, $\partial n/\partial t = 0$), but the band diagrams, currents, potentials, carrier densities are different from thermal equilibrium.

Quasi-Fermi levels Since the solar cell is not at thermal equilibrium when used, there is no Fermi level common to all carriers. However, in one band, thermalization is fast and the population of the band is at equilibrium. A *quasi-Fermi level* can be used to describe the population of the band. With F_n and F_p the quasi-Fermi levels for electrons and holes respectively, and in the case of non-degeneracy ($F_n \ll E_c$, $F_p \gg E_v$), the Maxwell-Boltzmann distribution is used instead of the Fermi one. It leads to

[2]There is also some carrier injection under thermal equilibrium, but it is fully related to the temperature, either generation via thermal or generation via optical from radiations of the black body.

$$F_n = E_c + k_B T \ln\left(\frac{n}{N_c}\right), \tag{1.3a}$$

$$F_p = E_v + k_B T \ln\left(\frac{p}{N_v}\right). \tag{1.3b}$$

Electrons and holes collected at each contact do not have the same potential. The difference $F_n - F_p$ is called the Quasi-Fermi Level Splitting (QFLS) and corresponds to the maximum voltage that can be obtained.

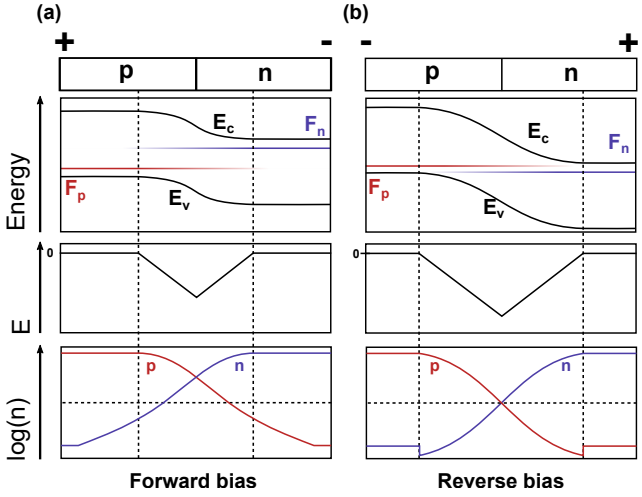

Figure 1.5: Schematic energy band diagram (top), electric field (middle) and logarithmic concentration of carriers (bottom) for a p-n junction under **(a)** forward and **(b)** reverse bias.

Bias When a bias (i.e. a voltage) is applied to the cell, carriers are electrically injected. Under forward bias (see Figure 1.5 **(a)**), electrons are injected through the n-doped region. They are pushed to the depletion region, where they start filling the donor states that were depleted. The depletion region shrinks and since there are less charges, the electric field decreases. More carriers can overcome the barriers and recombine. The diode current, called *recombination current*, increases. Conversely, under reverse bias (Figure 1.5 **(b)**), the depletion region becomes larger, the electric field is increased. The current, called *(reverse) saturation current*, corresponds to the carriers generated close to the depletion region that can be drifted to the region where they are the majority carriers.

Illumination Illumination generates an excess density of carriers in the cell. It affects the Fermi level of charge carriers and reduces the electric field, as shown in Figure 1.6 for a p-i-n junction.

At a position x, the density of charge carriers is determined by the density at equilibrium, n_0 or p_0, and the excess density, $\delta n = \delta p$. In the n-doped region (superscript n), $n^n(x) = n_0^n(x) + \delta n^n(x)$ and $p^n(x) = p_0^n(x) + \delta p^n(x)$. If this excess density is lower than the concentration of majority carriers at equilibrium, i.e. $\delta n^n \ll n_0^n$ and $\delta p^p \ll p_0^p$, the

cell is in the *low-injection regime*. Out of the depletion region, the distinction between minority and majority carriers remains. Most of the theory of solar cells is done for a low-injection regime, where the diffusion of minority carriers governs the recombination current.

In the *high-injection regime*, $\delta n^n \gg n_0^n$, and $n^n \simeq \delta n \simeq p$. In a doped region, the density of majority carriers is mostly determined by the doping density. For a c-Si cell, where the doping is typically around $2\times10^{16}\,\mathrm{cm}^{-3}$ in p-doped wafers, and for a lifetime of electrons of 50 µs, it is already the case under 1 Sun ($\sim3\times10^{16}\,\mathrm{pairs/cm}^3$ at 500 nm depth). Under high-injection, the diffusion of both charge carriers should be considered in the transport equations (ambipolar diffusion) and some simplifications used for the solving of equations in the low-injection regime are not valid anymore.

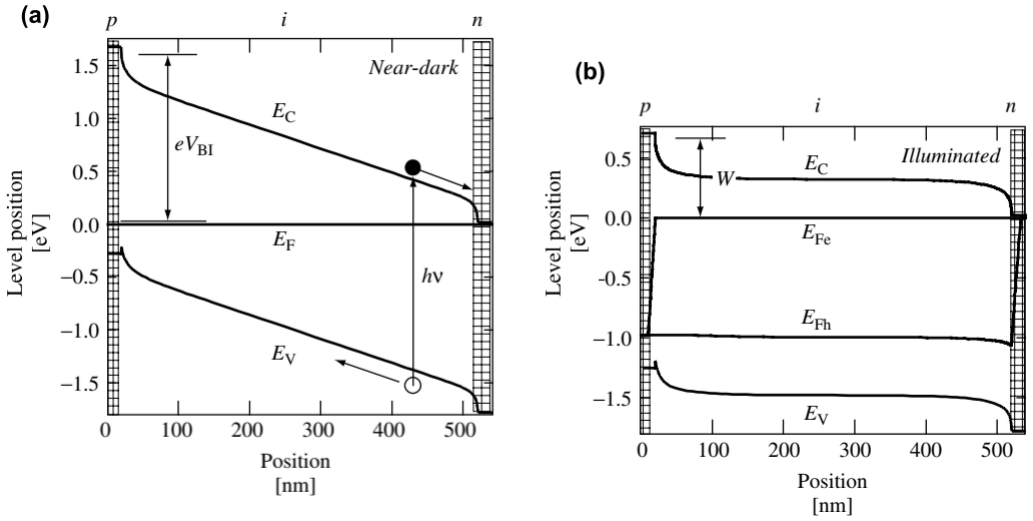

Figure 1.6: Band diagram of a p-i-n junction **(a)** in the dark and **(b)** under illumination under open-circuit conditions. From [Luque 2003].

1.1.5 Solar cell equivalent circuit

One-diode model of solar cells The ideal behavior of a solar cell can be modeled in an equivalent electrical circuit shown in Figure 1.7.

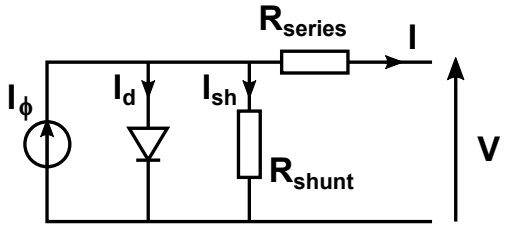

Figure 1.7: One-diode equivalent circuit of a solar cell as a power generator.

In this circuit, the properties of the device are modeled as lumped components. A current source delivers a current I_ϕ corresponding to the photocurrent. A diode, with a

diode current I_D, models the behavior of the p-n or p-i-n junction. Its current depends on the voltage following the relation derived by Shockley [Shockley 1949]

$$I_D = I_0\Big[\exp\Big(\frac{qV}{k_\mathrm{B}T}\Big) - 1\Big], \tag{1.4}$$

where I_0 is the reverse saturation current. The series resistance corresponds to different sources of resistance in the device. It is detailed in Section 1.4.2. Its effect is mostly evident beyond $\mathrm{V_{oc}}$, but in some cases it can affect the I-V line around the mpp and even close to short-circuit. It is given in $\Omega\mathrm{cm}^2$, with values as low as $0.32\,\Omega\mathrm{cm}^2$ ($1.7{\times}10^{-3}\,\Omega$) in present c-Si solar cells [Yoshikawa 2017]. The shunt resistance is a description of the alternative current paths that limit the collection of the photogenerated current. The higher $\mathrm{R_{shunt}}$ is, the better the device. Its effect is clear at reverse bias ($V < 0$), but when it is low, it can impact the I-V line around the mpp and even close to open-circuit. It is given in $\Omega\mathrm{cm}^2$.

From the equivalent circuit, an equation governing the current delivered by a solar cell under illumination can be derived,

$$I = I_\phi - I_0\Big[\exp\frac{q(V + R_\mathrm{se}I)}{k_\mathrm{B}T} - 1\Big] - \frac{V + IR_\mathrm{se}}{R_\mathrm{sh}}. \tag{1.5}$$

It describes the solar cell working as a power generator[3]. I_ϕ, $\mathrm{I_{sc}}$, $\mathrm{I_0}$ and $\mathrm{V_{oc}}$ are positive values.

2-diode model and n_id Depending on the mechanisms for recombinations and the cell imperfections, the dependence of the diode current on the voltage can vary. A two-diode model can be used, with each diode accounting for one recombination mechanism, or an ideality factor, n_id, can be added.

$$I_D = I_0\Big[\exp\Big(\frac{qV}{n_\mathrm{id}k_\mathrm{B}T}\Big) - 1\Big]. \tag{1.7}$$

The diode ideality factor n_id governs the rectifying behavior of the cell. Its impact is mostly seen around the maximal power point in the I-V curve.

1.1.6 PV technologies

Among the single junction solar cells under AM1.5G, the highest efficiency (29.1 %) has been obtained with GaAs. **III-V** materials are efficient, but expensive and their use is limited to spatial applications or CPV. **Crystalline silicon** is the leader of mainstream PV, with a 95 % share of the market [Fraunhofer ISE 2022]. The technology is advanced, with high record efficiencies as well for cells (26.7 %) as for commercial modules (20.4 % in average, up to 22.4 %). However, it needs a rather thick absorbing layer (∼200 µm)

[3]However, when applying voltage to the cell, it works as a passive component. The I-V curve as measured corresponds to the passive convention and would be described with

$$I = -I_\phi + I_0\Big[\exp\frac{q(V - R_\mathrm{se}I)}{kT} - 1\Big] + \frac{V - IR_\mathrm{se}}{R_\mathrm{sh}}. \tag{1.6}$$

In this case, $\mathrm{I_{sc}}$ is negative. We chose to display the I-V curves as they were recorded, i.e. following the passive convention. Nonetheless, for an easier understanding, we refer to the absolute value of $\mathrm{I_{sc}}$.

and a high purity. The purification requires a large amount of energy and the use of hydrocholoric acid (1.6 kg HCl at 30 % for 1 kg solar-grade Si) [Frischknecht 2020]. **Thin-film** solar cells (e.g. CIGS, CdTe or amorphous silicon (a-Si:H)) are a few µm - even a few 100s nm - thick. Apart from a-Si:H, they display good record efficiencies (23.4 % for CIGS, 22.1 % for CdTe). They represent the remaining 5 % share of the market, mostly with CdTe. **Perovskite** solar cells have experienced a tremendous development since 2010, reaching 25.7 % efficiency today. They are a family of hybrid organic-inorganic or fully inorganic materials in a crystalline structure called perovskite. They display a high absorption coefficient and a variety of compositions and properties can be obtained. Nonetheless, their lack of stability impedes their widespread use. Finally, one can also mention **organic** (18.2 %), **dye-sensitized** (DSSC) (12.3 %), **quantum dot** (18.1 %) and **kesterite** (13.0 %) solar cells.

The record efficiencies for each family are summarized in the NREL chart[4], which displays a good overview of technologies and their history. The record details can also be found in the biannual review by Green et al. [Green 2022], where modules record efficiencies are also presented.

Most of the established technologies are based on a planar structure (substrate and stack of thin films). However, non-planar structures such as NWs can be beneficial to solar cells regardless of the material.

1.2 Nanowire solar cells

1.2.1 Nanowires

Nanowires are structures with a high aspect ratio and a submicrometer diameter. They are typically several tens to hundreds of nanometers thick and a few micrometers long. Because of the high surface to volume ratio, they show properties that differ from the bulk material. In particular they show singular optical, electrical and mechanical properties. Semiconductor nanowires are therefore very promising for new architectures in many opto-electronic devices [Yan 2009].

Single NWs can be used, either lying or standing, but I will focus on arrays of standing nanowires, that are required for efficient solar cells. These arrays can be made from different materials, with different fabrication methods. This results in very different structures (density, uniformity and vertical alignment between nanowires), as shown in Figure 1.8.

1.2.2 Increased absorption

Nanowire arrays allow for an increased absorption compared to thin films, thanks to their light trapping and low optical reflectance.

Origin Due to their small diameter and high refraction index, radial mode resonances occur in single NWs illuminated along the NW axis and they act as waveguides. Specific electromagnetic modes develop, depending on the diameter, and wavelength [Fountaine 2014]. Figure 1.9 **(a)** displays the simulated electric field and absorbed

[4] https://www.nrel.gov/pv/cell-efficiency.html

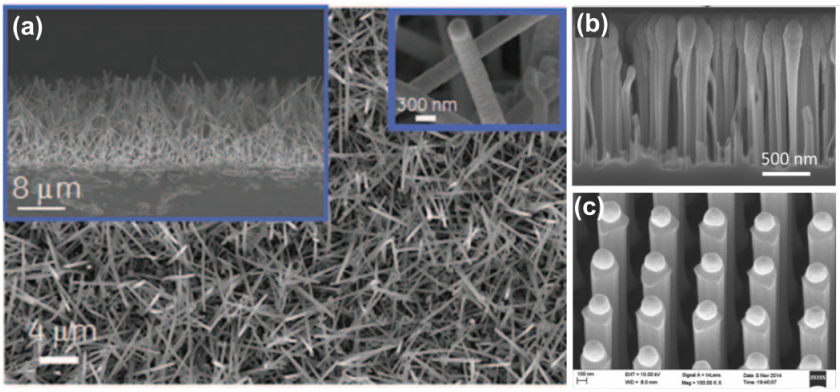

Figure 1.8: SEM images of solar cells made of a NW array. **(a)** Self-assembled with arbitrary direction c-Si/a-Si:H NWs. Extracted from [Tsakalakos 2007]. **(b)** Vertically etched Silicon Heterojunction (SHJ) Si NWs. Extracted from [Togonal 2016]. **(c)** Bottom-up, vertically-aligned GaAs NWs. Extracted from [Aberg 2016].

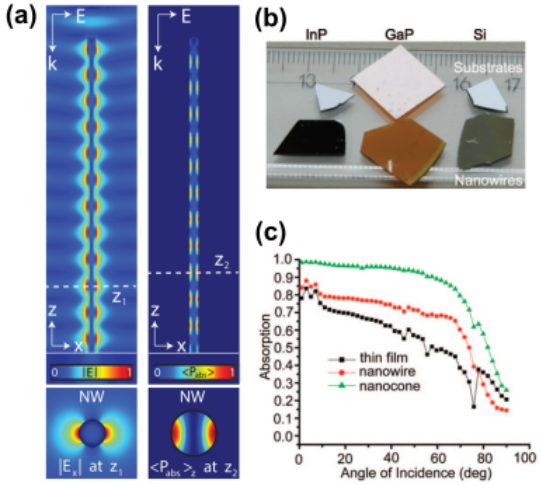

Figure 1.9: **(a)** Simulations of the (left) amplitude of the electric field around an InP nanowire under normal illumination and (right) absorbed power per unit volume in the NW under normal illumination. Vertical (top) and horizontal (bottom) cross-sections are displayed. The InP nanowire is standing on top of an InP substrate, the excitation wavelength is 532 nm. Extracted from [Grzela 2014]. **(b)** Picture of planar substrates and NW arrays made of InP, GaP and Si. The specular reflection is clearly lower with NWs. Extracted from [Muskens 2008]. **(c)** Experimental absorption in a thin film of a-Si:H compared to nanostructures at 488 nm. Extracted from [Zhu 2009].

power in a single InP nanowire. It results in an increased absorption compared to the amount of material, absorption which strongly depends on the wavelength and can be tuned by changing the NW diameter. For instance, simulations in [Krogstrup 2013] show that a single standing GaAs NW can present an absorption cross-section area 10 times larger than its geometrical cross-section. The effect of single NWs on the distribution of the electromagnetic field can be experimentally assessed, for instance with fluorescence confocal microscopy [Frederiksen 2017]. The increased absorption can be enhanced thanks to multiple reflections between the bottom and the top of the NW (observed as Fabry-Perot interferences in the spectra). In addition, collective effects also occur when NWs are in an array. Yet, according to [Mokkapati 2012], individual effects are responsible for most of the enhancement. Among collective effects, some are specific to well-ordered structures, such as the coupling of near-field evanescent waves [Azizur-Rahman 2015, Fountaine 2014]. Reduced reflection is also observed in disordered arrays, thanks to scattering between NWs with multiple angles. Muskens et al. showed that the effective medium model does not fully account for the behavior of (some) NW arrays [Muskens 2008].

Consequence It results in a lower reflectance of nanowire samples, especially the specular one, as can be seen in Figure 1.9 **(b)**. Measurements showed that it corresponds to an increased absorption in NW structures compared to flat ones, with a significant part of the absorption that occurs in the nanowires [Diedenhofen 2011]. A lower dependence on the illumination angle is observed (see Figure 1.9 **(c)**). For a given absorption, much less active material would be needed.

1.2.3 Stress distribution in NWs

Lattice mismatch In addition, NWs with low densities of defects can be grown on non-lattice-matched substrates. In bulk materials, dislocations enable the stress relaxation, but they cause defects, which act as recombination centers. Because of the geometry of NWs, the stress relaxation takes place at the free lateral surface and the NWs can be grown without defects on substrates despite the lack of lattice matching [Cirlin 2009, Kavanagh 2010]. It is of prime importance for III-V materials, whose lattice-matched substrates are very expensive, or for the development of III-V/Si tandem solar cells.

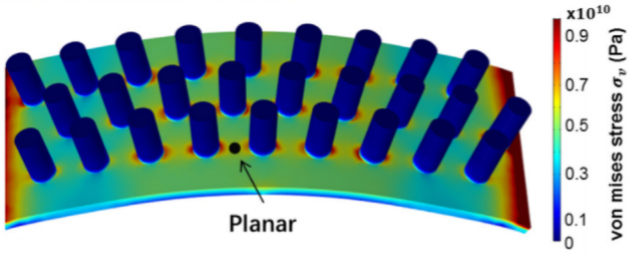

Figure 1.10: FEM-simulated stress distribution in a bent array of Si NW/a-Si:H on Al foil. From [Sun 2018].

Flexibility High-quality nanowires can therefore be grown on various substrates, especially inexpensive and flexible ones. Growth of NWs on flexible substrates have been reported, for instance on stainless steel, Al foil or Polyimide (PI) [Tian 2016]. Moreover, because of the small diameter of a nanowire compared to typical bending radii (<500 nm vs. >1 mm), nanowire arrays are inherently flexible compared to the bulk inorganic materials. This is clear in finite-element simulations such as the one presented in Figure 1.10. There is no stress in the NW, in contrast to the substrate. However, the junction between the NW and the substrate is a weak spot.

1.2.4 Architectures

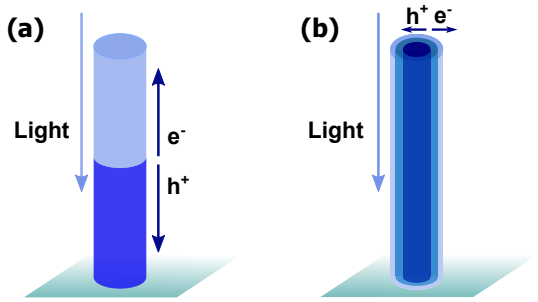

Figure 1.11: **(a)** Axial and **(b)** radial junction in a NW. The direction of light and the direction for the collection of charge carriers are shown with arrows.

p-n and p-i-n junctions in nanowires can follow an axial or a core-shell structure, as displayed in Figure 1.11. The axial geometry is similar to thin film solar cells, with contacts at the base and at the top of the nanowires. Nanowires are typically encapsulated in a transparent polymer, which serves as an electrical insulating layer and as a mechanical support for the transparent top contact. Radial junctions can be found in core-shell structures. This geometry allows for the decoupling of the electrical and optical directions. Whereas the light propagates along the axial direction, charge carriers are collected in the radial direction. Because of the nanowires aspect ratio, it leads to a large optical path and a short electrical path, enhancing both the light absorption and the charge carriers extraction. However, the outer layer of the NW has to be sufficiently conductive. It can be done with a highly doped shell or a supplementary electrode, which needs to cover the whole surface of nanowires. The core-shell morphology is particularly beneficial for cheap materials (e.g. amorphous Si), which suffer from short minority carrier diffusion lengths [Kayes 2005].

The two architectures presented are actual NW solar cells, with the junction inside the NWs. Nonetheless, other architectures employ both NWs and a planar cell, either with the junction in the planar cell or at the interface between NWs and the planar cell. These structures also benefit from the optical properties of NW arrays.

1.2.5 Fabrication

Different methods of elaboration were developed. Semiconductor nanowires can be made with a top-down approach, where the bulk material is etched into nanostructures. For

the patterning of the array, lithography can be used, in particular low-cost nanoimprint lithography, as well as Langmuir-Blodgett assembly [Hsu 2008]. Among the various etching methods, Metal-Assisted Chemical Etching (MACE) is often employed for c-Si [Hu 2014].

A bottom-up approach allows for material saving, but is more challenging in terms of the nanostructure control. Molecular Beam Epitaxy (MBE), Metal-Organic Chemical Vapor Deposition (MOCVD) and Plasma-Enhanced Chemical Vapor Deposition (PECVD) are common bottom-up methods for nanowire elaboration. A patterned substrate or a catalyst is needed to obtain well controlled nanostructures. In particular, the Vapor-Liquid-Solid (VLS) growth, where catalyst droplets are used to promote the material growth at given positions and along the nanowire axis, is widespread ever since the mechanism was detailed by Wagner and Ellis [Wagner 1964].

Common difficulties in the growth of NWs are the ordering of NWs, the doping (control and measurement) and the parasitic growths (radial and planar on the substrate) [McIntyre 2019].

1.2.6 NW solar cells today

Depending on the absorber material, different properties of NWs are relevant. They are summarized in Table 1.1.

Table 1.1: Benefits of NWs in solar cells for different materials. ✓✓✓ highlights the most important feature of NWs for a given material. ✓ describes a beneficial feature, - a feature that does not show specific benefits.

	Stronger absorption	Radial junction	No substrate constraint	Less material	Flexibility
a-Si:H	✓	✓✓✓	-	✓	✓
c-Si	✓✓✓	✓	-	✓	✓
III-V	✓	✓	✓✓✓	✓	✓

Today, the NW solar cell displaying the highest power conversion efficiency is made of InP. Due to their good properties for PV and the strong asset they could get from NWs, III-V materials have been extensively studied for NW solar cells. Table 1.2 summarizes the current records. Despite the improvement that could be expected from radial junctions, their performance remains far below the axial junctions. Detailed reviews can be found in [LaPierre 2013, Otnes 2017].

Si NW solar cells also reached rather good performance. They are summarized in Table 1.3. While disordered arrays are detrimental to III-V NW solar cells, they are not to Si ones. We can also notice the higher performance of radial junctions made with silicon compared to those made of III-V. A review of c-Si NW solar cells can be found in [Yu 2016], for c-Si/a-Si:H in [Zhang 2019].

Other absorbers in NW solar cells are being developed, for instance with Cu_2S [Tang 2011], or II-VI absorbers with heterostructures using ZnO nanowires [Xu 2011, Akbarnejad 2018]. In particular, Yu et al. suggest that the lower surface recombination

Table 1.2: Record III-V NW solar cells.

	Top-down	Bottom-up	Radial	Tandem on Si
PCE	**17.8 %**	**15.3 %**	**7.4 %**	**11.4 %** (9.4 % Si)
Structure	Axial	Axial	Radial	Axial
Fabrication	Nanoimprint + ICP etching	MOCVD	MOCVD	MOCVD
Material	InP	GaAs	GaAs	GaAs
Reference	[van Dam 2016]	[Aberg 2016]	[Mariani 2013]	[Yao 2015]

Table 1.3: Record Si NW solar cells. We added two references for the record cell due to the lack of information on the structure of the first one.

	Top-down		Bottom-up
PCE	**17.1 %**	**16.0 %**	**9.2 %**
Structure	Radial	Radial	Radial
Fabrication	MACE	MACE	VLS, PECVD
Structure	p-n	SHJ	p-i-n a-Si:H
Substrate	c-Si	c-Si	Glass
Reference	[Lin 2013]	[Dong 2017]	[Misra 2015b]

velocities of CdS and CdTe compared to III-V may lead to better performance for NWs [Yu 2012]. However, their experimental performance remains lower.

1.2.7 Limitations specific to NWs

While they are beneficial for solar cells in some aspects, NWs can also result in supplementary limitations. First, the growth of bottom-up NWs is often cost- and time-expensive, due to high vacuum and temperature conditions, a slow process and deposition on small areas. However, it depends on the material and the deposition method. For instance, Si NW/a-Si:H solar cells can be grown with PECVD at lower temperature, higher pressure and higher rate. They are the focus of this work and their structure is detailed in Section 1.3.

In addition, the collection of photogenerated carriers can be hindered in NWs for several reasons. Their high surface to volume ratio makes surface recombinations critical. Furthermore, depending on the type of surface states and the polarity of the material, a depletion or accumulation of charge carriers occurs at the surface (see Figure 1.12). The width of the depletion (or accumulation) layer depends on many parameters (e.g. doping, density of surface states). For thin NWs, it can be similar to the radius of NWs, which strongly limits the collection of charge carriers [Chia 2012]. The passivation of NWs is a possible solution [Black 2017, Alekseev 2015]. Finally, doping is difficult, both because of the specific conditions for the growth of NWs and because of the sophisticated methods needed to assess the doping density [Chen 2021a]. A supplementary layer could improve the collection of carriers, but usual transparent electrodes are not always suited.

This question is discussed in the second chapter of this thesis (chapter 2) where a hybrid contact is developed for Si NW/a-Si:H solar cells.

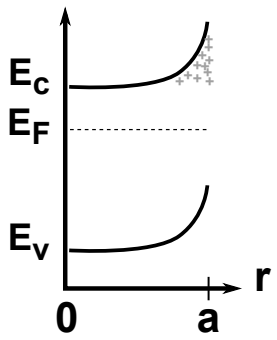

Figure 1.12: Band diagram along the radial direction of a n-doped semiconductor NW of radius a. The conduction (E_c) and valence (E_v) band edges and the Fermi level (E_F) are displayed. Because of surface states, there is a depletion of electrons close to the surface (shown by + signs).

1.3 Si NW/a-Si:H solar cells

1.3.1 Towards low-cost and large-area inorganic flexible solar cells

NWs are particularly beneficial when used with amorphous silicon. The performance of a-Si:H solar cells is indeed limited by the poor mobility and lifetime of carriers in a-Si:H. With radial junctions, thinner layers can be used, which improves the collection of carriers. A detailed presentation of a-Si:H and its use in (planar) solar cells can be found in Section 5.1.

Table 1.4 compares the current record NW solar cell with the record Si NW/a-Si:H cell. Although the efficiency is lower with Si NW/a-Si:H, it displays practical assets for a widespread use. Low-cost substrates (potentially even some types of plastics) can be used, much lower temperatures are required and larger areas can be achieved. In addition, due to the flexibility of NW arrays, this could result in low-cost and inorganic flexible solar cells.

Table 1.4: Comparison of the record bottom-up (III-V) NW and Si NW/a-Si:H solar cells.

	GaAs **p-n**	**Si NW/a-Si:H** **p-i-n**
PCE	**15.3 %**	**9.2 %**
Structure	Axial	Radial
Growth	MOCVD (400 °C/715 °C)	PECVD (400 °C/180 °C)
Substrate	GaAs	Glass
Area	~1 mm^2	13 mm^2
Reference	[Aberg 2016]	[Misra 2015b]

1.3.2 Structure

Figure 1.13 **(a)** shows the structure of Si NW/a-Si:H. It consists in a radial p-i-n junction of a-Si:H around a p-doped crystalline (c-Si) core. Thanks to the NW geometry, the intrinsic layer can be made as thin as 100 nm, which is half of the thickness in the best a-Si:H cells [Matsui 2015a, Sai 2016]. A parasitic flat cell of amorphous silicon also grows between NWs.

Figure 1.13: Cross-section **(a)** schematics and **(b)** SEM image showing the structure of a Si NW/a-Si:H array. The back-contact here is made of 100 nm Ag / 100 nm AZO and there is no top contact. The parasitic planar growth can be seen in the schematics and in the SEM image.

The Si NW/a-Si:H arrays are grown on a boro-aluminosilicate glass substrate. Other substrates have been used, such as thin glass, Al and Cu foils for flexible cells (chapter 4). The back contact can either be Fluorine-doped Tin Oxide (FTO) or Aluminium-doped Zinc Oxide (ZnO:Al) (AZO) with silver (Ag/AZO). Because of the growth conditions, the Si NW/a-Si:H are randomly oriented. Misra et al. observed that the optimal density is around 2.6×10^8 NWs/cm^2 [Misra 2015b]. At this density, Si NW/a-Si:H grow close and can partly merge (Figure 1.13 **(b)**). A high-density array of randomly oriented NWs is obtained, which is quite different from the NW array of the record bottom-up NW solar cell (Figure 1.8 **(c)**). They remain optically beneficial compared to flat a-Si:H.

1.3.3 Growth

All Si NW/a-Si:H solar cells used in this work were elaborated by Martin Foldyna and his team, especially Mutaz Al-Ghzaiwat and Weixi Wang, at LPICM, École polytechnique.

Silicon nanowires are grown by the VLS mechanism using PECVD. The a-Si:H layers are deposited by PECVD. If Ag/AZO is used as a back-contact, Ag and AZO are first deposited on the substrate by sputtering at room temperature[5]. A thin layer of tin (∼0.8 nm) is then evaporated. Tin is preferred over more conventional catalysts (e.g. Au), since Sn impurities in Si NWs do not alter much Si NWs properties (recombination and doping especially) and Sn-assisted growth can be carried out at low temperature. When the back-contact is made of FTO, no Sn deposition is needed, because the catalyst is obtained from reduced SnO_2 from the FTO.

Figure 1.14 describes the one-pump-down process for the growth of Si NW/a-Si:H solar cells on a FTO back-contact. In **(a)**, a H_2 plasma reduces the tin oxide present

[5]Room-temperature deposition of AZO may be responsible for the S-shape of low-density Si NW/a-Si:H and flat a-Si:H solar cells (see Figure C.2 **(c)**).

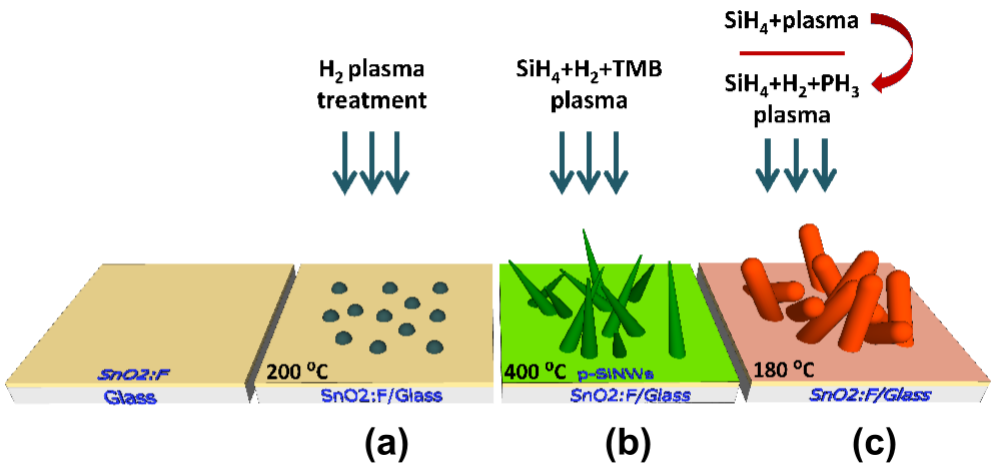

Figure 1.14: Growth process of Si NW/a-Si:H solar cells. Extracted from [Al-Ghzaiwat 2019a].

in FTO. A plasma is also applied with AZO back contact to promote Sn dewetting and to remove the oxide layer. **(b)** and **(c)** steps are common for both back contacts. In **(b)**, the silicon nanowires are grown by the VLS mechanism using PECVD with a gas mixture of SiH_4, H_2 and TMB at 400-425 °C. Plasma is required to dissociate precursors, because of the Sn poor catalytic properties. To improve V_{oc}, a p-doped layer of a-Si:H with a gradient in doping is added between the p-doped c-Si core and the intrinsic layer [Levtchenko 2018]. Figure 1.14 **(c)** describes the PECVD of a-Si:H at 180 °C. The p-doped a-Si:H is deposited by PECVD from SiH_4 and TMB (trimethylboron). The main part is an intrinsic layer of a-Si:H, deposited by PECVD with SiH_4. It is followed by an n-type a-Si:H deposition by adding PH_3 to the gas mixture. More details regarding the growth parameters can be found in [Misra 2015a, Al-Ghzaiwat 2019a].

1.3.4 Current research on Si NW/a-Si:H solar cells

The description of the VLS mechanism in 1964 focused on Si NWs [Wagner 1964]. Later, other catalysts than gold were developed and plasma was used to promote the growth of NWs at lower temperature [Hofmann 2003]. In 2007, Tsakalakos et al. reported the use of a heterojunction c-Si NW/a-Si:H for a solar cell, however with a low PCE (below 0.1 %). Systematic work on PECVD-grown Si NW and Si NW/a-Si:H solar cells started around 2010 [Yu 2010, Adachi 2010].

Table 1.5 shows the highest performance of Si NW/a-Si:H solar cells in different configurations. p-i-n structures (from substrate to contact) are now mostly used, but work on n-i-p structures has also been done in the State Key Laboratory on Integrated Optoelectronics, Beijing (China) [Xie 2012]. Intensive research on Si NW/a-Si:H was carried out at the University of Waterloo (Canada) [Adachi 2013], but has now shifted to ZnO NWs with an a-Si:H shell. Lately, LPICM at École polytechnique (France) and Nanjing University (China) show the most active research in this domain, as can be seen in the Table, with a focus on flexible cells. Finally, a team from the SSN College of Engineering, Tamilnadu (India), reported on the effect of the Sn thickness on the Si NW growth for Si NW/a-Si:H solar cells [Ahmed 2020].

Table 1.5: Record Si NW/a-Si:H solar cells. All efficiencies are given before light-soaking.

	PCE	Structure	Absorber thickness	Reference
Cell	**9.2 %**	p-i-n	100 nm	[Misra 2015b]
On Al foil	**5.6 %**	p-i-n	80 nm	[Sun 2018]
Module (10 cm^2)	**4.4 %**	p-i-n	100 nm	[Al-Ghzaiwat 2019b]
Tandem on Al foil	**8.1 %**	p-i-n a-Si:H p-i-n a-SiGe:H	(56±5) nm (45±6) nm	[Zhang 2021]

1.4 Impact of resistance in solar cells

The performance of Si NW/a-Si:H solar cells is strongly limited by the collection of current due to the disordered array and the insufficient conductivity of the outer shell. In chapter 2, we develop an electrode suited to the Si NW/a-Si:H array. To this end, we need to characterize the electrical properties of the top contact both on glass, using the *sheet resistance* $R_{\square}$, and on the solar cell, with the help of the *series resistance* R_{se}. In addition, the *shunt resistance* R_{shunt} is also critical for the performance of solar cells.

1.4.1 Sheet resistance $R_{\square}$

The *sheet resistance* $R_{\square}$ is often used to describe the conductive properties of an electrode. It is defined from the resistivity of the material ρ and its thickness t as

$$R_{\square} = \frac{\rho}{t}. \tag{1.8}$$

It is given in Ω (ohms), but to emphasize the specificity of this parameter, Ω/□ (ohms per square) are commonly used. The sheet resistance corresponds indeed to the resistance of a square film of thickness t. Since it is invariable under scaling (width and length), sheet resistance can replace resistivity as a way to compare materials in case of thin films. Whereas resistivity is an intrinsic property of bulk materials, it can change with the thickness of thin films. Therefore, a figure taking both the bulk resistivity and the film thickness into account is more relevant. The sheet resistance is thus a comparison parameter between thin films.

Besides, it can easily be assessed using a four-point probe method, for instance van der Pauw method or with aligned probes. In all 4-point measurements, the current is injected through two probes and the voltage is measured between two other probes. Because of the high resistance of the voltmeter compared to the typical resistance of samples, the measured voltage does not come from the contact and wire resistances, only from the resistance of the material. Specific positioning of the probes is required to obtain $R_{\square}$.

Van der Pauw measurement Van der Pauw showed that the sheet resistance of any homogeneous conductive film can be determined from two measurements of resistance with probes positioned on the edges of the conductive material [van der Pauw 1958].

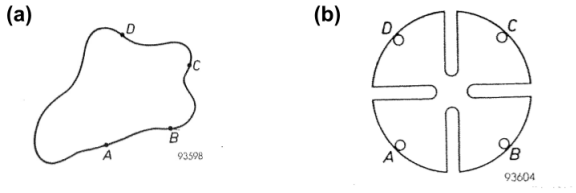

Figure 1.15: Schematics of two sample geometries that can be used in van der Pauw method with the position of the probes, **(a)** arbitrary and **(b)** clover-shape geometries. Extracted from [van der Pauw 1958].

Figure 1.15 presents two conductive films of different shapes with four probes positioned at A, B, C and D. The resistance obtained from the voltage measurement between probes A and B, and the current injected between probes C and D, is noted $R_{AB,CD}$. If the probes are on the edge of the film and their tip is infinitely small, the following relation holds

$$\exp\Big(-\pi\frac{R_{AB,CD}}{R_\square}\Big)+\exp\Big(-\pi\frac{R_{BC,DA}}{R_\square}\Big)=1. \tag{1.9}$$

The sheet resistance can be obtained. Supplementary measurements (for instance with inverted probes for current and for voltage, or inverted polarities) can help to get a more accurate value. However, the contact area between a probe and the sample is finite and not on the edge. Specific geometries of the conductive film can be used to mitigate the ensuing error, especially the clover-shape. Van der Pauw method has been derived and used for the characterization of the Hall effect.

Aligned 4-point probe measurement Van der Pauw method requires to control the shape of the conductive film and the contacts, which is cumbersome for some materials, for instance Ag NW networks. To this end, a simpler setup, the linear 4-point probe measurement, can be used (Figure 1.16).

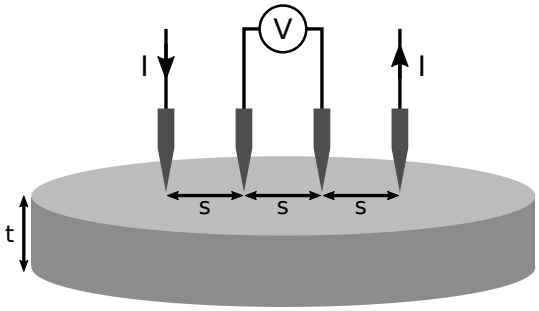

Figure 1.16: Schematics of the linear 4-point probe measurement of $R_\square$. Probes should be equally spaced to obtain the sheet resistance.

The probes are aligned and the distance s between them is constant. For a measured resistance R, it can be shown that the sheet resistance of a thin film is

$$R_\square=\frac{\pi}{\ln 2}\,R. \tag{1.10}$$

This expression is valid providing the spacing s between probes is much smaller than the size of the sample and much larger than the thickness t and the tip radius. In addition, ρ and t should be constant between the probes. For non-uniform films (change in material or in thickness), it does not strictly hold.

1.4.2 Series resistance R_{se}

A lumped parameter The series resistance of a solar cell is a parameter that gathers different sources of resistance in the solar cell. A high series resistance prevents the current from being collected and lowers the efficiency of the cell.

There are two main contributions to the series resistance, the in-plane and the out-of-plane contributions (named for a flat sample). The in-plane resistance depends on the collecting layers at the top and bottom of the cell (contacts or emitter layer). The out-of-plane resistance is a feature of the semiconductor stack. It depends on the conductivity of the material and the interface resistances between layers due to possible band misalignment. In Si NW/a-Si:H solar cells, the use of radial NWs improves the out-of-plane contribution but increases the in-plane one.

Limits of the equivalent model The series resistance is modeled as a lumped component in the equivalent circuit of a solar cell. If the cell is homogeneous, the vertical resistance is the same at every position and a lumped parameter to describe it is relevant. However, it is not the case for the lateral resistance. Even for a homogeneous sample, different parts of the cell do not experience the same current levels, due to crowding effects close to the contacts. The impact of this approximation depends on many factors, such as the contact geometry (central dot vs. circular line), the sheet resistance and current levels [Nielsen 1982].

It is an issue when fitting I-V curves following the diode model. Indeed, it results in an approximate estimation of R_{se}, which affects the value of other parameters such as the saturation current and the ideality factor [Breitenstein 2013]. An equivalent resistance, partly dependent on current, has been proposed and implemented to this end in a MATLAB code for I-V fitting[6].

1.4.3 How to determine the series resistance?

Several reasons make the assessment of R_{se} difficult.

- An equivalent resistance is necessarily an approximation and, treated as such, different values are obtained depending on the conditions. In particular, it does not consider the spatial distribution of the resistance.
- The equivalent resistance does not take into account the dependence of R_{se} on the charge injection, for instance under illumination or bias [Turek 2014].
- One should be able to distinguish the effect of R_{se} among other parameters, in particular the ones that determine the diode behavior.

In this work, we are interested in the comparison of the top contact for similar solar cells. If they are tested under the same conditions, the two first points should not be critical. Hence, we focus on the last point.

[6] Stephan Suckow, 2/3-Diode Fit (2014). http://nanohub.org/resources/14300

Fit A fit to the one- or two-diode equation can be used. However, there are many unknown parameters and it could result in an approximate value. It is even more difficult for materials or architectures that are not well described by the one-diode model, such as a-Si:H [Merten 1998].

Suns-V_{oc} In Suns-V_{oc} or J_{sc}-V_{oc} measurements, different illumination levels are shone on the cell, and V_{oc} and J_{sc} are measured each time. V_{oc} is not altered by the series resistance, as there is no current flowing at open-circuit. In addition, if R_{se} remains low, it does not affect J_{sc}. From the comparison between the J-V curve and the J_{sc}-V_{oc} one, the series resistance can be determined [Wolf 1963, Yoshikawa 2017]. Yet, due to high series resistances in Si NW/a-Si:H solar cells, this method cannot be applied.

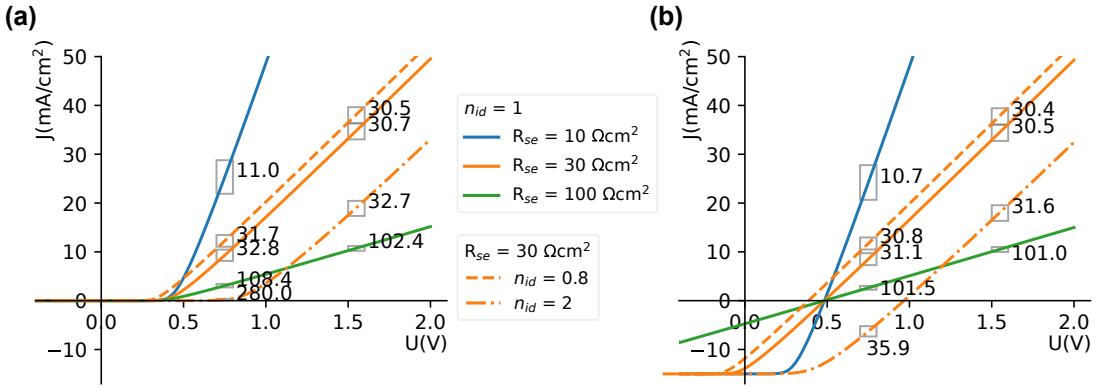

Figure 1.17: Simulated **(a)** dark and **(b)** light J-V curves corresponding to the one-diode model for different series resistances R_{se} and diode ideality factors n_{id}. Other parameters are $J_0 = 10^{-10}$ A/cm^2, $R_{shunt} = 10^8$ Ωcm^2 and $J_\phi = 15$ mA/cm^2. The slope was determined over two different voltage ranges, highlighted by frames, [0.7 V,0.8 V] and [1.5 V,1.6 V]. It is given in Ωcm^2.

From the I-V slope R_{se} is sometimes determined at open-circuit from the slope of the I-V curve, but it can lead to inconsistent values. With the code written by Stephan Suckow[6], I simulated I-V curves from the one-diode model for different values of the series resistance R_{se} and the diode ideality factor n_{id} under dark conditions. They are displayed in Figure 1.17 **(a)**. The resistance is calculated at different voltages, shown with grey frames. It clearly appears that a better estimation is obtained from the slope at high voltages. It is logical: under high forward bias, the diode is fully opened and is not limiting anymore. The only parameter governing the slope $^{dI}/_{dV}$ is R_{se}. Depending on the diode, the voltage required for a good estimation changes (see for instance the J-V curve for $n_{id} = 2$). One of the main drawback however is that high current levels are needed to determine R_{se} with certainty, which may damage the device. In addition, it makes it more sensitive to crowding effects and the current injection can change the resistance of the cell.

Dark or light? Photoconductive effects can affect R_{se} values under illumination. Even without any photoconductivity, the illumination has an effect on the determination of

R_{se}. Figure 1.17 **(b)** displays the same simulations as in **(a)** but under illumination ($J_\phi = 15\,mA/cm^2$). The region where R_{se} only is limiting the current is reached for lower voltages than in the dark. Under illumination, the voltage at the junction is lowered compared to dark (Figure 1.6). A lower bias is needed to open it fully. In addition, a working cell requires illumination, hence it is relevant to determine its series resistance from light measurements.

Other methods An accurate estimation of R_{se} has been the focus of many research works. In particular, we can cite the methods developed by Chibbaro et al. [Chibbaro 2011] and Zhang et al. [Zhang 2011], that do not rely on the assumption of a high value for R_{shunt}. In addition, electroluminescence can be used to map the resistance effects in a solar cell and understand their origins [Hinken 2007].

In this work The derivation method is an easy way of determining R_{se} beyond the diode effects. Nonetheless, I have mostly determined the series resistance from the slope at high voltage and under illumination since it is a faster and tangible method. It may lead to an overestimation, especially for low values. For this reason, I call it *apparent series resistance*.

1.4.4 Shunt resistance

The shunt resistance models the alternative paths of conduction in the solar cell. It may stem from physical pinholes (direct connection between top and bottom contacts), conductive paths in the material, due for instance to precipitates or grain boundaries, or from the conduction through defects in the junction. In Si NW/a-Si:H solar cells, physical pinholes can occur if Si NWs break during the process.

The shunt resistance can be easily estimated from the slope of the I-V curve, usually at 0 V. While it holds for close-to-ideal cells where $R_{shunt} \to \infty$ and $R_{se} \simeq 0$, it results in a poor estimation for cells with low R_{shunt} and high R_{se} values. Indeed, both resistances may affect the shape of the curve under low forward bias. Consequently, in the same way as for R_{se}, I chose to use the slope of the I-V curve under reverse bias, between -0.5 V and -0.4 V. Still, the value of the shunt resistance may be underestimated, especially under some conditions such as high illumination (see Section 5.3.4).

The description of the working principle of solar cells and the use of NWs were needed to figure out the issues Si NW/a-Si:H solar cells should handle. In addition, since we focus on the development of the top electrode for Si NW/a-Si:H, it was critical to understand the definition and signification of $R_\square$, R_{se}, R_{shunt} and the methods that can be used to assess them.

Chapter 2

Optimization of the top contact for nanowire solar cells

Contents

2.1 Transparent and flexible electrodes

2.1.1 What is transparency?

Transparency is evaluated by the amount of light able to go through a sample (a layer of material, a solution...). The light that is not transmitted is either reflected or absorbed by the medium. Hence, a transparent electrode should have the lowest possible absorption and reflection. Yet, these actually depend on the conductivity of the material and on the frequency range. Hence, no straightforward conclusion can be drawn.

Absorption coefficient α_{abs} and relative permittivity ε The optical response of a material is described by its permittivity (or dielectric constant). Notably, it determines the coefficients for absorption and for reflection at interfaces. A relative permittivity can be defined with respect to the vacuum permittivity ε_0, $\varepsilon_r = \varepsilon/\varepsilon_0$. For simplicity, the relative permittivity will be used and the subscript removed. Instead of the relative permittivity ε, the refractive index can be used, or its real and imaginary parts $\tilde{n}$ and $\tilde{k}$,

$$\varepsilon = (\tilde{n} + i\tilde{k})^2. \tag{2.1}$$

For a monochromatic progressive plane wave (angular frequency ω and wavevector $\vec{k}$, initial magnitude E_0), the electric field $\vec{E}$ is

$$\vec{E}(t, \vec{x}) = \vec{E_0}\, e^{-i\omega t + i\vec{k}\cdot\vec{x}}. \tag{2.2}$$

From Eq. (2.2), if we consider the wavevector along the z-direction ($\vec{k} = k \cdot \vec{e_z}$), and with $I_0 = |E_0|^2$, the light intensity $I(z)$ after a path of length z inside a bulk material is

$$I(z) = |E(t, z)|^2 = I_0\, e^{-2\,\mathrm{Im}(k)\,z}. \tag{2.3}$$

The wavevector is affected by the medium, through the dispersion relation. Using Eq. (2.1), with c the speed of light,

$$k(\omega) = \frac{\omega}{c}\sqrt{\varepsilon(\omega)} = \frac{\omega}{c}\left[\tilde{n}(\omega) + i\tilde{k}(\omega)\right]. \tag{2.4}$$

The absorption coefficient α_{abs} can be defined as

$$\alpha_{abs}(\omega) = 2\,\frac{\omega\tilde{k}(\omega)}{c}, \tag{2.5}$$

and the intensity $I(z)$ of the light after a path length z in a bulk material is then

$$I(z) = I_0\, e^{-\alpha_{abs}(\omega)z}. \tag{2.6}$$

Bulk reflectivity R and relative permittivity ε At normal incidence, Fresnel's formulas connect the reflectivity at the interface between two bulk materials to their refractive indices [Dressel 2002],

$$R = \frac{(\tilde{n_2} - \tilde{n_1})^2 + (\tilde{k_2} - \tilde{k_1})^2}{(\tilde{n_2} + \tilde{n_1})^2 + (\tilde{k_2} + \tilde{k_1})^2}. \tag{2.7}$$

The permittivity also determines the losses by reflection at interfaces. We now need to understand how a permittivity can be defined for a conductor and how it depends on the frequency and the conductivity. To this end, we will use the Drude model.

2.1.2 The free-carrier theory

We will mostly refer to an electron of charge $-q$, q being the elementary charge. However, the argument does not depend on the type of carrier and can be applied to a hole with a charge $+q$. Hence, the results also hold for semiconductors of any type of doping.

2.1.2.1 Drude model

In the Drude model, the electrons responsible for the conductivity are considered as a classical gas of free electrons [Drude 1900]. There is no restoring force and, apart from the thermal agitation, their movement is governed by the acceleration under an electric field and by scattering. In the Drude model, scattering corresponds to collisions between an electron and another particle. The scattering term was initially associated to collisions with the ionic cores. It is now clear that electrons may be slowed down by lattice vibrations, electron-electron interactions, defects and impurities, but this does not affect the results if an averaged scattering time τ is assumed, as it is done in the Drude model. No magnetic field is considered. For an average electron, which has a probability $^{dt}/_{\tau}$ of scattering and stops upon scattering, the change in momentum $\vec{p}$ between two collisions due to the electric field is

$$\frac{d<\vec{p}(t)>}{dt} = -\frac{<\vec{p}(t)>}{\tau} - q\vec{E}(t). \tag{2.8}$$

q is the elementary charge. For a monochromatic light, $\vec{E}(t,\vec{x}) = \vec{E_0}e^{-i(\omega t - \vec{k}\cdot\vec{x})}$, the velocity of one charge carrier can be derived from the solution of equation (2.8), with m^* the electron effective mass,

$$\vec{v} = -\frac{iq\tau}{m^*}\frac{\vec{E}}{\omega\tau + i}. \tag{2.9}$$

With n the density of charges per unit volume, the electron current density $\vec{j}$ is

$$\vec{j} = -nq\vec{v} \tag{2.10a}$$

$$\vec{j} = \frac{inq^2\tau}{m^*}\frac{1}{\omega\tau + i}\vec{E}. \tag{2.10b}$$

From Ohm's law, $\vec{j} = \sigma\vec{E}$, we obtain the complex and frequency-dependent conductivity $\sigma(\omega)$, also called the *optical conductivity* (we assume that the medium is isotropic and with a scalar conductivity). It holds for all conductors with free carriers, such as metals or highly doped semiconductors. Indeed, the kinetic energy of (some) electrons in these materials is high compared to the potential one and they can be considered as free carriers. The interaction with the lattice is taken into account via the electron effective mass m^*.

$$\sigma = \frac{nq^2\tau}{m^*}\frac{1 + i\tau\omega}{1 + \tau^2\omega^2}. \tag{2.11}$$

The DC conductivity σ_{DC} clearly appears in equation (2.11). It is defined as $\sigma(\omega = 0)$,

$$\sigma_{\mathrm{DC}} = \frac{nq^2\tau}{m^*}. \tag{2.12}$$

2.1.2.2 Optical conductivity σ and relative permittivity ε

Besides, we can also apply Maxwell's equations to the material [Griffiths 2013]. In SI units, Maxwell-Ampere's law is

$$\vec{\mathrm{rot}}\ \vec{H} = \vec{J}_{ext} + \frac{\partial \vec{D}}{\partial t} \tag{2.13}$$

$\vec{H}$ is the magnetic field, $\vec{J}_{ext}$ the current density due to free carriers and $\vec{D}$ the displacement field. In a medium without free carriers, the displacement field is

$$\vec{D} = \varepsilon_0 \varepsilon_\infty \vec{E}. \tag{2.14}$$

ε_0 is the vacuum permittivity. The relative permittivity ε_∞ describes the response of the material without free carriers. It also corresponds to the permittivity at high frequencies (hence the notation), where the free carriers do not alter the response of the material anymore.

The current density due to free carriers is

$$\vec{J}_{ext} = \sigma \vec{E}. \tag{2.15}$$

For a monochromatic wave, equation (2.13) results in

$$\vec{\mathrm{rot}}\ \vec{H} = \frac{\partial}{\partial t}\Big[\Big(-\frac{\sigma}{i\omega\varepsilon_0} + \varepsilon_\infty\Big)\,\varepsilon_0\,\vec{E}\Big]. \tag{2.16}$$

We can thus define the relative permittivity of the material with free carriers

$$\varepsilon(\omega) = \varepsilon_\infty + \frac{i\sigma(\omega)}{\varepsilon_0\,\omega}. \tag{2.17}$$

Hence, the real and imaginary parts of the relative permittivity, ε_1 and ε_2, are

$$\varepsilon_1 = \varepsilon_\infty - \sigma_{\mathrm{DC}}\tau \frac{1}{\varepsilon_0\,(1+\omega^2\tau^2)}, \tag{2.18a}$$

$$\varepsilon_2 = \frac{\sigma_{\mathrm{DC}}}{\omega}\,\frac{1}{\varepsilon_0\,(1+\omega^2\tau^2)}. \tag{2.18b}$$

The imaginary part of the dielectric constant clearly increases with an increasing DC conductivity. Although the extinction coefficient (hence the absorption coefficient) mostly depends on the imaginary part of the dielectric constant, it is actually related to both the imaginary and real parts and the contribution of each part depends on the frequency. Thus, we should consider various regimes.

2.1.2.3 The plasma frequency

If $\sigma_{\mathrm{DC}}\tau > \varepsilon_\infty\varepsilon_0$, it is clear from equation (2.18a) that there is a given frequency for which $\varepsilon_1(\omega_p) = 0$. This frequency is called the *plasma frequency* and is critical for the optical properties of the solid

$$\omega_p^2 = \frac{nq^2}{\varepsilon_\infty\varepsilon_0 m^*} - \frac{1}{\tau^2}. \tag{2.19}$$

Usually $(\omega_p\tau)^2 \gg 1$, and the plasma frequency is defined as

$$\omega_p^2 \simeq \frac{nq^2}{\varepsilon_\infty\varepsilon_0 m^*} = \frac{\sigma_{\mathrm{DC}}}{\varepsilon_\infty\varepsilon_0\tau}. \tag{2.20}$$

When the density of free electrons n increases, the plasma frequency increases (i.e. shorter wavelengths). We will see that depending on materials, the transparency window in the visible range can either become wider or narrower.

2.1.2.4 Frequency dependence of the permittivity and the refractive index

Figure 2.1 shows the typical change in permittivity and refractive index with frequency for gold following the Drude model (solid line). Three main regimes can be distinguished. At low energies (not discussed here), the reflection regime corresponds to very large values of ε_1 (negative) and ε_2 (positive) and $\tilde{n} \simeq \tilde{k}$. In the relaxation regime (below ω_p, around 3 eV), ε_1 increases towards zero. At the plasma frequency, there is no significant change in the slope of the permittivity, but there is a strong variation for $\tilde{n}$ and $\tilde{k}$. Beyond ω_p, the real part of the refractive index steeply increases, while $\tilde{k}$ is very close to zero. A very low absorption is expected in this region, hence called the transparency regime.

A discrepancy between the model and the experimental points appears beyond 2 eV, with a strong increase in ε_2. This is related to interband transitions in the metal, that are not taken into account in the model.

2.1.2.5 σ_{dc} dependence of the absorption coefficient and reflectivity

The dependence of the absorption coefficient on the conductivity σ_{DC} and the frequency can be explicitly written, using equations (2.1), (2.5) and (2.18). Simplifications can be obtained if we assume $\omega \ll 1/\tau$, $1/\tau \ll \omega \ll \omega_p$ or $\omega_p \ll \omega$, which highlights the link between α and σ_{DC}. The relation $\omega_p > 1/\tau$ is generally valid in metals and semiconductors, with more similar values for the latter (typical values are given in Section 2.1.3). The reflectivity expressions are more complex and the conductivity effect is less straightforward. The results are shown in Figure 2.2.

For all frequencies, the absorption coefficient increases with the conductivity. The strongest increase corresponds to $\omega \gg \omega_p$, but due to the high frequencies, values of α actually remain low.

This explicitly shows the interdependance between conductivity and transparency for all frequencies. In addition, we can clearly see different regimes, determined by the values of τ and ω_p. The conductivity σ_{DC} is related to both (see (2.12) and (2.20)) and determines the transparency ranges.

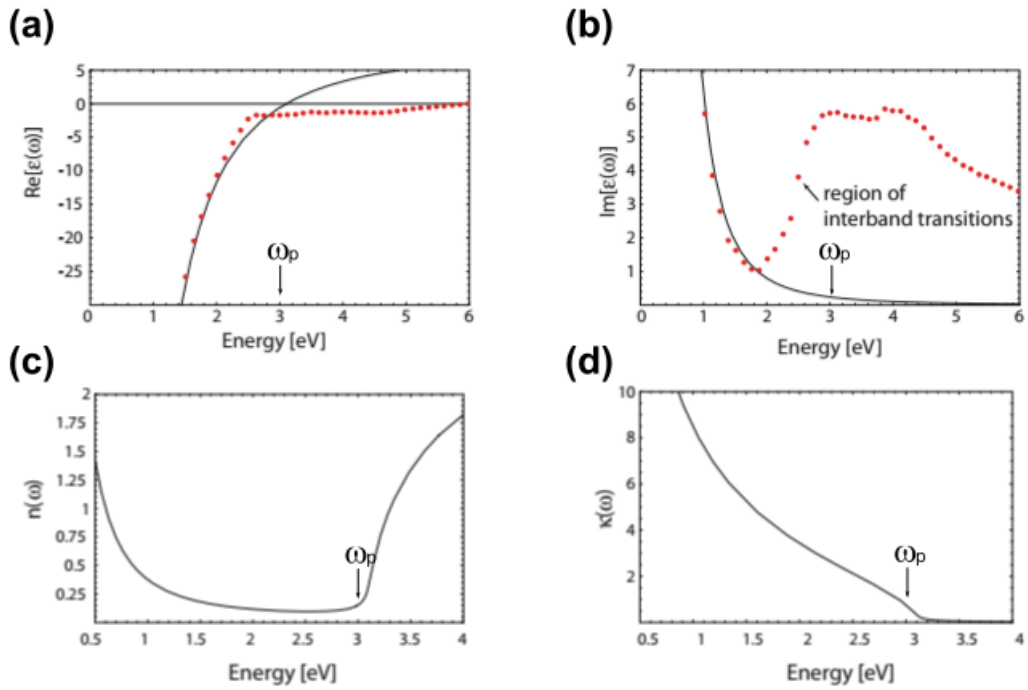

Figure 2.1: Measured (red dots) and fit to the Drude model (solid line) of real and imaginary parts of **(a, b)** the permittivity and **(c, d)** the refractive index of gold. The experimental results highlight the effect of interband transitions. The plasma frequency ω_p is shown. Modified from [Maier 2007], with experimental data from [Johnson 1972].

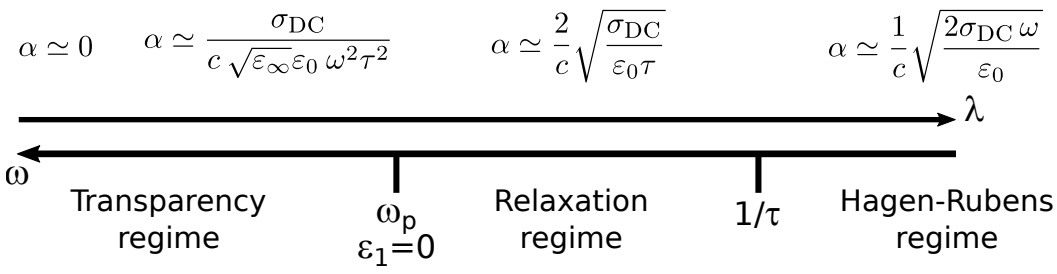

Figure 2.2: Expression of the absorption coefficient for the free-carrier theory depending on the conductivity for different frequency ranges.

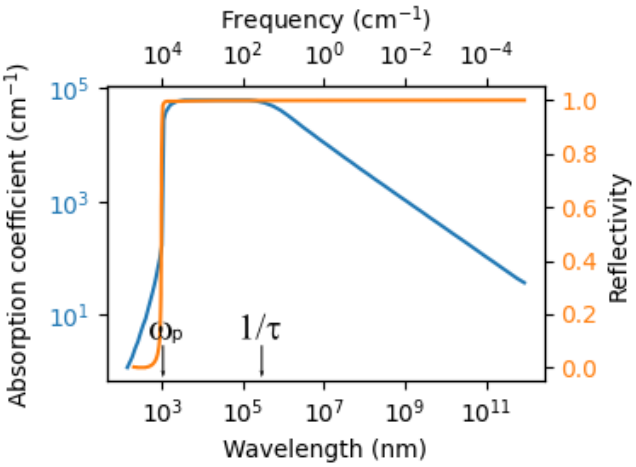

Figure 2.3: Absorption coefficient and reflectivity dependence on frequency with the free-carrier theory. $\nu_p = 10^4\,\mathrm{cm}^{-1}$ and $1/\tau = 16.8\,\mathrm{cm}^{-1}$. Replotted from [Dressel 2002].

2.1.2.6 Frequency dependence of the absorption coefficient and reflectivity

Figure 2.3 displays the absorption coefficient and the reflectivity following the Drude model. The dependency on ω from Figure 2.2 corresponds to the three regimes observed. It is clear that the absorption coefficient is maximal between $1/\tau$ and ω_p and close to zero for frequencies beyond ω_p. Even though α is also low at low frequencies, the corresponding reflectivity is high, almost equal to one. Consequently, the frequency range beyond ω_p would be the most suitable range for transparency.

2.1.2.7 Finite-thickness effects

From Eq. (2.6), it appears that the absorption in the material can also be described with a characteristic length δ_0, known as the *skin depth*. It is defined as

$$\delta_0 = \frac{2}{\alpha_{abs}}, \tag{2.21}$$

and it means that 86 % of the light which enters the medium is absorbed over a distance δ_0. Yet, for thinner films, a substantial amount of light reaches the bottom interface, where it can be reflected. This second reflection has to be taken into account for an accurate estimation of the reflectance and transmittance of the film. Moreover, interferences between the incoming and reflected parts of the light occur. Complete expressions of the reflectance and transmittance can be found in [Dressel 2002] for a normal incidence.

When the mean free path of electrons is larger than the skin depth estimated from Equation (2.21) (at low temperatures or high frequencies), the *anomalous skin effect* takes place. Only part of the electrons are involved in the absorption, which results in a larger effective skin depth. It is the case in silver at room temperature under optical excitation ($\sim 5\times10^{14}\,\mathrm{Hz}$), where the mean free path of electrons is 35 nm, larger than the estimated skin depth of 25 nm.

Consequently, even out of the transparency regime, conductors can be used for transparent electrodes as long as they are thin enough compared to the skin depth.

2.1.3 Metals vs. TCOs as electrodes

2.1.3.1 Transparency and visible ranges

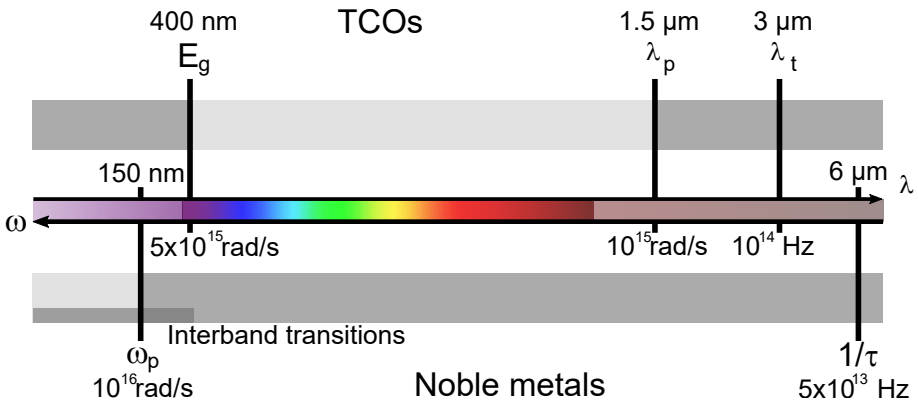

Figure 2.4: UV-visible-NIR spectrum with the reflection, relaxation, transparency and interband transitions regimes for TCOs and metals. The scattering frequency $1/\tau$ (introduced in Eq. (2.8)) is given in Hz. The plasma frequency $\omega_p = 2\pi/T_p$ (introduced in Section 2.1.2.3) is given in rad/s. The corresponding wavelengths are also shown. The colors refer to the different parts of the spectrum: light purple for the ultraviolet range, rainbow for the visible one, and shaded red to grey for the infrared one. The values are representative of metals and TCOs, but do not correspond to a given material. They come from [Ginley 2011, Ellmer 2012, Gordon 2000].

Figure 2.4 displays the UV-visible-NIR spectrum and the different absorption regimes for transparent conductive oxides (TCOs) and noble metals. TCOs are highly doped oxides with wide band gaps. Their properties are detailed in Section 2.1.4.1.

Metals For low-resistivity metals, the plasma frequency is typically around 10^{16} rads^{-1} (8 eV for Au, 11 eV for Cu) and scattering rates are close to 5×10^{13} Hz [Dressel 2002, Ellmer 2012, Maier 2007]. Thus, the visible part of the spectrum falls in the reflection regime. Besides, interband transitions occur for these metals in the short-wavelength range, sometimes for frequencies lower than the plasma frequency (around 2 eV for Au and Cu). The added absorption is shown with a supplementary shade in the figure. Hence, very thin metallic films are needed as (semi)transparent electrodes.

TCOs For TCOs, the plasma wavelength is generally given and falls in the near-IR, from 1 µm for ITO to 1.6 µm for FTO (1.0×10^{15}-2×10^{15} rads^{-1}). The scattering rate is higher than in metals, 10^{14} Hz, due to ionized impurities [Gordon 2000, Ellmer 2012, Ginley 2011]. While the transparency of TCOs in the UV range is limited by the interband transitions (around 4 eV for ITO), it is limited by free carriers in the IR, as displayed in Figure 2.5. The visible part of the spectrum hence corresponds to

the transparency range of ITO, the characteristic absorption length is around 2-40 µm ($\rho = 3.8{\times}10^{-6}\,\Omega$m, $1/\tau = 2{\times}10^{14}$ Hz).

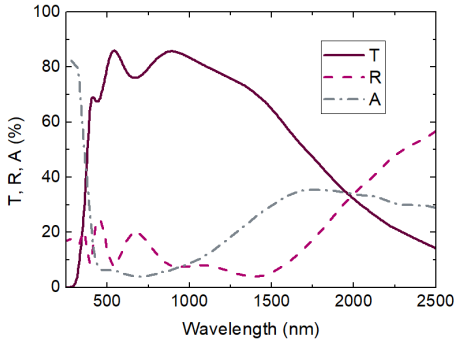

Figure 2.5: Measured total transmittance T and reflectance R and calculated absorptance A of 240 nm ITO on glass. Absorptance corresponds to $100 - T - R$. The plasma wavelength does not correspond to a specific feature of T, R or A.

2.1.3.2 How to improve transparency for a given conductivity?

A higher mobility of charge carriers The transparency window of a TCO is determined by its band gap energy and plasma wavelength λ_p. The region of interest for solar cells (from 350-400 nm to the band gap energy E_g) is generally comprised in this window. However, while the band gap energy does not depend on the doping of the TCO, the plasma wavelength is directly related to the density of charge carriers n, $\lambda_p \propto 1/\sqrt{n}$ (Eq. (2.20)). For a wide transparency window, the doping cannot be too high. Carriers with a high mobility are required to keep a good conductivity without optical losses.

Furthermore, in the transparency and reflection regimes, it is clear that the absorption coefficient is lower for a given conductivity when the scattering time increases (Figure 2.2). It corresponds to charge carriers with a higher mobility ($\mu = q\tau/m^*$), hence a lower density is needed for the same conductivity, which results in less absorption.

Consequently, regarding the absorption, materials with high mobility carriers should be preferred. Yet, the mobility remains limited in any case, at least by phonon scattering. In TCOs, the main limitation is the scattering by ionized impurities [Ellmer 2012].

Non-continuous films For a continuous film, lowering the resistance requires a thicker film, which decreases the transparency (not considering any interferences). With non-continuous materials, they are not interdependent anymore. For instance, in solar cells connected with a grid, the metallic fingers are made more conductive thanks to an increased thickness, but it does not affect the openings between them and does not reduce the transparency strongly.

2.1.4 Main strategies today

For the architecture mainly used in today's production of c-Si solar cells, Passivated Emitter and Rear Cell (PERC) [Fraunhofer ISE 2022], no additional transparent electrode is needed, because the top layer (the emitter) is highly doped and conductive

enough [Green 2015]. The current is then collected through a metallic grid (bus bars and fingers). However, c-Si heterojunction, thin-film, organic and nanostructured solar cells lack this conductive layer and a transparent electrode is needed.

Transparent conductive oxides (TCOs) are mostly used, thanks to their very good conductivity and high transparency. However, for different reasons (processing issues, flexibility, sustainability...), there is a search for alternative materials, with conductive polymers and nano-structured materials (graphene, carbon nanotubes or metal nanowires) as possible candidates. Reviews can be found in [Ellmer 2012, Hecht 2011].

2.1.4.1 TCOs used as top contact

Because of their properties detailed in Section 2.1.3.1, TCOs are a reference as top electrode for solar cells, especially ITO (Sn-doped In_2O_3), AZO (Al-doped ZnO) and FTO (F-doped SnO_2). A transparent electrode made of ITO can reach $R_\square \simeq$ 10-50 Ω/□ with a transmittance T at 550 nm larger than 90 % [Chen 2019].

They are metal oxides, mostly n-semiconductors, with a wide band gap (> 3 eV) and a rather low resistivity ($10^{-4}\,\Omega \times$ cm, compared to $10^{-6}\,\Omega \times$ cm for metals). Their conductivity stems from high doping levels (up to $10^{21}\,cm^{-3}$) and fair mobilities (up to $100\,cm^2/(Vs)$) [Ellmer 2012]. They present two distinctive features: even without doping, they show substantial electron densities and no compensation occurs at high doping levels, which results in high effective carrier densities [Lany 2007].

Despite these properties, TCOs show some limitations. Even if p-doped TCOs exist, they do not reach the same performance [Kawazoe 1997], which may hinder some solar cells structures. If the p-doped side of a junction is exposed to light and requires a transparent electrode, either a p-doped TCO (with poor opto-electrical properties) or a n-doped TCO (with a less efficient extraction of holes) can be used. Besides, ITO, which shows the highest performance among TCOs, requires indium. Indium has been listed as a critical raw material by the European Union for several years[1] and the current increase in the use of In could lead to supply issues.

Furthermore, TCOs are not suited to flexible applications. First, they are very brittle. Moreover, a low processing temperature is required for many flexible substrates (typically below 200 °C), whereas high-quality TCOs require a higher temperature (for instance 350 °C in an O-rich atmosphere for sputtering). Developing flexible TCOs is a challenge that has partly been overcome with amorphous and nanocrystalline TCOs. Amorphous TCOs remain partly conductive thanks to the spherical symmetry of the orbitals in the conduction band (type s), which are less affected by disorder [Hosono 1996]. Still, they display a rather high sheet resistance (around 100 kΩ/□) [Nomura 2004, Norton 2018].

2.1.4.2 Conductive polymers

Without reaching ITO conductivity, doped conductive polymers as PEDOT:PSS show electrical properties good enough to be used as electrodes in some applications (65 Ω/□ for 80 % transmittance) [Kim 2011b, Zhou 2008]. Moreover they are inherently flexible, solution-processed and made from abundant elements. Their main drawback concerns their fast degradation, leading to a loss of conductivity.

[1] https://rmis.jrc.ec.europa.eu/uploads/CRM_2020_Report_Final.pdf

2.1.4.3 Graphene

Because it is a nanosheet with very high in-plane mobility of carriers (up to $10^4\,cm^2/(Vs)$ [Novoselov 2004]), graphene is also expected to yield both desired properties. A high quality, highly doped single sheet should indeed transmit 97.7 % of the incoming light and have a sheet resistance around 62 Ω/□ [Nair 2008, Wu 2010]. Bae et al. [Bae 2010] demonstrated an electrode with excellent properties (four-layer doped graphene, 30 Ω/□ and 90 % transmittance) using high quality graphene.

Since the graphene quality is crucial, poorer properties are often obtained (for instance 200 Ω/□ for 85 % transmittance [Cai 2009]). MOCVD at high temperature (700-900 °C) is mainly used for the growth of graphene on copper. However, multiple grains (several tens of µm) are commonly observed, with a high resistance between adjacent grains. Achieving overall resistances as low as the state-of-the-art values is therefore difficult. Solution processes with graphite reduction could also be considered when looking for lower cost methods [Hsiao 2014]. In addition, transferred graphene cannot be used as a conformal coating.

2.1.4.4 Carbon nanotubes

Carbon Nanotubes (CNTs) are tubes made of a single or several layers of graphene. They have very thin walls (typically below 2 nm) and are a few µm long. They look promising given the high mobility of carriers in a single nanotube ($10^5\,cm^2/(Vs)$ [Dürkop 2004]), their ability to form a conductive network, and the possibility of solution processing. Yet limited properties have been obtained until now (up to 100 Ω/□ for 90 % transmittance [Shin 2009]) [Wu 2004, Zhang 2006]. These results are consistent with the lower mobility observed in random CNT films ($150\,cm^2/(Vs)$ [Snow 2005]). Beside the high junction resistance between tubes, a possible reason is that CNT solutions are made of nanotubes of different lengths, chiralities (thus metallic as well as semiconducting CNTs) and diameters. Purification is therefore needed, but is time and cost demanding.

2.1.4.5 Metal at the nanoscale

Finally, metals could be used to ensure a good conductivity. Since they transmit little light, new designs are needed to keep the transparency. Metallic grids could be used in solar cells. But spacing between fingers has to be large enough to reduce the light absorption and reflection, and a resistive loss to carrier collection could appear. Very thin continuous films of metals (e.g. Ni/Au semitransparent contacts used in nitride LEDs) can also be thought of, but a conformal coverage is a key parameter, which would be particularly difficult to achieve in nanowire-based solar cells. Besides, no solution process is possible in this case. Lastly metallic nanoparticles [Sugnaux 2015] or nanowires have been considered. Nanowires with the appropriate density could form a conductive network with large transparent holes in-between. Silver nanowires are particularly interesting because of the low resistivity of silver ($1.63\times10^{-6}\,\Omega \times cm$ at 300 K [Bid 2006]). Reported properties of Ag nanowires electrodes [De 2009, Hu 2010, Jang 2016, Lee 2008] confirm this interest with sheet resistances as low as 2.9 Ω/□ for 89.2 % transmittance [Lagrange 2015].

More details on Ag NWs are given in Section 2.4.

2.1.5 How to find the optimal combination of transparency and conductivity?

In order to compare candidate materials, figures of merit (FoMs) have been suggested. Since transparency and conductivity remain interdependent, a trade-off is needed. A relevant figure of merit should be easy to determine from experiments, be suited for various applications and representative of the performance of the final device.

Haacke's FoM Today the one that is mostly referred to is Haacke's FoM, actually a special case of Haackes's propositions [Haacke 1976]. One would naturally compare the transmittance T and the sheet resistance $R_\square$ of a thin film as Fraser and Cooke did [Fraser 1972]

$$FoM^{\text{Fraser}} = \frac{T}{R_\square}. \tag{2.22}$$

Both are related to the thickness, which enables to calculate the optimal thickness (resulting in the highest FoM) and the corresponding transmittance. With the FoM in Eq. (2.22) , it results in a transmittance of 37 %. For this reason, Haacke suggested a more general form of this figure of merit, with a weight w applied to the transmittance. This coefficient can be changed depending on how critical the transmittance is for the application

$$FoM^{\text{Haacke}} = \frac{T^{\text{w}}}{R_\square}. \tag{2.23}$$

The commonly used Haacke's FoM takes $\text{w} = 10$, for which an optimized transparent electrode yields 90 % transmittance. However, many references to the Haacke's figure of merit forget to mention that the weight w can be varied depending on the application.

Haacke's figure of merit is rather easy to use, especially since the material properties are macroscopic. It can also be adapted to various applications, with the value chosen for the weight power, but also with the value of T. The transmittance is often taken at 550 nm, but a different choice can be made depending on the objective. In particular for solar cells, the transmittance can be integrated with the solar spectrum up to the band gap energy of the absorber [Mendez-Gamboa 2016].

Other figures of merit have been developed. Some are summarized in Table 2.1 in three sections. Figures of merit that are derived from T and $R_\square$ measurements are general, and an easy way to compare materials. However, they are determined for a given thickness. In order to compare the material itself independently of the thickness, FoMs have been derived from material parameters. Yet, these values are not easy to determine and may not be relevant for very thin films or percolating networks where conductivity is ill-defined. In addition, they are not necessarily adapted to the application. Hence, some FoMs have also been suggested expressly for solar cells. Again, they can be rather general or perfectly suited to a specific type of solar cells and to specific dimensions (*scaling*). They gain in precision what they lose in generality. In addition, for a flexible electrode, the mechanical performance is needed as well. Shim et al. suggested a derived FoM to this end [Shim 2010].

Table 2.1: Possible figures of merit (FoMs) of transparent electrodes for solar cells.

FoM	Details	References
	From T and $R_\square$ measurements	
$\frac{T}{R_\square}$	Easy to measure For a thin film, optimal thickness leads to $T = 37$ %	[Fraser 1972]
$\frac{T^W}{R_\square}$	Easy to measure Weight W can be changed depending on application	[Haacke 1976]
$1/R_\square - \log T$	Linear fit Independent of thickness Several measurements needed	[Pekker 2010]
	From material constants	
$\frac{\sigma_{DC}}{\alpha}$	σ_{DC}, conductivity α, absorption coefficient Not easy to determine Not relevant for nanostructures	[Gordon 2000]
$\frac{\sigma_{DC}}{\sigma_{opt}}$	σ_{opt}, optical conductivity Not easy to determine Not relevant for nanostructures	[Dressel 2002]
$\left[\frac{\sigma_{DC}/\sigma_{opt}}{(Z_0 t_{min}\sigma_{opt})}\right]^{1/(n+1)}$	t_{min}, thickness transition between percolation and bulk regimes n, percolation exponent Z_0, impedance of free space For nanostructures Can be obtained from T and $R_\square$ measurements Would promote further increase in T (conversely $R_\square$) when it is already high [Jacobs 2016]	[De 2010]
	For solar cells	
$\frac{J}{R_\square}$	J computed from the transmittance spectrum and the solar spectrum or the EQE Optically adapted to solar cell technology Knowledge of solar cell required No scaling	[Mendez-Gamboa 2016, Hu 2017]
$\frac{J_{mpp}V_{mpp}}{J^0_{mpp}V^0_{mpp}}$	J_{mpp}/J^0_{mpp} estimated from loss in transparency V_{mpp}/V^0_{mpp} estimated from the ohmic losses Developed for a contact with a grid Knowledge of solar cell required	[Jacobs 2016]
$\frac{P_{mpp}(T(\lambda), R_{se})}{P^{ideal}_{mpp}}$	$P^{ideal}_{mpp} = P_{mpp}(T = 100\ \%, R_{sh} = 0.1 m\Omega/\square)$ Intended for comparison of FoMs Most precise Scaling Difficult to handle Needs to be done on the cell	[Anand 2021]

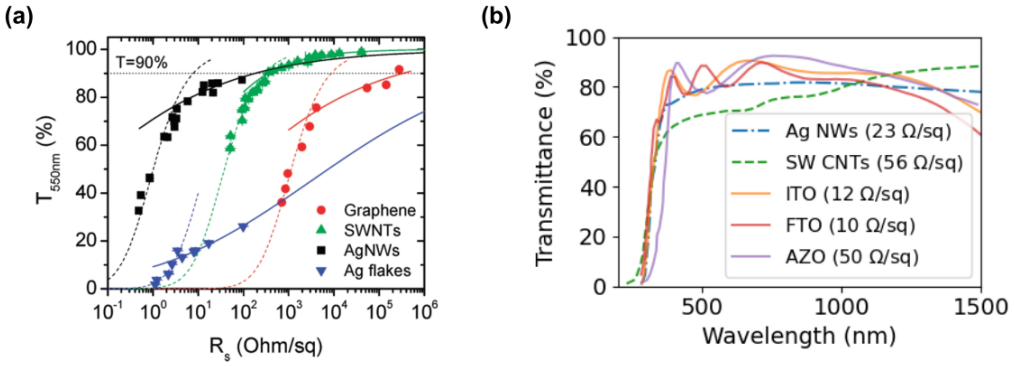

Figure 2.6: Comparison between TCOs and possible alternative materials: **(a)** Transmittance (550 nm) as a function of sheet resistance (from [De 2010]). The dashed lines represent fits to the bulk regime, while the solid lines represent fits to the percolative regime; **(b)** Transmittance over the visible-near-infrared spectrum (modified from [Ellmer 2012]).

2.1.6 Ag NWs are the most promising alternative material to TCOs

Figure 2.6 displays the properties of common alternative materials to TCOs. Ag nanowires are clearly the most promising candidate for a trade-off between optical and electrical properties. Even though discrepancies exist when comparing the figure of merit $\sigma_{opt}/\sigma_{\mathrm{DC}}$ between materials, silver nanowires also present the highest ratio (ca. 215-415) compared to ca. 120-240 for ITO [Ellmer 2012], which is corroborated by the figure of merit developed for very thin films [De 2010]. Besides, Ag nanowires show a flat transmittance in the visible-near infrared (NIR) range, which could be useful for applications in tandem solar cells.

2.1.7 Summary

A conductive material requires a high density of free carriers. Despite various origins, these carriers absorb and reflect electromagnetic waves, limiting the transparency of the material up to a given frequency. TCOs are suited to a use in the visible range, which corresponds to their transparency window. Because of their limitations (brittleness, n-doping, In content), alternative electrodes are developed, mostly with nanostructured conductive materials, such as metal nanowires, graphene or CNTs. Yet, because the transparency and conductivity of a film are tightly related, a trade-off is needed. Figures of Merit can be used for comparison between materials. The best-known one is Haacke's FoM, which compares transmittance and sheet resistance, $FoM = T^{10}/R_{\square}$.

2.2 Why a hybrid electrode is relevant for Si NW/a-Si:H solar cells

2.2.1 ITO only?

Non-conformal deposition ITO remains an effective top contact, especially for lab-scale cells. Misra et al. studied the deposition of magnetron-sputtered ITO on Si NW/a-Si:H cells. While an 80 nm layer is sufficient for a flat cell, a film corresponding to 240 nm on a flat substrate was optimal for the NW cell [Misra 2015a]. SEM and TEM observations of the ITO-covered nanowires reveal a strongly non-conformal deposition of ITO (Figure 2.7). A thick layer can be seen on top of the NWs, which results in optical losses, whereas almost no ITO covers the lower part of a-Si:H NWs.

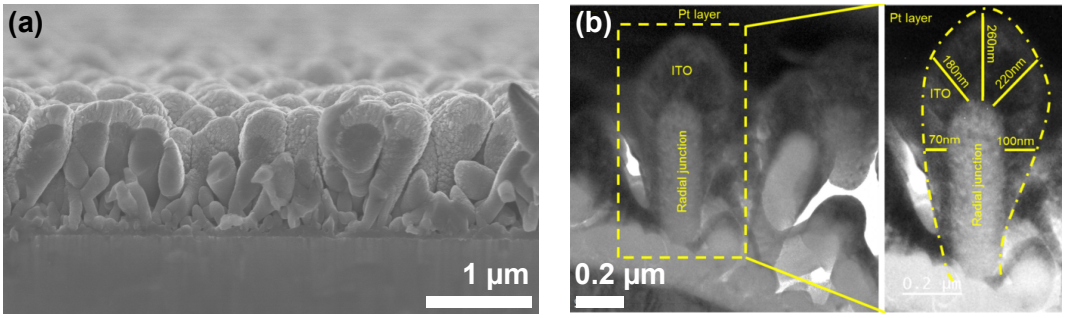

Figure 2.7: Cross-sectional **(a)** SEM and **(b)** TEM observations of Si NW/a-Si:H with 240 nm ITO as top contact (optimal thickness for a Si NW/a-Si:H cell under 1 Sun). **(b)** from [Misra 2015a].

Because of the NW array, a thick layer is needed to have a continuous electrode and for this electrode to be conductive enough on the scale of the cell (a few mm).

Why we dismiss planarization This concern is often encountered in nanostructured devices. With planarization, transparent electrodes developed for planar cells can be used with no risk of shunt. NWs are embedded in a dielectric material, with the top available for electrical connection [Chia 2011, Latu-Romain 2008, van Dam 2016]. However, it requires additional steps in the process (embedding and etching), and might be particularly challenging for a network with dense, randomly oriented NWs. In addition, this enables a connection only at the top of nanowires. For Si NW/a-Si:H cells, the benefit of core-shell NWs is then lost, because the outer n-doped layer (lowly doped and very thin) is not conductive enough to bring charge carriers to the top.

ITO is brittle In addition, we aim to design flexible electrodes, but ITO is a brittle material. It easily fractures for tensile strains around 1 % (for a 100 µm-thick substrate, it corresponds to a bending radius around 5 mm) [Cairns 2000, Leterrier 2004, Zardetto 2011]. The actual limit depends on the film thickness, with an onset for crack initiation and propagation at lower strains for thicker films. Once the cracks start propagating, a very quick increase in the sheet resistance is observed, which typically results in ${}^{R}/_{\Delta R_0} \sim 100 - 200$. Under bending, cracks in the thick layer of ITO on Si NW/a-Si:H

solar cells could therefore be expected and would be detrimental to the collection of the charge carriers.

2.2.2 Ag NWs only?

As detailed in Section 2.1.4.5, Ag NWs are a promising material for transparent and flexible electrodes, especially due to their high conductivity and easy processing. However, they cannot be used as a single material either. As displayed in Figure 2.8, Ag NWs lie on top of the array of Si/a-Si:H NWs, but they do not connect every Si NW. A high density of Ag NWs would be needed to this end, with adverse effects on transparency.

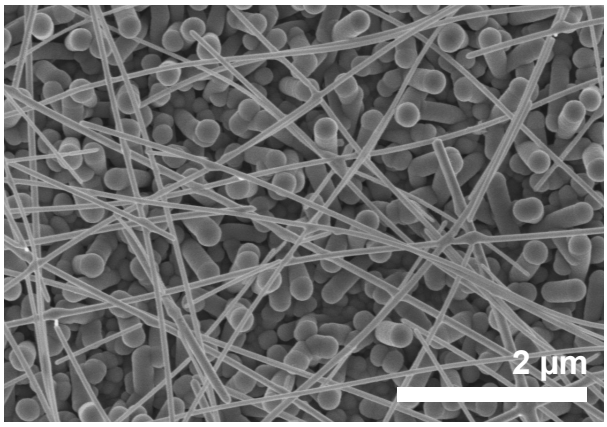

Figure 2.8: Top-view SEM image of Si NW/a-Si:H with Ag NWs only as top electrode.

2.2.3 Advantages of a hybrid electrode {ITO + Ag NWs}

Hybrid electrodes make use of several materials to benefit from the properties of each. We decided to combine ITO and Ag NWs, that have complementary properties for Si NW/a-Si:H solar cells. Figure 2.9 shows a schematics of the device. A thin ITO layer would collect charge carriers from each Si/a-Si:H NW. Due to the high density of the array of Si NWs, ITO connects groups of NWs together. A network of Ag NWs on top of the array collects the current from groups to the collecting point. This has for instance been shown by Pathirane et al. [Pathirane 2017].

This hybrid is similar to the top contact of PERC c-Si solar cells, where the collection of carriers is ensured both by the window layer (short-range) and the grid (long-range). Jacobs et al. showed how it is beneficial to keep metal wires for thin-film solar cells with new transparent electrodes, despite the optical losses [Jacobs 2016].

However, printing of fingers made of Ag paste on Si NW/a-Si:H presents some limitations. First the mesh has to be very fine due to the high resistance of the ITO layer on NWs. Typical metal wires of 20-40 µm width would result in too much shading. Moreover, Ag printing on high aspect ratio structures might be laborious, especially if trying to thin wires down, and would not display the flexibility of networks of silver nanowires.

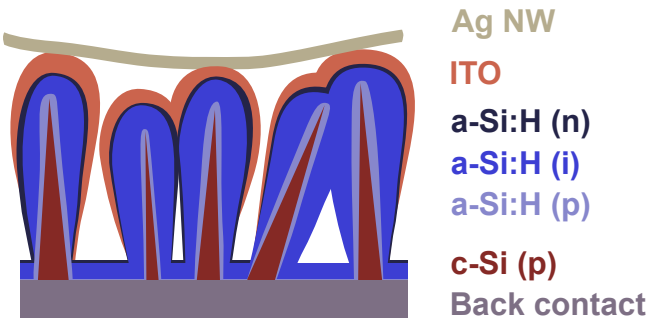

Figure 2.9: Schematic cross-section of the hybrid contact {ITO + Ag NWs} on top of Si/a-Si:H NWs.

2.2.4 Summary

In addition to the trade-off between transparency and conductivity, nanostructured devices present supplementary issues regarding the top contact. They alter the deposition of materials and usual electrodes for planar devices are not suited anymore. Furthermore, devices with NWs display two very different scales. The top contact has to collect the charge carriers at both scales. A hybrid electrode, made of different materials, is a possible solution, for instance with a TCO for the short-range collection and Ag NWs for the long-range collection.

2.3 A transparent conductive oxide for short-range conductivity

2.3.1 ITO and TZO as TCO

Because of its low resistivity ($0.77\times10^{-4}\,\Omega$cm for epitaxial ITO [Ohta 2000]), ITO is already the typical top contact for Si NW/a-Si:H solar cells [Al-Ghzaiwat 2018, Zhang 2021]. Despite its short plasma wavelength (∼0.77-1.0 µm [Gordon 2000, Ellmer 2012]), its transparency window is suited to a-Si:H. We choose to keep ITO in the composite electrode to highlight the possible benefits of using a hybrid.

However, as already mentioned, the sputtering deposition is not conformal, which may be detrimental to the collection of charge carriers from each NW and to the optical transmittance. Atomic-Layer deposition (ALD) results in conformal coatings, but is not so common for ITO. Instead, I used an ALD zinc oxide doped with titanium (ZnO:Ti or TZO), that had been developed at IPVF [Coutancier 2020]. For comparison, we measured the electrical and optical properties of ITO and TZO. They are displayed in Table 2.2 and their transmittance and reflectance spectra on glass are presented in Figure 2.10. The better conductivity of ITO is clear. In the 0.4-1.0 µm range, their optical properties are very similar. However, below 400 nm, the lower band gap energy of TZO is responsible for an increased absorption.

Despite the differences, ALD TZO enables us to assess the effect of a perfectly conformal top contact. In addition, as mentioned in Section 2.1.4.1, the sustainability of indium is questioned and alternatives to ITO should be promoted.

Table 2.2: Comparison of ITO and TZO properties. When no reference is given, measurements were made in the laboratory. [a] refers to [Coutancier 2020] for a 1:10 cycle ratio, [b] to [Yang 2006], [c] to [Ginley 2011] and [d] to [Tseng 2011].

	ITO	TZO
Thickness	80 nm	80 nm
Sheet resistance	47 Ω/□	160 Ω/□
Transmittance (550 nm)	∼ 80 %	∼ 80 %
Resistivity	3.8×10^{-4} Ω × cm	1.3×10^{-3} Ω × cm
Optical band gap energy	3.75 eV [2]	∼3.5 eV [a]
Refractive index (633 nm)	1.7 − 2 [b]	1.9 [a]
Work function	4.6-4.8 eV [c]	4.9-5.4 eV [d]

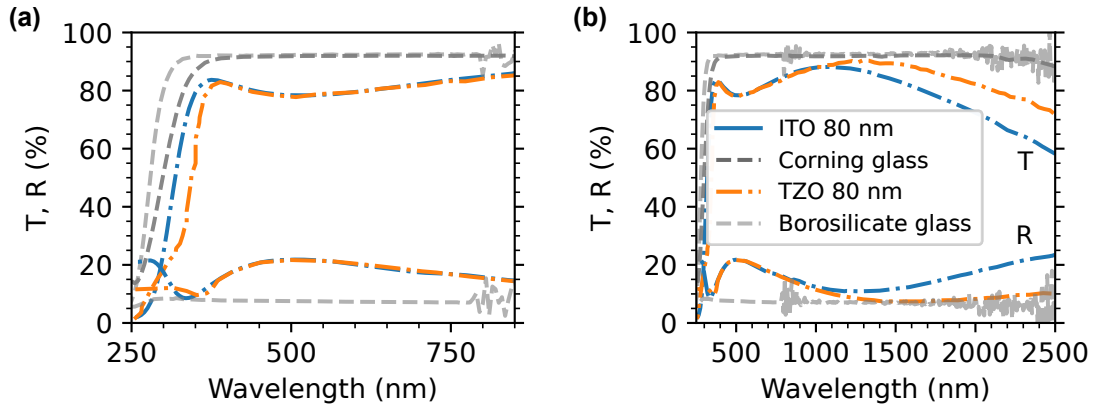

Figure 2.10: Total transmittance and reflectance of 80 nm sputtered ITO on Corning boro-aluminosilicate glass and ALD TZO on borosilicate glass. The TZO measurements were carried out by Shan-Ting Zhang. The legend is common to the two figures.

2.3.2 Magnetron-sputtering of ITO

Magnetron-sputtering with a radio-frequency (RF) power supply was used for the depositions of ITO and back-contact AZO.

Sputtering is a physical vapor deposition technique in which high-momentum particles (typically ions) bombard a *target* (thick film of the material to be deposited). Thanks to their momentum, they can break bonds and release atoms from the target. These kicked-off atoms are redeposited on the substrate.

Bombarding particles can stem from a plasma, an ionized gas. Cold plasmas, where there is no thermal equilibrium between electrons and ions, are generally used. For sputtering, plasmas are ignited and sustained through an electric field, which accelerates electrons and leads to collisions and ionization events. The power supply can either be DC (Direct Current) or RF (Radio Frequency). RF sputtering operates at 13.56 MHz

[2]Strong optical absorption of ITO films is observed around 3.75 eV. However, an absorption onset has also been shown at 2.9 eV, which corresponds to a direct band gap with mostly forbidden transitions [Walsh 2008]. We keep the value of the optical band gap.

and is particularly useful for non-conductive targets or substrates The plasma gas is often argon, because it is chemically inert and remains cheap compared to other noble gases. In addition, it is rather easy to ionize, and able to efficiently break bonds in the target. Finally, in magnetron-sputtering, a magnetic field increases the density of electrons close to the target, hence the amount of collisions and ionizations for a given pressure. Consequently, lower pressures are required to sustain the plasma. Various materials can be sputtered, e.g. oxides, metals, nitrides. It is a preferred technique for oxides, since there is little stoichiometry issues, in contrast to evaporation for instance.

Atoms leaving the target follow a rather vertical flux, but they may collide with atoms and ions from the plasma. Thus, the final deposition is not highly directional, especially at higher pressures. Still, step coverage remains difficult.

Experimental details We deposited ITO from a In_2O_3:SnO_2 target (9:1) in an Alliance Concept system. The conditions used for the deposition are the standard ones developed at LPICM. The substrate holder is heated at 180 °C and the chamber is pumped down to $<9\times10^{-7}$ mbar . Ar and O_2 (3 % in Ar) are used as gases, with a sputtering pressure around 6×10^{-3} mbar. To define circular solar cells with a 2 mm or 4 mm diameter, we used a shadow mask during the magnetron sputtering. We changed only the ITO thickness for the top contact optimization.

2.3.3 ALD for TZO

Atomic-Layer Deposition relies on chemical reactions. It is a step-by-step deposition, where each precursor is separately introduced in the chamber. Between steps, a purge removes the precursor molecules that have not reacted. During one step, the sites available for reaction are saturated by the precursor species. These sites limit the amount of reactions and enable a layer-by-layer growth. With this method, the total thickness is finely controlled. In addition, a very conformal deposition is obtained. Indeed, the precursors are able to reach all available sites, since they are in the gas phase and largely in excess compared to the reaction sites. However, deviation from an ideal layer-by-layer deposition can occur, especially at the beginning of the deposition process [Richey 2020].

ZnO ALD was first demonstrated by Tammenmaa et al. [Tammenmaa 1985] with zinc acetate and water as precursors. Now, diethyl zinc is mostly used with H_2O, and as many as 22 different elements have been reported for doping [Gao 2019].

Experimental details For this work, TZO was deposited from diethyl zinc, H_2O and titanium (IV) i-propoxide with one TiO_2 cycle for every 10 ZnO cycles (1:10 cycle ratio). The conditions standard conditions developed at IPVF, detailed in [Coutancier 2020] (sequence A). All depositions were made at IPVF by Shanting Zhang and Nathanaëlle Schneider. We changed only the TZO thickness for the top contact optimization.

2.3.4 Sputtered vs. ALD top contact on Si NW/a-Si:H solar cells

The deposition conditions for ITO sputtering and TZO ALD are summarized in Table 2.3. The long deposition time required for ALD is clear, it is an expensive method due to its slow growth.

Table 2.3: Comparison of ITO and TZO deposition conditions for 80 nm films.

	ITO Magnetron-sputtered	TZO ALD
Power	200 W	-
Atmosphere	Ar + O_2 (3 % in Ar)	N_2 + precursor
Deposition pressure	6×10^{-3} mbar	1-2 mbar
Temperature	180 °C	200 °C
Deposition time	45 min pumping/heating 2 min deposition	30 min pumping/heating ∼25 min deposition
Conformal	Roughly	Perfectly

Figure 2.11 presents the cross-section of Si NW/a-Si:H with 80 nm of both materials. While the ITO film on top of NWs correspond to the expected thickness (∼72 nm estimated from the broken Si/a-Si:H NW), there is almost no material on the NW sidewalls. In contrast, the ALD TZO strictly follows the NWs, down to the substrate. Furthermore, the morphology of ITO and TZO are rather different, with large grains in TZO and very small ones in ITO.

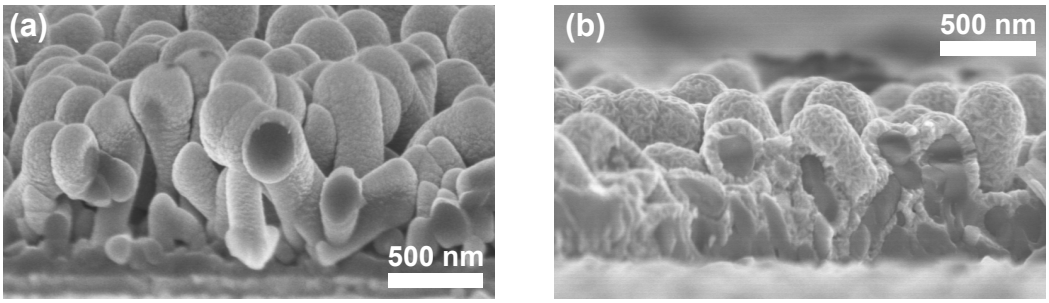

Figure 2.11: SEM images of Si NW/a-Si:H after **(a)** sputtering of 80 nm ITO, **(b)** ALD of 80 nm TZO. The bare Si/a-Si:H nanowires are easy to distinguish from the TCO thanks to a darker contrast.

It should be noted that while the TZO uniform thickness should improve the optoelectronic properties of the film compared to sputtered ITO (no supplementary loss of light at the top, collection from the whole NW), it could electrically connect the bottom of the array, including potential pinholes and the parasitic flat cell, which would result in a degraded shunt resistance.

2.3.5 Summary

TCO is the best option for the collection of charge carriers from single Si/a-Si:H NWs. Magnetron-sputtered ITO is preferred because of its good optoelectrical properties. Yet it does not conformally cover the NWs. Because the core-shell NWs require the collection of charge carriers along the whole NW, an ALD TCO is also considered, namely ZnO:Ti.

2.4 Ag NWs for long-range conductivity

2.4.1 A conductive network

Percolation threshold Ag nanowire electrodes rely on percolation, i.e. the formation of a conductive pathway through the connection of elements whose typical dimensions are much smaller than the dimensions of the final pathway. When connecting enough Ag NWs, electrons are able to travel a large distance following the obtained path. The minimal density depends on the design and the morphology of the small elements.

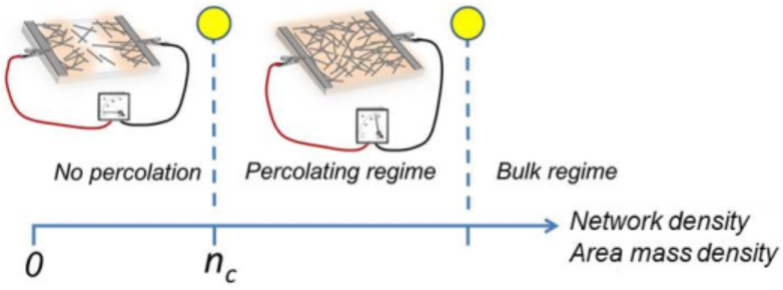

Figure 2.12: Schematics of the different regimes in Ag NW electrodes depending on the density of Ag NWs. Extracted from [Sannicolo 2018].

Because of their very high aspect ratio (> 150 in our work) Ag nanowires are prone to connect and lead to a conductive network. The density required to reach percolation can be assessed with the *percolation threshold*, which corresponds to a percolation occurrence probability of 50 %. As a first assumption, Ag NWs can be considered as objects of one dimension. For a 2D square network made of rods of length L_w (straight, with the same length) randomly deposited, Monte Carlo simulations [Li 2009] show that the percolation threshold N_{th}^{random} is given by

$$N_{th}^{random} = \frac{5.637}{L_w^2}. \tag{2.24}$$

It clearly appears that longer nanowires reach percolation more easily.

Design But design also has an impact. When considering an ordered network with a square lattice (the lattice constant equal to the nanowire length) instead of a random network, the percolation threshold is ten times smaller

$$N_{th}^{square} = \frac{0.5}{L_w^2}. \tag{2.25}$$

Whereas no control exists for a random network, in an ordered array, connections are rather optimized and a wire is more likely to be connected to the conductive pathway. However, well-ordered nanowire networks are more difficult to achieve by low-cost methods such as solution depositions.

Conductivity For a given amount of wires, the nanowire length also impacts the conductivity of the network beyond the percolation threshold. For a density N such that $1.3 < N/N_{th} < 2$, the conductivity of the network follows, with $\beta \sim 1.3$ [Lagrange 2015],

$$\sigma \propto (N - N_{th})^{\beta}. \tag{2.26}$$

Equation (2.26) shows that adding nanowires quickly increases the conductivity. Indeed, close to N_{th}, few possible paths exist and new connections easily lead to less resistive paths. Even after the percolation regime, the conductivity still increases with the amount of nanowires, until the bulk conductivity is reached. In 85 nm-diameter silver nanowires, this transition to bulk properties occurs for a (non-continuous) film with a thickness ~160 nm, around twice the diameter [De 2009].

2.4.2 Optical properties

Nanowires versus bulk silver The transmittance of bulk silver is very low over the UV-Vis-NIR spectrum, with either a high reflectance (visible and near infrared) or absorptance (UV region). Despite its conductivity, bulk silver can therefore not be used. However, with silver wires, a conductive and non-continuous network can be obtained. Hence, large bare areas remain, which reduces the optical losses. This benefit stems from the non-continuity of the film, not from the nanometric scale of nanowires. The effect of their diameter is discussed in Section B.1.2.

Haze factor Because they are particles, Ag NWs also strongly scatter light, in agreement with Mie scattering theory [Khanarian 2013]. The haze factor is used to quantify scattering (usually forward scattering) and is defined as

$$\text{Haze} = \frac{I_{scattered}}{I_{scattered} + I_{direct}}.$$

The haze factor increases with the amount of material (areal mass density) and the diameter of nanowires. For instance, at a 80 % transmittance, the haze factor ranges from 10 % to 40 % for diameters between 25 nm and 117 nm [Lagrange 2015]. Forward scattering at the device surface increases the optical path of the light into the active material, which should be beneficial to solar cells, thanks to an increase in the photo-generated current [Zeman 2000].

Surface plasmons in Ag nanowires Silver nanowires also present specific optical properties at given wavelengths. Due to their small diameter and their metallic nature, localized surface plasmon resonance (LSPR) occurs. Plasmons are collective oscillations of the free electrons. At the interface between a metal and a dielectric, these oscillations are confined close to the surface and result in surface plasmons. In nanostructures with at least one dimension similar to the oscillation wavelength, a sharp resonance can take place. At this frequency, extinction is particularly significant. For Ag nanowires with diameters around 50-100 nm, the resonance occurs at 350-420 nm and results in a yellowish color of the suspension and deposition [Garnett 2012, Khanarian 2013]. For non-circular cross-sections, more resonances can be observed [Kottmann 2001].

2.4.3 Flexibility of Ag NW networks

Ag NW networks have been used as flexible electrodes, both in bending and stretching configurations, with improved properties compared to TCOs. For instance, Song et al.

showed almost no change (< 1 %) in the sheet resistance $R_\square$ of a PET/Ag NWs electrode for a bending radius down to 0.2 mm, while the ITO film displayed many cracks and a resistance twice as high as initially [Song 2013].

This flexibility comes from the network structure, which can accommodate to the deformations of the substrate. In addition, and in contrast to bulk materials, there is no propagation of cracks. When there is fracture in a NW, it is not a starting point for further cracks. Besides, there is a size effect in the mechanical properties of single NWs, which results in a higher ultimate tensile strength than for bulk silver. However, ductile fracture can still be observed [Schrenker 2021]. In order to improve the mechanical properties of the network, pre-straining can be carried out [Ho 2013, Lee 2012]. Ag NWs are initially deposited on a strained substrates. Hence, Ag NWs on the device at equilibrium are in a compressive strain state and the tensile straining of the network results in a decrease in the strain of individual NWs. Nevertheless, its application to top contacts raises some issues regarding the pre-straining of the device.

2.4.4 Preparation process

Ag NWs are commonly synthesized by the reduction of Ag nitrates in a polyol in the presence of polyvinylpyrrolidone (PVP) [Sun 2002]. After purification, they are dispersed in a solvent. Solution processing is then used for the fabrication of electrodes. A post-deposition treatment is required to improve the electrical properties.

For this work, we used commercial suspensions of silver NWs supplied by Sigma Aldrich. Before the optimization of the hybrid electrode, we had to determine the processing of Ag NWs, including their dimensions, the deposition method and the annealing conditions (temperature and atmosphere). More details regarding the processing of Ag NWs and the choice of parameters for this work can be found in Appendix B.

Two suspensions in isopropanol have been used, both with nanowires of 60 nm diameter and 10 µm length. Depending on the dimensions of the sample, Ag NWs were either drop-cast at room temperature or spin-coated. After deposition, the substrates were annealed. Typical annealing was carried out for 20 min in an oven under ambient atmosphere. The temperature was 240 °C for the first suspension, 180 °C for the second one. When Ag NWs were coated on TZO, annealing was done under N_2 atmosphere.

2.4.5 Summary

Ag NWs are a promising alternative to TCOs for transparent electrodes. They are highly conductive (metal) and remain transparent (non continuous). Furthermore, they can be used for flexible devices and are easy to process.

2.5 A two-step optimization directly on the device

More degrees of freedom With a hybrid electrode, more parameters can be tuned. Hence, optical and electrical optimizations can be (partially) separated. The main parameters that can be varied and that will determine the transparency and the resistance of the contact are the TCO thickness and the density and size of Ag NWs. Because we rely on Ag NWs for the long-range conduction, the transparency is the key feature that

will be considered for the thickness of ITO. In a second step, the density of Ag NWs will be changed to achieve the maximal performance of the device.

Deposition altered by the NWs Deposition and characterization of transparent electrodes are usually done on glass. The transmittance and resistance of the contact are easy to measure. However, it requires that the deposition of the electrode does not depend on the morphology (especially for evaporation, sputtering and solution techniques) or chemical composition (for instance for ALD, and solution processes) of the substrate. Because NWs display a high aspect-ratio structure, they strongly alter the deposition. For instance, in our work, 80 nm of magnetron-sputtered ITO on a planar substrate resulted in a sheet resistance of 60 Ω/□, while a thicker ITO on NWs (deposition 3.5 times longer) led to 2 kΩ/□. The wetting of the substrate by the Ag NW suspension is also affected by the morphology of the substrate. Less wetting is expected for a nanostructured substrate. One could optimize the hybrid on glass and use the optimized electrode on the NW array, as was done by Pathirane et al. [Pathirane 2017], but this optimization is not relevant for the nanostructured device.

Characterization on the device Consequently, the optimization has to be done directly on the NW solar cell. Yet, once on the device, the optical and electrical properties of the electrode cannot be disentangled. For example, the measured sheet resistance of the top contact would be related to the conductivity of the layers below and to the possible shunts in the cell. A mock cell could be made (same structure, but no doping), which would favor a correct measurement of the sheet resistance of the contact. However, the measurement of the transparency through the absorber would remain low and sensitive to errors.

2.6 Step 1: ITO thickness and optical properties

2.6.1 Use of EQE to probe the optical properties

To evaluate the transparency of the ITO film on the Si NW/a-Si:H solar cells, we used External Quantum Efficiency (EQE) measurements. EQE is defined as

$$EQE = \frac{N_e}{N_\gamma},$$

with N_e the amount of generated and collected charges and N_γ the amount of impinging photons. The amounts of electrons and photons can be respectively related to the short-circuit current in the solar cell, J_{sc}, and the incoming power density P_0, with E_γ the energy of one photon:

$$EQE(\lambda) = \frac{J_{sc} E_\gamma(\lambda)}{q P_0}.$$

It is wavelength-dependent.

In an EQE setup, a single-wavelength light is shone on the cell and the short-circuit current density is measured. The light intensity is low (a few µW), resulting in a low current (µA), which is crucial to dismiss the resistance effects.

We measured the EQE values with an Oriel IQE200. A grating-monochromator selects the wavelength of the illuminating light. The area of the spot is a few mm^2. A

scan between 300 nm and 800 nm with a step of 10 nm enables to assess the response of the cell over the UV-Vis-NIR range. Furthermore, to mitigate the impact of the ambient light, we used synchronous detection with a lock-in amplifier (30 Hz modulation, 0.1 s time constant). The modulation frequency is rather low due to the response time of solar cells. A two-wire setup measures the current.

2.6.2 80 nm ITO results in the best optical performance

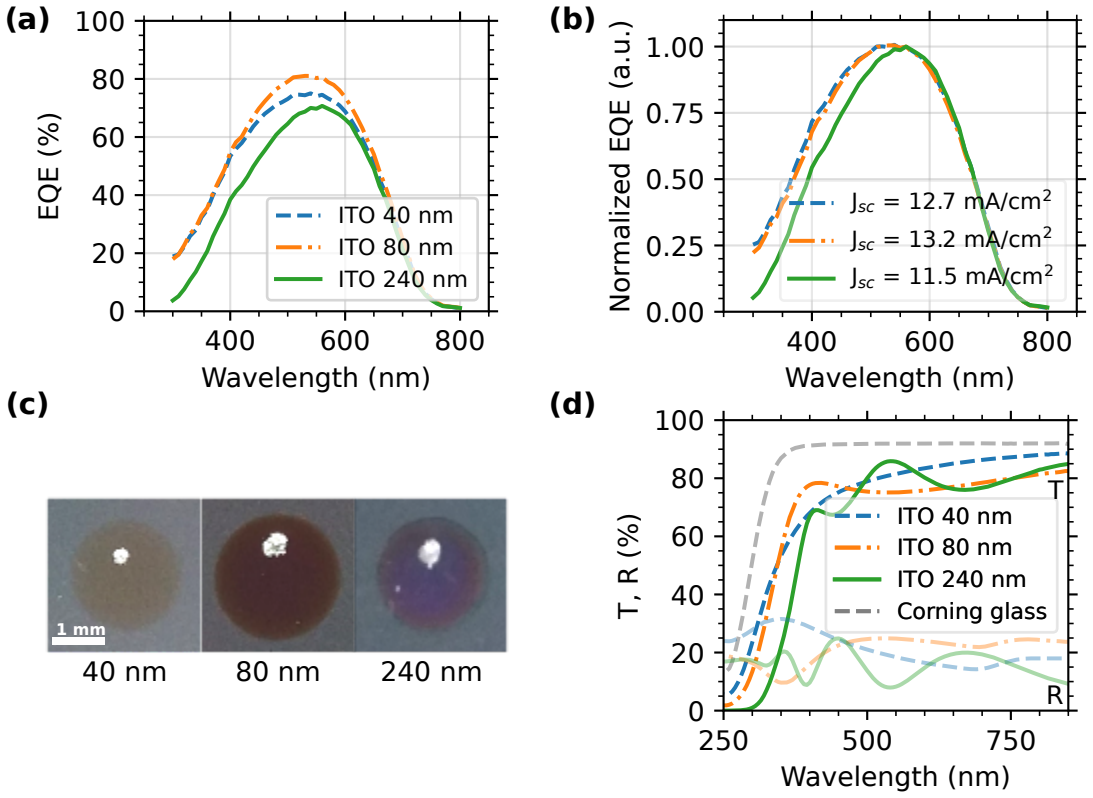

Figure 2.13: **(a)** EQE, **(b)** normalized EQE, **(c)** pictures of Si NW/a-Si:H solar cells with ITO only as top contact and **(d)** total transmittance and reflectance of ITO on Corning glass. The dot of Ag paste used for contact can be seen.

We deposited three different thicknesses of ITO on top of Si/a-Si:H NW cells (standard growth, FTO back-contact). The thicknesses corresponding to these deposition times had previously been determined by ellipsometry from reference samples on glass. They equal to 40 nm (ITO 1'), 80 nm (ITO 2') and 240 nm (ITO 7'). Then, I measured their EQE spectra to compare their transparency. They are displayed in Figure 2.13 **(a)**. The integrated values of EQE are displayed in Table 2.4.

Low transmittance of 240 nm ITO We observe lower EQE values for the thickest ITO (240 nm) below 600 nm. In the 350-520 nm range, the EQE values of 80 nm ITO are higher than that of 240 nm ITO by more than 10 %. This is consistent with the lower transmittance measured for the flat substrate (see Figure 2.13 **(d)**). It is mainly attributed to absorption, either residual absorption or from interband transitions (below

350 nm, consistent with the reported value of the optical band gap of 3.75 eV). Nevertheless, the blueish color of the cell with 240 nm ITO in Figure 2.13 **(c)** also suggests an increased reflection in the short-wavelength range.

Despite the optical thickness and hence the absorption path twice as long, 80 nm ITO shows slightly higher EQE values than 40 nm ITO, with a maximal difference around 550 nm.

Anti-reflection effect The higher EQE of 80 nm ITO could be related to the anti-reflection effect of the ITO. ITO acts as an anti-reflection coating thanks to its intermediate refractive index, close to the optimal one $\sqrt{n_1 n_3}$ (around 2.1 for ITO [Yang 2006] compared to 3.6 for a-Si:H [Swanepoel 1983] at 550 nm). Even though NW arrays trap light much better than thin films, the reflection losses are still present [Zhu 2009] and we can expect an improvement for the appropriate thickness of ITO. In addition, interferences can occur in thin films and lower the reflection around specific wavelengths, as can be clearly seen in Figure 2.13 **(d)**. For flat a-Si:H cells, taking into account the solar spectrum and the absorption of a-Si:H, Fan et al. found an optimal thickness around 60 nm [Fan 2010]. Yet, on the transmittance spectra, the lowest reflection for the 80 nm ITO occurs for shorter wavelengths (around 350 nm) than the increase in EQE. The difference in the actual ITO morphology between the flat and the NW substrates is a possible explanation. The anti-reflection effect is supported by the picture of both cells in Figure 2.13 **(c)**. The cell with 80 nm ITO looks much darker than the cell with 40 nm ITO. It could be due to an increased absorption in the ITO film, but the better EQE values suggest otherwise. The difference between the EQE measurements and the transmittance on a flat glass highlights the importance of a characterization directly on the substrate of interest.

Electrical limitations? However, we could wonder whether the difference between 40 nm and 80 nm is related to the electrical properties of the ITO film. When considering the normalized EQE spectra (Figure 2.13 **(b)**), the 40 nm and 80 nm ITO lines overlap well, except for short wavelengths where the absorption of ITO can be seen. This suggests that the main difference in the EQE values does not depend on the wavelength. It could point towards electrical limitations of the 40 nm ITO film. Measurements with another EQE setup and current values below 10 µA (∼2 mm^2 area) also presented higher EQE values in the 400-600 nm range for the 80 nm film. In addition, SEM observation of the cross-section shows a rather continuous layer (Figure 2.14). Hence, the collection of low currents should be possible even with the 40 nm ITO. Electrical effects cannot be fully ruled out, but seem unlikely.

Among the values we measured, we found that 80 nm ITO is the optimal thickness on top of the Si NW/a-Si:H ensembles.

2.6.3 Discrepancy between J_{sc} values from EQE and 1 Sun J-V measurements

Low performance of 80 nm ITO under 1 Sun We characterized the same cells with different ITO thicknesses under 1 Sun illumination, Figure 2.15 displays the J-V

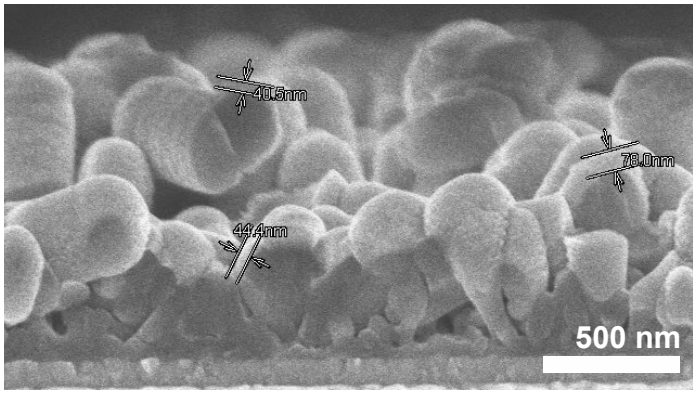

Figure 2.14: SEM image of a cross-section of a Si NW/a-Si:H solar cell with 40 nm ITO as top contact.

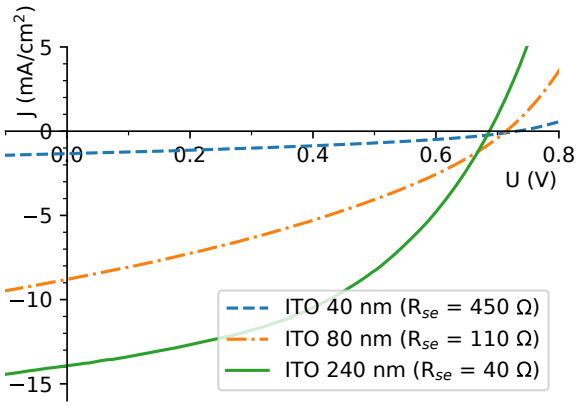

Figure 2.15: J-V curves under AM1.5G illumination of Si NW/a-Si:H cells with 40 nm, 80 nm or 240 nm ITO only as top contact. The series resistance is given in the legend.

curves. Despite the higher optical transmittance of 80 nm ITO, it did not function as the most efficient top contact for the solar cell under 1 Sun. The cell with 240 nm ITO presents the highest efficiency (4.3 %) thanks to higher fill-factor and short-circuit current. 40 nm and 80 nm ITO show low fill-factors, around 35 %. It stems from a poor collection of the charge carriers, due to the high in-plane resistance of the top contact.

J_{sc} from EQE vs. J-V under 1 Sun From the EQE measurements integrated over the solar spectrum, we computed the optically expected J_{sc} values under AM1.5G illumination. They are reported in Table 2.4 alongside the measured values.

Table 2.4: J_{sc} under 1 Sun computed from the EQE values with the AM1.5G spectrum or from J-V measurements under 1 Sun.

	J_{sc} (mA/cm^2)	
	From EQE measurements	From J-V under 1 Sun
ITO 40 nm	12.7	1.3
ITO 80 nm	13.2	8.8
ITO 240 nm	11.5	13.9

The measured J_{sc} for the cell with 240 nm ITO is higher than expected. We anticipated a discrepancy between EQE and J-V values, it may come from instrumental errors, especially regarding the intensity and the spectrum of the solar simulator. For this reason, EQE measurements can be preferred to get an optically relevant value of J_{sc}. In contrast, for cells with 40 nm and 80 nm ITO films, the measured current density is lower than the expected one (much lower for the 40 nm cell). This originates from the difference in illumination level. The high in-plane resistance of the thinner films of ITO prevents the substantial amount of charge carriers generated under 1 Sun from being fully collected. In EQE measurements, the illumination and the resulting photocurrent are much lower, which makes the setup almost insensitive to the differences in the contact resistance.

In conclusion, EQE measurements should be chosen to assess the optical properties of the electrode on the device, but a relevant value of J_{sc} for devices with a high series resistance requires AM1.5G illumination.

2.6.4 Summary

Thanks to the use of a hybrid electrode, we can carry out the trade-off between the transmittance and the resistance in two steps. First, we changed the thickness of the TCO layer to achieve a high transparency. We had to do it on the device, since the ITO deposition is altered by Si/a-Si:H NWs. EQE measurements showed that 80 nm was the optimal thickness. We could not reach this conclusion with J-V measurements due to the high in-plane resistance of the contact.

2.7 Comparing ALD TZO with ITO contact

We can use the same method with ALD TZO instead of ITO to determine whether the conformal coating is beneficial. In addition, because of different optical properties and morphology of the oxide, the optimal thickness may differ and several thicknesses should be tested. The samples had the a structure similar to the previous one, except for the back contact, which is made of Ag/AZO (100 nm/100 nm) instead of FTO. The substitution of the back-contact comes from a different series of samples. We did not change it on purpose in relation with the top contact.

2.7.1 Optimal TZO thickness

We deposited 60 nm, 80 nm and 100 nm TZO on top of Si NW/a-Si:H cells from the same series. Because of ALD, a shadow mask was not sufficient to avoid TZO deposition and Kapton tape was needed to define cells. We removed Kapton tape prior to measurements.

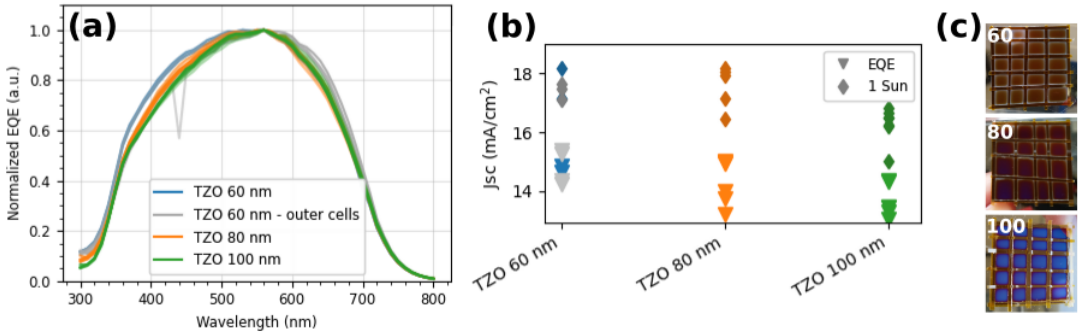

Figure 2.16: **(a)** Normalized EQE, **(b)** J_{sc} values from EQE and J-V under 1 Sun and **(c)** pictures of Si NW/a-Si:H solar cells with TZO only as top contact.

We recorded the EQE spectra and J-V curves for the cells with the three TZO thicknesses. Figure 2.16 **(a)** shows the normalized EQE measurements. Some of the 60 nm TZO and one of the 100 nm TZO cells presented an increased EQE at longer wavelengths. A stronger absorption of the cell in this range stems from increased scattering. It can be related to the front contact, because it scatters the incoming light, or because it affects light-trapping via enhanced internal reflections [Söderström 2009]. Since we observed an increase for 60 nm and 100 nm TZO and since all of the cells in question were located close to the edge of the sample, we attribute the variation to non-uniformities, namely non-uniformities in the Si NW/a-Si:H array. The density of Si NW/a-Si:H is likely lower in the outer region, which alters the scattering of light by NWs. Hence, we disregarded these measurements for a better comparison of the top contact effect, but they are shown in grey.

The thickness of the top contact can affect its transmittance (hence the EQE values of Si NW/a-Si:H cells with the TZO contact) due to absorption or a change in the reflectance. The latter can be clearly seen from the color of the samples in Figure 2.16 **(c)**.

Because of interferences, the reflectance strongly depends on the wavelength. Hence, no conclusion on the overall value of the transmittance can be drawn.

We chose to show the normalized EQE values because they highlight the change in the spectral response of the cells with different TZO thicknesses (Figure 2.16 **(a)**). In particular, the absorption of the top contact should mostly affect the region of short wavelengths. This effect can be clearly seen in the normalized EQE values. Below 500 nm, they display a decrease for thicker TZO films. Below 350 nm, this is attributed to inter-band transitions. Between 350 nm and 500 nm, residual absorption can be responsible.

J_{sc} values The overall transparency of the TZO films on Si NW/a-Si:H under 1 Sun can be assessed with the J_{sc} values computed from the EQE (Figure 2.16 **(b)**). There is some dispersion, likely related to different densities of Si NWs. Nonetheless, it is clear that the thickest TZO film (100 nm) is not transparent enough for the Si NW/a-Si:H solar cells. Further measurements would be needed to determine the most transparent thickness of TZO.

We also measured J_{sc} values under 1 Sun, they are displayed in Figure 2.16 **(b)**. In contrast with ITO, these values are higher than the ones computed from EQE for all TZO thicknesses. It means that the collection of charge carriers is not strongly limited by the in-plane resistance of the top contact, even for very thin films. While the TZO resistivity is higher than the ITO one (Table 2.2), the ALD technique results in a continuous and uniform layer, which reduces the overall resistance. On the contrary, in ITO, there are regions with very thin ITO or no ITO. As we had already observed for the thickest ITO layer, the values from 1 Sun measurements are higher, which we attribute to the calibration of the solar simulator. This suggests that even thinner films of TZO could be used in a hybrid contact, but we did not have the opportunity to test such thicknesses. In addition, we observe a similar trend with the TZO thickness with EQE or 1 Sun J_{sc}. 60 nm or 80 nm TZO result in similar current densities and TZO 100 nm displays a lower J_{sc}.

2.7.2 Comparison with ITO

EQE measurements Figure 2.17 displays the normalized EQE of cells with 60 nm, 80 nm and 100 nm of TZO and 80 nm of ITO. All cells belong to the same growth. Due to different parameters used during the a-Si:H deposition, their EQE outlines differ from the previous cells. Yet, the conclusions regarding the effect of the TZO thickness hold, with thinner TZO displaying a higher transparency in the short-wavelength region. For the same nominal thickness, ITO leads to less optical losses than TZO. It is mostly attributed to the higher transparency of ITO in the short-wavelength range, as shown in Figure 2.10.

I-V measurements From the SEM cross-section (Figure 2.11 **(b)**), it is clear that the material deposited by ALD can go to the bottom of NWs. Hence, a possible drawback of ALD TZO is the direct connection between top and bottom contacts through pinholes or the connection of more defective parts of the cell, such as the parasitic flat one. This could result in a decreased shunt resistance.

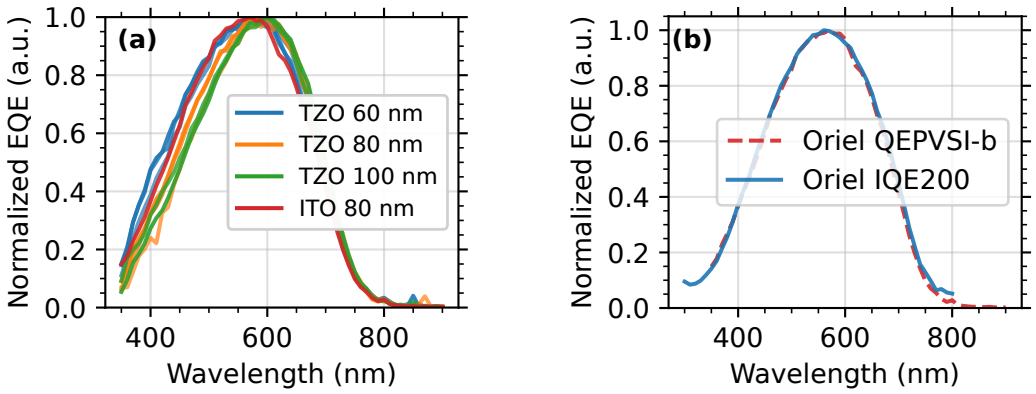

Figure 2.17: **(a)** Normalized EQE measurements on samples from a same series with different thicknesses of TZO and ITO as top contact. A new EQE setup was used for most measurements. **(b)** displays a comparison of the two setups for a cell with ITO as top contact. They show good agreement.

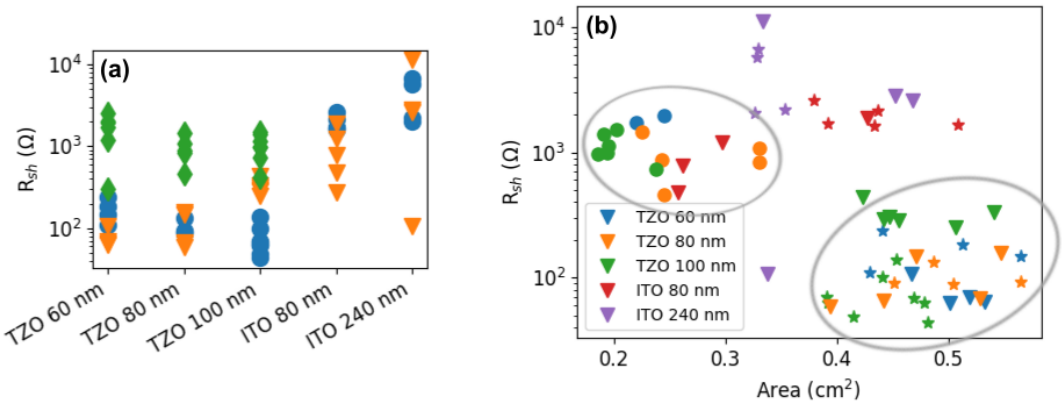

Figure 2.18: **(a)** Shunt resistance from 1 Sun measurements for 3 series of samples shown with different symbols. Because the growth of the Si NW/a-Si:H is critical for the shunt values, we make the distinction between different growths. Samples from a same batch are displayed with the same color and marker. **(b)** Same data as in **(a)** plotted against the area of the cells. The different colors show the different top contacts. Again, because a trend could come from the different Si NW/a-Si:H growths, we use different markers for the different series of samples. Two (arbitrary) ellipses show that there are two groups of Si NW/a-Si:H with TZO as top contact, depending on the cell area.

Figure 2.18 **(a)** displays the shunt resistance R_{shunt} of three series of cells with TZO or ITO as top contact. The shunt resistance indeed looks higher with ITO as top contact. However, the size of the cell or the growth can also affect the R_{shunt} value. Figure 2.18 **(b)** presents the same values of R_{shunt} against the area of the cells. Three series of samples are displayed, with different symbols. The cells with TZO as top contact belong to two groups, shown with grey ellipses: small area and high R_{shunt} or large area and low R_{shunt}. It confirms the dependence of R_{shunt} on the area. In addition, it confirms that ITO cells (red and purple symbols) show a different behavior, with higher values of R_{shunt}. The low values of R_{shunt} in the TZO cells result in a loss of performance due to low fill-factor and V_{oc}.

2.7.3 Summary

Used instead of ITO, ALD TZO covers the NWs with a conformal layer. EQE measurements showed no strong improvement in the optical properties compared to ITO. However, comparison between the EQE measurements and the J-V curves under 1 Sun proved that we were far from limitation due to the in-plane resistance, even for 60 nm TZO. Hence, the use of TZO could result in lower Transparent Conductive Oxide (TCO) thicknesses. Yet, the conformal deposition also leads to lower shunt resistances, probably related to the electrical connection of the bottom. This strongly impedes the performance of the cell. Hence, I chose to keep magnetron-sputtered ITO in the hybrid electrode.

2.8 Step 2: Ag NW density and highest PCE

Once the TCO has been optimized for its transparency on the cell (namely with 80 nm ITO), Ag NWs can be added to the cell/ITO structure to make a device with a hybrid electrode. Their density is varied to find the best trade-off between the conductivity of the network and its transparency.

2.8.1 Experimental details

Process On a Si NW/a-Si:H sample, I defined six cells (4 mm diameter) with ITO sputtering (nominally 80 nm). On each cell except for one, I drop-cast 2 µL of Ag NW suspension with a different concentration. I used a commercial suspension of 60 nm diameter and 10 µm length silver nanowires in isopropanol (IPA), with an initial concentration of 0.5 wt.% (around 3.9 mg/L). I further diluted the suspension in IPA with final concentrations of 20, 40, 60, 80 or 100 % of the initial one. After the deposition of Ag NWs, I annealed the sample in air at 240 °C for 20 min, including the bare ITO cell. I tested different deposition and annealing conditions, they are reported in Appendix B. The process described here led to the best performance of the Ag NW electrode.

J-V curves I determined the average density of Ag NWs on each cell from the total area and the quantity of deposited NWs. I tested the cells under a AM1.5G illumination, with a four-wire setup. To avoid any possible change of the effective solar cell area due to the spreading of Ag NWs, I used an optical mask (3 mm diameter) to keep the

illuminated area constant. While the PCE is the decisive factor for the optimal density, I also analyzed R_{se} and J_{sc} values.

2.8.2 Effect on R_{se} and J_{sc}

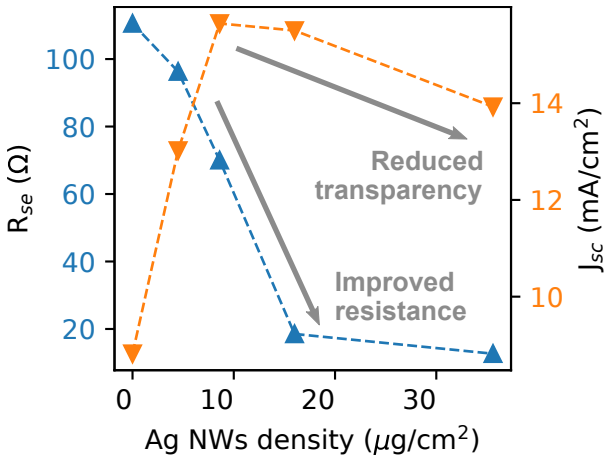

Figure 2.19: Series resistance R_{se} and short-circuit current density J_{sc} of Si NW/a-Si:H solar cells with {80 nm ITO + Ag NWs} as top contact. Parameters were probed under 1 Sun illumination.

I extracted the series resistances and short-circuit current densities obtained for the different Ag NWs densities. They are presented in Figure 2.19.

Change in R_{se} A significant reduction in R_{se} is achieved in the solar cell with a dense network of Ag NWs (six times lower than that in the same type of solar cell without Ag NWs). More specifically, the series resistance first decreases for denser Ag NW networks, then becomes steady at around 20 Ω for a density above 16 µg/cm^2. Adding more Ag NWs does not seem to further improve the electrical properties of the cell. The series resistance of the complete cell is an equivalent resistance, including the resistance of the NW core and a-Si:H layers, the contact resistance between materials, and the in-plane resistances of the top and back contacts. The decrease of series resistance with increasing Ag NW density suggests that the series resistance of the Si NW/a-Si:H cell is mainly governed by the in-plane resistance of the top contact. This is indeed the only parameter contributing to the equivalent resistance which is sensitive to the change of density of the deposited Ag NWs.

Comparison with theoretical percolation threshold We can compare these densities to the percolation threshold as defined in Eq. (2.24). For randomly deposited NWs with a 10 µm length, the percolation threshold corresponds to a density of 1.7 µg/cm^2, much lower than the densities in Figure 2.19. The first reason is an overestimation of the experimental density, for instance due to the drying ring. Indeed, because of surface tension effects (detailed in Appendix B), many particles deposit on the edge of the droplet. Moreover, reaching percolation means that one conductive path exists but its resistance can still be high. Thus, a percolating network does not necessarily

result in a good conduction [De 2010]. Densities close to 4-10 µg/cm^2 for NWs around 100 nm×10 µm are required for $R_\square$ below 50 Ω/□ [De 2009, Pathirane 2017]. A much higher Ag NW density is expected to be used in optoelectronic devices which require a particularly low resistance such as solar cells.

Change in J_{sc} Figure 2.19 also shows the evolution of the short-circuit current density as a function of the density of Ag NWs. Because of the reflection and absorption by Ag NWs (see Figure 3.6), less light is transmitted into the cell (i.e. lower absorption of a-Si:H) and a decrease in J_{sc} is expected. Yet, at low Ag NW densities (≤9 µg/cm^2), J_{sc} quickly increases with increasing Ag NW density.

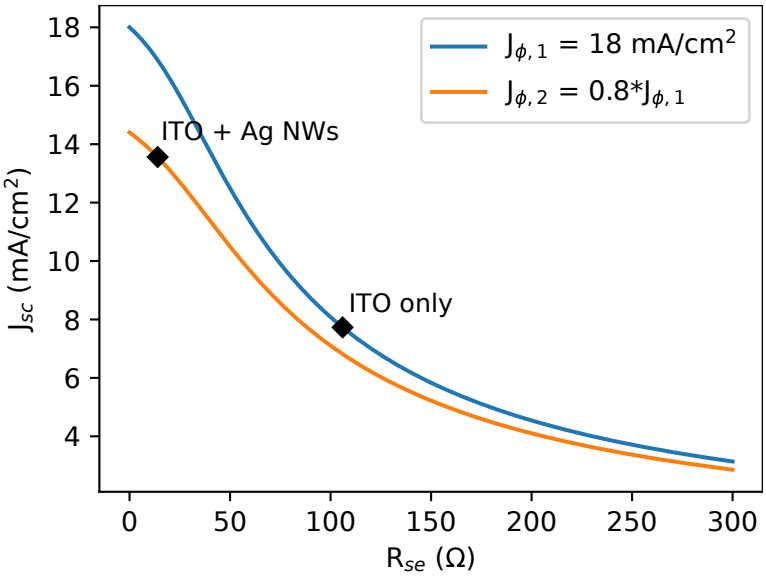

Figure 2.20: Short-circuit current density against the series resistance for two different illumination currents. The values of J_{sc} and R_{se} in case of ITO only and ITO + Ag NWs are displayed with ♦. The values are computed from the one-diode model with the following parameters: $J_0 = 1.1\times10^{-3}$ A/cm^2, area A = 7.1×10^{-2} cm^2 (3 mm diameter), $R_{shunt} = 4\times10^3$ Ω, T = 293 K. This model is rather simple, as can be seen from the high J_0 value required to correspond to the experimental values.

To understand the effect of Ag NWs on the short-circuit current density, I used the one-diode model (see Section 1.1.5). Figure 2.20 highlights the dependency of J_{sc} on the series resistance for two different illuminations, $J_{\phi,1}$ and $J_{\phi,2}$, with J_{sc} computed from Eq. (1.5). The higher illumination current (blue line) models the bare cell (ITO only), while the lower one corresponds to the cell with a medium density of Ag NWs (transmittance around 80 %, as measured with a spectrometer). Figure 2.20 shows indeed a loss in transmittance when adding Ag NWs, with a shift of the short-circuit current for all resistances. This shift is more pronounced for lower resistances. Yet, Ag NWs also strongly reduce the series resistance, ensuring a better collection of the charge carriers, hence a higher J_{sc}. Less charge carriers are generated, but more are finally collected.

This increase in J_{sc} demonstrates that the short-circuit current density was limited

by the series resistance of the cell. Above 11 µg/cm^2, however, J_{sc} slowly decreases with further increase of the Ag NW density. With a higher Ag NW density, the transparency loss is more important than the gain by reduction in series resistance. The moderate steepness of the J_{sc} decrease, compared to its increase, highlights the critical impact of the series resistance on the J_{sc} value.

2.8.3 Optimal density

The optimal density results from a trade-off between the optical properties (represented by J_{sc}) and the electrical properties (represented by R_{se}, but also J_{sc}). The highest efficiency under 1 Sun is obtained for a Ag NW density around 20 µg/cm^2 with 80 nm ITO, which corresponds to a R_{se} close to the minimal one and a J_{sc} close to the maximal one. It ensures a good collection of charge carriers and a low amount of light absorbed or reflected by the contact.

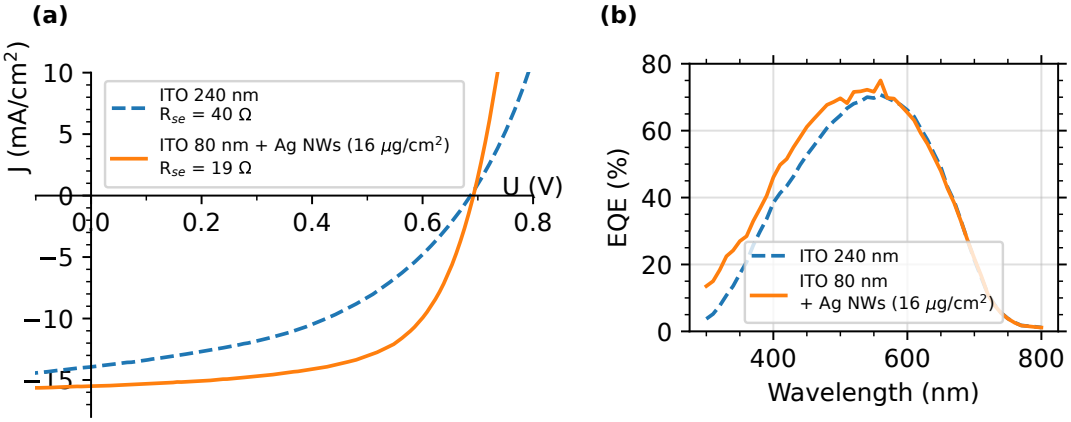

Figure 2.21: **(a)** J-V curves under 1 Sun and **(b)** corresponding EQE of the Si NW/a-Si:H cells with the contact optimized for ITO alone and the optimized hybrid contact {ITO + Ag NWs}.

Figure 2.21 **(a)** compares the J-V curves of the contact optimized with ITO alone (nominally 240 nm ITO) with the optimized hybrid contact made of ITO and Ag NWs. With the latter, the short-circuit current is higher, thanks to a higher transparency, as confirmed by EQE measurements (Figure 2.21 **(b)**). With the hybrid contact, the fill-factor too is clearly improved (from 45 % to 62 %) thanks to a much lower in-plane resistance of the top contact. The power conversion efficiency is therefore increased by more than 2 point percentage (from 4.3 % to 6.6 %), which highlights the key role of the top contact in a nanostructured device.

I optimized this contact for a AM1.5G illumination, but the method holds for any illumination. In addition, higher illumination powers can be used to characterize the electrical limitations of the solar cell.

2.8.4 Strong illumination to probe the electrical properties

I changed the power density of the light shone on the cell with a 532 nm laser (suited to the absorption of a-Si:H) and recorded the I-V curves. Figure 2.22 displays the short-

circuit current density depending on the illumination power for Si NW/a-Si:H solar cells with two different hybrid contacts.

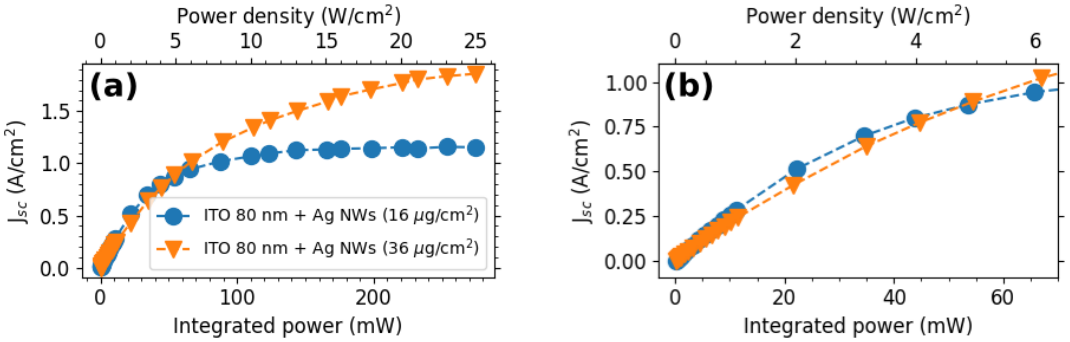

Figure 2.22: **(a)** J_{sc} of Si NW/a-Si:H solar cells with hybrid {ITO + Ag NWs} top contacts for increasing illumination power (illumination beam at 532 nm with a 1.18 mm diameter). A low and a high density of Ag NWs are shown, respectively in blue and orange. **(b)** Close-up of **(a)** where the change of optimal contact can be seen (around 5 W/cm^2).

We expect a linear dependence, as the photocurrent should increase linearly with the illumination. Yet, if resistances are important, the short-circuit current can significantly differ from the photocurrent. We observe a sublinearity for Si NW/a-Si:H solar cells with both contacts. The hybrid contact with the lower density of Ag NWs even presents a saturation around 1.2 A/cm^2. This contact corresponds to the optimal hybrid for the 1 Sun exposure. However, it cannot sustain current levels beyond 1.2 A/cm^2 and is limiting under strong illuminations. In contrast, for the contact with a higher density of Ag NWs, J_{sc} is first limited by the transparency, but finally results in the highest short-circuit current density, beyond 5 W/cm^2.

In the same way as EQE measurements can be used to characterize the optical properties of the contact directly on the device, strong illumination can be used to characterize the electrical properties of the contact directly on the device.

2.8.5 Summary

After optimizing the ITO thickness for transparency, I adapted the density of Ag NWs to the amount of charge carriers for 1 Sun measurements. Because the collection was initially limited by the resistance of the ITO, an increased density of Ag NWs first led to an improved J_{sc}. With the right density of Ag NWs, the performance of the device was greatly improved compared to the cell with the thick ITO film, with an increase of both J_{sc} and FF.

2.9 Takeaway messages

- Transparent electrodes require a trade-off between transparency and conductivity.

The exact trade-off depends on the device (e.g. solar cell technology and area). TCOs and nanostructured materials, such as Ag NWs, are the best options.

- A hybrid electrode made of {ITO + Ag NWs} is relevant for Si NW/a-Si:H.

For a dense array of randomly oriented core-shell nanowires (NWs), a hybrid electrode is needed. It also gives more freedom for optimization. A hybrid made of {ITO + Ag NWs} collects the electrons from each Si NW and from the whole cell. A higher transparency is obtained compared to ITO alone, thanks to the thin ITO layer. A higher fill-factor is obtained compared to ITO alone, thanks to the high conductivity of the network of Ag NWs.

- For nanostructured devices, the optimization of parameters has to be carried out directly on the device.

It is necessary for NW solar cells, as the substrate affects the deposition of the electrode. A low (high) illumination can be used to probe only the optical (electrical) properties.

- The series resistance can affect J_{sc}.

If the series resistance is high, it can hinder the collection of carriers and result in a lower J_{sc}. Thus, the short-circuit current does not always correspond to the transparency of the top contact.

- With Atomic-Layer Deposition, a thin conformal layer of TCO can be used, but it increases shunts.

ALD ZnO:Ti proved to be conformal around Si NW/a-Si:H. Because of its lower band gap energy, there is no improvement on the optical properties compared to ITO for similar thicknesses, but thanks to the better conductivity of the film, thinner films are required. Nevertheless, the electrical connection of the bottom of the cell lowers the R_{shunt} value and impedes the performance.

Chapter 3

Aging of Ag nanowires

Contents

3.1 Observed changes

Eight months after their deposition on Si NW/a-Si:H solar cells, we observed a strong morphological change of Ag NWs (Figure 3.1 **(b)**, **(c)**). For comparison, **(a)** displays the SE image of as-deposited, smooth, Ag NWs. Numerous particles are visible on the Ag NWs, many have even fallen on the ITO below. The lower magnification image shows larger aggregates and no more NWs. The consequence of such change on the electrical properties of the electrode is obvious. For this reason, we wanted to understand the origin of the degradation, monitor its evolution and find solutions to mitigate the damage.

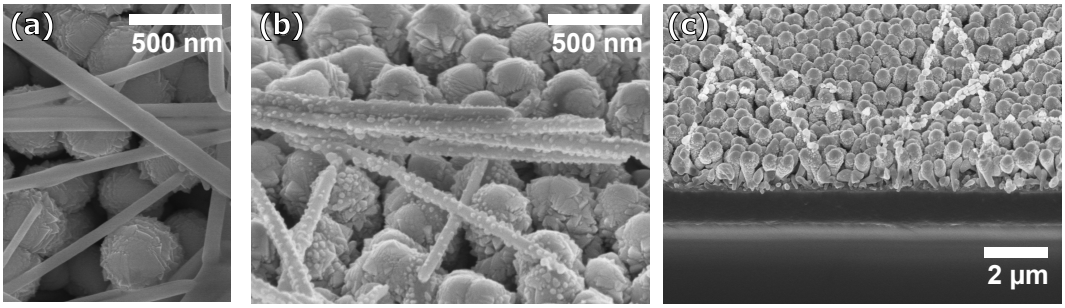

Figure 3.1: SE micrographs of Si NW/a-Si:H cells with ITO (240 nm) and Ag NWs: **(a)** as-deposited Ag NWs, **(b)**, **(c)** degraded Ag NWs, 8 months after deposition.

3.2 Review of studies on Ag NW degradation

3.2.1 Mechanism and timescale

Sulfur corrosion of Ag This change in Ag NWs has been identified in the literature as sulfur corrosion, which results in Ag_2S particles. TEM-EDS in particular showed the strong presence of sulfur in this kind of particles [Elechiguerra 2005, Deignan 2017]. Sulfur is known to be responsible for corrosion in bulk Ag [Bennett 1969], especially due to H_2S and OCS (carbonyl sulfide) [Franey 1985]. Despite their low concentrations in atmosphere (0.3 ppb and 0.6 ppb, respectively) [Graedel 1992], these gases present a high corrosive activity, which makes them the main mechanism for corrosion.

Contributing factors Different degradation timescales in ambient air have been reported, from a few days [Jiu 2015] to more than two years [Mayousse 2015]. Many parameters affect the stability of NWs and can account for these discrepancies. They can be related to the experimental conditions during aging or to the process of Ag NWs, e.g. growth, deposition, annealing. In particular, temperature and humidity accelerate the degradation [Graedel 1992]. Adsorbed water may act as a common medium for Ag^+ and sulfur gases. Deignan and Goodthorpe also showed the effect of the network density, the plasma treatment of the substrate before deposition, and the annealing conditions [Deignan 2017]. The presence of current is also important. Joule heating increases the temperature in the whole electrode, very strongly in some NWs, and can favor corrosion, even for rather low current densities ($\sim$20 mA/cm^2) [Khaligh 2017].

Fundamental instability of NWs In addition to corrosion, which also affects bulk silver, Ag NWs are unstable due to their high surface-to-volume ratio. They are thermodynamically unstable and, when Ag atoms diffuse, particles can be obtained. Energy sources (e.g. heating, light) increase the mobility of Ag atoms and accelerate the mechanism [Jiu 2015]. This is obvious when NWs are heated as explained in Section B.3.1. The density of the network also affects the degradation rate [Deignan 2017].

3.2.2 Deposition of a protective layer

To mitigate these mechanisms (sulfur corrosion and reshaping of NWs), the deposition of a protective layer on top of the network has been implemented, mostly with metal oxides, even though conductive polymers or graphene [Khaligh 2017, Hwang 2016] have also been employed. Metal oxides can be deposited by sol-gel methods, sputtering or ALD. They can be amorphous or crystalline, with thicknesses ranging from 5 nm to ~100 nm. Finally, they can be doped or not.

Thermal stress of Ag NWs networks shows that an encapsulation layer made of metal oxide (e.g. ZnO, SnO_2 or TiO_2) prevents the diffusion of Ag atoms [Kim 2013, Song 2015, Bardet 2021]. NWs keep their shape instead of becoming particles. The encapsulation layer can also protect the Ag NWs from atmospheric degradation, as has been clearly shown for TiO_2 [Song 2015] and Al_2O_3 [Hwang 2017]. In addition to the lower diffusion of Ag atoms, such a layer hinders the contact of Ag with atmospheric gases (H_2O or sulfur compounds). The main reason here may be the impermeability to water, which strongly affects the sulfur corrosion of Ag NWs.

3.3 Our solution: encapsulation with an ALD ZnO:Ti layer

3.3.1 Why TZO

Many encapsulations use materials with rather low conductivity. As detailed in Table 2.2, TZO (ZnO:Ti) displays good opto-electrical properties. Even if a rather thick encapsulation layer is needed, we expect no significant degradation of the electrode properties. In addition, ALD ensures a conformal coverage of the NW surface.

3.3.2 Process

I made several series in order to carry out optical, electrical measurements and SEM observations without interferences. There are six samples in each series, as detailed in Table 3.1.

I spin-coated Ag NWs on the substrate (see Section B.2.3). Most series have a glass substrate, but I also made two series with a glass/ITO substrate for comparison (ITO deposited as detailed in Table 2.3 for 2 min). I annealed all samples following the conditions suitable for these Ag NWs (180 °C for 20 min in air).

While the standard ALD process requires a substrate heating to 200 °C, we lowered the temperature to 160 °C to ensure that it would not damage the NWs during the time required for the process. For each series, one sample experienced the ALD conditions but without the precursors (hence no TZO), it is called *mock process*. In addition, I also made one sample with ITO as encapsulation layer. t0 corresponds to the day of Ag NW annealing. The encapsulation was made at t0+1, the deposition of Ag NWs at t0-1.

Table 3.1: Samples in a series. The given thickness corresponds to the thickness obtained on a flat glass substrate.

Name	Encapsulation	Thickness	Heating
Usual process	-	-	-
Reference	-	-	160 °C, 45 min (mock process in ALD reactor)
ITO 20nm	Sputtered ITO	20 nm	160 °C, 45 min
TZO 5nm	ALD TZO	5 nm	160 °C, 45 min
TZO 10nm	ALD TZO	10 nm	160 °C, 45 min
TZO 20nm	ALD TZO	20 nm	160 °C, 45 min

3.3.3 How to follow the change?

Most studies monitor the sheet resistance, since it is critical for the use of Ag NWs as electrode and is strongly altered by the formation of particles (either Ag or Ag_2S). When focusing on the mechanism, methods for the characterization of materials are employed, as SEM, TEM, or XPS [Elechiguerra 2005, Mayousse 2015]. However, these techniques probe only part of the network, while degradation can substantially depend on position. For this reason, I also monitored the optical properties of the Ag NWs. I used the three methods in parallel. To dismiss the possible effect of repeated current or light exposure, I kept series for purely electrical or purely optical observations and one series experienced both.

Electrical properties To have results that could be compared to literature, I wanted to measure the sheet resistance. Methods to determine $R_\square$ imply a homogeneous layer, but they are generally used for Ag NWs electrodes nonetheless. A Van der Pauw measurement requires strict conditions on the dimensions of the sample and is quite time consuming (see Section 1.4.1). Consequently, I chose to measure the sheet resistance of the sample directly with four probes in a straight line, with no supplementary contact.

Apart from the homogeneity, the setup fulfills the requirements on the dimensions for a relevant value measured with the four-point probe method, since the separation between the tips is much smaller than the size of the sample (1 mm vs. 2.5 cm). To enable optical measurements on the same samples and to avoid the effect of the solvent on the network of Ag NW, I chose not to add any metallic contact. I also checked beforehand that the probes were not damaging the sample and saw no evidence of it. I chose low levels of currents (up to 1 mA, with 0.1 mA step, typically corresponding to 0.32 mV). Despite the low voltage, they are not prone to errors (measurements with currents up to 10 mA showed no difference).

Nonetheless, the obtained values for $R_\square$ are rather dispersed. Because it could be easily repeated, I made several measurements, in both directions, yet the dispersion remains strong and the precision limited. This dispersion is likely related to non-uniformities in the Ag NW network. The tip radius is several tens of microns which should be sufficient to contact many NWs (diameter ~60 nm). Still, these NWs may be differently connected to the network, hence the exact position of the tip matters. It does not seem to be a question of pressure, as I sometimes applied more or less pressure, with no consequence

on the obtained resistance.

Morphology I assessed morphology changes with SEM, under the same conditions. I used different magnifications to have representative images and to be able to see the tiny particles. In addition, I did not monitor the change in given positions, because particles seem to be removed due to the electron beam, as shown in Figure 3.2.

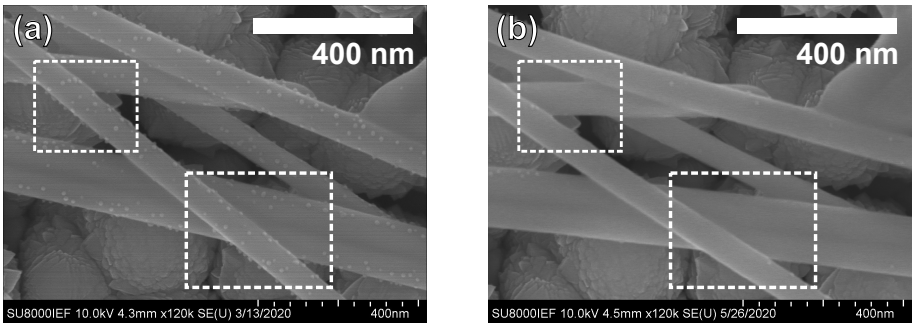

Figure 3.2: SEM images of Ag NWs on Si NW/a-Si:H/ITO, **(a)** 2 months and **(b)** 4 months after the deposition and annealing. Most of the particles that I first observed cannot be seen anymore. Lower magnification images, that are not displayed, show a difference between regions exposed to different doses.

Optical properties I measured the total transmittance and reflectance in the 250-2500 nm range with an integrating sphere. The illumination beam is around 1 cm×1.8 cm.

3.4 A minimal thickness is needed for a conformal ALD layer

3.4.1 Deposition on glass substrates

SEM I observed the morphology of Ag NWs in SEM directly after the encapsulation process, as displayed in Figure 3.3. First, we can see no difference in the surface of Ag NWs between the two samples with bare NWs, despite the long heating of the reference sample. In addition, ITO sputtering results in an apparently conformal and polycrystalline layer. Moreover, there is no evidence from SEM of TZO on Ag NWs for the 5 nm sample. A change in the optical properties compared to the reference confirms the deposition of TZO (Figure 3.6). However, its distribution is not certain. As ALD relies on chemical interactions between the substrate and the precursors, Ag NWs may experience a different deposition compared to glass. In 10 nm TZO, distinct crystallites on the glass substrate demonstrate TZO presence, but only a few are on the surface of Ag NWs. The latter have diameters around 5-10 nm. On the 20 nm TZO sample, the Ag NWs are fully covered with TZO crystallites.

Deposition on Ag vs. on glass The 10 nm TZO sample shows that the growth of ZnO on Ag NWs differs from the growth on glass. The growth of ZnO relies on -OH groups on the surface of the substrate, which are expected to be more present on the

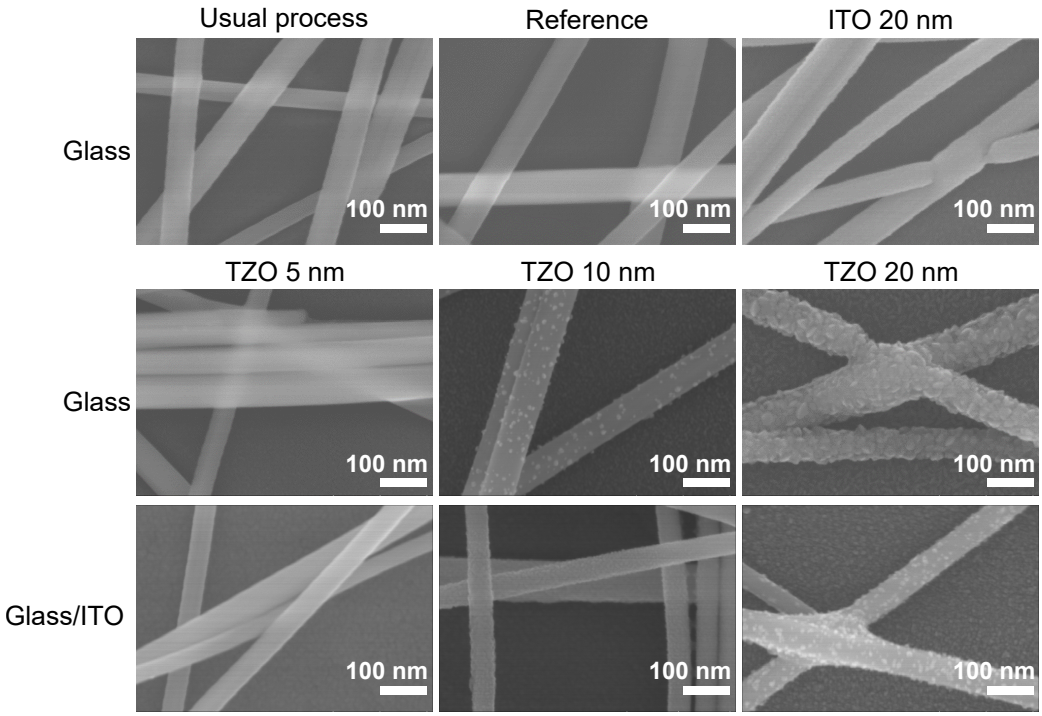

Figure 3.3: SEM images of Ag NWs on glass and glass/ITO after the encapsulation process. They were recorded 3 days after the last process for samples on glass, 20 days after the last deposition for samples on glass/ITO. See Table 3.1 for sample description.

surface of glass compared to silver. This is a known effect [Pham 2016] and a possible solution is the use of Al_2O_3 as an adhesion layer [Chen 2015]. Al-precursor trimethyl-aluminum has indeed been shown to strongly be adsorbed on Ag surface [Hwang 2017].

XRD X-Ray Diffraction (XRD) of glass substrates covered with TZO during the same deposition is shown in Figure 3.4. It proves the amorphous feature of the thinnest TZO layer, the partial crystallinity of 10 nm TZO and the crystallinity of 20 nm TZO on glass. From these observations, we cannot tell whether Ag NWs with 5-10 nm TZO are fully encapsulated (by an amorphous layer) or not.

TEM Transmission Electron Microscopy (TEM) observations are useful to assess the presence of a continuous layer of TZO on the two samples with the thinner layers. They were carried out in PICM by Éric Ngo. Bright-field images of a silver NW with 5 nm TZO are displayed in Figure 3.5. They do show a change on the edge of NWs, but it may be related to the geometry of Ag NWs (pentagonal cross-section), which results in different thickness and orientations of planes close to the edge. From the High-resolution TEM (HRTEM) images, such as in **(b)**, this apparent layer looks crystalline. Because XRD measurements suggested an amorphous layer, it is unlikely to be TZO. No certain conclusion could be drawn from these observations. There is no evidence of a continuous TZO layer. Yet, if this very thin layer is amorphous, as expected, it would be difficult to assess.

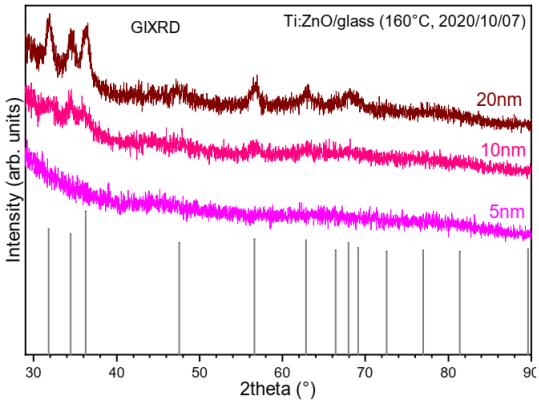

Figure 3.4: XRD of glass substrates covered with TZO during the same process (160 °C). TZO deposition and XRD were made by Shan-Ting Zhang.

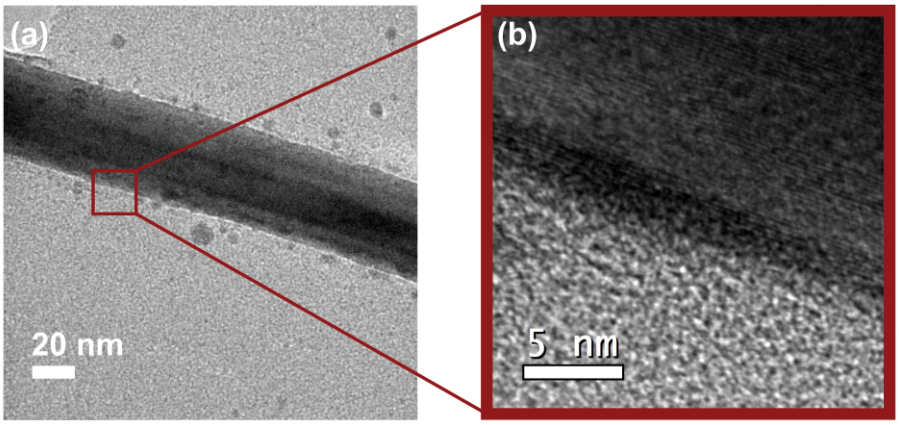

Figure 3.5: **(a)** TEM and **(b)** HRTEM images of a silver nanowire with 5 nm TZO. Observations were made 11 months after deposition and annealing. Degradation had already started and accounts for the particles observed in **(a)**. TEM observation by Éric Ngo.

Degradation of Ag NWs during encapsulation The use of O_2 during ITO deposition and H_2O for ALD raises the question of a possible degradation of Ag NWs during the process. I observed an improvement in $R_\square$ for ITO and TZO depositions, but there still may be an increase in the sheet resistance of Ag NWs. I observed no change in the optical properties. If there is some degradation, it remains limited.

3.4.2 Deposition on ITO substrates

SEM In order to mimic the chemical environment where the NWs could degrade (in case of a hybrid electrode), I also made two series on glass/ITO substrates. The comparison with samples on glass in Figure 3.3 highlights the effect of the substrate on the morphology of the TZO on Ag NWs. For both 5 nm and 10 nm, Ag NWs look fully covered by small particles (not clear on this image of 5 nm TZO, but on another one), which was not observed on glass only. Besides, I saw no crystallites on the 10 nm sample, contrary to the 20 nm sample, where it is difficult to tell whether there is a continuous layer. The TZO morphology directly on the substrate is not clear. I observed no difference between all (no-)encapsulation layers. The TZO morphology on Ag NWs is strongly different from glass, especially for 20 nm TZO, which displayed typical rice-grain-shaped crystallites. The sputtered ITO did not show any difference for both substrates, as we could expect.

ZnO ALD on ITO From SEM observations, crystallites seem slower to form on ITO substrates. ALD often starts with an amorphous layer, which becomes crystalline beyond a given thickness (see Figure 3.4). A slower deposition can explain the difference between glass and ITO. Even though ITO and glass are both oxides, they differ in morphology (crystallized ITO vs. amorphous glass) and in chemical composition. We expect the latter to be more significant in the ALD process, especially regarding the very different crystal structures of ZnO and ITO (hexagonal vs. cubic).

Effect of ITO substrates on ALD on Ag NWs Crystallites look also slower to form on Ag NWs on ITO substrates. Similarly, a possible reason for the difference could be a lower deposition rate of TZO on Ag NWs when they are lying on ITO. However, it is surprising that the ITO film affects the growth of ZnO on Ag NWs. In ALD, precursors species should reach every reaction site (see Section 2.3.3). Hence, there is no competition between substrates which could explain the difference. The observation suggests that the growth on Ag NWs stems from the growth on the substrate. Even though an ideal ALD process should be layer-by-layer, the formation of islands that finally merge is observed [Richey 2020]. Lateral growth can therefore occur and would be particularly important for substrates that do not present many nucleation sites, as Ag.

3.4.3 Optical effect

Figure 3.6 presents the total transmittance, reflectance and the calculated absorptance of Ag NWs with different encapsulation layers on glass in the 250-850 nm range. The spectra of Ag NWs on glass/ITO are not displayed because the different glass/ITO

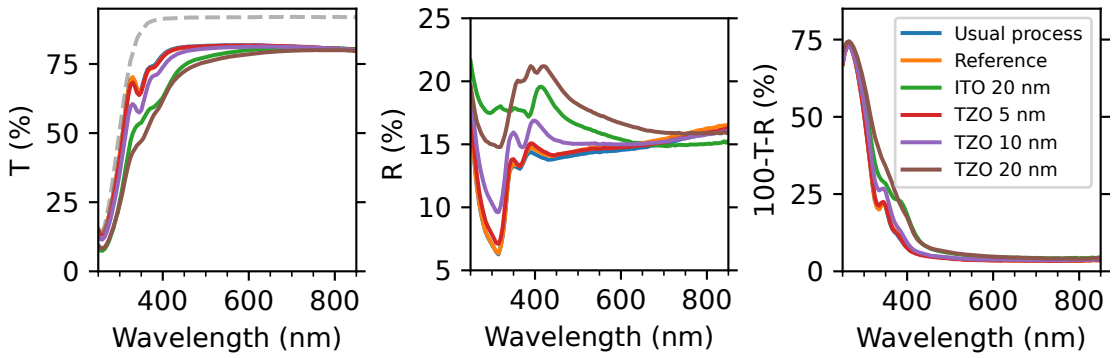

Figure 3.6: Measured total **(a)** transmittance T and **(b)** reflectance R and **(c)** calculated absorptance of Ag NWs on glass for different encapsulation layers. Absorptance corresponds to $100 - T - R(\%)$. Spectra of ITO and TZO on glass are displayed in Figure 2.10.

substrates showed different optical properties from the start. Consequently, we could not determine the effect of the TZO deposition.

ALD TZO Bare Ag NWs and Ag NWs with 5 nm TZO show very similar spectra, with a transmittance close to 82 % at 550 nm. At short wavelengths, two dips in transmittance are observed, which are attributed to localized plasmon resonance [Kottmann 2001, van de Groep 2012, Garnett 2010]. With 10 nm TZO, the general shape remains, but the transmittance is lower due to the increased reflectance and absorptance. With 20 nm TZO, a brutal change can be observed in the short-wavelength region. The typical features cannot be seen anymore.

Sputtered ITO Compared to 20 nm TZO, ITO results in less modification, mostly due to its lower absorptance around 350 nm.

Deposition of TCO has several effects. First, it covers the glass. Because the glass substrate has a very low reflectance, the film of TCO, either TZO or ITO, increases the reflectance. In addition, it covers the silver NWs, which alters the metal/dielectric interface, the NW diameter and their roughness. Hence, the TCO deposition can affect the behavior of plasmons and the scattering. In particular, it accounts for the change observed with 20 nm TCO. It is likely due to the full coverage of Ag NWs.

3.5 Slow degradation of Ag NWs under ambient conditions

I regularly monitored these samples through optical, electrical measurements and SEM observations. The samples were stored in ambient air, in dark.

3.5.1 Optical changes

I observed no significant change, for any of the sample, over 20 months, as shown in Figure 3.7. There seems to be a slight shift with time, but it has to be confirmed over time. Glass/ITO samples are not displayed, because I observed no change either.

However, I did not specifically monitor the haze of the Ag NW network, which is expected to increase when Ag NWs become particles [Hwang 2017].

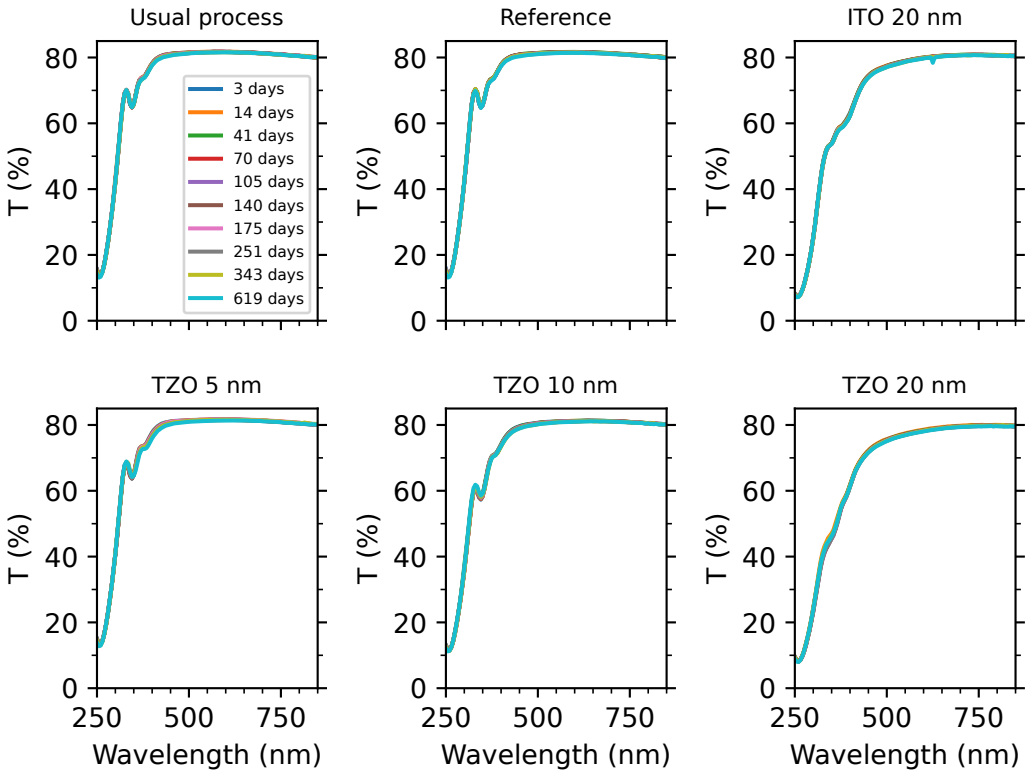

Figure 3.7: Total transmittance of Ag NWs on glass with different encapsulation layers.

3.5.2 Electrical changes

I observed no strong increase of the sheet resistance over 20 months for samples on glass as shown in Figure 3.8. There still seems to be a slight increase in $R_{\square}$, especially for samples with bare NWs (*Usual process* or *Reference*), but it is difficult to determine due to the dispersion of values. This increase is clearer in the samples on glass/ITO, shown in Figure 3.9, where encapsulated Ag NWs also present an increased sheet resistance. For comparison, the sheet resistance of 80 nm ITO was monitored as well and stayed around 47 Ω/sq. The sheet resistance of Ag NW samples still remains much lower.

The dispersion for glass/ITO substrates is narrower (mean standard deviation over 66 measurements of 0.50 Ω/□ vs. 0.89 Ω/□ on glass). This is likely due to the continuous ITO layer, which connects the whole network and makes the measurement less position-dependent. The good connection between ITO and the network of Ag NWs can be apprehended through the $R_{\square}$ values of the glass/ITO/Ag NWs samples (≃12 Ω/□). It is consistent with two resistances in parallel (with measured $R_{\square}^{ITO}$ = 47 Ω/□ and $R_{\square}^{AgNWs}$ ≃15 Ω/□) and no resistance of contact.

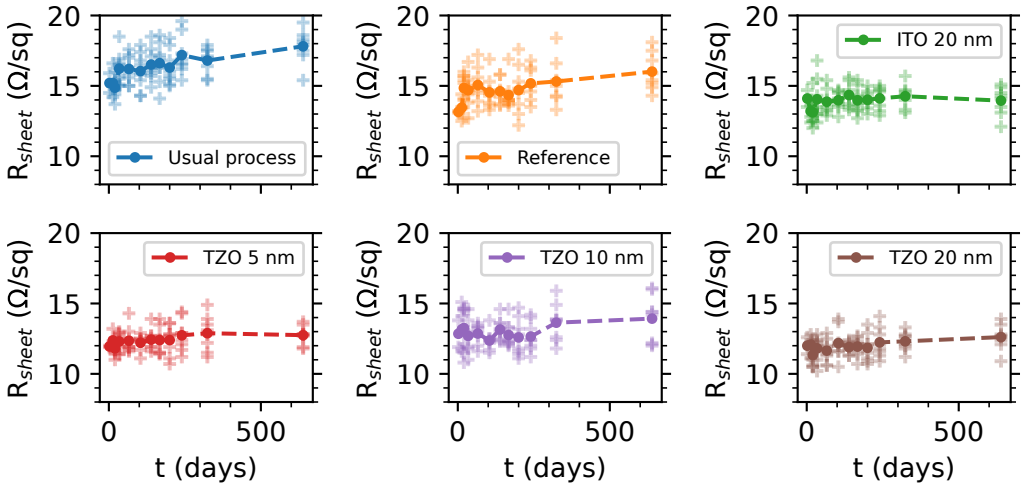

Figure 3.8: Sheet resistance of Ag NWs on glass for different encapsulation layers. All measured values are plotted with +, their average with ●. The two first datasets (t0+2 days and t0+13 days) consist in 2 measurements only (8 for others). Hence, their values are not accurate. In particular, we cannot conclude on the possible increase at the very start of the monitoring. For comparison, the sheet resistance of 80 nm ITO remained around 47 Ω/sq.

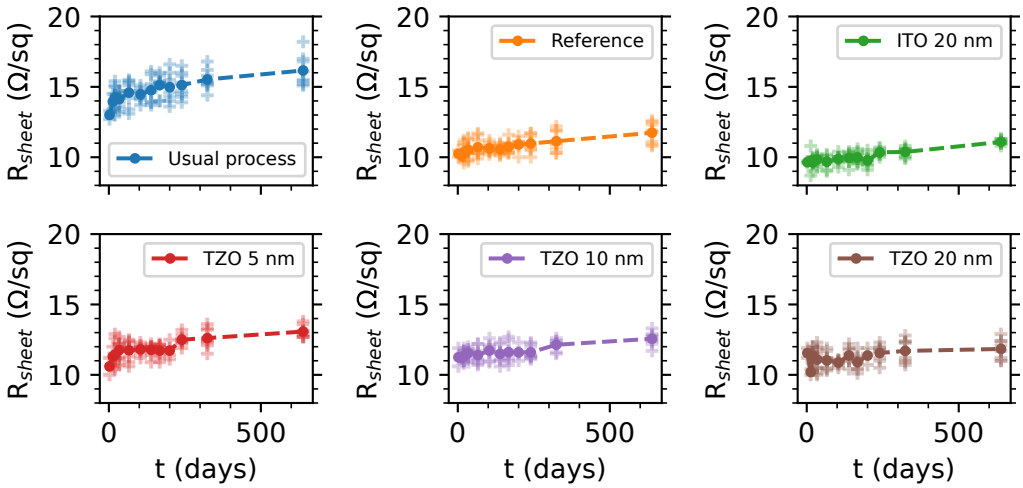

Figure 3.9: Sheet resistance of Ag NWs on glass/ITO for different encapsulation layers. All measured values are plotted with +, their average with ●. The two first datasets (t0+2 days and t0+13 days) consist in 2 measurements only (8 for others). Hence their values are not accurate. In particular, we cannot conclude on the possible increase at the very start of the monitoring. For comparison, the sheet resistance of 80 nm ITO remained around 47 Ω/sq.

3.5.3 Morphological changes

I also followed the degradation of NWs with SEM. I did not perform Energy-Dispersive X-ray spectroscopy (EDX), although it would have been relevant for the study of degradation in samples which show crystallites from the encapsulation layer, namely 10 nm or 20 nm TZO, or 20 nm ITO. SEM EDX has a too large probing volume and I had no access to TEM or STEM EDX.

I observed small particles already after 30 days on some bare NWs and NWs with 5 nm TZO, as shown in Figure 3.10 **(a)**. They are around 10 nm wide, with larger ones close to 20 nm. They are typical of Ag_2S particles. This observation shows that 5 nm of TZO is not enough to protect Ag NWs, probably because it does not fully cover Ag NWs. Larger particles are observed over time, for instance after 20 months in Figure 3.10 **(b)**. They also become more numerous with time. As can be seen in Figure 3.11, after almost 8 months, some positions in networks of bare Ag NWs show particles on most nanowires. It is however impossible to distinguish the particles on the encapsulated Ag NWs. Although the morphological change of bare NWs is considerable in the SEM images, it does not result in strong electrical and optical modifications.

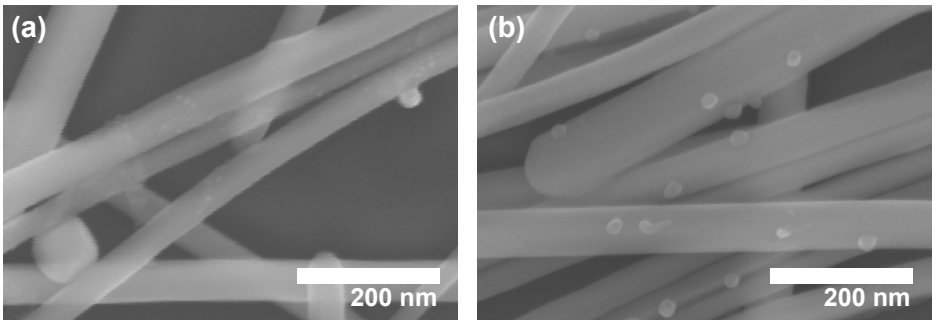

Figure 3.10: SEM images of bare Ag NWs on glass (*Usual process*), **(a)** 34 days and **(b)** 20 months after the encapsulation process. In **(b)**, particles range from 17 nm to 32 nm diameter, with a mean diameter around 25 nm.

SEM monitoring presents some limitations: there is a strong dependence on the position (inherent to the degradation mechanism) and on the microscope setup and focus (because of the very small size of particles). This prevents us from drawing conclusions.

3.5.4 Several methods needed for proper characterization

From these observations, it clearly appears that different methods should be used to monitor the degradation, depending on the purpose. There is an evident microscopic change before any macroscopic modification. This could be easily understood from a simple calculation. If we consider that there is an Ag_2S particle (10 nm) every 200 nm in a NW (circular cross-section assumed, 60 nm diameter), it corresponds to an atomic loss of silver from the NW of 0.1 %. Since these particles are well-distributed, it should not significantly affect the optical and electrical properties of the Ag NW network. In addition, this assumption is already an overestimation of the amount of particles. Although SEM observation can detect degradation early on, it does not provide quantitative information.

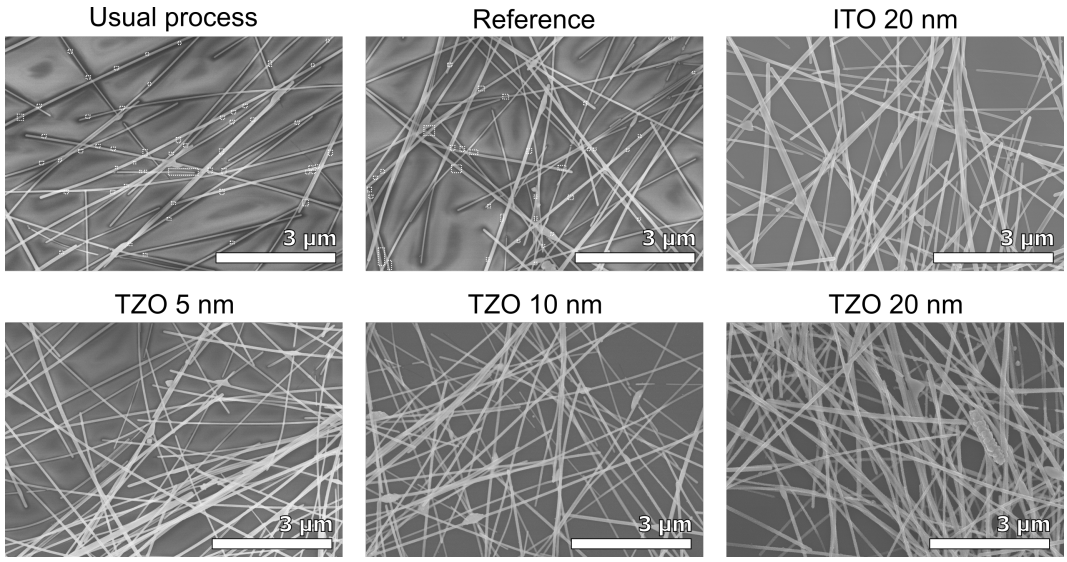

Figure 3.11: SEM images of Ag NWs 230 days after the encapsulation process. For the samples with Ag NWs only (*usual process* and *reference*), the positions of particles are shown with white frames. Regarding the other samples, we cannot distinguish them from the TCO.

3.6 Supplementary stress: light and current

Even after 20 months, Ag NWs on glass do not show a degradation as strong as Ag NWs on Si NW/a-Si:H after 8 months (Figure 3.11 compared to Figure 3.1). The storage conditions are different and can account for this discrepancy. Ag NWs on Si NW/a-Si:H solar cells are exposed to strong light (1 Sun illumination, at least for a few minutes during our measurements, often more), and high current levels (up to $\sim$80 mA/cm^2). It has been reported that both light and current can accelerate the degradation of Ag NWs [Jiu 2015, Khaligh 2017].

The effect of current is difficult to control as current levels are inhomogeneous in the electrodes made of Ag NWs. This is partly due to the cumulative effect of the collection (*crowding*), which is common to all electrodes. When getting closer to the collecting point(s), currents generated in the absorber add up to the current already in the electrode. An increasing density of Ag NWs when approaching the collection point would be efficient. In addition, the network made of Ag NWs is not uniform. NWs in regions of low density experience higher currents than NWs in regions of high density. This is one of the reasons for the strong non-uniformity observed in the degradation rate.

In order to assess the effect of light exposure and current effects, we could do the same observations on pre-stressed solar cells (either exposed to light, current, or both), compared to not stressed ones. It is critical to the use of Ag NWs as electrodes for solar cells.

3.7 Takeaway messages

- According to literature, Ag NWs suffer from two degradation mechanisms: sulfur corrosion and NW instability (Section 3.2 and Section 3.3).

These two degradation mechanisms have been heavily characterized in previous studies, and their origin detailed. A wide dispersion of degradation rates has been reported (a few days to more than two years). It is related to the effect of many parameters on the degradation (e.g. storage conditions, Ag NWs process). NWs can be encapsulated to prevent the degradation. We chose to use ALD TZO, because of its conformal coating and its good conductivity.

- With ALD, an encapsulation layer made of 20 nm TZO can be conformally deposited on Ag NWs (Section 3.4).

I observed that a minimal thickness (>10 nm) was required for a full coverage of Ag NWs, due to a slower deposition rate on silver. The exact thickness may depend on the substrate (glass vs. glass/ITO), as it seemed to change the ALD on Ag NWs. On glass, 20 nm of TZO demonstrated a continuous layer, but resulted in a strong decrease in transmittance. 20 nm of sputtered ITO performed better, but its protective effect against degradation has to be confirmed.

- Under the tested conditions (ambient atmosphere, dark), the degradation rate of Ag NWs was low and I could draw no conclusion on the protective effect of the encapsulation layers (Section 3.5).

I used three methods in parallel to monitor the degradation. Over 20 months, I observed no changes in the optical and electrical properties. Nonetheless, SEM images demonstrated a slow degradation of Ag NWs. All these observations were not sufficient to assess the protective effect of 10 nm and 20 nm TZO and 20 nm ITO over a year due to this low degradation rate.

- The absence of any stress (light or current) can account for the apparent discrepancy between the slow degradation of this study and the previous observations I made on Si NW/a-Si:H solar cells (Section 3.6).

I intended to monitor the degradation of Ag NWs without any external stress and for this reason chose low illumination and current levels. Since the tolerance to light and current is critical to solar cells, we could do the same study on pre-stressed samples, with and without encapsulation layers.

Chapter 4

Inorganic flexible solar cell

Contents

Some photovoltaic applications require bendable or flexible cells. While organic materials are rather bendable, they are also prone to degradation. Arrays of standing nanowires are intrinsically bendable and could be made of inorganic materials. Hence, Si NW/a-Si:H should result in low-cost, bendable solar cells, that are stable over time. The hybrid electrode developed with Ag NWs should improve this flexibility. In this chapter, I studied their flexibility.

4.1 What are flexible solar cells?

4.1.1 Mechanical consequences of bending

By definition, a flexible - or bendable - solar cell can be bent, with no (significant) change in its performance, either under bending, or when back to flat[1]. For solar cells, the bending radius is often used as an indication of how much the cell is bent. Figure 4.1 shows how a bending radius is determined. It should be noticed that the radius corresponding to the bottom of the substrate (R') is smaller than the bending radius of the active region (R_c). It is thus a device parameter, which is affected by the dimensions of the sample, especially the thickness of the substrate.

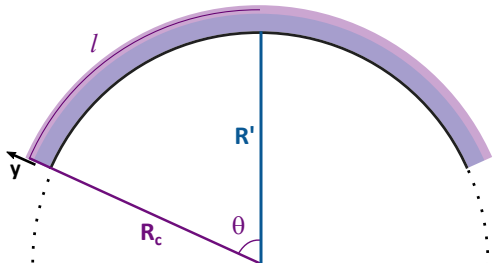

Figure 4.1: Bending radius for a bent solar cell (purple) on a substrate (blue).

During bending, the device is strained, either with a load at the edges or with a uniform load. For a convex bending as shown in Figure 4.1, the upper part is in tensile strain, while the lower part is in compressive strain. If the sample is thin enough compared to the substrate, we can assume that it undergoes tensile strain only. The limit between tensile and compressive strains corresponds to the *neutral plane*. Its position depends on the mechanical properties of the different layers and does not always correspond to the middle plane of the stack. The bending radius can be directly related to the strain ε in the material. ε is defined as the relative elongation Δl compared to the initial length l. With y the position from the neutral plane in the bending direction and R_c the bending radius corresponding to the neutral plane,

$$\varepsilon = \frac{\Delta\, l}{l} = \frac{y}{R_c}. \tag{4.1}$$

Stresses under bending The applied strain induces stress inside the material. In the elastic regime (reversible), stress σ and strain ε are linked by the generalized Hooke's law,

[1] There is necessarily a change in the performance under bending compared to flat, since the angle of incidence of the light is increased.

$$\sigma_{i,j} = C_{i,j,k,l}\, \varepsilon_{k,l}. \tag{4.2}$$

Indices refer to the directions of the stress and strain. C is the stiffness tensor, which describes the elastic response of the material. For symmetry reasons and if we consider a homogeneous and isotropic material, the components of C are reduced to two parameters. The Young modulus E and the Poisson ratio ν are often chosen. The Young modulus determines how much a material will strain under a given uniaxial stress, or how strong the stress is for a given uniaxial strain. The higher the Young modulus, the stiffer the material. The Poisson ratio describes how the material elongated along one axis deforms in the orthogonal directions (usually shrinks),

$$\nu = -\frac{\varepsilon_{yy}}{\varepsilon_{xx}}. \tag{4.3}$$

If the device is very thin, the Kirchhoff's theory, with equations for the bending of plates, can be used. The strain in the normal direction, and the transverse shear strains are assumed to be zero. Depending on the exact geometry of the device and the loading conditions, different assumptions can be made. Detailed explanation can be found in [Reddy 2007].

Irreversible changes While in the elastic regime, changes are reversible. Under higher stresses, irreversible changes can occur to release part of the accumulated energy, namely plastic deformation, cracks, delamination. The yield strength, the fracture toughness or the interface energy give an idea of how much stress or energy is needed for each of the phenomena to occur. However, it strongly depends on the geometry of the bent device and the possible regions of accumulated stress.

4.1.2 Different meanings depending on application

Even with the bending radius as a common parameter, the term *flexible* can refer to very different mechanical properties depending on the application, as shown in Table 4.1. Figure 4.2 presents some images corresponding to these applications. Not shown here are also domains which take advantage of the light weight of thin cells on flexible substrates, typically spatial applications.

Table 4.1: Mechanical properties required for different applications of flexible solar cells.

Application	Bending radius	Repeated	Use	References
Building-integrated PV Vehicle-integrated PV	1-10 m	No	Bent	[Heinrich 2020], Gochermann[2]
Roll-to-roll process Rolled transportation	10-50 cm	Yes	Flat	[Zuo 2018], Heliatek[3]
Wearable electronics	1-10 mm Stretchable	Yes	Bent	[Hashemi 2020], Solar-cloth[4]

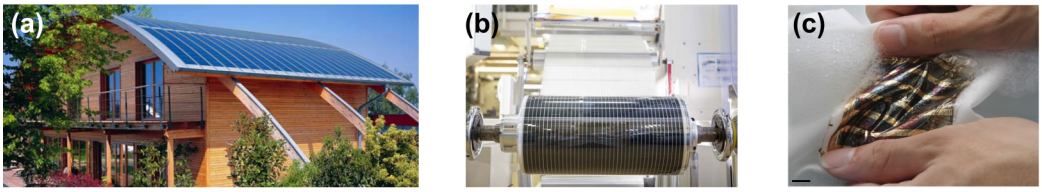

Figure 4.2: **(a)** Building-integrated PV, from Uni Solar (a-Si:H). **(b)** Roll-to-roll process of solar cells, from Asca (organic PV). **(c)** Stretchable solar cells [Jinno 2017] (organic PV).

In addition to the mechanical issues, flexible cells imply the growth on new substrates. Polymers are ideal for flexibility, but they need lower deposition temperatures, lack transparency and can degrade under UV light. Metal foils may lead to contamination by diffusion. Thin glass (typically 50-100 µm) is quite bendable, and does not require major changes in the fabrication process, but remains very brittle. Finally, for some materials, as III-V, a direct growth on a flexible substrate is not possible and a transfer is needed.

4.1.3 State of the art

Table 4.2: Established-technology solar cells grown on flexible substrates with current record power conversion efficiency (PCE) under AM1.5G. PI stands for polyimide, PEN for polyethylene naphthalate, PET for polyethylene terephthalate, SS for stainless steel. * corresponds to the stabilized efficiency for cells with a-Si:H.

Material	Substrate	PCE	Certified	Bending tests?	Reference
III-V	?	29.1 %	Yes	No	Alta Devices [Green 2021]
CIGS	PI (?)	21.4 %	Yes	No	EMPA[5]
Perovskite	PEN	20.7 %	(19.9 %)	1000 x10 mm	KRICT [Chung 2020]
Organic	PET	16.6 %	No	1000 x1.5 mm	NIMTE [Wan 2021]
CdTe	Glass	16.4 %	Yes	No	NREL [Mahabaduge 2015]
a-Si:H (Si & Ge, 3J)	SS	13.6 %*	No	No	United Solar Ovonic [Guha 2013]
a-Si:H (Si only, 3J)	SS	13.3 %*	No	No	United Solar Ovonic [Yan 2006]
a-Si:H	PEN	8.8 %	No	No	EPFL Neuchâtel [Söderström 2008]

[4]https://www.gochermann.com/semi-flexible-modules/
[4]https://www.heliatek.com/en/technology/roll-to-roll-series-production/
[4]https://www.solar-cloth.com/canvas-shelters/
[5]https://www.empa.ch/en/web/s604/cigs-efficiency-record-2021

Flexible cells can refer to all those topics and comparison may thus be difficult. Table 4.2 summarizes the current record efficiencies for cells of established technologies grown on flexible substrates. It shows that mechanical properties have not been tested for most of the cells, especially inorganic ones. Figure 4.3 **(a)** presents a perovskite sample with a bending radius (and a spacing) of 10 mm, similar to the bending radius of the record flexible perovskite cell.

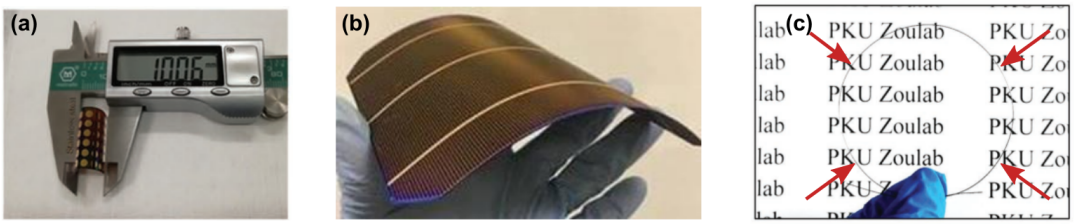

Figure 4.3: Examples of bent perovskite and inorganic solar cells. **(a)** Flat perovskite solar cell [Feng 2018], **(b)** 84-µm thick c-Si solar cell [Ohshita 2019], **(c)** fiber-shaped perovskite solar cell [Dong 2019].

4.2 How to make solar cells flexible

Several techniques can be used to increase the flexibility of devices.

4.2.1 Material

To obtain bendable cells, a soft material (low E) can be used. This material will easily follow the strain without high induced stresses. That is the case for organic solar cells ($E \simeq 1 - 2$ GPa for active layers [Dauzon 2022, Lee 2021]). For comparison, $E \simeq 4$ GPa for PI and $E \simeq 0.5$ GPa for Polytetrafluoroethylene (PTFE). Inorganic materials are much stiffer ($E \simeq 130 - 190$ GPa for c-Si depending on the crystal orientation [Hopcroft 2010], $E \simeq 130$ GPa for a-Si:H [Gaspar 2008, Kuschnereit 1995]) and specific architectures are needed to reduce the stress.

4.2.2 Design

Thin devices As Eq. (4.1) shows, the maximal strain is directly related to the thickness of the sample. Hence, the thinner the sample, the lower strain (and stress) it has to sustain. Even crystalline silicon can be used in flexible cells, when it is made thin enough (Figure 4.3 **(b)**). However, it also reduces the absorption of light. In addition, the total thickness is relevant, including the substrate. For thin films, although the absorber is typically 1-4 µm thick, the substrate is much thicker (50-100 µm for thin glass, 10-25 µm for polymers) and the resulting strain is increased.

Neutral plane Under bending, the neutral plane does not sustain any strain. The device can be designed to take advantage of this position, by placing the active layers at this position, for example through encapsulation. The mechanical properties of all layers have to be carefully chosen.

NWs NW arrays are flexible by nature, because their footprint (a few hundreds of nanometers) is much smaller than typical bending radii [Hwang 2018] (see Section 1.2.3).

Fiber-shaped For wearable PV, fiber-shaped solar cells are promising. Figure 4.3 **(c)** shows one such fiber, highlighted by red arrows. They can be woven together - and with textile fibers - to make a fabric. The network feature can accommodate the deformation.

4.2.3 Top contact

The flexibility of the top contact is crucial for the device. If cracks occur in the contacts (top or bottom), lateral conduction and the collection of charges carriers are hindered. This is not as critical in the absorber layer, where the main current is vertical (although recombinations are expected to increase with new surfaces). Furthermore, as the top contact is on the outward part of the sample, strain will be higher than in the bottom electrode.

4.2.4 Si NW/a-Si:H solar cells with {ITO + Ag NWs} as top contact

Because they are made of NWs, Si NW/a-Si:H solar cells should sustain the bending deformation. Moreover, the reference process for the growth of Si NW/a-Si:H cells uses an amorphous substrate, glass, and can easily be transferred to a flexible substrate as a metal foil or polyimide. The growth of Si NWs on polyimide has already been reported, at 350 °C [Tian 2016]. However, no other plastic substrates are possible, because temperatures below ∼300 °C strongly affect the shape of the Si NWs [Yu 2009].

As detailed in Section 2.2.1, the flexibility of ITO is limited, but the hybrid contact is expected to present better mechanical properties. First, the ITO layer is thinner. In addition to the possible effect on strain (not evident on a NW array), it should delay the onset of cracks [Peng 2011]. Moreover, the network of Ag NWs can follow the deformation (see Section 2.4.3) and, in case of ITO fracture, bridge parts that are not connected by ITO.

Sun et al. reported the degradation of Si NW/a-Si:H solar cells with ITO as top contact for bending radii down to 5 mm [Sun 2018]. They observed a change in all parameters, but gave no details on the degradation mechanism. However, the strong change in J_{sc} and the 60 % increase in R_{se} suggest that cracks in the top electrode played a role in the degradation. Pathirane et al., who studied a similar structure, showed the better performance under bending of a composite electrode (AZO and Ag NWs) [Pathirane 2017]. Yet, they tested its mechanical properties only on a planar substrate. We characterized the effect of bending on the whole NW solar cell.

4.3 Bending-induced changes in Si NW/a-Si:H solar cells under 1 Sun illumination

4.3.1 J-V curves under bending

In order to assess the effect of bending on the contact, we grew Si NW/a-Si:H cells with different top contacts (different ITO thicknesses and with or without Ag NWs) on thin glass (70 µm) and compared their behavior under illumination and under bending. All

cells had a Ag/AZO back contact. In the set-up, I mounted the sample on double-sided tape ($\sim$ 0.1 mm thick) and a plastic substrate ($\sim$ 1 mm thick). The deformation is applied to the plastic card (Figure 4.4 **(e)**).

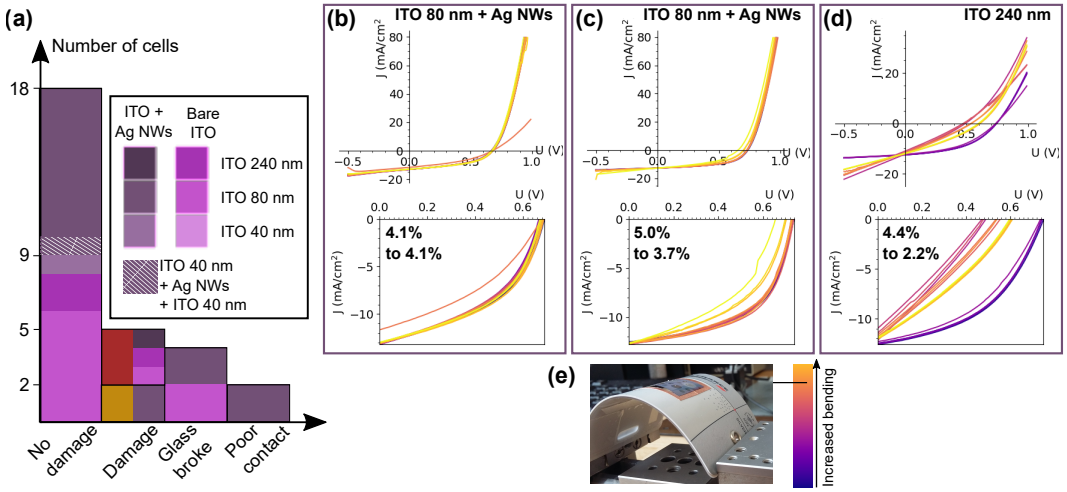

Figure 4.4: **(a)** Summary of the behavior of the 29 cells tested under bending under AM1.5G illumination. Damaged cells are shown with yellow (decrease in V_{oc}, FF and R_{shunt}) or red (decrease in I_{sc}, V_{oc}, FF and R_{shunt}). The *poor contact* label refers to measurements that were noisy. It was attributed to the loss of contact between the Ag paste and the cell. **(b)**-**(d)** J-V curves under bending for three cells on the same sample but with different contacts showing either **(b)** no degradation, **(c)** small degradation or **(d)** strong degradation. The efficiency before and after the whole bending process is displayed for each curve. The left cell showed one odd measurement (displayed, but deemed irrelevant). The change in efficiency is written. **(e)** Picture of the sample under bending (last bending before the degradation of the center cell).

Figure 4.4 **(a)** summarizes the degradation in the solar cell performance after bending. The minimal curvature radius changes from sample to sample, but no correlation with the degradation (correlation either with the substrate or the cell) was observed. Typically we used bending radii down to $\sim$2 cm.

From these results, it appears that the glass substrate is the main limitation. We can also notice that there is no strong difference between contacts at these bending radii. In particular, the thickest ITO does not result in stronger degradation. In addition, Ag NWs do not lead to multiple shunt paths by falling between Si NWs. Finally, the first parameter of the cell affected by bending is the shunt resistance, which affects the open-circuit voltage and the fill-factor. It differs from what could be expected from a broken top contact (higher series resistance, lower fill-factor and perhaps lower J_{sc}) and from what was reported by Sun et al. [Sun 2018].

4.3.2 Apparent or actual decrease in the shunt resistance?

As detailed in Section 5.3.4, a lower R_{shunt} can stem from collection issues. However, a closer look at the J-V curve can help to determine whether a lower collection of charge carriers is responsible or whether shunt paths are more important. Figure 4.5

displays the series of J-V curves of Si NW/a-Si:H solar cells showing a decrease in R_{shunt} during bending. **(a)** corresponds to an actual decrease in R_{shunt}: the short-circuit current density J_{sc} remains the same, while the current under reverse bias increases, as highlighted by the arrow. In addition, the open-circuit voltage V_{oc} decreases. In contrast, **(b)** shows an apparent decrease in R_{shunt}, due to collection issues: the J_{sc} value becomes lower and under reverse bias (when collection is enhanced), the current approaches the initial value of J_{sc}, but remains lower.

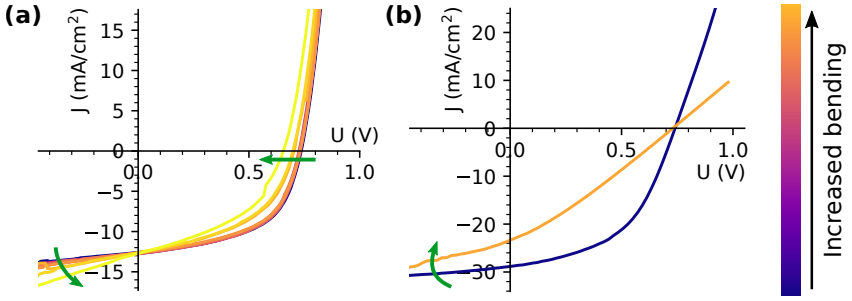

Figure 4.5: J-V curves of Si NW/a-Si:H solar cells with {ITO + 80 nm ITO} top contact displaying a decrease in R_{shunt} during bending: **(a)** actual decrease in R_{shunt}, **(b)** apparent decrease in R_{shunt} related to collection issues. The arrows show the main differences.

4.3.3 Possible degradation mechanisms

We consider that the adhesion of the sample to this card is good enough to transmit the deformation to the sample. Due to the thickness of the plastic card, all elements in the sample are submitted to tensile stress, when bent downward. In addition, because the cell is made of layers with different mechanical properties, there should also be some shear stress.

We are only interested in the irreversible damage. It is expected to stem from cracks in the different layers of the cell or from delamination between layers, as shown in Figure 4.6.

A decrease in the shunt resistance as observed during the bending tests corresponds to new conductive paths in the cell. It likely comes from openings in the bottom flat a-Si:H (because of cracks or removal of dust), and connection between the back contact and fragments fallen from the top contact (either ITO, Ag NWs, or the n-layer). J-V curves give macroscopic information, which is not sufficient to understand how Si NW/a-Si:H arrays are actually degraded under bending.

4.4 Understanding the mechanism at the microscale

4.4.1 EBIC to probe the degradation

Electron-Beam Induced Current (EBIC) is a characterization tool that maps the current generated and collected in semiconductor junctions. e^-/h^+ pairs are generated under the electron beam in a Scanning Electron Microscopy (SEM) chamber and collected. Both a current map and a SEM image can be recorded at the same time. Its principle is detailed in Section A.1.

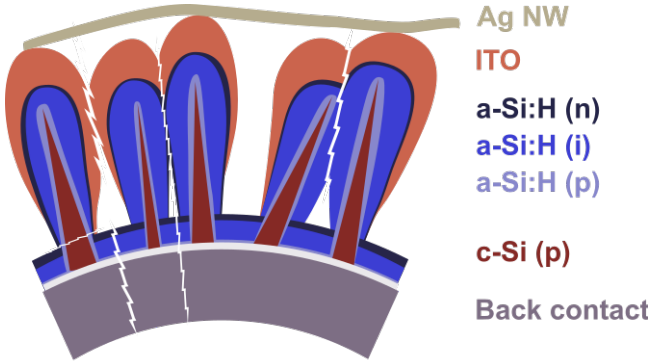

Figure 4.6: Main degradations in a Si NW/a-Si:H cell. No crack through a single Si NW/a-Si:H is expected, since NWs are not submitted to stresses. Delamination is more likely to occur between the back-contact and the a-Si:H layer, because their mechanical properties are different.

How to characterize shunts? Given the J-V curves, we mostly expect the creation of shunts under bending. Usually, electroluminescence or thermography techniques are employed to make shunts visible [Gerber 2015]. In thermography, a low forward bias results in a current flowing preferentially through the shunting paths. The locally induced Joule heating can be probed with infrared detection. A spatial map of shunts can be obtained. The same measurement can be done under reverse bias as well, which enables to make the distinction between shunts with an ohmic or a diodic behavior [Breitenstein 2008]. For electroluminescence (EL), a current is injected into the cell (forward bias applied) and the luminescence is collected. At shunt positions, the luminescence signal decreases because non-radiative recombinations are enhanced.

Why EBIC instead? However, due to heat wave propagation, thermography maps display a rather low resolution, even when using lock-in thermography. EL measurements are highly spatially resolved and can be quickly recorded, yet they present some drawbacks, especially for a-Si:H. Since EL relies on radiative recombinations, the signal is expected to be quite low in a-Si:H, even though measurements are possible. Furthermore, the required analysis is different due to the important part of tail-to-tail recombinations [Gerber 2015]. Finally, the EL signal can be quenched by shunts over a large part of the cell, which prevents a precise location and shape determination of the shunt defect [Gerber 2015, Kasemann 2006].

Consequently, EBIC can be a useful tool to characterize the bending degradation of Si NW/a-Si:H solar cells. Maps of the collected current are drawn, with scales ranging from a few mm (the whole cell) to a few 100 nm. In addition, the observed defects can be related to the morphology of the sample through the SEM image. This could help to understand the origin of the degradation. The acceleration voltage can also be changed to probe different depths in the sample [Sugimura 2012], although it is not relevant for core-shell nanowires.

How degradation defects should look like in EBIC? Cracks and delamination result in collection issues. If part of the cell is fully disconnected, no induced current

will be obtained and the degradation will be clear in EBIC maps. However, if the disconnection is partial, it may not appear in EBIC maps due to the low levels of currents (10 µA for our cells).

How shunting paths should look like in EBIC? Depending on the mechanism of shunt and the EBIC connection, the effect of shunting paths on EBIC may differ. For instance, in a specific configuration, shunts corresponding to an inversion channel in a c-Si cell result in enhanced current [Breitenstein 2007]. However, this should not be relevant in our setup. Shunts should appear as regions with lower to no induced current, and with different shapes depending on the exact type of shunt, as observed both in EBIC and LBIC [Fernandes 2015, Breitenstein 2004, Brown 2010, Naumann 2014, Kaminski 2004].

It may remain difficult to discriminate between these shunts and other defects that reduce EBIC (for instance region not electrically connected). Yet, because they are very conductive, shunts should draw current from a larger region than the defective one, with an apparent damaged area depending on the conductivity of the top-layer [Fernandes 2015, Vorasayan 2011]. No sharp transition should be observed [Xiao 2019]. A slow transition in the current on the edge of the defect and a larger defective region in the EBIC map compared to the SEM image can point towards a shunt.

Finally, shunts can make EBIC observations difficult due to a strong current, which saturates the pre-amplifier. In order to get a correct signal to noise ratio, AC e-beam with a lock-in detection can be used. As mentioned in Section A.1, a single-contact EBIC measurement can also be used to avoid the related noise.

4.4.2 Indentation tests

To confirm the expected features of a shunt in EBIC (regions with slow transition to lower current and a larger defective region in the EBIC map compared to the SEM image), I used a diamond pen to make a shunting path on one cell with 80 nm ITO as top contact. A strong decrease in the EBIC level over the whole cell was observed. However, it may be related to poor electrical contacts. No I-V curve was measured afterwards to confirm the change. Figure 4.7 presents the EBIC signal in two different regions with indentation. The damaged parts result in much lower to no signal in EBIC. But the region corresponds to the damage observed in SEM. In addition, profiles show a rather steep decrease of the signal, in contrast with the expected slow transition. An I-V measurement would have been needed to confirm the presence of shunts.

4.4.3 EBIC after bending

Figure 4.8 displays low-magnification SEM images and EBIC maps of a cell that failed during bending and a cell that did not (from the same sample). They do not show differences after bending. In both cases, the current is collected from the whole cell. We can see small defects, but their origin remains unclear and cannot be attributed to bending or to the breakdown of the cell. Some defects are observed both for degraded and not-degraded cells. EBIC observations directly on bent cells may bring more information.

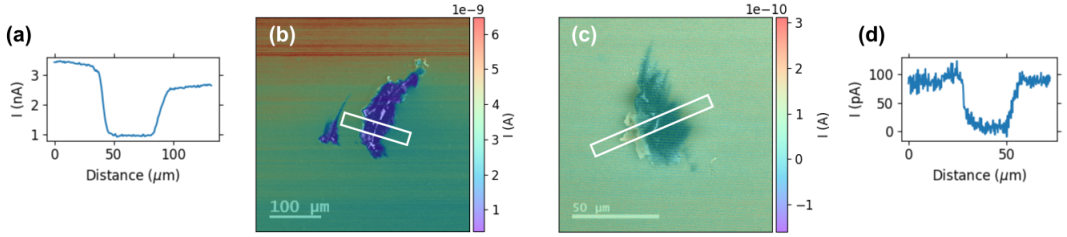

Figure 4.7: **(b)** and **(c)** EBIC maps superimposed on SEM images of a Si NW/a-Si:H cell after indentation with a diamond pen, with **(a)** and **(d)** profiles of the current corresponding to the framed region (left to right). The top contact is 80 nm ITO. $V_{acc} = 20$ kV. The current from the p-i-n junction is displayed as positive.

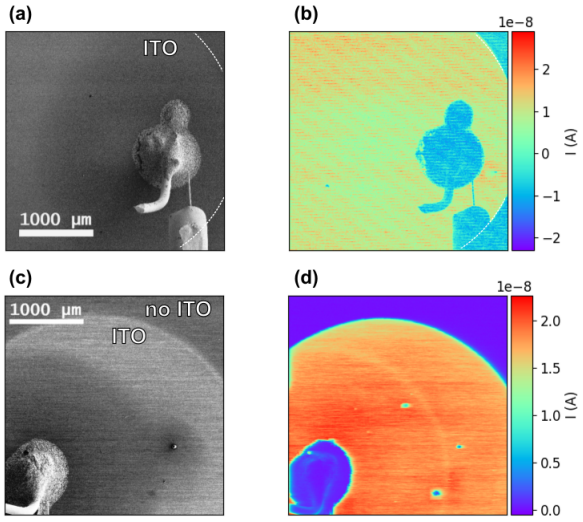

Figure 4.8: SEM image and EBIC map after bending of Si NW/a-Si:H cells that **(a)**, **(b)** failed and **(c)**, **(d)** did not fail during bending. The top contact is made of 80 nm ITO. The electrical connection is done with Ag paste and a probe (see the SEM image and EBIC, where they lead to zero signal). The contrast differs between observations because of the electrical noise during the observation of the top cell. V_{acc}=15 kV (top), V_{acc}=20 kV (bottom). The current from the p-i-n junction is displayed as positive.

4.4.4 Metal foils as new substrates

To overcome the limitation of the glass in the previous bending tests and for the in-situ observation, we decided to use more bendable substrates, that are not likely to break. Because of the temperature of growth (400 °C at the substrate holder), we chose metal foils (Cu and Al, 6 µm and 9 µm thick respectively), for flat and NW solar cells. Yet, their coefficient of thermal expansion is higher than that of glass or a-Si:H: around $20\times10^{-6}\,K^{-1}$ for copper (0-1000 °C), $29\times10^{-6}\,K^{-1}$ for Al (0-600 °C), compared to $4\times10^{-6}\,K^{-1}$ for a-Si:H. After deposition, an internal compressive strain in the a-Si:H layer is thus expected [Suo 1999].

I used the usual back contact, Ag(100 nm)/ZnO(100 nm), to prevent shunts due to direct connections to the conductive substrate. Nonetheless, NW solar cells on Al and Cu were strongly shunted and could not be observed with EBIC. It could be improved with a better handling of substrates and smaller areas (∼1 cm^2 for these cells).

4.4.5 Bending in SEM

I folded solar cells on Al or Cu foil on the substrate holder, as can be seen in the picture (Figure 4.9 **(d)**). Thanks to the substrate, the bending radius is much smaller (around 1 mm). I observed the folded cells in the SEM chamber, with SEM and EBIC.

With SEM, changes in morphology under strong bending can be assessed. In particular, I observed many cracks in both cells, flat and with NWs, as displayed in Figure 4.9. These cracks are parallel and follow the direction of maximal strain. We therefore attribute them to bending.

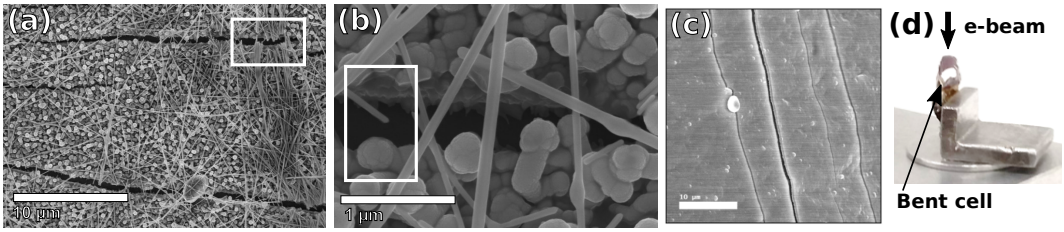

Figure 4.9: SEM images of bent **(a)**, **(b)** Si NW/a-Si:H, **(c)** flat a-Si:H solar cells on Al foil. **(d)** Picture of the flat a-Si:H cell on Al foil on the substrate holder before observation. The white frame in **(a)** highlights the fracture of Ag NWs, the frame in **(b)** highlights the crack going between Si/a-Si:H NWs.

Contrary to the expectation, Si NW/a-Si:H arrays do not stand extreme bending. There may be two reasons to this. First, instead of single, free nanowires, the array is actually made of aggregates of NWs. Because NWs are quite dense, this almost results in a film. This film is more prone to degradation under bending. As can be seen in Figure 4.9 **(b)**, cracks zigzag between NWs. NWs themselves are not broken, but the layer between them can be (mostly ITO, but a-Si:H too). Moreover, there are some continuous layers as well in the NW cells, namely the back contact (100 nm Ag + 100 nm ZnO:Al) and the parasitic a-Si:H cell which grows between NWs (thickness around 150-200 nm). A close-up on cracks in flat and NW samples shows that (at least) some go through all the layers of the cell, which suggests that strong bending stresses are also present in the bottom layers. On a metal foil, the bottom layers could be removed

to mitigate the degradation, but the parasitic cell and the film-like behavior of the array would remain. As can be seen in Figure 4.9 **(a)** and **(b)**, Ag NWs can go over cracks and bridge together broken parts. With a metal foil as substrate and back contact, cracks, even through the whole layer, will not fully break the cell. Nonetheless, under some conditions, Ag NWs finally fracture. This is likely related to the density and is a supplementary reason for well-dispersed networks.

From the bending tests on flexible glass and on Al foil, it appears that the minimal bending radius that Si NW/a-Si:H solar cells can stand is between ∼2 mm and ∼2 cm. The exact value depends on the substrate (thickness, hence actual strain in the active layers, and thermal expansion coefficient, hence internal strain in flat device).

4.4.6 EBIC during bending

While the SEM observations are useful to understand the ultimate degradation of the Si NW/a-Si:H cells, they do not explain the change observed in J-V curves. Indeed, we observed no such cracks after the first bending tests.

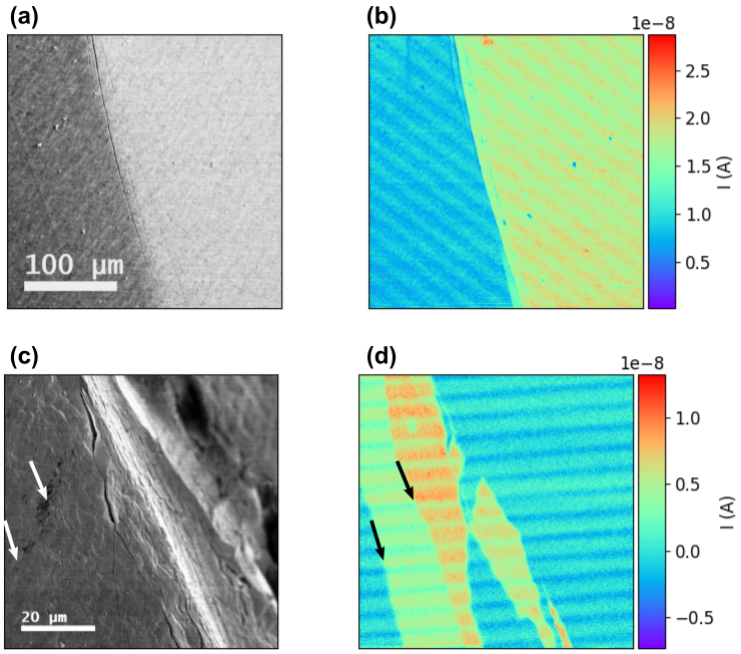

Figure 4.10: **(a)** and **(b)**, **(c)** and **(d)** SEM image and corresponding EBIC map of a bent a-Si:H flat cell. $V_{acc} = 20\,kV$. The current from the p-i-n junction is displayed as positive.

Figure 4.10 presents EBIC maps of a flat a-Si:H cell bent inside the SEM chamber together with the corresponding SEM images. While many cracks are visible in the SEM images, they do not necessarily hinder the collection of the current. All cracks in Figure 4.10 **(a)** can be seen in the EBIC map (lower signal), but only one strongly prevents the current from being collected. Other cracks are likely partial, and each side of the cell remains connected.

The effect of such cracks depends on the conductivity of the top contact and on the amount of current. In EBIC, currents are low compared to 1 Sun illumination.

The excitation is indeed lower and it is localized (no cumulative effect). Although cracks increase the in-plane resistance of the top contact, this has almost no effect on the current collection. Nonetheless, the decrease in the EBIC signal at cracks which otherwise do not show a discontinuity in the current may be surprising. EBIC is related to both the generated amount of charge carriers and the finally collected amount. Here the decrease in signal can be related to a lower generation rate at the position due to less material. EBIC maps unveil features that are not visible in the SEM image, as the arrows in Figure 4.10 **(d)** highlights. These discontinuities in current, which are parallel to the crack in SEM, are likely to be related to hidden cracks.

In conclusion, EBIC is not sufficient to determine the collection issues and to map the possible shunt paths with certainty. Nonetheless, it can show damages that are not observed in SEM.

4.5 Takeaway messages

- Among the reported record flexible cells, none of the inorganic ones was tested under bending.

Flexible cells refer to different properties depending on the application. Due to the stiffness of inorganic materials, design solutions have to be used to avoid cracks and delamination, for instance with NW arrays. Because they determine the stresses inside the sample, the mechanical properties of the substrate are also critical, both for the design of devices and for a thorough understanding of the mechanical state in the sample.

- We obtained an inorganic solar cell that can be bent to $R_c \simeq 2\,\text{cm}$.

We grew Si NW/a-Si:H cells on thin glass. Tests under 1 Sun proved that they could sustain bending radii down to 2 cm. For these bending radii, we observed no difference between thin or thick ITO and bare ITO or {ITO + Ag NWs}.

- J-V curves showed that the creation of shunts was the main degradation mechanism.

Some cells showed no degradation, while others did. They showed a decrease in V_{oc} and FF (sometimes in J_{sc}), attributed to a lower R_{shunt}. We believe it comes from new shunting paths, but SEM and EBIC observations after bending did not bring conclusions.

- The flexibility of Si NW/a-Si:H arrays remains limited by the density of NWs and the parasitic layer between NWs.

To probe smaller bending radii and to observe Si NW/a-Si:H under bending with SEM and EBIC, we then grew cells on Al and Cu foils. SEM observations showed that the flexibility of Si NW/a-Si:H is limited by their high density and film-like behavior and by the parasitic flat cell.

- Although EBIC maps highlighted defects that are not observed in SEM, they did not bring a better understanding of the Si NW/a-Si:H early degradation. The origin of the decrease in R_{shunt} could not be found.

EBIC observations should help for the understanding of the degradation mechanism, thanks to the parallel observation of the generated and collected current and the morphology and the various magnifications (from 100 nm to mm). However, due to the low current, collection issues are not necessarily observed. Besides, despite the expectations, we did not observe in EBIC any distinctive signal for shunts.

Chapter 5

Strong illumination of a-Si:H solar cells

Contents

5.1 Properties of a-Si:H

5.1.1 Amorphous semiconductors

Features of an amorphous structure While a crystalline material is determined by the repeated translations of a unit cell, no long-range order can be found in amorphous structures. Nevertheless, the coordination of an atom (number of bonds to its immediate neighbors) in an amorphous material is well-defined and the local structure is retained. For instance, a Si atom in a-Si:H remains tetrahedrally bonded to its neighbors. This is in contrast to states without any order, such as gases. Because of the lack of long-range order, the lengths and orientations of bonds can slightly vary to accommodate to the structure (typically around 10 % for bond lengths, less for angles [Street 1991]). Beyond a few bonds, order is fully lost.

Because of less stringent rules on bond orientations, an amorphous structure can accommodate singularities that would result in defects in crystals, for instance missing atoms or substitutional atoms with a different valence. It is an issue for doping, since most of the doping atoms do not result in a ionized atom. However, such an accommodation is sometimes not possible, and the coordination of an atom may differ from the expected one (a three-bond Si atom for example). This is a defect in amorphous structures. They lead to deep states in middle of the gap.

Consequences on the wavefunction The wavefunction of electrons is significantly altered by the long-range disorder and differs from crystals. In crystals, it is coherent over a long distance, but in amorphous materials, changes in potential lead to strong scattering and a loss of coherence. No momentum can be defined for the wavefunction. Consequently, the energy dispersion with momentum is not relevant anymore, and there is no *direct* or *indirect* transition [Mott 1969]. Hence, the absorption is not limited by the conservation of momentum and amorphous semiconductors display a high absorption coefficient. In addition, because of the potential disorder, the wavefunction is more localized than in crystals. When the disorder is particularly strong, it results in *localized states*. In a-Si:H, it corresponds to a localization length of 3-10 Å [Street 1991]. These localized states form band tails in the band gap of amorphous semiconductors.

Consequences on the band gap A band gap can indeed be defined in amorphous semiconductors, because of the short-range interactions (bonding and antibonding orbitals are separated) [Weaire 1971]. However, the local disorder (bond distances and angles) results in bandtails made of localized states. Figure 5.1 displays a schematic band structure of an amorphous semiconductor. The density of states shows a exponential decrease in the band tails.

Beyond the band tails, the behavior is closer to a crystalline semiconductor. In these *extended* states, the wavefunctions extend over larger distances. Together with the increased density of states, it leads to a higher mobility. The limit between the localized and extended states is the *mobility edge*. The *mobility band gap* corresponds to the separation of the valence and conduction band mobility edges. It is the value of interest in amorphous semiconductors since it governs the electronic transport. It differs from the band gap of crystalline semiconductors as it does not completely correspond to a forbidden band. An optical band gap can also be defined from absorption measurements.

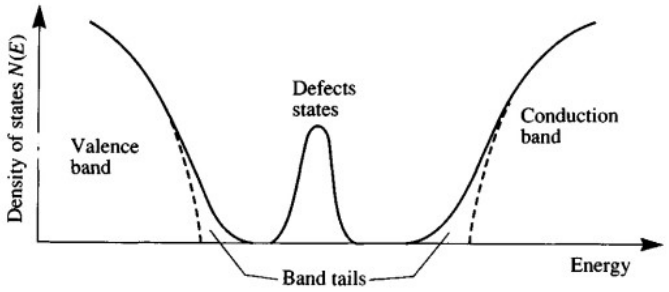

Figure 5.1: Band structure of an amorphous semiconductor (solid line), compared to a crystalline one (dashed line). Extracted from [Street 1991].

The optical band gap does not probe the mobility, but relies on the density of states only (no momentum conservation). Optical transitions between localized states are limited by the poor overlap between wavefunctions. Hence, values lower but similar to the mobility band gap are obtained for the optical one.

Consequences on the electronic transport In the extended states, the electronic transport is similar to crystalline semiconductors. It is described by the *free-carrier mobility* μ_0 (also called the *microscopic mobility*). However, in localized states, the usual electronic transport is not effective anymore. Instead, hopping, which corresponds to tunneling from atom to atom, becomes significant. This mechanism strongly depends on interatomic distances, hence on the densities of carriers, and on temperature. Besides, at low temperature, electrons do not have enough energy to reach the conduction band and the conduction mostly takes place in the localized states. In a-Si:H, room temperature is sufficient for the electrons to reach the extended states and the contribution of localized states is lessened. The *drift mobility* μ_D takes into account the successive trapping/detrapping in the localized states. It is the value obtained with time-of-flight measurements and is lower than the free-carrier mobility. In addition, when the effect of localized states is important, a dispersive transport of charge carriers is observed. There is a change in velocity with time, hence distance and time are not proportional anymore.

Consequences on doping Amorphous networks are able to adapt to atoms with different valences. Hence, atoms do not need to ionize and no additional electron or hole is created. Nonetheless, substitutional doping has been shown in amorphous semiconductors, but with a low doping efficiency.

5.1.2 History of a-Si:H

Chittick et al. first described the deposition of *hydrogenated* amorphous silicon from silane gas (SiH_4) with an RF-discharge in 1969 [Chittick 1969]. While the presence of hydrogen is not mentioned in the article, a strong photoconductive effect, possible only when H atoms reduce the density of defects, was reported. Later studies confirmed the presence of hydrogen in PECVD amorphous silicon. In 1975, Spear and Le Comber reported the substitutional doping of glow-discharge a-Si:H from phosphine PH_3 and

diborane B_2H_6 [Spear 1975]. The properties of a-Si:H have been extensively studied in the 1970s-1980s, and its use in devices in the 1980s-1990s. Details regarding the development and characterization of a-Si:H can be found in [Street 1991].

5.1.3 a-Si:H material structure

Local order Coordination and bond features can be estimated with X-ray or neutron diffraction measurements [Laaziri 1999, Fortner 1989]. From these data, the Radial Density Function (RDF) can be computed. It displays the averaged distribution of atoms at a distance r from an atom.[1]

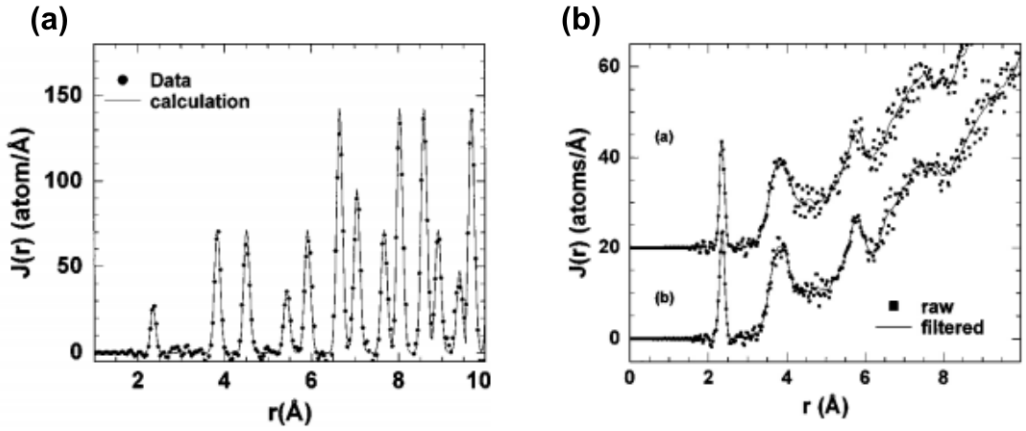

Figure 5.2: RDF of **(a)** crystalline and **(b)** amorphous silicon. From [Laaziri 1999].

Figure 5.2 presents the RDF of crystalline and amorphous silicon. The short-range order in a-Si, similar to c-Si, is clear, as well as the loss of order at longer distances. The Si−Si bond length (2.35 Å) is very close to the bond in c-Si (2.35-2.36 Å). From the width of the peak (for c-Si and a-Si), the variation due to disorder in a-Si was estimated to 0.03 Å (< 2 % variation) [Laaziri 1999]. The estimated bond angle is (108.4±0.2)°, close to 109.5° for c-Si. The effect of disorder is slightly stronger, ∼10° (< 10 % variation) [Fortner 1989]. Finally, amorphous silicon shows a lower coordination number than c-Si, close to 3.6-3.9, lower than the 4 coordination required in a tetrahedral structure.

Coordination defects The lower coordination number suggests that some Si atoms show a three-fold coordination, with a dangling bond (unpaired electron). Other coordination defects exist in amorphous silicon (two- and five-fold silicon atoms), but the dangling bonds are the main one, with densities around $10^{15}\,cm^{-3}$ for materials with a low density of defects (well-passivated a-Si:H) to $10^{18}\,cm^{-3}$ for highly defective materials [Street 1991]. They are responsible for mid-gap states and strongly limit the electrical conductivity. However, the hydrogenation of amorphous silicon results in the passivation of most of these defects.

[1] Peaks in RDF correspond to high densities of atoms. The distance to the first peak is thus typical of the bond length between nearest neighbors, and the area is related to the coordination. The width of the peak is determined by the experimental resolution, the thermal disorder and the static disorder.

Figure 5.3 shows an example of bonding in amorphous silicon. A two-dimension representation is displayed, in which Si should be bonded to three atoms. Different orientations and lengths of bonds can be observed. One silicon atom is only bonded to two atoms. It is a defect. This makes the basis of the structure of amorphous silicon, but other features have been observed, such as rings or voids.

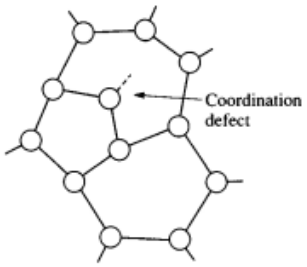

Figure 5.3: Schematic bondings in amorphous silicon. From [Street 1991].

Hydrogenation An important feature of a-Si:H is the presence of hydrogen atoms in the structure. They are required to achieve a material with a low density of defects by passivating dangling bonds (unpaired electrons of Si atoms that have a coordination of 3 instead of 4). Because hydrogen is so necessary for the electronic properties, the term *amorphous silicon* is now generally used for *hydrogenated amorphous silicon* in electronics. The optimal concentration of H is around 10 at.%.

Nuclear Magnetic Resonance and IR absorption measurements have evidenced the different bondings of hydrogen in a-Si:H. 2 to 4 at.% of H atoms are bonded as monohydrides (one H atom among the neighbors of the Si atom), around 1 % are in voids as molecular H_2 and the rest are bonded in clusters, especially at the surface of voids [Fritzsche 2001].

In addition to the passivation of dangling bonds, hydrogen can passivate dopants. Through the breaking of Si−Si bonds and diffusion, it also eases the reconstruction of the network.

5.1.4 a-Si:H band structure

The band diagram of hydrogenated amorphous silicon displays the typical features of an amorphous semiconductor. It is presented in Figure 5.4.

5.1.5 Optical and electrical properties

5.1.5.1 Absorption

Because no conservation of momentum is needed, amorphous silicon has a high absorption coefficient, especially compared to c-Si. The optical band gap energy is around 1.7 eV. Figure 5.5 displays the absorption spectra of a-Si:H and c-Si.

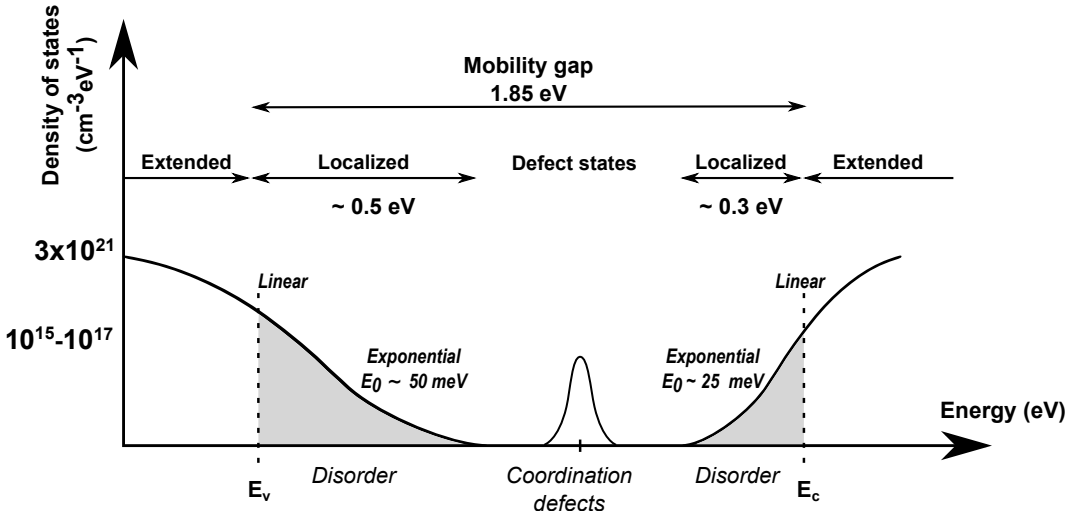

Figure 5.4: Band structure of amorphous silicon. The densities of states are shown in a linear scale, but not to scale, as the band tails would be very small. The Fermi level is around 1.1 eV above the valence band edge. The position of the defect states is not well-known and appears to depend on the doping of a-Si:H and the density of defects. Data from [Street 1991] and [Luque 2003].

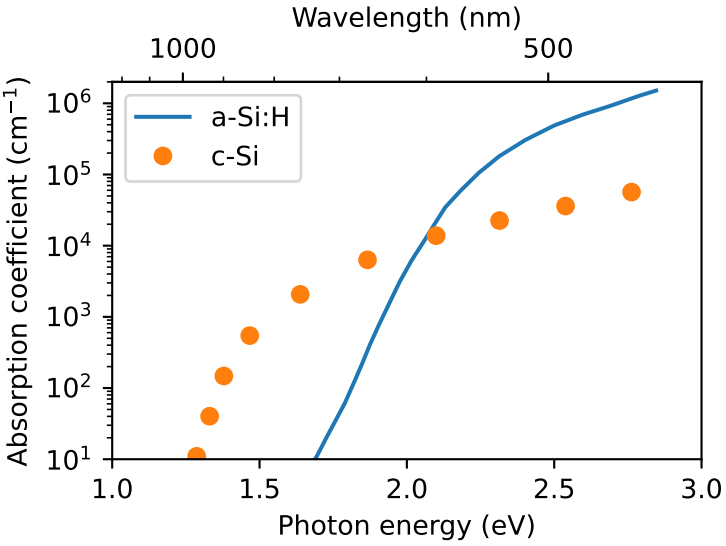

Figure 5.5: Absorption spectrum of a-Si:H and c-Si. Redrawn from [Vaněček 1998].

5.1.5.2 Conductivity

In a-Si:H, values for the free-carrier mobility μ_0 around 10-20 $cm^2/(Vs)$ for electrons and 0.5-4 $cm^2/(Vs)$ for holes have been reported [Street 1991]. These values are already low compared to most crystalline semiconductors ($\mu \sim 10^3\,cm^2/(Vs)$ for c-Si for instance). The drift mobility at room temperature is around 1 $cm^2/(Vs)$ for electrons and $10^{-3}\,cm^2/(Vs)$ for holes. Holes are more affected by the dispersive transport because of the larger tail of the valence band.

The conductivity of amorphous silicon strongly depends on temperature, because thermal energy can excite carriers from the localized states to the extended ones. In a-Si:H, room temperature is sufficient for this transition to occur in the conduction band. At room temperature, undoped a-Si:H shows a conductivity around $10^{-9}\,\Omega^{-1}cm^{-1}$. a-Si:H can be p-doped with boron B, which results in a conductivity around 10^{-6}-$10^{-2}\,\Omega^{-1}cm^{-1}$. N-doping employs phosphorus P and is more efficient, with a resulting conductivity around 10^{-4}-$10^{-2}\,\Omega^{-1}cm^{-1}$ [Spear 1976].

5.1.6 Growth of a-Si:H

Hydrogenated amorphous silicon is now mostly deposited by PECVD with silane (SiH_4) as precursor, whose dissociation is promoted by plasma. Early articles refer to this technique as *glow-discharge deposition*. Physical vapor deposition has also been studied, but results in high densities of defects. Hot-wire chemical vapor deposition, which employs a hot tungsten wire (∼2500 °C) for the dissociation of silane, enables higher deposition rates up to 30 Å/s [Alpuim 1999]. In PECVD, the hydrogen dilution of silane is a key parameter regarding the structure of a-Si:H. The H presence also limits the deposition temperature below 400 °C. A summary can be found in [Luque 2003]. For an intermediate rate (15 Å/s), a 500 nm thickness, typical of a-Si:H absorber if the light-trapping is not optimized, requires a 5 min deposition. In addition, the large-area (∼1 m^2) deposition with PECVD is also an asset for the use of a-Si:H. Guha gives some figures regarding the manufacturing process of a-Si:H for solar cells in [Guha 2000].

Two main applications can be mentioned for a-Si:H. Solar cells will be detailed below. The low cost (material and deposition) of a-Si:H and the possibility to deposit over large areas have also made it suitable for thin-film transistors, especially in commercialized flat panel displays.

5.1.7 a-Si:H in solar cells

A-Si:H is beneficial to solar cells because of its high absorption. A film thinner than 1 µm is sufficient, compared to a few 100 µm for c-Si. In addition, its high band gap energy should result in a high V_{oc}. However, due to the band tails, usual doping levels are not sufficient to bring the Fermi level at the (conduction or valence) band edge. A ∼0.2 eV separation, corresponding to the band tail extension, remains. The highest quasi-Fermi level splitting is hence limited to at least ∼1.2 V.

5.1.7.1 History and current status

The first homojunction solar cell with a-Si:H was reported in 1976 by Carlson and Wronski [Carlson 1976]. A n-i-p structure with a 1 µm thick layer of intrinsic a-Si:H resulted in a PCE of 2.4 % in AM1 sunlight. Figure 5.6 presents the increase of the performance of a-Si:H cells, both single- and multi-junctions, compared to other thin-film technologies, CIGS and CdTe. The current record at 14.0 % PCE is a triple junction made of a-Si:H/μc-Si:H:H/μc-Si:H:H [Sai 2016]. The record single junction cell with a-Si:H has a stabilized efficiency of 10.2 % [Matsui 2015b]. Records for Si NW/a-Si:H solar cells are also shown with red stars.

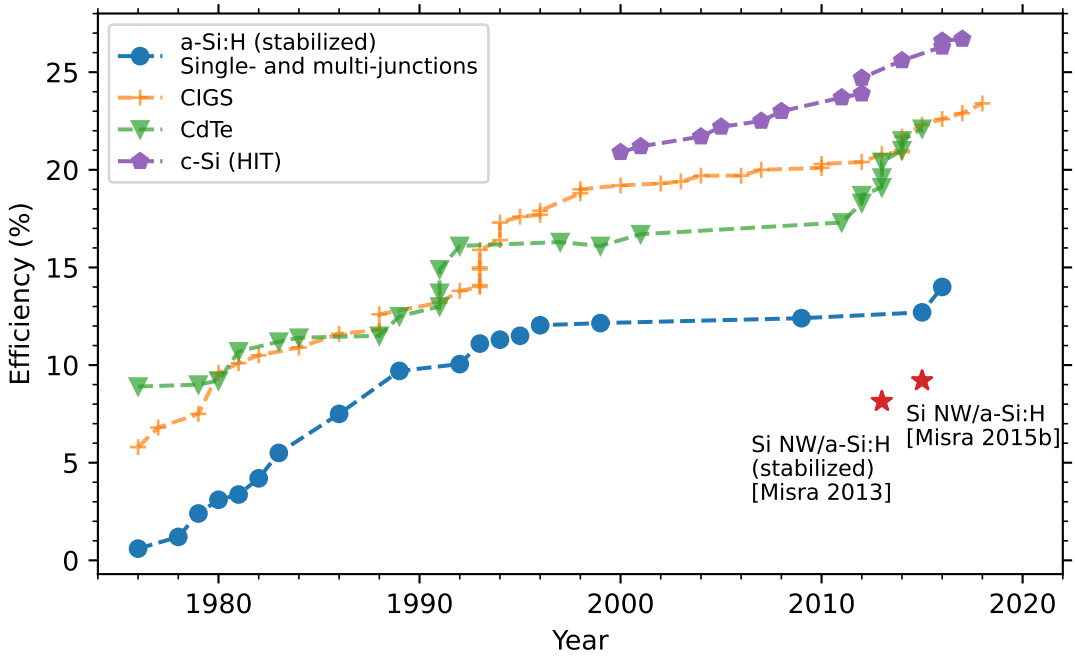

Figure 5.6: Efficiency chart for thin-film and SHJ technologies, with the current record of Si NW/a-Si:H. Data from the NREL data file[1].

Maximal conversion efficiency Carlson and Wronski also gave an estimation for the highest efficiency achievable with a single junction made of a-Si:H, namely 14-15 %. It is determined from the maximal current density (22 mA/cm^2 from the absorption spectrum), fill-factor (0.78-0.87 depending on the limiting recombinations) and open-circuit voltage (that they estimate to be 0.80 V). Kuwano estimated the maximal PCE from double and triple junctions with amorphous silicon alloys to 21 % and 24 % (at the 16th IEEE PVSC in 1982, cited in [Guha 2000]).These estimations show the potential improvement for a-Si:H solar cells. Yet, it is also clear from the chart that little progress has been made over the last 25 years.

As passivation layer However, a-Si:H has undergone a renewed interest in the 2000's for heterojunctions with a crystalline silicon absorber (SHJ). Indeed, its higher bandgap

[1] https://www.nrel.gov/pv/cell-efficiency.html

compared to c-Si and the properties of the amorphous network make it ideal for the passivation of surfaces in c-Si cells. With the addition of an intrinsic buffer layer between the absorber and the doped layer, silicon heterojunctions now play a leading role in the c-Si technology. This architecture is called *Heterojunction with Intrinsic Thin-layer (HIT)*[2] and owns the current c-Si record efficiency of 26.7 % [Yamamoto 2018]. As a side note, the acronym *HJT* is also used for silicon heterojunction solar cells. In this work, we focus on the use of a-Si:H as an absorber.

5.1.7.2 Structure

a-Si:H solar cells are typically made of a n-i-p stack with the p-doped layer towards the impinging light. Doped layers are very thin (5-10 nm). The thickness of the intrinsic layer is around 500 nm, the exact value depending on the management of light. Substrate and superstrate structures can be made, as displayed in Figure 5.7, with higher performance obtained for the substrate one.[3]

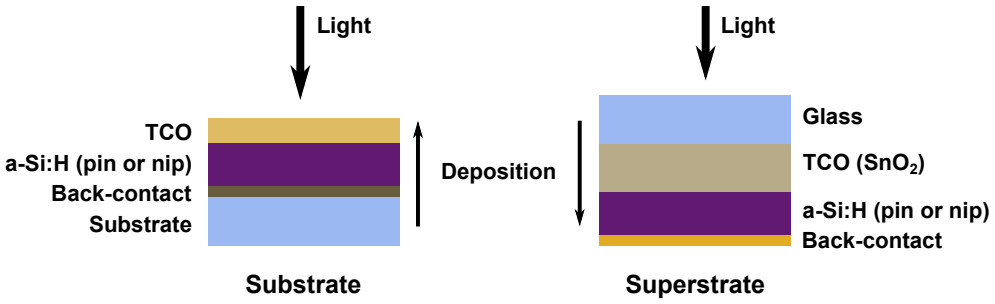

Figure 5.7: Substrate and superstrate structures for a-Si:H.

p-i-n structure Because of their low mobility and their short lifetimes, especially in doped layers, the charge carriers in a-Si:H present short diffusion lengths (around 100 nm). The performance of a-Si:H in a p-n structure, which relies on diffusion, is thus low. For this reason, a p-i-n structure is used instead, with very thin doped layers (band diagrams in Figure 1.4). The electric field governs the collection of carriers, at least under low biases. Consequently, the *drift length* L_{drift}, the *collection length* or the $\mu\tau$ product are often referred to in the literature on a-Si:H solar cells. In a simple approximation, if we disregard the dispersive mobility of amorphous semiconductors (see Section 5.1.1), the drift length can be written as

$$L_{\text{drift}} = \mu\tau \; E, \tag{5.1}$$

with E the electric field in the intrinsic part and τ the lifetime. A relationship between the diffusion length L_{diff} and the drift length is easily derived for one carrier, using Einstein's relation $D_n/\mu_n = k_B T/q$,

$$L_{\text{drift}} = \frac{q}{k_B T} \; E \; L_{\text{diff}}^2. \tag{5.2}$$

[2] HIT structures can rely on different carrier-selective passivating contacts, such as SiOx with poly-Si.

[3] The superstrate-type requires a thick TCO layer for texturing (>0.5 µm), which reduces J_{sc}. In addition, the quality of the p-layer is better when grown on a-Si:H compared to the TCO.

p-doped layer close to light In a-Si:H, the mobility of holes is much lower than that of electrons (see Section 5.1.5). Because e^-/h^+ pairs are mostly generated close to the surface, the p contact on top maximizes their collection.

5.1.7.3 Staebler-Wronski effect

The second limitation to the performance of a-Si:H absorber is a characteristic light-induced degradation, called the *Staebler-Wronski Effect (SWE)*. It was reported in 1977 as a change in conductivity after exposure to light (four orders of magnitude change in dark conductivity after 4 h under 200 mW/cm^2) [Staebler 1977]. In all a-Si:H solar cells, it results in a decreased efficiency with use. Nonetheless, the degradation slows down and a steady value for the performance is finally reached. This decrease of PCE is around 10-20 % for good cells [Matsui 2015b, Guha 2013], and down to 4 % for the record cell. For this reason, the *stabilized* efficiency, for instance after 1000 h under 1 Sun, is given for a-Si:H cells. This degradation is reversible, in particular with heating (a few hours at 150 °C).

Microscopic mechanism Under light-soaking, Electron Spin Resonance (ESR)[4] shows an increase of the density of dangling bonds up to a saturation value (typically from $10^{15}\,cm^{-3}$ to $10^{17}\,cm^{-3}$). The saturation value depends on the illumination and the temperature, with higher densities of defects for higher illuminations and lower temperatures [Isomura 1991]. These new recombination centers decrease the lifetime of carriers in a-Si:H and account for the loss in conductivity. The creation of defects stems from recombinations of e^-/h^+ pairs, as the same light-soaking conditions under reverse bias do not show similar degradation. The energy from the recombination can break bonds, leading to new dangling bonds. The presence of H helps making it stable, by separating the dangling bonds. Nonetheless, the mechanism is not fully understood. In particular, different reactions have been suggested, either involving the breaking of weak Si−Si bonds or of Si−H bonds. In addition, it is likely that the diffusion of H stabilizes the defects, by separating the newly formed dangling bonds. However, experimental observations did not show a spatial correlation between the dangling bonds and H atoms or between dangling bonds, even though it may come from the difficulty to see the signal [Stutzmann 2000]. While the Staebler-Wronski effect refers to the light-induced degradation, similar defects can be created with current injection, particle bombardment [Schneider 1987] or thermal generation (it can be observed after rapid quenching).

Kinetics Models have been developed to try and better understand the dependence on the different parameters, especially the light generation rate and the temperature.

[4] ESR measurements are widely used in a-Si:H to determine the density of dangling bonds and their environmental structure. Because electrons in dangling bonds are unpaired, a change in spin can occur. When a magnetic field is applied, the energy of each spin state is different. The transition energy can be probed with an electromagnetic field. Typically, the absorption of a microwave field is monitored, while varying the magnitude of the magnetic field. The strength of absorption can be related to the density of spins (hence dangling bonds in a-Si:H), with a good sensitivity, down to $10^{11}\,cm^{-3}$. The resonance in absorption gives the energy of the transition, which depends on the local structure through hyperfine interaction with surrounding nuclei (H, ^{29}Si). Details on the use of ESR for a-Si:H can be found in [Street 1991].

For instance, if the creation of defects is governed by band-to-band (nonradiative) recombinations and the carrier densities by recombinations on dangling bonds, the density of dangling bonds N_s shows the following dependence on the illumination rate G and time t,

$$N_s \propto G^{\frac{2}{3}} t^{\frac{1}{3}}. \tag{5.3}$$

It accounts for the stronger degradation observed under high power, short pulses, compared to the long pulses with the same energy. It is confirmed by experimental data, at least up to 400 mW/cm^2 [Stutzmann 1985]. Moreover, according to this model, the stabilization of the degradation is intrinsic to the degradation mechanism and does not rely on a balance between the creation and the annihilation of defects.

Overcoming the SWE The SWE is a reversible mechanism. The conductivity of a-Si:H can be recovered. While thermal annealing is mostly used, current- and light-induced recoveries are also possible [str 1991, Meaudre 1992, Gleskova 1993]. The structure of a-Si:H solar cells can also be adapted to mitigate the light-induced degradation, for instance with thinner layers. Although the collection length is still reduced by light-soaking, it remains larger than the thickness of the intrinsic region.

5.1.7.4 NWs

Thinner intrinsic layers improve both the collection of carriers and the tolerance to light-degradation. The single junction a-Si:H record cell thus displays a 220 nm thick intrinsic layer [Matsui 2014]. Because thin layers also reduce the amount of absorbed light, a good performance requires light management, with the use of highly structured substrates and antireflection coatings [Haug 2015]. NWs are the next step to this end. With the separation of the directions for light absorption and for carrier collection, much thinner layers can be used, namely ∼100 nm in Si NW/a-Si:H. The thin layer also reduces the effect of the light-induced degradation, as Misra evidenced with the comparison of different a-Si:H thicknesses [Misra 2013]. Using 3-dimension rigorous coupled-wave analysis, Misra estimated the short-circuit current density that could be obtained with Si NW/a-Si:H to 20 mA/cm^2 [Misra 2015a]. With the 1-dimension solving of the Poisson's equation, he also estimated the possible values of the fill-factor (79 %) and V_{oc} (0.90 V). This results in a maximal efficiency of 14.2 %. It is lower than the values given by Carlson and Wronski (see Section 5.1.7.1), that are probably overestimated.

5.1.8 Summary

The properties of amorphous materials are affected by their lack of long-range order. A band gap can still be defined, but localized states and coordination defects are more important than in their crystalline equivalent. The hydrogenation of amorphous silicon mitigates the effect of the coordination defects and enables its use in opto-electronic devices. A-Si:H is a better absorber than c-Si, but the mobility and lifetime of its charge carriers are low. Thus, its use in planar solar cells is limited by the drift length. The light-induced degradation also impedes its development. However, thanks to a low-temperature deposition, on various substrates and over large areas, a-Si:H, together with nc-Si, μc-Si:H, Ge and alloys, leads to low-cost multijunction solar cells. In addition, the use of NWs helps to relieve the limitations of a-Si:H. The difference in architecture

between the planar a-Si:H and Si NW/a-Si:H can be enhanced when the illumination is increased.

5.2 Why study Si NW/a-Si:H solar cells under high illumination?

Under increasing illumination, both the short-circuit current and the open-circuit voltage of an ideal solar cell should increase (linearly for I_{sc}). If the collection efficiency remains constant, the resulting increase of power is larger than the increase of the illumination power and the efficiency rises. That is one of the main benefits of light concentration in photovoltaics and led to a wide field of research, CPV.

Because of its early degradation due to light-soaking (SWE) and its optical and electrical properties (good absorption, but poor mobility), a-Si:H as absorber has been mostly chosen for low-illumination applications, either outdoors or indoors. Amorphous silicon solar cells have already been developed to this end, for instance in small calculators and more recently by Solems[5], or Panasonic[6] for buildings or solar-powered watches. Few works consider the change in the parameters of a-Si:H solar cells under varying illumination and they focus mostly on low-illumination levels (typically below 1 Sun) [Yoshihiro 1994, Al Tarabsheh 2015]. Studies of higher illuminations are related to the light-induced degradation [Yang 1991]. For this reason, and despite the decrease of performance that could be expected, we wanted to check how a-Si:H solar cells could sustain strong illumination. In addition, the use of NWs should improve the collection of carriers and can affect the behavior of a-Si:H solar cells under strong illumination. We were interested in determining the consequences of using Si NW/a-Si:H compared to flat a-Si:H.

In contrast to concentration setups, we do not change the angle of impinging light and use a monochromatic light. Consequently, we do not use the term *concentration* for our experiments. For solar cells with a sufficiently low series resistance and a linear relation between the photocurrent and the illumination power, the short-circuit current is proportional to the illumination power $I_{sc} = I_{\phi} = KP_{ill}$. Thus, many studies under increased illumination regard I_{sc} as a direct quantification of the concentration ratio. However, in our case, the short-circuit current is quickly limited by the poor collection of carriers. Hence, parameters are displayed against the illumination power.

5.3 Overall behavior

5.3.1 Experimental details

Light source Figure 5.8 presents a picture of the setup for the illumination measurements. Depending on the exact set of measurement, power densities between 0.1 W/cm^2 and 1.2 kW/cm^2 (powers equivalent to 1-12 000 Sun) have been used. A 532 nm laser was chosen, as it corresponds to the maximal absorption of the Si NW/a-Si:H solar cells (see EQE in Figure 2.13). Most measurements employ a continuous-wave laser (Millennia Edge). The diameter of the laser spot is originally around 2.3 mm. However, a

[5] https://www.solems.com/en/photovoltaic-modules
[6] https://industry.panasonic.eu/products/energy-building/amorphous-solar-cells

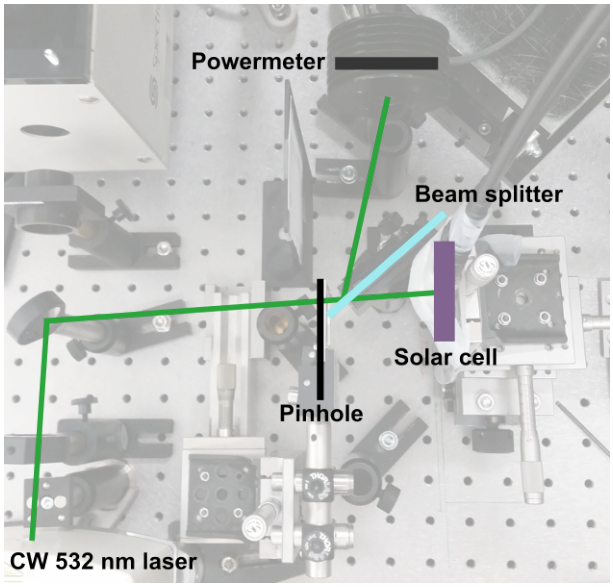

Figure 5.8: Picture of the experimental setup. The path of the laser beam is shown in green.

pinhole was used to change the beam size. Pinholes of 400 µm, 800 µm and 1400 µm led to $1/e^2$ diameters of 0.26 mm, 0.57 mm and 0.97 mm. Profiles are displayed in Appendix (Figure C.1). Since the beam is not uniform, both the total power and the (averaged) power density are given. The light intensity on the cell was monitored by the reflected part after a beam splitter. Two photodiodes were used for the measurement, a Si diode and a thermopile, depending on the power range.

Electrical measurements I fixed all samples with Ag paste on an Al plate. The cells were connected with two wires to a Keithley SMU. For each illumination, I recorded a complete I-V curve, from 0 V to 1 V and back from 1 V to −0.5 V to check for a potential hysteresis. Between measurements, the shutter of the laser was closed for >60 s. Each set of measurements on a cell approximately corresponds to 1 h 30 min of illumination, with every measurement lasting around 2 min.

Time-reversible changes To assess whether the observed changes were reversible with time, I made repeated measurements after different illumination levels for a given power density (called *probe power*). Repeated measurements correspond to the same illumination power, however the history of the cell (highest illumination power and total illumination energy) differs.

Measured solar cells I measured Si NW/a-Si:H solar cells, as well as a crystalline silicon and a flat a-Si:H cells. Details are presented in Table 5.1. Illumination with the 800 µm pinhole will mostly be discussed. Their performance under 1 Sun before and after the measurements are shown in Appendix, in Figure C.2. The planar cell with a-Si:H displayed a so-called *S-shaped* I-V curve. I still assessed the behavior of the flat a-Si:H cell under strong illumination, however, V_{oc} and its variations are strongly

impacted by the barrier and cannot be compared with Si NW/a-Si:H solar cells.

Table 5.1: Si NW/a-Si:H, flat a-Si:H and c-Si cells measured under high intensity 532 nm light. Details regarding the crystalline silicon cell can be found in [Sobkowicz 2014].

Cell	Stack	Area	Pinhole
Si NW/a-Si:H	Glass/Ag/AZO/ p c-Si NW/p-i-n a-Si:H (intrinsic ~90 nm)/ 240 nm ITO (Figure 1.13 **(a)**)	0.03 cm^2 (2 mm ⌀)	400 µm 800 µm 1400 µm
Flat a-Si:H	Glass/Ag/AZO/ p-i-n a-Si:H (intrinsic ~200 nm)/ 80 nm ITO	0.03 cm^2 (2 mm ⌀)	800 µm
c-Si (SHJ)	Ag/n c-Si (~250 µm)/p a-Si:H/ ITO	1 cm^2	400 µm 800 µm 1400 µm

5.3.2 I-V curves

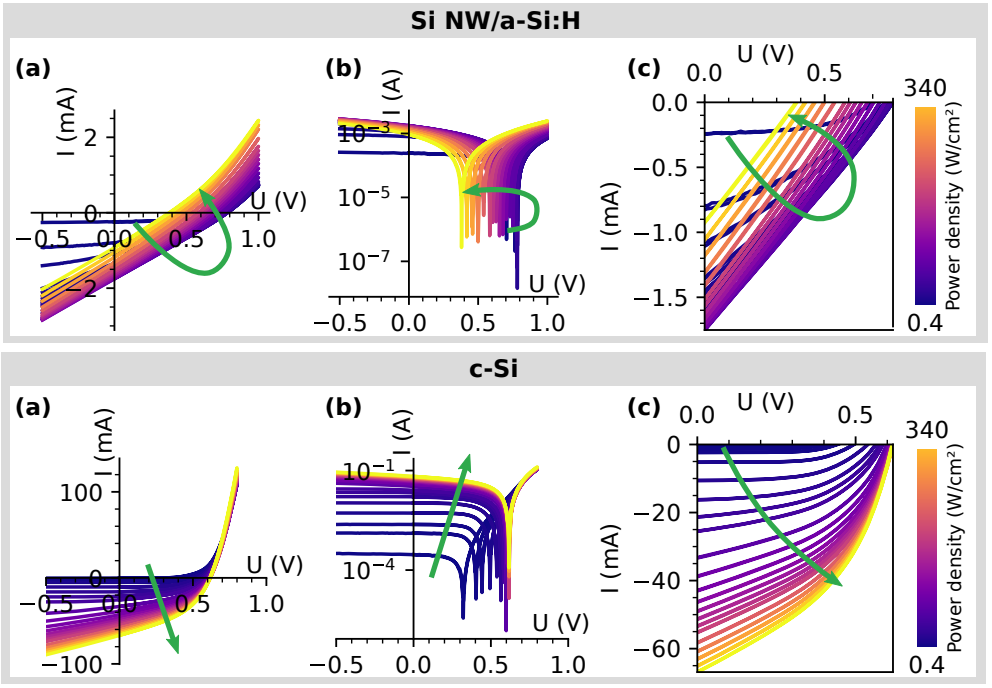

Figure 5.9: **(a)** Linear, **(b)** semi-logarithmic and **(c)** close-up I-V curves of a Si NW/a-Si:H cell (top) and a c-Si cell (bottom) with a 800 µm pinhole (repeated measurements are not shown). The color scale is linear.

Figure 5.9 shows an example of a series of I-V measurements under increasing illumination for a Si NW/a-Si:H (top) and a c-Si (bottom) solar cells. For an ideal solar

cell (no series resistance, no shunts), the I-V curve would keep the same shape and only be shifted to higher short-circuit currents and open-circuit voltages. I_{sc} and V_{oc} would increase with the illumination. It is nearly what is observed for c-Si, where the rectifying behavior remains and I_{sc} and V_{oc} increase. Yet, the fill-factor is reduced when the illumination rises, which can be explained by a stronger impact of resistance at high current levels or by screening effects. The Si NW/a-Si:H cell displays a very different performance. The rectifying behavior is quickly lost, and I_{sc} and V_{oc} both present a decrease beyond a certain power (different for I_{sc} and V_{oc}).

5.3.3 I-V parameters

From each I-V curve, the following parameters can be extracted: J_{sc}, V_{oc}, FF, efficiency, apparent series and shunt resistances (the term *apparent* is explained in Section 5.3.4). All parameters corresponding to the data in Figure 5.9 are shown in Figure 5.11. The graphs are not straightforward, as they summarize different effects, that need to be disentangled. I display them now as an overview of the behavior of the Si NW/a-Si:H and c-Si cells under strong illumination, but the change in I_{sc} and V_{oc} together with the mechanisms in play, are analyzed in detail in the following sections. In addition, as an example of how to understand the different symbols, I present quickly the I_{sc} variation in Figure 5.10.

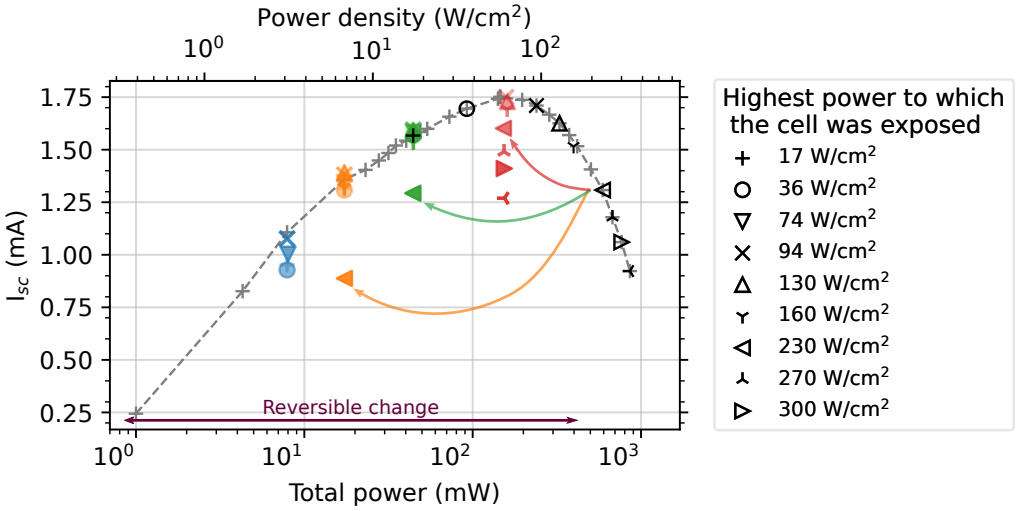

Figure 5.10: I_{sc} dependence on the illumination power extracted from I-V curves of a Si NW/a-Si:H cell under 532 nm illumination. The repeated measurements are added at the probe power with color symbols. The color corresponds to the probe power, while the symbol indicates the highest power to which the cell was exposed before the measurement. These highest powers are detailed in the legend on the right and are also displayed with black open symbols in the Figure. The pinhole diameter is 800 µm.

During measurements, I gradually increased the illumination power, which results in the grey line with + symbols. In addition, I wanted to assess the possible degradation of the cell. To this end, after a few steps, I measured again the I-V curve of the cell at lower powers. These repeated measurements have two important parameters: the

illumination under which the measurement is made, called the *probe power*, and the highest power that the cell had experienced at that time, called the *highest illumination power*. The repeated measurements are displayed in the Figure with color symbols. I used four probe powers, shown in blue ($3\,W/cm^2$), orange ($7\,W/cm^2$), green ($17\,W/cm^2$) or red ($62\,W/cm^2$). The different symbols refer to the highest illumination power. These highest powers are detailed in the legend on the right and are also displayed with black open symbols in the Figure.

When these repeated measurements show no difference compared with the initial ones, it means that there is no degradation. In Figure 5.10, we see that for measurements above $160\,W/cm^2$, the repeated I_{sc} drops, which attests some irreversible degradation[7]. The arrows present the three repeated measurements made after the exposure to $230\,W/cm^2$. In particular, the red arrow shows the increase of I_{sc} when the probe power goes back to lower values, which evidences the (partial) reversibility of the final I_{sc} decrease.

5.3.4 Apparent R_{se} and R_{shunt}

Section 1.4 explains how series and shunt resistances of a cell can be estimated from an I-V curve. We chose to estimate them from the relation between I and V in high forward or reverse bias regions respectively. However, the obtained values may be impacted by the collection efficiency of the solar cell.

In the previous chapters, the solar cells differed by their top contact and the measurement conditions were the same. Hence, the values obtained for the resistances could be compared. However, under increasing illumination, the regions chosen for the estimation of resistances correspond to different states of the diode. Their comparison is not direct. For this reason, we call the obtained values of resistance *apparent*.

Apparent R_{shunt} For instance, the apparent value of the shunt resistance is strongly decreasing under higher illumination, as in clear in the I-V curves (Figure 5.9), both for the Si NW/a-Si:H and the c-Si solar cells. It has been reported for crystalline silicon [Terrón 1994] and CIGS [Paire 2012] and is related to collection issues. Strong illumination reduces the collection efficiency for different reasons. With increasing current, the present resistance results in high voltage drops. At short-circuit, the junction is actually forward biased. If we consider R_{se} coming mostly from out of the junction, $V_b \simeq R_{se} I_{sc}$. Because of the forward bias, the collection is less efficient. Other effects are possible, such as the screening of the electric field by the high concentrations of photogenerated carriers.

5.3.5 Si NW/a-Si:H do not behave as a solar cell for low-illumination

No significant degradation up to 770 W/cm^2 From the repeated measurements, it appears that the cell can sustain very high illumination intensities without significant degradation of its performance. It is not significantly degraded up to a power density of at least $160\,W/cm^2$ with the 800 µm pinhole. This power density increases for smaller illuminated areas, up to $770\,W/cm^2$ (equivalent to 7700 Sun) with the 400 µm pinhole.

[7] We can notice an initial degradation for the $3\,W/cm^2$ probe power (blue symbols). It will be discussed in the following, but is not considered here for the damage of the cell, because it should be reversible under heating.

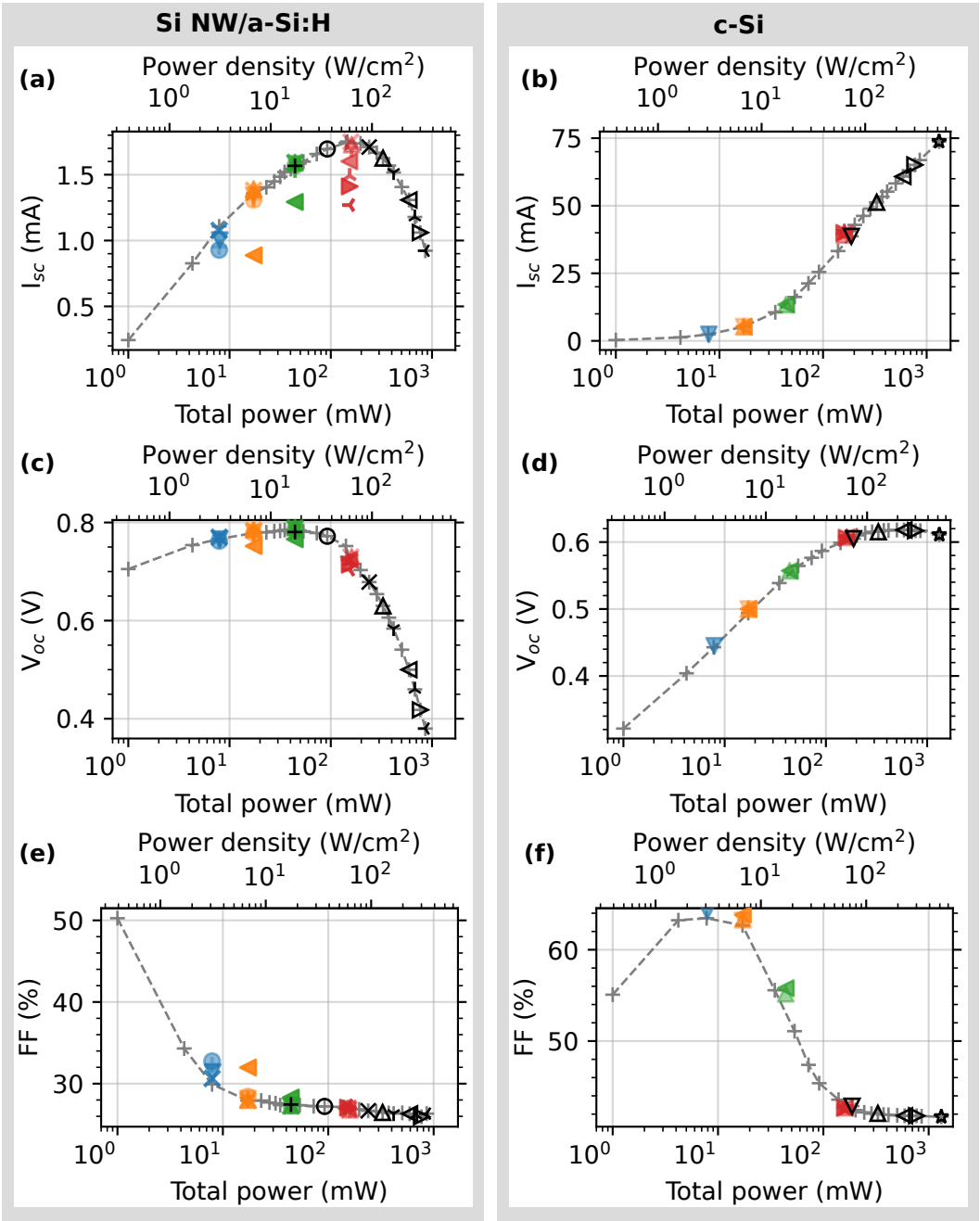
Si NW/a-Si:H
c-Si
(a)
(b)
(c)
(d)
(e)
(f)
Power density (W/cm^2)
10^0 10^1 10^2
I_{sc} (mA)
V_{oc} (V)
FF (%)
Total power (mW)
10^0 10^1 10^2 10^3

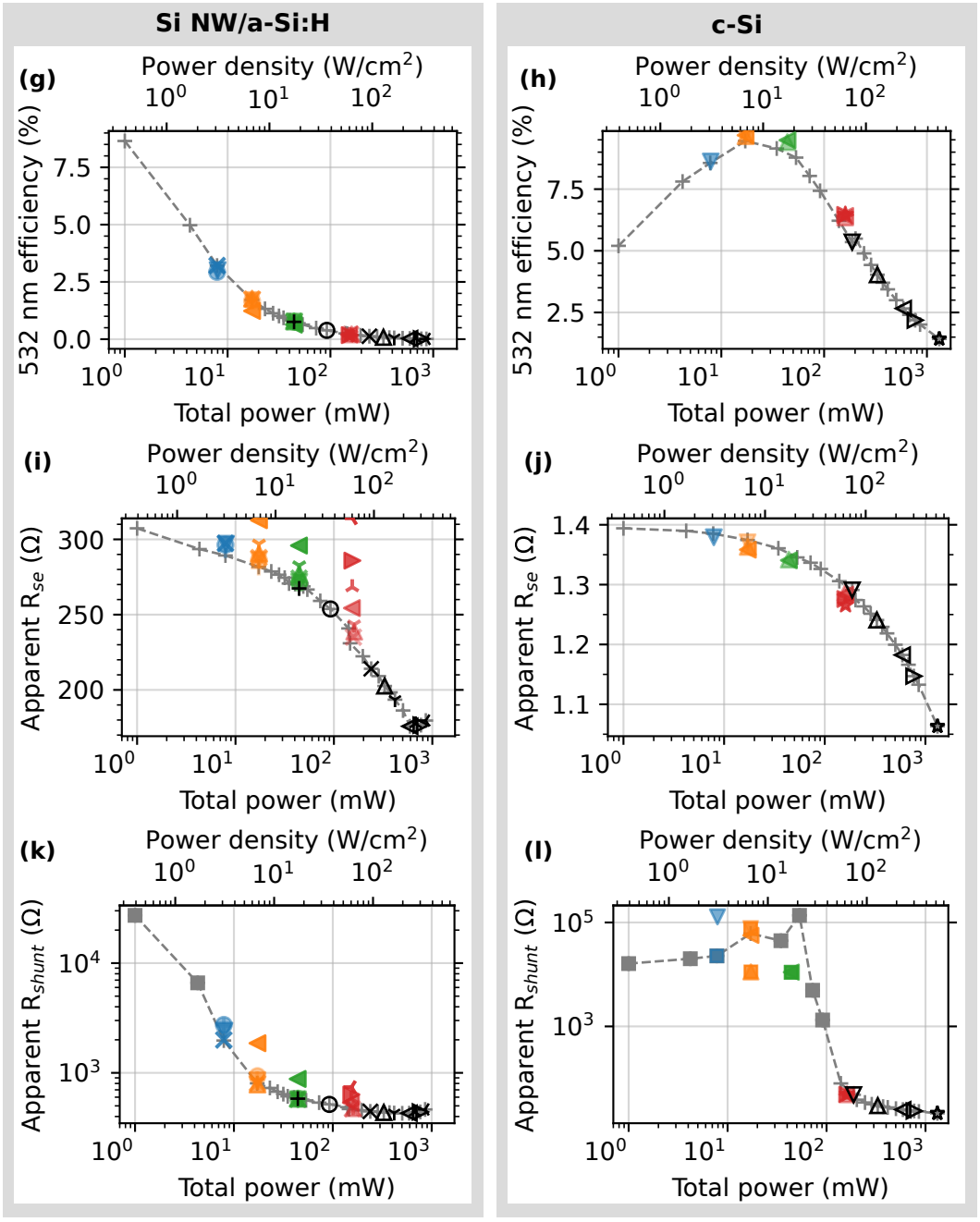

Figure 5.11: Parameters extracted from I-V curves of a Si NW/a-Si:H cell (left) and a c-Si cell (right) under 532 nm illumination: **(a, b)** I_{sc}, **(c, d)** V_{oc}, **(e, f)** fill-factor FF, **(g, h)** PCE, **(i, j)** apparent R_{se} and **(k, l)** apparent R_{shunt}. The increasing power measurements are shown in grey (+). In **(i)**-**(l)**, when the fit done to obtain the resistance is poor ($r^2 < 0.95$ for R_{se}, $r^2 < 0.9$ for R_{shunt}), the value is displayed with ■. The layout for the repeated measurements is described in Figure 5.11. The pinhole diameter is 800 µm.

Optimal illumination power Figure 5.11 shows that in Si NW/a-Si:H solar cells under moderate illumination, the short-circuit current and the open-circuit voltage increase, although less than expected. However, the fill-factor is strongly reduced from the start, which results in a decreasing efficiency with increasing power. This is attributed to the high in-plane resistance of the top contact. The effect of resistances is lower under lower illumination and indeed measurements under lower illumination intensities (Figure 5.12) show that the efficiency of Si NW/a-Si:H first increases with the increasing illumination power. Because of the lower current level, the charge carriers are better collected. The optimal illumination is around 0.1 W/cm^2 for the top contact made of ITO only. It is equivalent to 1 Sun in power density, but corresponds to larger current densities because of the high absorption of a-Si:H at 532 nm.

The top contact limits the performance Figure 5.12 shows that adding Ag NWs for a more conductive contact shifts the optimal illumination to 0.5-0.6 W/cm^2 and increases the maximal efficiency. This optimal illumination (equivalent to 5 Sun) is higher than what is usually expected of a-Si:H and what is experimentally observed for the planar a-Si:H cell. Thanks to the radial junction in Si NW/a-Si:H, the thickness of the intrinsic a-Si:H layer is reduced and the collection of charge carriers improved. Si NW/a-Si:H cells remain limited compared to c-Si, especially because of the series resistance of the NW cell. The value of the efficiency is an optimistic estimation since the 532 nm illumination is suited to a-Si:H. Concentrated sunlight, made of polychromatic light, would increase the part of non-absorbed photons and the heating of the cell, which is detrimental. Still, the Si NW/a-Si:H solar cells show an optimal illumination power above 1 Sun and are first limited by the top contact.

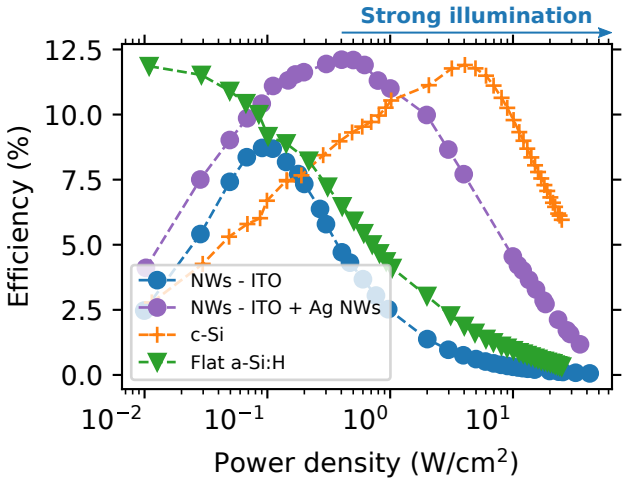

Figure 5.12: Efficiency of a Si NW/a-Si:H solar cell with different top contacts (240 nm ITO or {240 nm ITO + Ag NWs}) under increasing illumination at 532 nm. The behavior of a c-Si cell and flat a-Si:H (p-μc-Si:H/$\sim$240 nm i-a-Si:H/n-a-Si:H) cell are also displayed. Compared to Figure 5.11 **(e)**, we probed lower power densities. In addition, the samples used are different (FTO back-contact instead of Ag/AZO), which reduces the light absorption in a-Si:H and may slightly alter the optimal illumination to higher values.

5.3.6 Summary and outline

With these measurements, reversible and irreversible changes (with respect to time) can be sorted out. We first observe an early irreversible decrease of I_{sc} (see repeated measurements at $3\,W/cm^2$ - blue symbols in Figure 5.11 **(a)**). It is attributed to light-soaking effects and is discussed in Section 5.4. A strong and reversible decrease of V_{oc} is also observed (Figure 5.11 **(c)**). When looking at the I-V curves, the V_{oc} change seems to come from a lower shunt resistance. In addition, high-illumination effects, such as Auger recombinations, should be considered. Thermal effects can also account for the change in V_{oc}. We establish in Section 5.5 that the increase of temperature is actually responsible for the V_{oc} decrease. Under higher powers, a reversible decrease of I_{sc} (highlighted by arrows in Figure 5.10) occurs. We show that it is a side effect of the V_{oc} decrease (Section 5.7). Finally, the irreversible change in all parameters after $160\,W/cm^2$ illumination is attributed to a change in the material. We evidenced for instance the crystallization of a-Si:H (Section 5.8).

5.4 Time-irreversible decrease of I_{sc} after moderate illumination

5.4.1 I_{sc} decrease and recovery under stronger illumination

Figure 5.13 displays the repeated measurements of I_{sc} after exposure to light for several probe powers. An initial decrease is observed with values down to 80 % of the initial current. It reminds of light-soaking effects observed in a-Si:H solar cells.

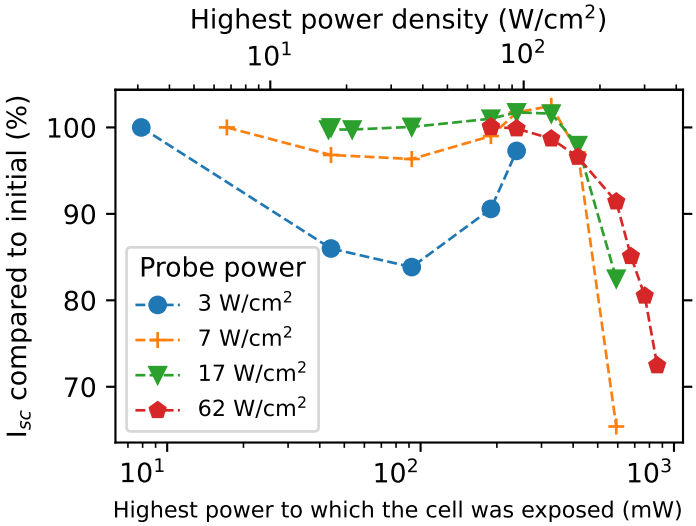

Figure 5.13: Irreversible change in relative I_{sc} with exposure to higher illuminations for four probe powers. The pinhole diameter is 800 µm.

The change depends on the illumination power used for the probe, with stronger apparent decreases for lower illumination probe powers. This is probably because the graph is presented in relative values and the initial value of current for higher probe powers is already a degraded I_{sc}. When the total illumination (time and power) is

increased, the current rises towards the initial value because of in-situ annealing. V_{oc} does not show any change, the fill-factor increases, as is discussed below. A c-Si cell measured under the same conditions presents no significant variation (< 4 %) in I_{sc}, V_{oc} or FF. After stronger illumination, I_{sc} plummets to values down to 65 % of the initial one, tentatively attributed to irreversible SWE and partial crystallization, as is discussed in Section 5.8.

5.4.2 Staebler-Wronski effect

The decrease of I_{sc} is attributed to the SWE, whose mechanism was detailed in Section 5.1.7.3. Under illumination, new dangling bonds are created which prevent some charge carriers from being collected. A decrease in the efficiency of a-Si:H solar cells under 1 Sun is typically observed over several hours (tens of hours for stabilization), while the decrease of Figure 5.13 starts only after a few minutes of illumination. This is due to the high power densities, equivalent to 60-200 Sun, especially as the effect has been shown to be more sensitive to the illumination power than time [Stutzmann 1985].

SWE reduces the PCE of the solar cell because it lowers the short-circuit current and the fill-factor [Smith 1985]. Figure 5.14 **(a)** displays the change in I_{sc} and FF depending on the exposure to light. The change in the fill-factor looks correlated to the change in I_{sc}, but an increase is observed instead of a decrease. It is likely due to the already low values of FF (below 30 %), as can be seen in Figure 5.14 **(b)**. The strong decrease of I_{sc} becomes beneficial for the fill-factor.

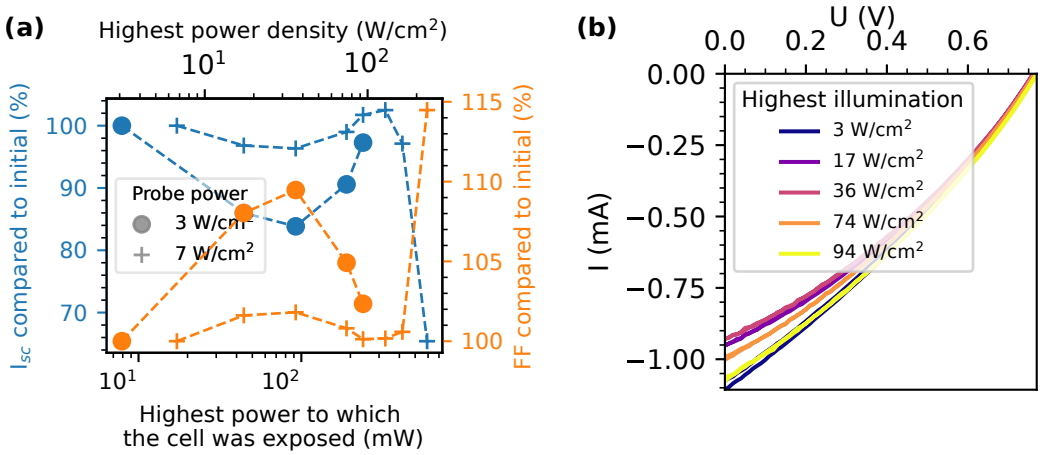

Figure 5.14: **(a)** Time-irreversible change in the relative I_{sc} (blue) and FF (orange) for two probe powers, 3 W/cm^2 (●) and 7 W/cm^2 (+), **(b)** I-V curves under 3 W/cm^2 illumination after exposure to different illuminations (see legend). The pinhole diameter is 800 µm.

5.4.3 In-situ annealing

The change in I_{sc} with exposure to light (Figure 5.13) displays a typical outline, observed for different probe powers, diameters of the laser spot and Si NW/a-Si:H cells. The short-circuit current decreases, then increases. In a single set of experiments (cell + pinhole), the increase is observed for all probe powers after the same exposure (35-75 W/cm^2 for

the displayed data). The decrease is lower for higher probe powers, because the change in the material had already started for the initial measurement.

An interesting effect of the light-induced degradation of a-Si:H is its reversible character under thermal annealing (>1 h at 150 °C, shorter time for higher temperatures). When the power density rises, the solar cell can heat up and in-situ annealing of defects can occur as well. It is likely responsible for the recovery of the initial value of current.

Size effect (pinhole) and temperature The role of temperature can be assessed using different pinholes for illumination: the larger the illuminated area, the lower the thermal dissipation and the higher the temperature. Figure 5.15 displays the change in I_{sc} after the exposure to different power densities for illumination with 400, 800 and 1400 µm pinhole diameters. The decrease is stronger and the recovering occurs later for the smallest area (400 µm). It is consistent with a thermal explanation of the I_{sc} recovery. The creation of defects should only depend on the power density. No difference is expected between all illuminated areas under the same illumination density. However, the temperature differs. More defects are annealed when the temperature is the highest (in the largest illumination area). Consequently, the recovery is faster. The cell used for the 1400 µm measurement shows no initial decrease of I_{sc}. We think it was already degraded by light exposure before measurements.

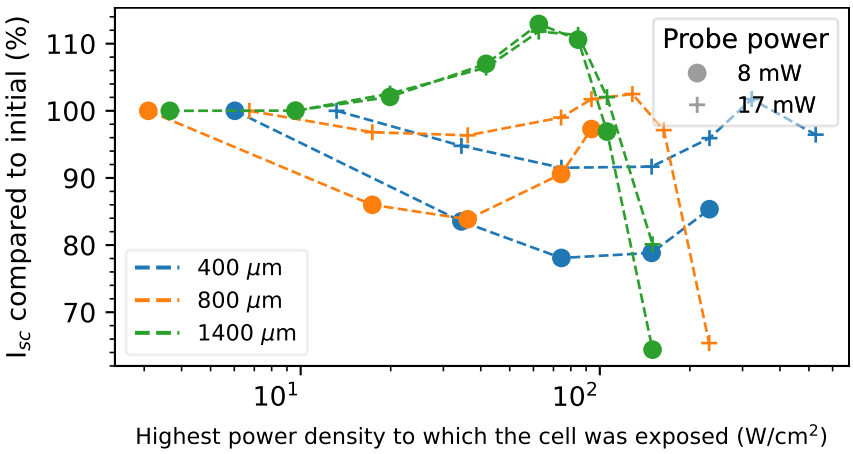

Figure 5.15: Irreversible change in the relative short-circuit current I_{sc} after exposure to different illumination levels for the NW cells and different diameters of pinhole: 400 µm (blue), 800 µm (orange) and 1400 µm (green). The symbols refer to the probe power. Only two probe powers are displayed, 8 mW (●) and 17 mW (+). The corresponding power density differs for each pinhole.

Temperature estimation from comparison with literature The recovery of I_{sc} depends on the temperature and duration of annealing. The annealing rate decreases with time and an annealing of defects close to complete requires at least 2 hours at 140 °C. Shorter times are needed at higher temperatures [Stutzmann 1985]. The 3 W/cm² probe power shows a > 95 % recovery in I_{sc} between 36 W/cm² and 94 W/cm². As 5 measurements with a power density higher than 36 W/cm² were performed between

these measurements, the recovery corresponds to an annealing time around 10 min, i.e. a rather short time. These approximate values suggest that the temperatures reached inside a-Si:H were quite high, above 160 °C. Both because of the heat dissipation through the edge of the illuminated surface and because of the gaussian shape of the laser beam, the temperature is expected to be inhomogeneous. Such a recovery (close to 100 %) indicates that a large part of the illuminated surface is affected by this high temperature.

Light- and current-induced recoveries are dismissed because they rely on lower (illumination or current) levels than the ones leading to degradation [Gleskova 1993, str 1991]. In contrast, our cells are exposed to increasing illumination and current densities. Higher injection levels are expected to increase the amount of defects, not to assist their recovery. Nonetheless, Carlson et al. showed that heating under a reverse bias accelerates the recovery [Carlson 1998]. The change in the applied voltage during the I-V measurement makes the estimation of temperature less accurate.

5.4.4 Comparison with flat a-Si:H

The SWE is one of the strongest limitations in the use of a-Si:H in solar cells and its mitigation has been the focus of many works [Guha 1981], with a renewed interest due to its use in SHJ cells [El Mhamdi 2014]. For flat a-Si:H solar cells, one of the possibilities is the reduction of the absorber thickness, since the shorter collection length induced by the SWE would remain longer than the thickness [Smith 1985]. Si NW/a-Si:H have a rather thin absorber layer (∼100 nm), but they still show a significant change in I_{sc} under illumination.

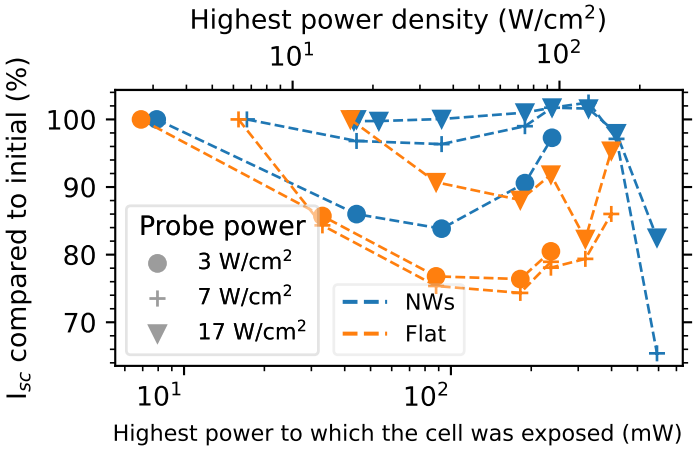

Figure 5.16: Irreversible change in the relative short-circuit current I_{sc} after exposure to different illumination levels for the Si NW/a-Si:H cell (blue) and the flat a-Si:H cell (orange). The results for three probe powers (3 W/cm², 7 W/cm², 17 W/cm²) are displayed with different symbols. A 800 µm pinhole is used.

For comparison, I measured a flat a-Si:H solar cell under the same conditions. Its intrinsic layer is twice as thick compared to the Si NW/a-Si:H (∼90 nm vs. 200 nm). The change in I_{sc} is plotted for both in Figure 5.16. The minimal I_{sc} value for the flat cell is substantially lower than for the NW cell (75 % compared to 84 %). Because the initial current is higher for the flat cell (3.4 mA (flat) compared to 1.6 mA (NWs) under

17 W/cm^2 illumination), the absolute decrease is even stronger. In addition, the final increase is observed for both cells, but later (higher illumination levels) for the flat cell. In particular, for the probe power of 17 W/cm^2 no initial decrease is seen for the NW cell, while the flat a-Si:H looses at least 10 % of its I_{sc} value.

Two reasons can explain these differences. The absorber thickness of the Si NW/a-Si:H is half the thickness of the planar cell. Hence, for the same degradation rate, the performance of Si NW/a-Si:H cells remains better. In addition, the thermal behavior of both devices can differ. The heat dissipation is expected to be easier in the flat a-Si:H cell thanks to lateral conduction in the different layers. In Si NW/a-Si:H, lateral conduction is more difficult due to the morphology. While this may be an issue, here it enables an annealing of the defects at lower illumination, which mitigates the degradation.

5.4.5 Summary

Under moderate illumination (starting below 10 Sun), a decrease of I_{sc} is observed for cells with a-Si:H, either NWs or flat ones. It is typical of the Staebler-Wronski effect in a-Si:H, where light-soaking leads to the formation of new recombination centers. Because of the high powers, short times are sufficient for degradation. Thanks to the thinner absorber of Si NW/a-Si:H solar cells, this degradation is reduced compared to the planar cell. The SWE should reduce the fill-factor as well as the current, but an increase is observed. It is likely related to the already low FF value, which is strongly dependent on the current intensity. The I_{sc} decrease is not reversible with time, but a recovery is observed when the total illumination (power and time) is increased. It is due to the in-situ annealing that can occur when the heat from illumination is not well dissipated. The estimated time for annealing is short (∼10 min), which suggests that high temperatures (>160 °C) are reached based on the literature results. These thermal effects are stronger in NWs compared to a flat cell, which results in a quicker recovery of the initial current.

5.5 Reversible decrease of V_{oc}

As can be seen in Figure 5.11, Si NW/a-Si:H solar cells presented a significant decrease of V_{oc} starting from a certain illumination, although a continuous logarithmic increase with the illumination is expected. To better understand this observation, we briefly remind the origin of a logarithmic increase. A change in the material, the high injection of carriers or the increase of temperature are possible reasons. I-V measurements under constant illumination combine all phenomena. To sort out the one responsible for the V_{oc} decrease, other characterizations are needed.

5.5.1 V_{oc} behavior under high illumination

One-diode model The logarithmic increase of V_{oc} is clear from the one-diode model (Section 1.1.5). If the shunt resistance is large[8] and neglecting the unity term, the V_{oc} dependence on the photocurrent I_ϕ is logarithmic. With a reference illumination P^0_{ill} for which the photocurrent is I^0_ϕ, the open-circuit voltage under illumination P_{ill} is

[8] $V_{oc}/R_{sh} \ll I_\phi$ and $V_{oc}/R_{sh} \ll I_0 e^{qV_{oc}/k_B T}$.

$$V_{\mathrm{oc}}(P_{ill}) \simeq V_{\mathrm{oc}}(P^0_{ill}) + \frac{n_{id} k_{\mathrm{B}} T}{q} \ln\Big(\frac{I_\phi}{I^0_\phi}\Big). \tag{5.4}$$

The photocurrent is often assumed to be linear with the illumination power, which results in a logarithmic dependence of $\mathrm{V_{oc}}$ on the illumination power P_{ill}. As long as the shunt resistance is large enough, $\mathrm{V_{oc}}$ is not affected by the series resistance.

The equivalent circuit relies on the superposition principle, which assumes that the total current is the sum of the photocurrent and the diode current. In particular, no dependence of the photocurrent I_ϕ on the voltage across the cell is considered, which is a strong limitation of the model for some materials or illumination conditions.

Quasi-Fermi levels The increase of the open-circuit voltage $\mathrm{V_{oc}}$ with illumination comes from the increase of the densities of excited carriers and the resulting higher potential of electrons and holes. From the band diagram perspective, an increase of the generation rate and of the n and p densities results in a stronger splitting of the quasi-Fermi levels, $E_{F_n} - E_{F_p}$. The maximal voltage that can be extracted directly depends on the voltage at the junction V_{jn}

$$V_{jn} = E_{F_n} - E_{F_p}. \tag{5.5}$$

When the Boltzmann approximation is valid (quasi-Fermi levels inside the band gap, a few $k_{\mathrm{B}}T$ from the band edge), and with N_c and N_v the effective densities of states, respectively in the conduction and valence bands,

$$V_{jn} = E_c - E_v + k_{\mathrm{B}} T \ln\Big(\frac{np}{N_c N_v}\Big). \tag{5.6}$$

The densities of excess carriers increase with the illumination level, in an almost linear way if the Shockley-Read-Hall (SRH) mechanism is the most important one. Consequently, a logarithmic increase of $\mathrm{V_{oc}}$ should be first observed. Yet, if the radiative or Auger recombinations become the main mechanism of recombinations, the increase of the densities of excess carriers is lower than the increase of the generation rate. Hence, a smaller increase of $\mathrm{V_{oc}}$ than the logarithmic one is expected.

Deviation from the Boltzmann distribution Under very strong illumination, the quasi-Fermi levels are expected to reach the bands. If the quasi-Fermi level is deep into the corresponding band, the Fermi integral can be approximated as $F_{1/2}(x) \simeq {}^4/_{(3\sqrt{\pi})} x^{3/2}$ [Grundmann 2006], and

$$V_{jn} \simeq E_c - E_v + k_{\mathrm{B}} T \Big(\frac{3\sqrt{\pi}}{4}\Big)^{2/3} \Big[\Big(\frac{n}{N_c}\Big)^{2/3} + \Big(\frac{p}{N_v}\Big)^{2/3}\Big]. \tag{5.7}$$

In this case, the expected increase of $\mathrm{V_{oc}}$ would be larger than the logarithmic one. This approximation should be used for a density of charge carriers larger than the effective density of states in the conduction band. Values for N_c in the range 10^{19}-$5\times10^{20}\,\mathrm{cm^{-3}}$ are usually considered for a-Si:H [Misiakos 1988, Levtchenko 2018]. Such densities of charge carriers can be expected with the illuminations used in our experiments. It should be noted that this approximation of the Fermi integral has been derived for a parabolic band edge, which is not the case in a-Si:H. Even if we do not consider the exponential band tails, the Density Of States (DOS) in a-Si:H is linear with

the energy (see Section 5.1.4). In real conditions, recombinations, resistance or thermal effects limit the V_{oc} increase under high illumination, and an increase to the power of $^2/_3$ is not observed. Nonetheless, it is still relevant to remember that the logarithmic increase of V_{oc} is related to the Boltzmann distribution.

5.5.2 Decrease of V_{oc} observed for Si NW/a-Si:H and flat a-Si:H

In contrast with these expectations, Si NW/a-Si:H solar cells presented a smaller than logarithmic increase under moderate illumination and even a significant decrease of V_{oc} under stronger illuminations (beyond 40 W/cm^2 for the 800 µm pinhole), as can be seen in Figure 5.17. When probing back V_{oc} with lower illuminations, no change was observed, which proves that the decrease only depends on the present illumination level and does not correspond to an irreversible change in the material. In addition, as displayed in Figure 5.17, the same measurements on a flat a-Si:H cell showed a similar decrease, while the V_{oc} of the c-Si kept increasing until it reached a limitation value of 0.61 V (the saturation can stem from recombination mechanisms, for instance Auger recombinations). Hence, the NW morphology is not the main reason for the V_{oc} decrease.

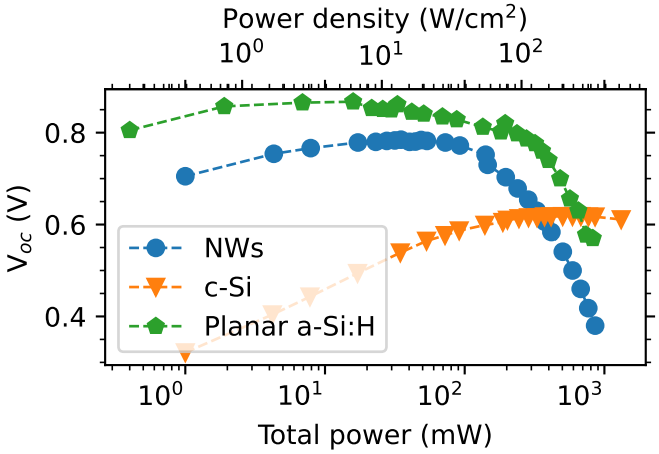

Figure 5.17: Change in V_{oc} with illumination power for solar cells made of Si NW/a-Si:H, flat a-Si:H or c-Si. A 800 µm pinhole is used.

The decrease of V_{oc} can be due to an increase of recombinations. A higher recombination rate can stem from larger densities of charge carriers, as is observed with Auger recombinations. A higher temperature also facilitates recombinations. Time- and area-varying measurements help to distinguish between the two.

5.5.3 Auger recombinations

Limiting the performance of solar cells The value of V_{oc} is usually related to the recombination rates in the cell. Distinction is made between intrinsic recombinations (radiative and Auger recombinations) and recombinations due to the material defects, either in the bulk or at interfaces. Different mechanisms show different dependencies

on the density of charge carriers. In particular, the Auger recombination rate strongly increases with the carrier densities and can become the major contribution under strong illumination. It corresponds to a recombination involving three charge carriers, two that recombine and a third one that takes the released energy (and the change in momentum in crystalline materials). The effect on the performance of the solar cell is mostly a limitation in V_{oc}, possibly I_{sc}, with increasing power [Sinton 1987]. No decrease of values is expected with increasing illumination intensity.

Dependence on material In addition, although Auger recombinations are expected to occur in every material, the consequences depend on the other recombination rates[9]. As mentioned in [Vossier 2010], Auger recombinations are more significant in materials with an indirect bandgap since their radiative recombination rates are very low. For instance, in c-Si, Auger limitation has already been observed for 100 Suns, which could account for the saturation observed in Figure 5.17.

Auger recombinations in a-Si:H Not much literature can be found on Auger recombinations in a-Si:H. There are two likely reasons for it. First, the study of a-Si:H under strong illumination is not so frequent. In addition, potential Auger effects would be difficult to evidence due to the high rate of trap-assisted recombinations. Because the latter are much lower at low temperatures (mostly localized states are filled, which prevents carriers from reaching recombination centers), other mechanisms can be highlighted. In particular, a quenching in the PL signal has been attributed to Auger recombinations [Street 1981, Esser 1990] (respectively for excitations $\geq 10^{20}\,cm^{-3}s^{-1}$ or excess carrier densities $\geq 5\times10^{18}\,cm^{-3}$). In both cases, it was considered as a bimolecular process involving two geminate pairs[10]. However, there is still controversy regarding this attribution [Vollmar 1993, Shkrob 1998]. In any case, it seems dubious that Auger recombinations have a significant impact at higher temperatures (beyond 250 K, sufficient to overcome the band tail [Mott 2012]). Finally, Zhai et al. have included Auger recombinations in their FEM simulations of a-Si:H and a-Si:H/μc-Si:H:H NW solar cells [Zhai 2015]. The change in V_{oc} from the Auger recombinations in a-Si:H was negligible (30 mV in a-Si:H compared to >180 mV in μc-Si:H). Yet, the value used for the Auger coefficient ($10^{-30}\,cm^6s^{-1}$) may not be reliable. It is higher but rather similar to the coefficient in c-Si, unfortunately no source or explanation is given.

5.5.4 Pulsed vs. continuous illumination

To assess the potential thermal effect, we performed V_{oc} measurements under pulsed and continuous illumination with a diode laser (520 nm). The beam had a $1/e^2$ diameter around 0.3 mm (total diameter around 0.75 mm). The pulsed illumination had a 10 Hz frequency with a 1 ms pulse duration. The voltage was measured with an oscilloscope. Its sampling frequency ensured a relevant temporal resolution and its high impedance the open-circuit condition.

Figure 5.18 shows the change in V_{oc} depending on the illumination power for a continuous and a pulsed illuminations. For lower powers (around $10\,W/cm^2$), the V_{oc}

[9] Besides, the governing coefficient may differ. Still the order of magnitude for c-Si, GaAs, is similar, may be due to a limited knowledge.

[10] e^-/h^+ pairs stemming from the same generation mechanism.

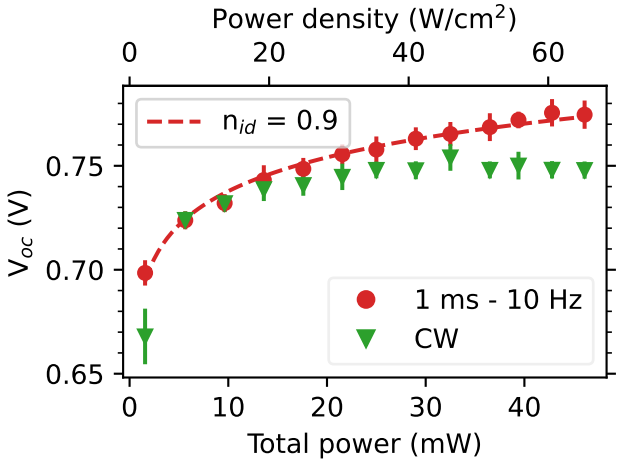

Figure 5.18: V_{oc} depending on power, either with continuous illumination (CW) or cycled illumination (1 ms at 10 Hz). The average value is displayed with the standard deviation. A logarithmic fit of the pulsed measurements following the one-diode model (Eq. (5.4)) is also shown. The very low value for the continuous illumination at 2 mW is attributed to a difference in the actual output of the laser diode between the two measurements, since it is very close to the onset of lasing. The dispersion was not taken into account for the fit.

values overlap. However, when the power increases, the continuous illumination results in lower V_{oc} compared to the pulsed illumination. Repeated measurements showed that it is reversible. The comparison of pulsed and continuous illuminations proves that a mechanism taking place on a timescale larger than 1 ms is responsible for the reversible decrease of V_{oc}. In particular, this allows us to discard the effect of Auger recombinations in a-Si:H up to 65 W/cm^2 illumination. The role of trapped carriers is also to be dismissed, since carriers are likely to be (fully or significantly) trapped on a timescale shorter than 1 ms. Hence, this difference should be attributed to a local increase of temperature.

Logarithmic fit With the pulsed illumination, the dependence of V_{oc} on the illumination power is similar to the expected behavior, as the fit with Eq. (5.4) highlights. An ideality factor close to 1 is obtained. This is surprising as the ideality factor of a-Si:H solar cells is usually higher, due to numerous trap-assisted recombinations [Kind 2011]. Yet, I-V curves are mostly used to determine the ideality factor, which likely affects its value.

Thermal diffusion in a-Si:H is expected to be slow and if it is responsible for the V_{oc} decrease, it should be possible to monitor the change in V_{oc} with time when the shutter is open.

5.5.5 Time variation of V_{oc}

For a given setup, we measured both the change in the open-circuit voltage with time (25 ms time resolution) and the full I-V curve.

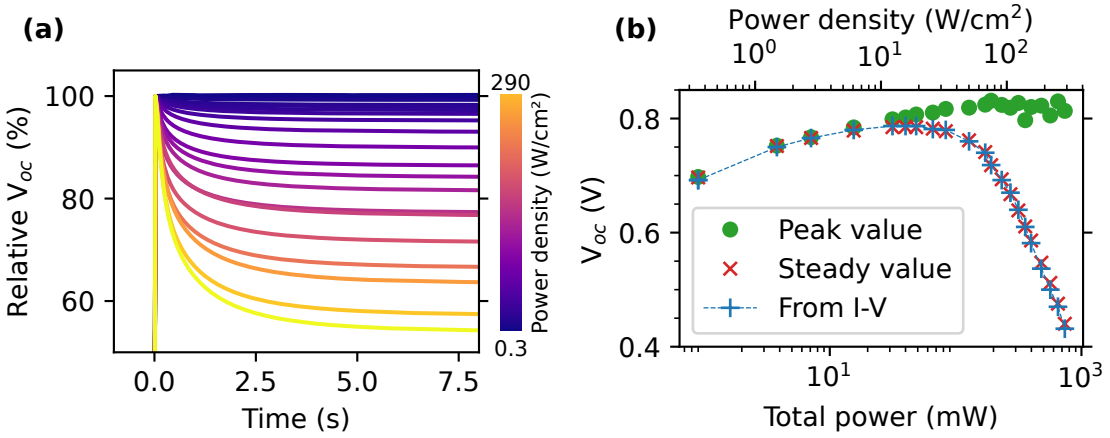

Figure 5.19: **(a)** Relative V_{oc} change with time. The shutter is open at $t = 0$ s. **(b)** V_{oc} against power when measured either from I-V curve, from the peak value or from the steady value (> 15 s) in **(a)**. The pinhole is 800 µm.

Figure 5.19 **(a)** shows the relative change in V_{oc} for increasing powers. When the shutter is opened, a peak value is reached, which slowly decreases with time (3-3.5 s are needed to carry out 95 % of the change). The decrease cannot be well described by an exponential decay. The relative decrease is more significant when the illumination increases. Repeated measurements show that this slow decay is reversible.

Comparison with values from I-V curves It clearly appears that different values for V_{oc} could be considered, in particular the peak value (right after the start of illumination) and the steady value (at the end of the decrease). We compared both with the values obtained from the I-V curves. For each power, the I-V curve was recorded, followed by the dependence of V_{oc} on time. Thus, the history of the cell is almost the same in both cases. The values are plotted in Figure 5.19 **(b)**.

First, the IV-V_{oc} values correspond perfectly to the steady values. It is expected, since the I-V recording is rather slow and thus corresponds to a steady-state. In addition, while the IV- and steady values decrease with increasing illumination, the peak value keeps on increasing, as expected. It is similar to the behavior observed with pulsed illumination and indicates that thermal effects are observed when measuring I-V curves. The variations at very high power are due to the limited temporal resolution of our recording. The actual peak occurs between two measurements and an already degraded value is considered as peak value. The effect is significant at high illuminating powers, where the change in V_{oc} is fast.

Camera I used an infrared (IR) camera (Compact camera from Seek Thermal, framerate between 5-8 Hz) to monitor the (relative) change in the surface temperature with time during the change in V_{oc}. I observe a rather long stabilization time, close to a few seconds.

Figure 5.20 displays the change with time in V_{oc} as well as some temperature maps. It appears that the change in temperature with illumination is rather slow. This can come from the poor thermal conductivity of a-Si:H or from the glass substrate. In

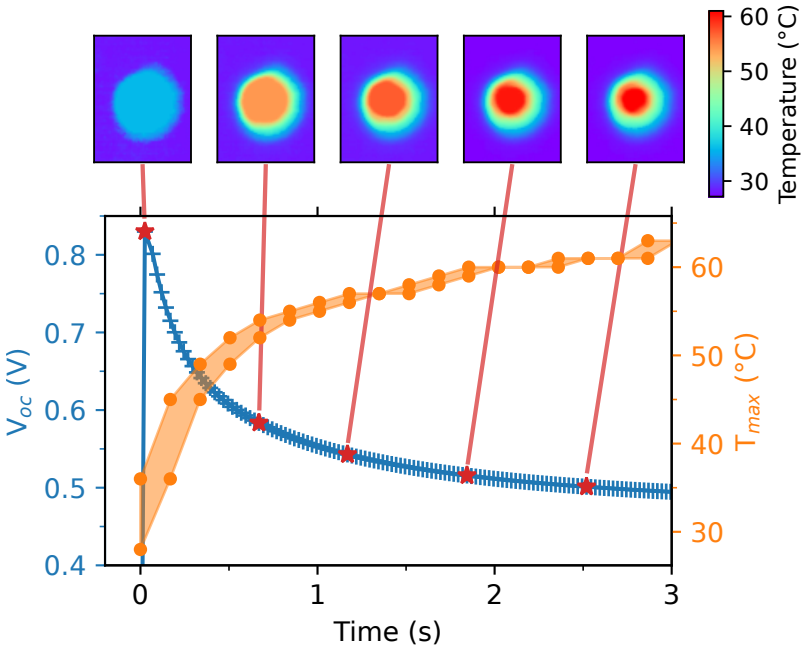

Figure 5.20: Change with time of V_{oc} and the maximal surface temperature measured with an IR camera. Some temperature maps of the cell corresponding to different times are displayed. They show the area that is heated by the laser (∼1.3 mm in diameter, larger than the beam, smaller than the cell which cannot directly be seen on these maps). The shutter is open at $t = 0$ s. Due to the rather low framerate of the camera, there is an uncertainty on the initial time for the temperature change. It is shown as the shaded orange region. The pinhole is 800 µm and the power density is 260 W/cm^2.

addition, the timescales for the change in V_{oc} and temperature are very similar, which confirms the origin of the observed change. Because the light was absorbed rather deep (mostly in a-Si:H, below 240 nm ITO) and we measured the surface temperature, the actual heating close to the junction was probably faster than the observed variation in temperature. However, the vertical heat conduction through the ITO layer is probably easier than the lateral one between nanowires. Consequently, the observed change would give a correct estimation of the heating timescale at the junction.

V_{oc} compared to the temperature Figure 5.21 **(a)** displays the maximal surface temperature depending on the shining power. Above a threshold (100 W/cm^2), the increase of temperature is linear with the power as is expected [Yuan 2009]. Even though the measured temperature is lower than the actual temperature of carriers, we assume that they remain proportional. Thus, the relative change should be relevant. The decrease of V_{oc} compared to the maximal temperature reached at each illumination power follows a linear behavior, with a slope of 8.7 mV/K. Here we attribute the whole change in V_{oc} to the temperature, although it is also impacted by the illumination level, but to a much lesser extent (see Figure 5.19). This value is commented in Section 5.6.5. I planned the same measurements with a flat a-Si:H solar cell, but the flat a-Si:H cell presented a S-shape, which strongly affected the V_{oc}value.

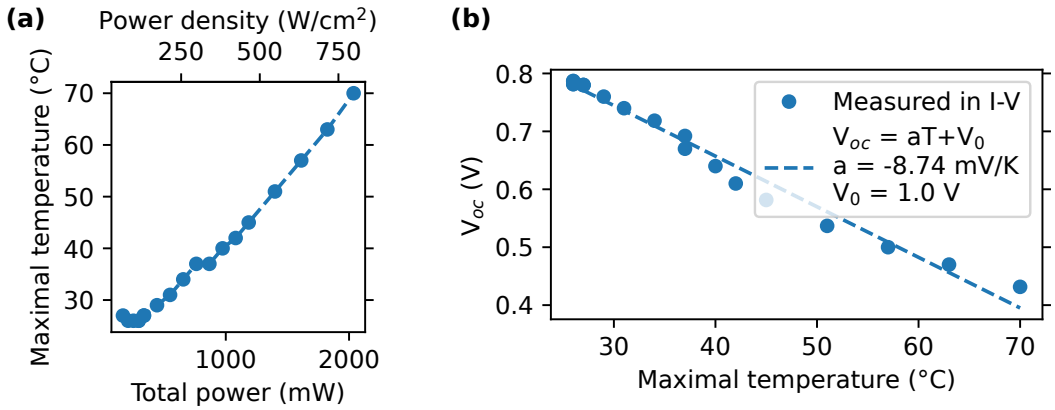

Figure 5.21: **(a)** Change in the maximal surface temperature measured with the IR camera depending on the illumination power. **(b)** V_{oc} against maximal temperature measured at the surface for each illumination power shown in **(a)**. The pinhole is 800 µm.

5.5.6 Area dependence

To characterize the thermal effects, the illuminated area can also be changed. I used three different pinhole diameters, 400 µm, 800 µm and 1400 µm (with $1/e^2$ diameters of 0.026 mm, 0.057 mm and 0.97 mm).

Figure 5.22 **(a)** presents the value of V_{oc} depending on the averaged power density. The larger the beam diameter, the earlier the V_{oc} decrease. The V_{oc} behavior is thus not governed by the local amount of charge carriers. If we consider it as a 2D problem, the ratio between the edge, where the heat dissipation occurs, and the illuminated surface

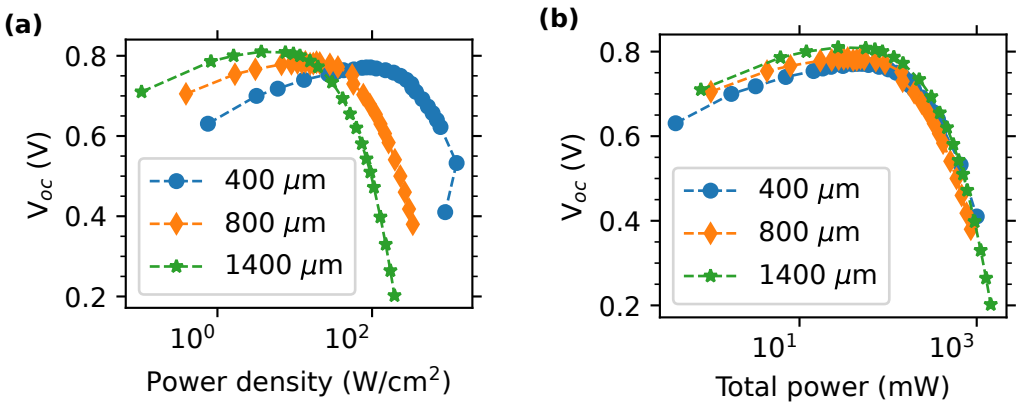

Figure 5.22: V_{oc} of Si NW/a-Si:H solar cells for three pinholes, 400 µm, 800 µm and 1400 µm. The open-circuit is plotted against **(a)** the averaged power density, **(b)** the total power.

follows $1/r$. When the illuminated area increases, the ratio decreases and heat dissipation is more difficult. The same trend is observed for c-Si, where a very small decrease can be seen for the two larger illumination beams (around 20 mV starting at ~100 W/cm^2 for 1400 µm). In contrast, when plotted against the total power (Figure 5.22 **(b)**), the three lines seem to overlap. It seems that V_{oc} mostly drops with the total amount of energy in the beam, the illuminated area is less important.

5.5.7 Summary

A strong decrease of V_{oc} (over 400 mV) is observed for Si NW/a-Si:H solar cells under strong illumination, when a logarithmic increase is expected. It is reversible and not related to material damage. It occurs in flat a-Si:H as well, but to a lesser extent. A small decrease is observed for very high illumination powers in c-Si (below 25 mV). The comparison between a pulsed and a continuous illuminations proves that the decrease corresponds to a phenomenon taking place on a timescale larger than 1 ms, most likely heating. The monitoring with time of V_{oc}, as well as the change in the thermal temperature with an IR camera, shows that the decrease of V_{oc} occurs at the same time as the increase of temperature in the cell, over 3-4 s. The maximal value of V_{oc} (obtained at $t = 0$ s before heating takes place) keeps on increasing as expected. The V_{oc} decrease occurs earlier and is stronger for larger illuminated areas, which confirms the thermal origin.

5.6 Measurements of temperature in the a-Si:H p-i-n junction

5.6.1 Thermocouple

A thermocouple could be used for the measurement. However, it raises many issues. First, only the surface temperature would be measured. In addition, the sensor should be positioned on the illuminated area and would change the illumination. A very small sensor would be needed. Finally, the surface of the cell is nanostructured, which makes

even more difficult the fabrication of such a sensor, with a good thermal contact. For these reasons, we dismissed this solution.

5.6.2 IR camera

In order to assess the increase of temperature under strong illuminations, I first used an IR thermographic camera. However we cannot fully rely on the obtained values. First, the measured temperature is at best an estimation of the surface temperature, and is probably below the actual temperature of carriers. In addition, the amount of IR waves that exit a material for a given temperature strongly varies with the emissivity of the material. It can lead to discrepancies between materials. Hence, to determine the temperature of carriers in a-Si:H, we considered photoluminescence and Raman characterizations.

5.6.3 Photoluminescence

Principle Analysis of Photoluminescence (PL) spectra can be used to determine the temperature of the carriers of a solar cell [Abou-Ras 2016]. The expected PL signal can be derived from the distribution of carriers in the bands and the radiative recombination coefficient. The latter can be related to the absorption coefficient of the material, α, through the detailed balance at thermal equilibrium. If thermalization is fast enough to ensure an intraband thermal equilibrium, quasi-Fermi levels can be defined and the PL signal depends on the quasi-Fermi level splitting, $\Delta\mu$. The generalized Planck's law is obtained, valid under illumination (i.e. outside of thermal equilibrium). The PL signal emitted at an energy E is

$$PL(E) = \frac{1}{4\pi^2\hbar^3c^2}\frac{\alpha(E)E^2}{\exp\left(\frac{E-\Delta\mu}{k_BT}\right)-1}. \tag{5.8}$$

The absorption coefficient and the quasi-Fermi level splitting are often unknown. Possible solutions are a full fit of the spectra [Chen 2021b], or the use of both sides to first determine α, then $\Delta\mu$. When the temperature is a supplementary unknown value, a ratio of the spectrum of interest with a reference one is possible [Paire 2011][11],

$$\frac{PL(E)}{PL_{\text{ref}}(E)} = \exp\left[\frac{E-\Delta\mu}{k_B}\left(\frac{1}{T_{\text{ref}}}-\frac{1}{T}\right)\right]. \tag{5.9}$$

PL of a-Si:H Amorphous silicon displays a broad peak centered around 1.4 eV, which is attributed to recombinations between the band tails[12]. The peak is rather broad even at low temperature (0.3 eV width), due to the extension of the band tails [Austin 1979, Street 1991]. A defect peak can also be observed around 0.9 eV, whose intensity depends on the preparation of the sample, for instance on the doping. Photoluminescence studies of a-Si:H are often done at low temperatures, because the PL efficiency weakens at higher temperatures [Engemann 1976]. Carriers are indeed excited to the extended states, which makes it easier to find other, non-radiative, recombination paths.

[11] There seems to be a missing "-" in [Paire 2011]

[12] Energy matches, increases when defect density decreases, and long recombination times suggest localized states.

PL cannot be used for temperature estimation of a-Si:H Although the PL signal is most interesting for the estimation of the temperature closest to the junction, it cannot be used for a-Si:H, for practical and more fundamental reasons. We tried to record the PL signal of Si NW/a-Si:H solar cells with micro-PL and 532 nm excitation at room temperature, but we were not able to distinguish any signal, despite the use of a good collecting setup and long acquisition times. In addition, even if this very low signal could be recorded, the broad peak would prevent a precise estimation of temperature. Finally, the filling of tail states in a-Si:H leads to a strong change in the absorption (low DOS in the band tails and rapid change in DOS with energy). Hence the absorption coefficient does not depend only on the photon energy, but also on the QFLS. A modified law has to be used to take into account this change [Wong 2021]. It is particularly significant for amorphous semiconductors, where band tails are important.

5.6.4 Raman scattering

Because of the low PL signal of a-Si:H, we looked for other methods to determine the temperature. As Raman scattering enables to probe some vibration modes in the material, an increase of temperature is expected to result in a broadening of the peak and a decrease in the Raman shift.

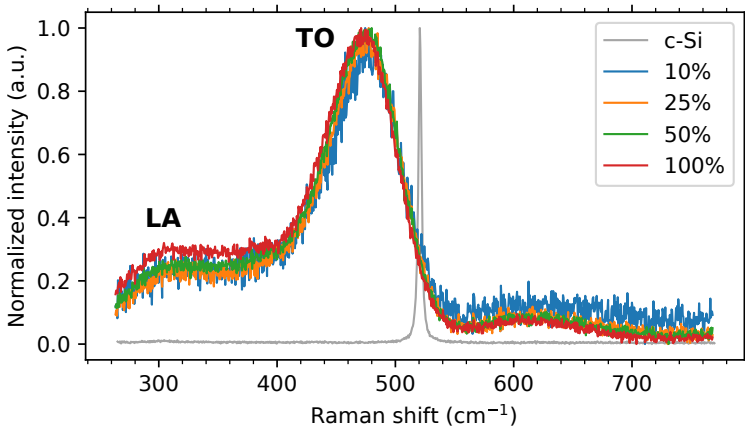

Figure 5.23: Raman scattering signal of Si NW/a-Si:H solar cell under 532 nm illumination. The 100 % intensity corresponds to a power density around 2 kW/cm^2. The solar cell has 80 nm of ITO as the top contact, but comparison of the Raman signals with and without ITO did not show any difference. Transverse optical (TO) and longitudinal acoustic (LA) modes are shown.

We measured the Raman scattering of 532 nm light from the Si NW/a-Si:H solar cells[13]. As displayed in Figure 5.23, a peak is obtained around 470 cm^{-1}, corresponding to the TO (transverse optical) mode in a-Si:H. The low-intensity peak around 310 cm^{-1} is related to the LA (longitudinal acoustic) phonons [Zhigunov 2018, Viera 2001] . Due to the amorphous feature of a-Si:H, broad peaks are observed. We do not see any signal from the c-Si core. It is likely too low compared to the a-Si:H one because of the small

[13]No crystallization is observed, although a lower power density (1.2 kW/cm^2) resulted in crystallization in another setup (see Section 5.8.2). This apparent discrepancy comes from the very different illumination areas (400 µm vs. ∼20 µm diameters) and resulting temperature increases.

amount of material of the (thin) c-Si NWs and may be limited by the short absorption length of the green light in a-Si:H.

Successive measurements under increasing illumination in Figure 5.23 present indeed a very slight decrease in the Raman shift, as was reported for a-Si:H [Viera 2001] or for c-Si [Piscanec 2003]. They confirm an increase of temperature under illumination, but the change is small and cannot allow for a sufficiently precise estimation of the temperature.

5.6.5 Change in performance parameters with temperature

I was not able to precisely determine the temperature inside the p-i-n junction under laser illumination. Instead, I separately assessed the effect of heating on Si NW/a-Si:H solar cells.

5.6.5.1 Experimental details

I tested the thermal behavior of Si NW/a-Si:H solar cells under limited illumination. The samples were placed on a thermally conductive substrate holder. The measurements were done in air, in a closed chamber. I heated the substrate holder up to 140 °C. The sample experienced a continuous slow heating from the backside. I did not assess the temperature of the sample, but I monitored the variation in the supplied power and recorded I-V curves once the power was steady (waiting times 10-20 min). I used a 520 nm laser diode for the illumination. Both cells are illuminated over a 2 mm area. While it corresponds to the whole Si NW/a-Si:H solar cell, it is a small part of the c-Si one. It accounts for the low V_{oc} that I measured.

5.6.5.2 Strong decrease of V_{oc} and FF

Figure 5.24 displays the I-V curves for a Si NW/a-Si:H and a c-Si solar cell under heating. The most affected parameters are V_{oc} and the FF, both for Si NW/a-Si:H and c-Si cells. I_{sc} does not present any significant change. The shunt resistance in the Si NW/a-Si:H solar cells remains the same, while it decreases for c-Si. Measurements during cooling down (not shown) proved that the change in V_{oc} is reversible, as well as the decrease in R_{shunt} for c-Si.

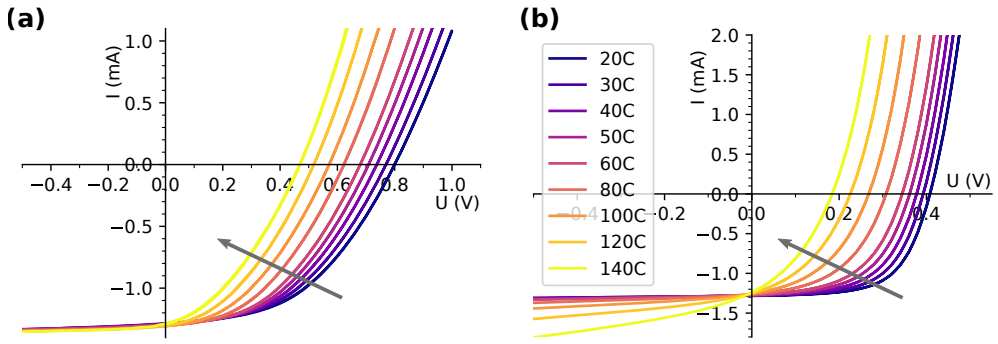

Figure 5.24: I-V curves under 520 nm illumination for increasing temperature for **(a)** Si NW/a-Si:H and **(b)** c-Si solar cells.

In the Si NW/a-Si:H solar cell, the magnitude of the decrease of V_{oc} (300 mV over 100 °C) confirms the strong effect of temperature on the open-circuit voltage and suggests that it plays a significant role in the high-illumination measurements, as discussed in detail in Section 5.6.5.3. The fill-factor is decreasing as well. Since R_{se} and R_{shunt} remain constant (at least for Si NW/a-Si:H), the increase of the recombination rates with temperature is likely responsible. In literature, an increase of the fill-factor of a-Si:H solar cells with temperature has been reported [Carlson 2000]. In planar a-Si:H cells, the collection of carriers is indeed strongly limited because of poor diffusion lengths. This limitation is reduced with increasing temperature. However, in Si NW/a-Si:H cells, the collection of carriers is not limited by the absorber, but by the top contact. Hence, we do not expect an improvement of the fill-factor with temperature.

In the c-Si solar cell, we observe a lower R_{shunt} under increasing temperature. The current under reverse bias becomes much higher than the (rather constant) short-circuit current. Hence, we believe that the change is mostly due to an actual change in the shunting paths and only partially to a lower collection efficiency.

5.6.5.3 Temperature dependence of V_{oc} in a-Si:H solar cells

Theoretical dependence The decrease of the open-circuit voltage with temperature comes from the increased recombinations compared to the generation rate. A derivation based on the equivalent circuit model of solar cells, on the common dependency of recombination mechanisms on the *np* product [Green 2003], or on the external radiative efficiency[14] [Dupré 2015] leads to the following expression

$$\frac{dV_{oc}}{dT} = \frac{1}{T}\left(V_{oc} - \frac{E_g^0}{q}\right) - \frac{\gamma k_B}{q}. \tag{5.10}$$

The meaning of γ depends on the model. For the equivalent circuit model of solar cells, $\gamma \simeq 3$. In addition, the changes in the band gap energy and photocurrent with temperature are dismissed. More complex expressions of γ are used in [Green 2003] and [Dupré 2015], and the band gap energy refers to the value linearly extrapolated at 0 K.

When the expression is derived from the *np* product, the γ value is close to 3 and the last term is 0.26 mV/K. In addition, V_{oc} is lower than E_g and the term in brackets is negative. For the best c-Si cells (V_{oc} around 0.75 eV), we find a decrease of 1.2 mV/K at 300 K. In a-Si:H, if this expression holds, the difference between the band gap energy and the open-circuit voltage is particularly large (0.9 eV vs. 1.7 eV) and the first term corresponds to a decrease of 2.7 mV/K.

Temperature coefficient Over the temperature ranges assessed (typically 20-60 °C), the change can be considered linear. To compare the sensitivity to temperature of each performance parameter and of different materials, a single value is then needed. A relative temperature coefficient, β (often given in %/°C), can be used. The reference value corresponds to $T_0 = 298K$. For V_{oc},

[14] With the external radiative efficiency, the total recombination current can be replaced by the radiative recombination current. Its expression can be derived from thermodynamic considerations.

$$\beta_{V_{oc}}(T_c) = \frac{1}{V_{oc}(T_0)} \frac{V_{oc}(T_c) - V_{oc}(T_0)}{T_c - T_0}. \tag{5.11}$$

The power conversion efficiency is given by

$$PCE = V_{oc}\, I_{sc}\, FF. \tag{5.12}$$

If the coefficients β are sufficiently small, we can neglect second order terms and the overall change in the power conversion efficiency can be easily written,

$$\beta_{PCE} \simeq \beta_{V_{oc}} + \beta_{I_{sc}} + \beta_{FF}. \tag{5.13}$$

Consequently, the efficiency of Si NW/a-Si:H and c-Si solar cells decreases with temperature, mostly because of the change in V_{oc}. An absolute temperature coefficient can also be found,

$$TC_{V_{oc}}(T_c) = \frac{V_{oc}(T_c) - V_{oc}(T_0)}{T_c - T_0}. \tag{5.14}$$

I obtained the V_{oc} temperature coefficients for Si NW/a-Si:H and c-Si cells from a linear fit, displayed in Figure 5.25. I present a comparison between coefficients in Table 5.2. I did not assess the temperature dependence of V_{oc} for a flat a-Si:H cell because of the S-shape of the I-V curve of the samples. The experimental coefficient (from the fit) and the theoretical one (from Eq. (5.10)) for Si NW/a-Si:H are similar to those reported in literature for a-Si:H. This is not the case for c-Si. Whereas we observe a lower effect of temperature on c-Si compared to a-Si:H, the opposite is expected from literature.

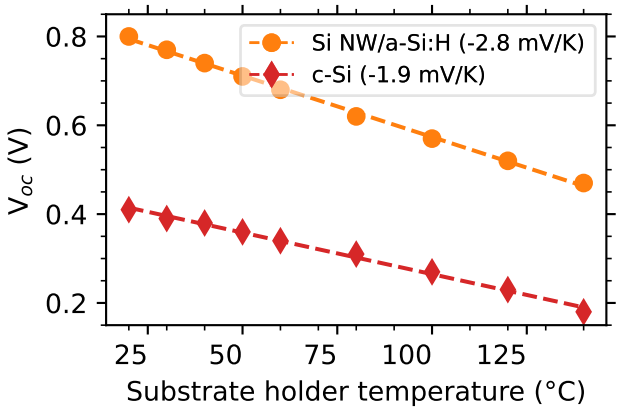

Figure 5.25: V_{oc} change with temperature for Si NW/a-Si:H and c-Si solar cells. A linear fit is added.

a-Si:H performance under heating in literature Figure 5.26 presents the relative change in efficiency and V_{oc} under heating for the main PV technologies. **(a)** shows that the PCE is not linearly dependent on temperature for a-Si:H. In addition, a-Si:H is less sensitive to an increase of temperature than other materials. The similar scale in **(a)** and **(b)** proves that the main parameter which reduces the efficiency under heating is V_{oc}. Yet, the change in the open-circuit voltage of a-Si:H is similar to the other technologies.

Table 5.2: V_{oc} temperature coefficients for a-Si:H and c-Si solar cells. For the values computed from Eq. (5.10) and derived from the fit in Figure 5.25, the reference temperature is 298 K and the open-circuit voltages are ${V_{oc}}^{NWs} = 0.80$ V and ${V_{oc}}^{c-Si} = 0.41$ V. The low value of V_{oc} due to the partial illumination strongly affects the coefficients for c-Si. Because they are not relevant, they are displayed in grey. The references are [a] [Virtuani 2010], [b] [Carlson 2000], [c] [Riesen 2016], [d] [Stiebig 1996], [e] [King 1997].

Material	Origin	$\beta_{V_{oc}}$ (%/°C)	dV_{oc}/dT (mV/°C)
Si NW/a-Si:H	Figure 5.25	−0.35	−2.8
Si NW/a-Si:H	Eq. (5.10)	−0.42	−3.3
a-Si:H	References	−0.25-−0.33 [a, c, d]	−2.9-−4.3 [c, e]
c-Si	Figure 5.25	−0.46	−1.9
c-Si	Eq. (5.10)	−0.64	−2.6
c-Si	References	−0.33-−0.4 [a, b]	−3.8-−4.1 [e]

Its peculiar behavior regarding the efficiency comes from the thermal annihilation of light-induced defects in a-Si:H and the possible increase of the collection length with increased temperature that mostly affects the fill-factor.

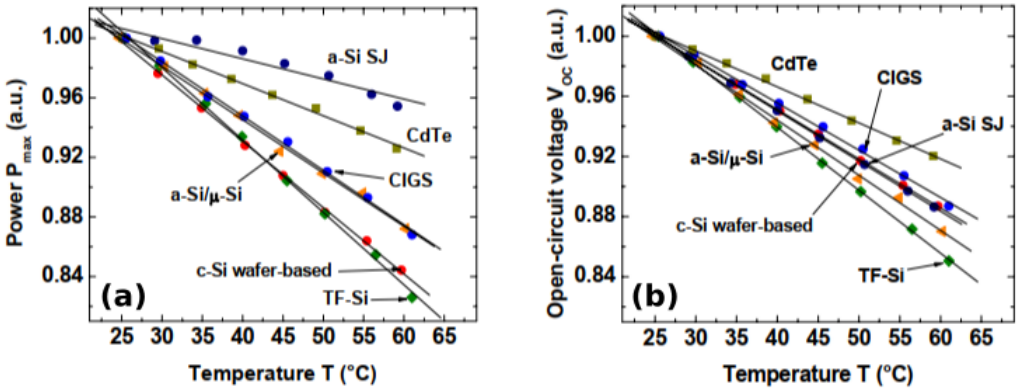

Figure 5.26: Temperature-induced relative change in **(a)** power conversion efficiency and **(b)** open-circuit voltage for different PV technologies under 800 W/m^2 illumination. From [Virtuani 2010].

5.6.5.4 Relation with laser experiments

The decrease of V_{oc} under laser illumination was mostly observed for the amorphous silicon cells. From the I-V measurements under heating, we saw that the open-circuit voltage of Si NW/a-Si:H solar cells is slightly more sensitive to temperature than c-Si. However, it cannot explain the strong difference observed under strong illumination. The increase of temperature is likely much higher in a-Si:H cells than in the c-Si one. It may be due to the low thermal conductivity of a-Si:H compared to c-Si (see Table 5.3),

or to the low thermal conductivity of glass (a-Si:H substrate) compared to c-Si. Indeed, there is no heat sink for the sample. To assess the effect of the substrate, I measured the change in temperature under the same laser illumination for cells made of Si NW/a-Si:H on glass and on a c-Si wafer[15]. The temperature maps are shown in Figure 5.27. According to the IR camera, the cell on glass reaches a temperature larger than 60 °C, whereas on the c-Si substrate, there is no significant heating (<1 °C). The effect of the laser can still be seen right after the start of illumination (0.16 s), but the heat dissipates quickly. The steady-state heat map (2.76 s) does not show any difference between the illuminated part of the cell and the dark one. Therefore, the V_{oc} decrease is mostly a consequence of the substrate. As in bending tests, the substrate can be a key parameter for the properties of the whole device. To understand the effects of strong illumination on the a-Si:H material only, or and the NWs, I-V measurements for a Si NW/a-Si:H or a flat a-Si:H cell on c-Si could be used.

Table 5.3: Room temperature thermal properties of a-Si:H, c-Si and glass. The values come from [a] [Zink 2006], [b] [Street 2000],[c] [Weber 2003], [d] Corning data sheet.

Material	Thermal conductivity ($Wm^{-1}K^{-1}$)	Specific heat ($Jg^{-1}K^{-1}$)
a-Si:H	$1-2$ [a]	$\simeq 1$ [a]
c-Si	165 [b]	0.71 [c]
Corning glass (Eagle XG)	1.1 [d]	0.77 [d]

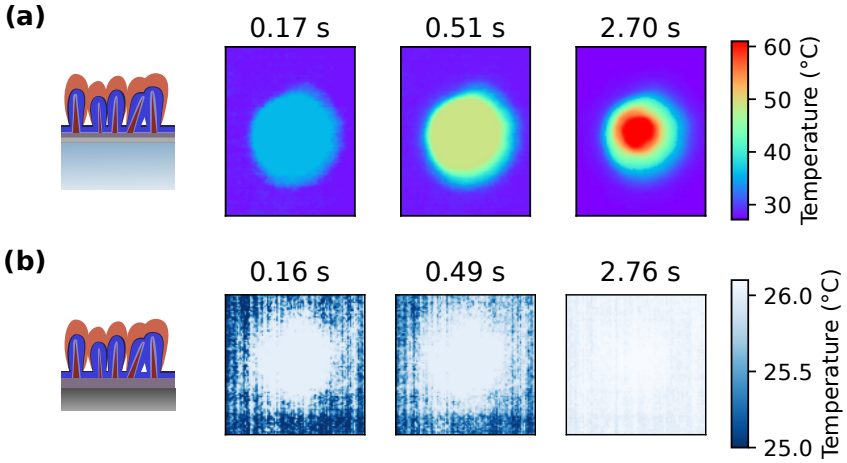

Figure 5.27: Temperature maps of Si NW/a-Si:H **(a)** on glass and **(b)** on c-Si. The illumination power is the same, 260 W/cm^2. Both cells have a top contact made of ITO. A 800 µm pinhole is used. The heated spot on glass has a diameter around 1.3 mm, the heated spot on c-Si is smaller.

If one expects no dependence of the V_{oc} change with temperature on the illumination intensity, an estimation of the temperature in the Si NW/a-Si:H cell under laser

[15] I wanted to perform I-V measurements on the Si NW/a-Si:H cell with a c-Si substrate, but the samples displayed no rectifying behavior, possibly because of the high resistivity of the c-Si wafer used as the substrate and back-contact.

illumination could be obtained. In Figure 5.19, a 400 mV difference is observed between the peak and steady values at the highest power, 290 W/cm^2. If it is only due to heating, it corresponds to a difference in temperature close to 140 °C, i.e. a total temperature around 165 °C. It is consistent with the previous estimation from the in-situ annealing which had set a lower limit of 160 °C. Table 5.4 gives an overview of all the temperature estimations in Si NW/a-Si:H solar cells under strong illumination.

Table 5.4: Summary of the temperature estimations in Si NW/a-Si:H solar cells under 532 nm illumination. The power density refers to a power at which we clearly observed the phenomenon. Nonetheless, the change, when it is irreversible, can be the result of a longer change, which started at lower power densities.

Method or phenomenon	Temperature	Illuminated area or local temperature	Junction?	Power density	Illumination area (diameter)	Section(s)
Thermal camera	>70 °C	∼ Local[a]	Surface	290 W/cm^2	800 µm	5.5.5
In-situ annealing	>160 °C	Illuminated area[b]	a-Si:H	130 W/cm^2	800 µm	5.4.3
V_{oc} decrease + $\beta_{V_{oc}}$	≃165 °C	Illuminated area	a-Si:H	290 W/cm^2	800 µm	5.5.5, 5.6.5
Crystallization (solid-phase)	<650 °C	∼Local	a-Si:H	<1.2 kW/cm^2	400 µm	5.8.2
Photoluminescence	No conclusion	Illuminated area	a-Si:H	<2 kW/cm^2	>10 µm	5.6.3
Raman	No conclusion	Illuminated area	a-Si:H	<2 kW/cm^2	>10 µm	5.6.4

[a] Depends on the camera's resolution.
[b] Full recovery of I_{sc}.

5.6.6 Summary

In the previous section, we attributed the V_{oc} decrease to thermal effects without assessing the temperature. Direct and indirect measurements of temperature at the junction are difficult in a-Si:H. To understand the thermal effects, we instead studied the change in the performance of Si NW/a-Si:H solar cells under heating and V_{oc} was indeed the most affected parameter. A decrease such as the one observed with the laser would correspond to a temperature around 165 °C. While the sensitivity of a-Si:H solar cells to temperature is lower than for other inorganic materials, we observed no strong difference between the behavior of c-Si and Si NW/a-Si:H, which may be related to the morphology of NWs. It highlights that the specific behavior of a-Si:H cells (both flat and NWs) under strong illumination stems from the difficult dissipation of heat, mostly due to the glass substrate.

5.7 Reversible decrease of I_{sc}

5.7.1 I-V curves

Figure 5.10 displays a significant decrease of I_{sc} under high illumination levels. Repeated measurements show that there is an irreversible change, attributed to material damage and detailed in Section 5.8. However, a closer examination proves that part of this decrease is also reversible, as the red arrow in Figure 5.10 highlights. Both 800 µm and 1400 µm measurements present a reversible part in the final I_{sc} decrease, which starts before the irreversible one. For the 400 µm pinhole, we cannot tell with certainty whether the decrease is partly reversible or not. No decrease is observed for c-Si, it is unclear for flat a-Si:H.

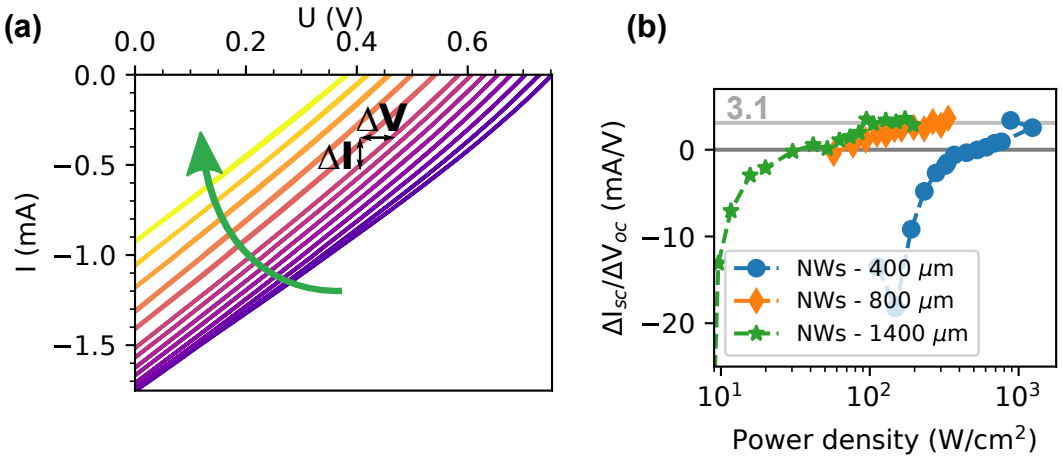

Figure 5.28: **(a)** I-V curves under increasing illumination (above 55 W/cm^2) that show the decrease both in V_{oc} and I_{sc}. **(b)** $^{\Delta I_{sc}}/_{\Delta V_{oc}}$ ratio for Si NW/a-Si:H solar cells with different illumination areas. The ΔI and ΔV differences between one I-V curve and the previous one are shown in **(a)**. For the ratio, we computed them at short-circuit and open-circuit conditions respectively. Only part of the probe power densities are displayed. A horizontal line is drawn at $^{\Delta I_{sc}}/_{\Delta V_{oc}} = 3.1$ to show how all ratios converge (arbitrary value).

The I-V curves corresponding to this decrease, displayed in Figure 5.28 **(a)**, show almost no rectifying behavior. It is due to the high series resistance of the Si NW/a-Si:H solar cells. Under high illumination levels, it limits the collection of charge carriers, even at the short-circuit condition (same behavior as in Section 2.8.2). A saturation in the current that can be collected would be expected. However, these illumination levels also correspond to a strong change in temperature and a decrease of the open-circuit voltage. With a fill-factor limited to $\simeq 25$ %, a decrease of V_{oc} necessarily goes with a decrease of I_{sc}. In addition, for geometrical reasons, the ratio of their change, $^{\Delta I_{sc}}/_{\Delta V_{oc}}$, should remain constant. To determine whether both decreases are correlated, I computed this ratio for different illumination powers in Figure 5.28 **(b)**. The ratio is first negative because of the V_{oc} decrease ($\Delta V_{oc} < 0$). It becomes positive at higher power densities, when the decrease of I_{sc} starts. When the power density keeps on increasing, ratios for all pinholes seem to converge to a constant value, around 3.1 for the Si NW/a-Si:H cells. It is consistent with a current decrease that is governed by the fill-factor limitation and the change in V_{oc}. In addition, the convergence is faster for a larger illumination area. For instance, it is not completed yet for the smaller pinhole. This difference probably comes from the thermal effects, which are more important for a given power density with larger areas.

5.7.2 A consequence of heating

The reversible decrease of I_{sc} is thus due both to a limitation in the collection efficiency and to the heating of the cell, which increases recombinations. This can be clearly seen in the one-diode equation for the short-circuit current. In the passive convention, corresponding to the I-V measurements ($I_{sc} < 0$),

$$I_{sc} = -I_{\phi} + I_0\Big[\exp\Big(-\frac{q(R_{se}I_{sc})}{k_{\mathrm{B}}T}\Big) - 1\Big] - \frac{(I_{sc}R_{se})}{R_{sh}}. \tag{5.15}$$

The series resistance R_{se} limits the short-circuit current through ohmic losses (last term of Eq. (5.15)). In addition, because of R_{se}, when the device is in short-circuit, the junction is forward-biased ($-R_{se}I_{sc} > 0$). Hence, the recombination current affects I_{sc}. If the saturation current I_0 is increased, as it is the case at higher temperatures, I_{sc} decreases. The thermal origin explains why the reversible I_{sc} decrease is clear with the larger pinholes and not with the 400 µm one.

5.7.3 Reversible and irreversible

In Figure 5.28, both reversible and irreversible changes in I_{sc} are displayed. The onset of irreversible decrease does not correspond to any significant change in Figure 5.28 **(b)**, because the irreversible part in the total decrease is slowly growing, from $\simeq 17$ % at the onset to almost 60 % for the last measurement (800 µm pinhole). The irreversible decrease of I_{sc} is detailed in Section 5.8.

5.7.4 Summary

In addition to the decrease of the open-circuit voltage, we observed a reversible decrease of I_{sc} in the Si NW/a-Si:H cells. According to I-V measurements under increasing temperature (Section 5.6.5), we do not expect such a change in I_{sc} due to thermal

effects. Yet, a careful observation showed that together with a low value of the fill-factor, thermal effects are likely to account for the reversible decrease of I_{sc}.

5.8 Final degradation of the solar cell

5.8.1 Second light-soaking after recovery

After the recovery from the Staebler-Wronski effect, a second irreversible decrease of I_{sc} is observed, also due to light-soaking. Figure 5.29 displays this variation for two probe powers. The $7\,W/cm^2$ measurement shows that the second decrease is much stronger than the first one. In addition, the change in I_{sc} is accompanied with a change in all parameters, especially the apparent series and shunt resistances. R_{shunt} is also presented in Figure 5.29. The reference c-Si cell does not show any difference. The same behavior is observed for all illumination areas. For larger illumination areas, the second decrease starts at lower power densities (see Figure 5.15), which suggests a correlation with thermal effects.

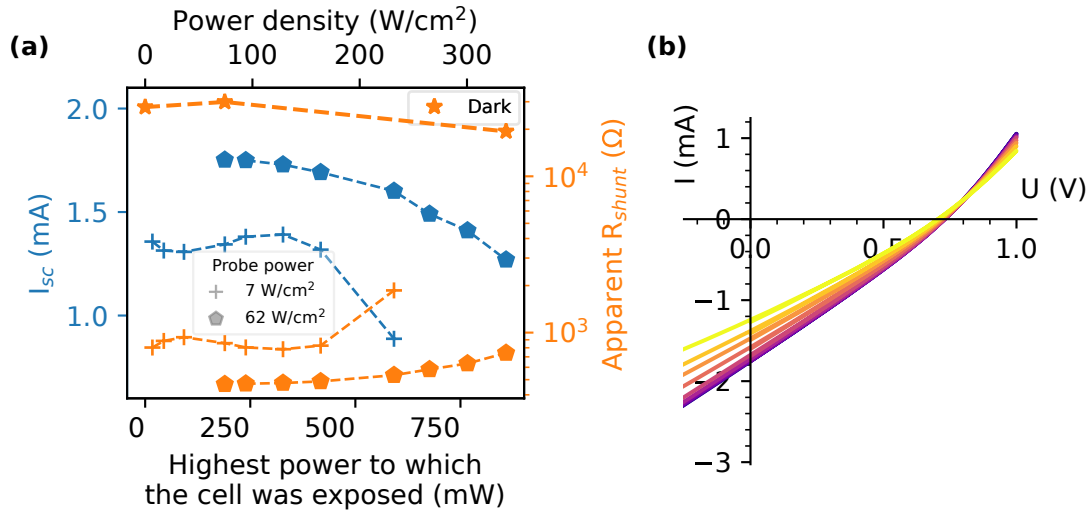

Figure 5.29: **(a)** Irreversible change in I_{sc} and apparent R_{shunt} with exposure to different illuminations. They are displayed for two probe powers, $7\,W/cm^2$ (+) and $62\,W/cm^2$ (⬠). The measured value of R_{shunt} in the dark is also displayed. **(b)** Repeated I-V curves under $62\,W/cm^2$ illumination. They show the change in the rectifying behavior with I_{sc} decrease.

This second decrease was also observed for probe powers which had already experienced a first decrease ascribed to SWE and a recovery due to in-situ annealing. Although higher temperatures are reached under increasing illumination, they are not sufficient to anneal the increasing concentration of defects. There may be several reasons to it. First, the annihilation of a defect (a dangling bond) relies on the bonding of a hydrogen atom to this dangling bond. If the amount of defects exceeds the quantity of (available) hydrogen, no recovery is possible, even with an increasing temperature. The creation rate can also exceed the diffusion rate of H, which thus limits the recovery. Finally, high temperatures result in the removal of hydrogen from the material. Depending on

the structure of the a-Si:H film, two peaks of H effusion have been reported in literature, around 350 °C and 600 °C [Beyer 2003]. They are respectively attributed to H desorption from internal microvoids or to atomic H outdiffusion. In our experiments, the temperature likely went beyond 350 °C for very high powers, at least locally (crystallization, detailed in Section 5.8.2). However, this probably does not account for the whole I_{sc} change.

Change in R_{se} and R_{shunt} The decrease of I_{sc} goes with a significant increase of the apparent values of R_{se} and R_{shunt} (Figure 5.29 **(a,b)**). The change in R_{shunt} is a direct consequence of the I_{sc} decrease. As mentioned in Section 5.3.4, the limited collection efficiency results in a slope in the I-V curve, even under reverse bias. It is the value that we compute and in this case it does not correspond to the actual R_{shunt}. This is clear in Figure 5.29 **(a)**, where the apparent R_{shunt} under illumination is much lower than the one measured in the dark. When the short-circuit current is lower, the collection efficiency is better and the shunt resistance becomes closer to its actual value. The decrease of I_{sc} can also affect the value of the apparent R_{se}. However a comparison of its dark value before and after measurements also shows an increase. Hence, there is likely a material change as well. It can stem from the light-soaking, but other degradation mechanisms have been demonstrated under very strong illumination.

5.8.2 Crystallization of a-Si:H

With SEM and Raman, we evidenced the recrystallization of the absorber of a-Si:H NWs after high power illumination, which was accompanied with a pronounced shape change. It may play a role in the irreversible I_{sc} decrease.

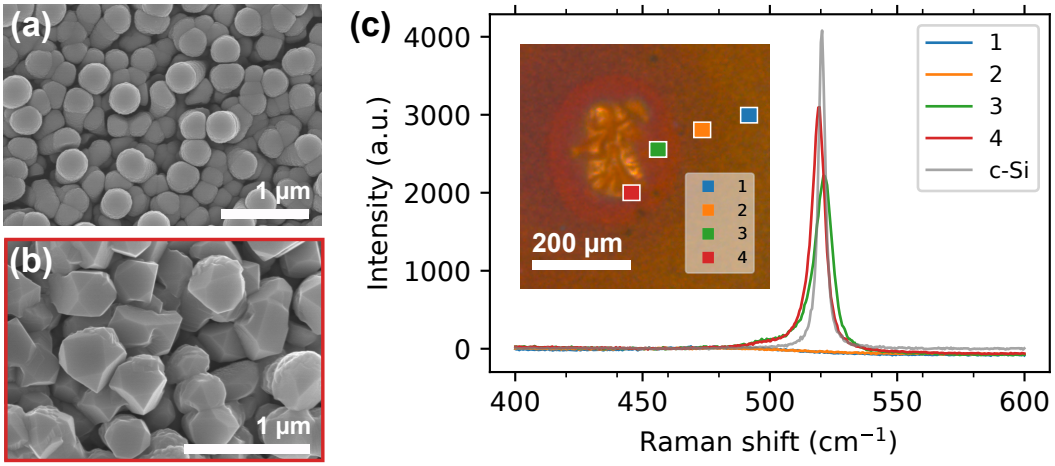

Figure 5.30: Si NW/a-Si:H cell after illumination with the laser and the 400 µm pinhole. The highest (spatially averaged) density was around 1.2 kW/cm^2. **(a, b)** SEM images of a non-damaged region and a crystallized region respectively. **(c)** Raman scattering of the same Si NW/a-Si:H solar cell at different positions. For comparison, the signal of a c-Si wafer is also displayed. The inset is an optical microscopy image of the region exposed to the laser. The damage is clear. The region corresponding to **(b)** is shown in red.

The inset in Figure 5.30 **(c)** presents a picture of the region exposed to the laser illumination using the 400 µm pinhole. The damage is obvious at the center (over ∼200 µm), although regions beyond the illuminated area look affected too. Figure 5.30 **(a)** displays the SEM top-view of pristine Si NW/a-Si:H. Figure 5.30 **(b)** shows a region close to the center of the illuminated area. Crystallites are clear on top of NWs (over ∼100 nm height), with a cubic structure that points toward the transformation of a-Si:H into c-Si. They were observed at different positions, over a distance of 100-200 µm. No evidence of crystals was found with SEM after illumination with larger areas. As they correspond to lower maximal power densities (0.34 kW/cm^2 and 0.19 kW/cm^2 compared to 1.2 kW/cm^2), this is not surprising. Still, the presence of smaller crystallites that cannot be observed with SEM cannot be excluded.

Furthermore, Raman scattering measurements confirm the transformation of a-Si:H to c-Si under laser illumination (Figure 5.30 **(d)**). Close to the center of the illuminated area, a signal coming from (poly-)crystalline silicon can be observed (around 520 cm^{-1}). A signal around 500 cm^{-1} shows the presence of μc-Si:H in the damaged region. Away from the most degraded zone, only the weak a-Si:H signal is observed, typical of original Si NW/a-Si:H. We do not see any c-Si signal in the regions 1 and 2, but we can draw no conclusion regarding the presence of smaller crystallites due to their weak signal. For instance, the signal from the c-Si cores cannot be distinguished from the a-Si:H one in the Raman spectra of Si NW/a-Si:H (Figure 5.23).

Maximal temperature reached under illumination This phenomenon can help us determine the magnitude of the maximal temperature under illumination, but we need to determine which crystallization mechanism is involved. Post-deposition crystallization of a-Si:H has been the subject of extensive research, with the objective of high-quality poly-Si for Thin-Film Transistor (TFT) on low-temperature substrates [Voutsas 2003]. Amorphous silicon can transform to c-Si through melting and recrystallization, with a lower melting point than c-Si ($T_m = 1150\,°C$ vs. 1410 °C) [Donovan 1983]. It is the usual mechanism under pulsed-laser excitation, where heating times are short (20-250 ns) and power densities are very high. A very high temperature ($> T_m$) is locally achieved.

Because it is metastable, a-Si:H is also prone to become crystalline through a solid-phase transformation. Temperatures much lower than the melting point are sufficient (down to 550 °C for a few days or 800 °C for a few minutes). It is typically the mechanism of recrystallized poly-Si in furnaces [Hatalis 1998], but has also been reported for continuous-wave laser illumination [Morales 2014]. Solid-phase transformation is likely responsible for the crystallization in our experiment. It occurs over a 10-20 min illumination (determined from the irreversible change), which would correspond to a temperature below 650 °C for a-Si:H according to [Mahan 2006]. This study also shows that most of the crystallization time is actually an incubation time. Because of the c-Si core that can act as a nucleation site, this time might be shorter in the Si NW/a-Si:H and lower temperatures might be sufficient to account for the observed kinetics. We can be certain that the maximal temperature reached in a-Si:H is much higher than the surface one measured with an IR camera, even though it is very localized. It is probably below 650 °C.

Crystallization effect on solar cell parameters The impact of crystallization on the parameters is difficult to determine, since the resulting cell is a mixture of cells with a-Si:H, μc-Si:H and c-Si absorbers. Still, we could expect a decrease of V_{oc} (lower band gap energy of c-Si and μc-Si:H) and I_{sc} (indirect band gap). But no increase of R_{se} is expected. In addition, we did not observe large-scale crystallization in the cell that was illuminated using the 800 µm pinhole, although it displays an irreversible decrease of I_{sc} and V_{oc}. A thorough study of crystallization would be needed to understand its role in the change in parameters.

5.8.3 Thermally induced cracks

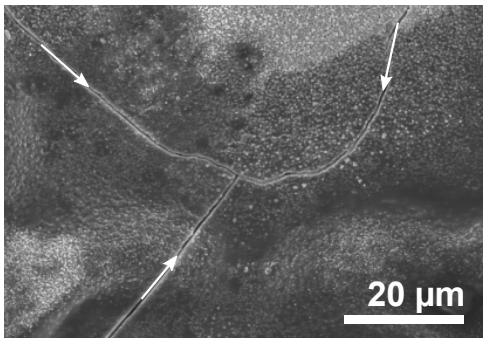

Figure 5.31: SEM image of the Si NW/a-Si:H cell after illumination with the laser and the 400 µm pinhole. The center of the illuminated area is clearly damaged. Cracks are indicated with white arrows.

SEM observation of the cell which experienced the highest power density (400 µm pinhole) also showed cracks originating in the center of the illuminated area (Figure 5.31). These cracks are believed to be due to the difference in thermal expansion between materials (probably between Ag and glass). Because they disconnect part of the cell, they account for the increase of R_{se}, and (part) of the decrease of I_{sc} and V_{oc}. They are also expected to lower the fill-factor, but an increase is observed. This may be due to the fact that the low fill-factor is strongly dependent on I_{sc}.

5.8.4 Summary

Under higher illumination intensities, we observed a strong change in all parameters. Its onset is not determined by the power density. It occurs earlier (lower power densities) for larger illumination areas, where the thermal effects are stronger. Partial crystallization to μc-Si:H and c-Si is a likely explanation, which would account for the change in I_{sc} and V_{oc}. Full crystallization of some NWs has been evidenced for the highest illuminations, but partial crystallization can occur as well. Nevertheless, it does not explain the change in R_{se}. Thermally-induced cracks, observed in one of the cell, do. Yet, it is not clear if they could occur on smaller scales, not visible in SEM. In addition, a fully irreversible SWE (no recovery with heating) can also account for the observed changes.

5.9 Takeaway messages

- Si NW/a-Si:H solar cells can sustain illumination powers up to 770 W/cm^2 (Section 5.3).

Under 532 nm illumination, the performance of Si NW/a-Si:H solar cells is first limited by the top contact. With a high density of Ag NWs on top of ITO, an optimal illumination power of 0.5 W/cm^2 (equivalent to 5 Sun) can be reached. Nonetheless, the performance of Si NW/a-Si:H solar cells is also strongly affected by the decrease of V_{oc} and I_{sc}. However, no strong irreversible degradation is observed until very high powers (770 W/cm^2, equivalent to 7 700 Sun for the 400 µm pinhole).

- SWE and in-situ annealing are observed under strong illumination (Section 5.4).

The first irreversible change in a-Si:H/NWs is the degradation of the material through light-soaking. Because of the high powers used, it occurs quickly. With higher powers, in-situ annealing enables the recovery of I_{sc}. Si NW/a-Si:H solar cells are more beneficial than planar ones due to the lower thermal conductivity. A temperature above 160 °C is expected.

- The performance of a-Si:H cells is strongly limited by the poor thermal conductivity of the glass substrate (Section 5.5 and Section 5.7).

A strong (over 400 mV) and time-reversible decrease of V_{oc} is observed. Measurements of temperature (thermocouple, IR camera, PL or Raman) are not reliable enough to confirm that the change is fully related to a temperature increase. However, indirect measurements (cycled illumination, time- and area-dependence) point to a thermal effect. The temperature coefficient of a-Si:H and c-Si solar cells under controlled heating does not account for the observed difference with laser illumination. The different behaviors of Si NW/a-Si:H and c-Si solar cells is related to the poor thermal conductivity of the glass substrate of the Si NW/a-Si:H solar cells. Because of the limited collection efficiency, the temperature also reduces the short-circuit current under increasing power in a-Si:H cells.

- With the 800 µm pinhole, a final degradation is observed for power densities above 230 W/cm^2 (Section 5.8).

It likely stems from thermal effects. Evident crystallization of Si NW/a-Si:H is observed at very high powers, but it could locally occur in NWs and change the performance of the cells. A fully irreversible SWE (no recovery with heating) can also account for the observed changes.

Conclusion

With the climate change induced by greenhouse gases, sources of energy alternative to fossil fuels are urgently needed. Photovoltaics, which consists in the conversion of solar energy to electrical energy, has a role to play in the energy mix with other renewable sources of energy such as wind or hydraulic energy. Indeed, the potential of solar power is huge, there are multiple technologies available and crystalline silicon PV has demonstrated high power conversion efficiencies, in the lab (26.7 % compared to a theoretical efficiency of 32 % for silicon) and in commercialized modules ($\sim$ 20 %). Nonetheless, there is still some room, either for new principles and structures that enable to reach higher efficiencies, or for new applications, suited to an absorber's strengths and shortcomings. Nanowires, that are high aspect ratio structures with a submicron diameter, can replace bulk and thin film materials. In particular, they help to make the most of amorphous silicon. Amorphous silicon is made of an abundant element and its deposition is less energy-consuming than the fabrication of c-Si wafers. Yet, it is limited by the low mobility and short lifetime of its charge carriers. Its use in NWs with a radial junction results in a separation of the directions for the propagation of light and the collection of charge carriers. Very thin layers can be used, which overcomes the short collection length. Furthermore, NW arrays also display good optical and mechanical properties (lower reflection, inherent flexibility). For a-Si:H, PECVD is used, which corresponds to a rather low temperature deposition (180 °C), and correct deposition rates on large areas. Various substrates can be used, including amorphous one. Since the start of the development of Si NW/a-Si:H solar cells ($\sim$ 2010), their efficiency has now reached 8-9 %.

Nonetheless, the low mobility of carriers in a-Si:H, especially in doped layers, does not allow for the collection of current at the scale level. In addition, the disordered NW array affects the deposition of electrodes developed for flat cells and results in a poor lateral conduction. For this reason, we proposed to use two different kinds of materials for a hybrid electrode (chapter 2). Even for planar substrates, transparent electrodes are a challenge. Because free carriers are responsible for the absorption and reflection of light and for the conduction, a trade-off between transparency and conduction is needed. Among the possible materials, TCOs are mostly used, because their transparency window corresponds to the visible and near IR range. Yet, a thick layer of ITO is needed on top of the Si NW/a-Si:H, which affects the optical performance of the cell. Networks made of Ag NWs show properties that are complementary to ITO. Ag NWs make a percolative (non continuous) network of conductive NWs. Together with a transparent conductive oxide, they ensure a good collection of carriers on short and long ranges. The use of a hybrid also gives more freedom in the optimization. Instead of the magnetron-sputtered ITO, ALD Titanium-doped Zinc Oxide (ZnO:Ti) (TZO) could be used. However, I showed that the conformal layer connected the bottom of the cell and resulted in lower R_{shunt} values. Hence, I kept the magnetron-sputtered ITO in the hybrid and first worked on its transparency. I did it directly on the device, since the NW morphology affects the deposition of the electrode materials. To probe only the electrical properties of the contact, I used a very low illumination with EQE. I then

characterized the complete hybrid under 1 Sun. Thanks to the increased transparency of the thin ITO film and the higher conductivity of the network of Ag NWs compared to a thick ITO layer, I improved the short-circuit current and the fill-factor of Si NW/a-Si:H solar cells, with a resulting PCE increase from 4.3 % to 6.6 %.

While many studies showed the assets of Ag NW electrodes, many also raised the issue of the degradation of Ag NWs. According to literature, it stems both from corrosion with sulfur, greatly enhanced by the water concentration in atmosphere, and from the thermodynamic instability of the NWs. In chapter 3, I studied the protection of Ag NWs with TZO and ITO. I observed that a minimal thickness ($\sim$20 nm) is needed for a full coverage of ALD TZO on NWs. For a better characterization of the degradation process, I monitored the change in morphology (SEM), optical (total transmittance and reflectance) and electrical properties ($R_{\square}$) of the Ag NWs on glass and on glass/ITO substrates. Without any external excitation, I demonstrated that the Ag NWs deposited following our process degrade very slowly. After 20 months, by performing SEM observation, I observed the formation of nanoparticles that do not strongly affect the resistance. I could distinguish them only on bare NWs. Consequently, no conclusion was possible regarding the effect of the different protecting layers. However, Ag NWs are sensitive to the stress due to light or current and the same study under stress could help to determine the lifetime of Ag NWs for solar cells and the effect of the protective layers. This should lead to a three layered electrode, with protected Ag NWs.

The solar cells with the highest efficiencies today are made of crystalline materials and are brittle. Yet, some applications would benefit from flexible solar cells, for instance Building-Integrated Photovoltaics (BIPV) (low flexibility), roll-to-roll processes (moderate flexibility) or wearable devices (high flexibility). Organic materials are more flexible, but they are prone to degradation over time. Apart from the material, the structure can be adapted to be flexible, either with thinner layers or with NWs. Arrays of standing nanowires are inherently flexible. In addition, the hybrid electrode should sustain the deformation better than the thick ITO. Using Si NW/a-Si:H, we could thus develop (rather low cost) flexible solar cells that are made of inorganic materials. In chapter 4, I reported the characterization of Si NW/a-Si:H solar cells grown on thin glass under 1 Sun, for bending radii down to $\sim$2 cm. Some cells did not show any degradation with bending, while others displayed a limited degradation (especially in R_{shunt}) and others became completely shunted. We could not establish any correlation with the top contact. Furthermore, the glass substrate often broke, which limited the study. Observations of the cells with Electron-Beam Induced Current did not reveal any degradation. To test the cells at smaller bending radii, I used thin Al and Cu foils as substrates and studied these devices with SEM and EBIC. It evidenced that their flexibility is limited by the density of the Si NW/a-Si:H, that behave as a quasi-film. In addition, I observed current collection issues with EBIC that I did not assess in morphological SEM images.

In chapter 5, I analyzed the behavior of Si NW/a-Si:H solar cells under strong illumination, up to 10^3 W/cm^2. They showed both reversible and irreversible decreases in I_{sc}, V_{oc} and fill-factor, for different powers. Thanks to a thorough analysis, I identified the origins of the different phenomena. The performance of Si NW/a-Si:H solar cells was first limited by the series resistance of the NW array. The light-induced degradation (Staebler-Wronski effect) and thermal effects then impacted the short-circuit current and the open-circuit voltage respectively. While the mechanism of light-induced degradation was due to the a-Si:H material, the thermal effects were mostly related to the glass

substrate. Besides, the final degradation of the Si NW/a-Si:H solar cells occurred under very high powers ($> 770\,W/cm^2$). In conclusion, the performance of Si NW/a-Si:H solar cells under strong illumination was not limited by a-Si:H at first. With radial junction NWs, the performance of a-Si:H can remain correct above 1 Sun.

In addition, I characterized various structures with EBIC, reported in Appendix A. Unfortunately, amorphous silicon is easily degraded by the electron beam and no in-depth study of the p-i-n junction in Si NW/a-Si:H was possible. Nonetheless, the distance over which the degradation occurred helped me to determine the size of the probe. Furthermore, we used EBIC to analyze the electrical properties in NWs for tandem solar cells and for LEDs.

While I optimized the hybrid contact for Si NW/a-Si:H, the architecture and optimization steps can be adapted to any nanostructured device. The use of two materials is particularly suited to this case, since the length scale of nanostructures is much smaller than the one of the device. In addition, nanostructured devices require an optimization directly on the device. Changing the illumination is a useful tool to assess only the optical or only the electrical properties.

Besides, there is still some work to be done on the optimization of the hybrid contact for Si NW/a-Si:H solar cells. We evidenced the stability of Ag NWs without any stress, but we should assess the change under light and current. The effect of the ITO substrate should also be further studied. Once an efficient encapsulation layer has been demonstrated, a three-layer hybrid electrode {TCO / Ag NWs / ALD TCO} could be used. Its flexibility should be confirmed (it may be stiffer than a two-layer hybrid). Small cells with a lower density of Si NW/a-Si:H on a metal foil would be ideal for these tests. Increasing the bending in the SEM chamber with EBIC observation could help to understand the degradation.

Through this work, I showed how the performance of Si NW/a-Si:H is mostly limited by the resistance of the top contact. Measurements under high illumination also evidenced that Si NW/a-Si:H are not significantly damaged up to very strong illumination. Because the main limitation was related to the glass temperature, the comparison of the performance of a Si NW/a-Si:H and a planar a-Si:H cells on a c-Si substrate would help to determine the limits of a-Si:H and of the NWs.

Appendices

Appendix A

EBIC

Contents

A.1 Electron-Beam Induced Current (EBIC)

A.1.1 Principle

In EBIC, a sample is scanned with an electron beam. Figure A.1 shows a schematics of the setup. Electrons from the beam are responsible for the excitation of e^-/h^+ pairs in the semiconductor. If there is a gradient in the electrochemical potential of the generated charge carriers and electrical contacts are made, a current can be collected. Scanning with the probe results in a current map, that shows where the current was generated and collected. The signal of secondary electrons is collected at the same time. Hence, the morphology and the electrical properties can be compared. In addition, the same magnifications as in SEM can be used, with observed regions ranging from hundreds of nm to a few mm. Because of the small size of the e-beam probe and the interaction volume, a high resolution map can be obtained. Plane-view and cross-section observations are possible. For an EBIC observation, one has to choose the acceleration voltage of electrons, V_{acc}, the current of the electron beam and the bias applied to the sample. The acceleration voltage affects the generation volume (probe depth and the lateral spreading) and indirectly the density of generated electrons, the current the

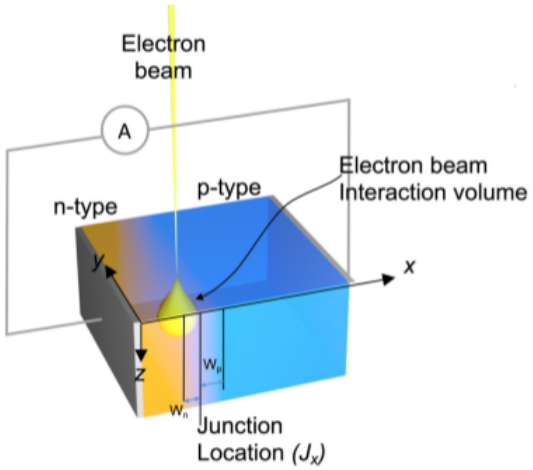

Figure A.1: Working principle of EBIC method on a p-n junction. From [Zhou 2020].

quantity of electrons. A reverse bias can be applied to the junction of interest for a better collection of charge carriers. When several diodes of opposite polarity are present, it also enables to probe one junction or the other.

EBIC is relevant for the observation of junctions in semiconductors. Under "illumination", a current is generated and collected. Consequently, EBIC measurements are used to determine the position of the junction of interest, the width of the depletion region, the diffusion lengths of minority carriers or the doping [Saket 2020]. It also enables the mapping of potential barriers in the device or defects such as dislocations.

Variations of the method exist. For instance, STEM EBIC has also been reported, with an improved resolution [Mecklenburg 2019]. Alternating e-beam exposure (*lock-in EBIC*) can also be used to get rid of strong offset currents [Breitenstein 2009]. Meng et al. also suggested a single-contact EBIC measurement where the charge and discharge of the sample are used for EBIC mapping [Meng 2015] .

EBIC in C2N A Kleindiek prober shuttle is used in the Hitachi SU8000 SEM chamber (displayed in Figure A.2 **(a)**). Thanks to piezoelectric micromanipulators, the electrical connection is done inside the chamber and several locations can be easily probed. In addition, sharp tungsten tips (0.5 µm tip radius) enable the contact with a single nanowire. The prober shuttle is connected to triaxial cables. The current value is obtained after amplification by a low-noise current preamplifier (Standford SR570), with gains typically around 2×10^6. A bias can be applied. I kept the same connections for all samples: a positive bias always corresponds to a positive potential connected to the top of the sample, a negative one to the bulk. When the n-doped region is on top, it results in a negative current. The polarity of the electrical connections, the bias and the current sign are important parameters for the analysis of the EBIC signal as several junctions of opposite polarity can be present in the device. For this reason, and even if it may look irrelevant in some cases, I chose to keep the same electrical connections for all EBIC observations. When only one junction is considered (Section 4.4 and Section A.2), its current is displayed as positive for a more straightforward representation. It is written in the caption.

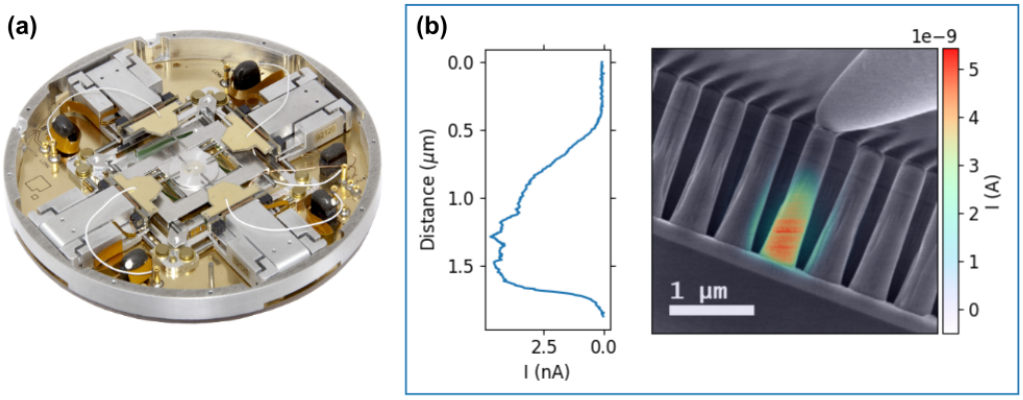

Figure A.2: **(a)** Kleindiek PS4 prober shuttle. Its diameter is 10 cm. The four micromanipulators can be seen. **(b)** EBIC map of an InGaP NW with an axial p-i-n junction (Section A.4.2). The EBIC signal is displayed on the SEM image. Thanks to the sharp tip, a single NW can be contacted. From the map, a profile along the junction (axial direction) can be drawn.

A.1.2 What determines the shape of the signal?

A typical EBIC profile of a p-i-n junction that was measured in C2N is shown in Figure A.2 **(b)**. A high current corresponds to the intrinsic region, where generated carriers are easy to collect. The decrease in the signal on the top part can be related to the diffusion length of minority carriers. However, an accurate explanation of the EBIC profile can differ from this description and the resulting profile can also be altered. Surface effects [Zhou 2020], short diffusion lengths or high injection effects [Nichterwitz 2013, Haney 2015] are possible issues.

The obtained profile for EBIC is a combination of the generation profile and the collection efficiency. In particular, the volume where e^-/h^+ pairs are generated strongly affects the observation. Several models have been suggested for the generation profile [Donolato 1981, Everhart 1971, Werner 1988]. The current understanding of the generation corresponds to a pear-shaped volume with a lateral gaussian distribution and a depth-dose dependence based on [Everhart 1971]. Increasing the acceleration voltage of electrons (V_{acc}) increases the generation volume and lowers the resolution. In addition, the use of different V_{acc} enables an in-depth probing of the sample.

A.1.3 EBIC vs. photocurrent

EBIC is particularly relevant for solar cells, since it corresponds to a similar mechanism. Yet, because the impinging electrons are significantly more energetic than visible photons, they are able to generate much more carriers. Electron-hole pairs generated by the e-beam are a consequence of ionization by secondary electrons. The e^-/h^+ pairs that are finally stable have a low kinetic energy (insufficient for further ionization). It has thus been estimated that about three times the band gap energy is needed to generate an e^-/h^+ pair from one high energy particle [Klein 1968],

$$E_{e^-/h^+}^{ebeam} \simeq 3E_g. \quad (A.1)$$

Hence, much larger generation rates can be expected in EBIC compared to the typical rates under 1 Sun illumination (10^{24}-10^{27} $cm^{-3}s^{-1}$ vs. 10^{21} $cm^{-3}s^{-1}$). Their precise value depends on the probe current and the acceleration voltage. A higher V_{acc} increases the interaction volume and decreases the generation rate.

In addition, the generation in EBIC is spatially limited, while the whole cell is usually illuminated for 1 Sun observations. This may affect the collection of charge carriers.

Electron-Beam Induced Current (EBIC) is a powerful method to understand the electrical properties of a semiconductor junction. During my thesis, I had the opportunity to characterize various samples, including Si NW/a-Si:H (Section A.2, Section A.3), III-V nanowires on Si for tandem solar cells (Section A.4) and GaN nanowires for Light-Emitting Diode (LED) devices (Section A.5). Although most observations are not related to the work described in the main part of this thesis, I wanted to report them to illustrate the use of EBIC for semiconductor NWs. The electrical connections have been detailed in Section A.1.

A.2 a-Si:H degradation under electron beam

I wanted to record the EBIC signal from Si NW/a-Si:H to determine how charge carriers are collected in the p-i-n junction. However, a-Si:H degrades under exposure to an electron beam.

A.2.1 Loss of EBIC signal reversible with annealing

I analyzed this degradation in Si NW/a-Si:H. Figure A.3 **(a)** displays a top-view SEM image of a Si NW/a-Si:H solar cell. The corresponding EBIC map prior to any high-magnification is presented in **(b)**. Apart from the Ag paste region, the whole cell generates a current under e-beam exposure. **(c)** shows the same map after high-magnification SEM of two regions (one highlighted). They do not display any EBIC signal. Interestingly, no change is observed in SEM. It is thus related to a modification of the electronic properties of a-Si:H. Because charging effects could occur, I left the sample for 12 days in air (map **(d)**), but it was not sufficient to recover the original current level, therefore the degradation is persistent. Directly after this observation, I annealed the cell at 180 °C on a hot plate for 20 min. The resulting EBIC map **(e)** shows no more difference between regions which were exposed to a high dose or not. A new region had been damaged just before the annealing process and perfectly recovered with annealing (not shown).

A.2.2 Relation with light-induced defects

The degradation of a-Si:H under e-beam has been previously reported, as well as the annihilation of defects by annealing. Schneider et al. showed that this degradation

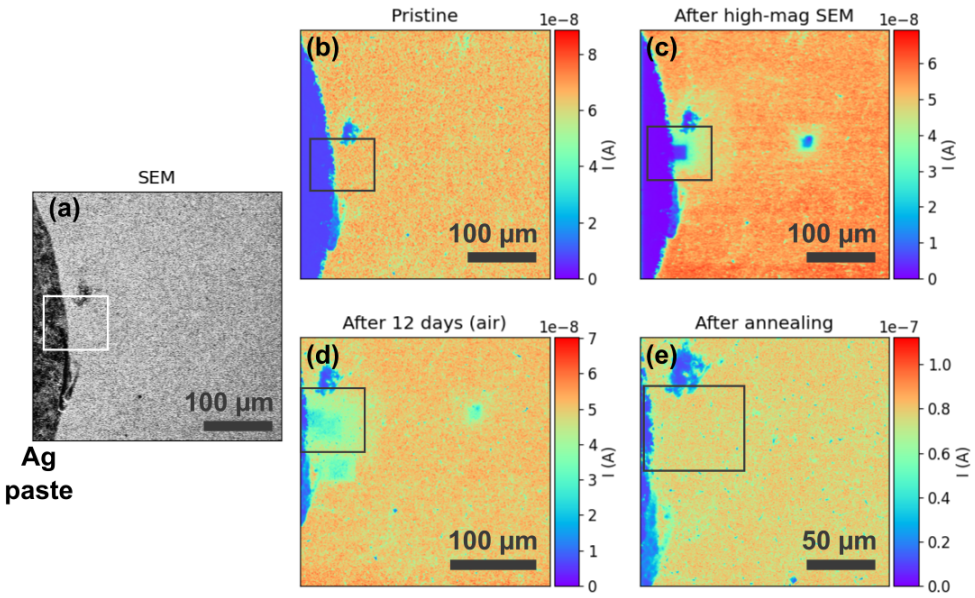

Figure A.3: Plane-view **(a)** SEM image and **(b)**-**(e)** EBIC maps of the same Si NW/a-Si:H solar cell, **(b)** before, **(c)** after high-magnification observation, **(d)** after 12 days stored in air, **(e)** after annealing at 180 °C (right after **(d)**). The damaged region is highlighted. A new damaged region can be seen in **(d)**, following a high-magnification observation the day after the first session. The blue region on the left (no current) corresponds to the Ag paste, which prevents e^- from reaching a-Si:H. $V_{acc} = 15\,kV$. The current from the p-i-n junction is displayed as positive.

depends on the dose of electrons [Schneider 1987]. It explains why this effect is only observed for high-magnification observations, but we did not assess the electron dose. In literature, different methods have been used to characterize them and their relation with light-induced defects. Some similarities exist, as they both result in increasing defect densities, that go to a saturation value and can be annihilated by similar annealing conditions. However, it has been shown that the e-beam generates different types of defects, with one type at an energy level similar to the defects mostly found in SWE mechanism [Babras 1990]. A two-stage annealing kinetics has been observed [Grimbergen 1993], which confirms a partial similarity with SWE mechanism. However, the creation of defects with e-beam is much more efficient. More defects are created with e-beam compared to light for similar energies [Schneider 1987], and even for the same rates of e^-/h^+ pair recombinations [Yelon 2000]. This corresponds to our experiments, where most current is lost after a <1 min observation.

A.2.3 Difficult EBIC acquisition of Si NW/a-Si:H

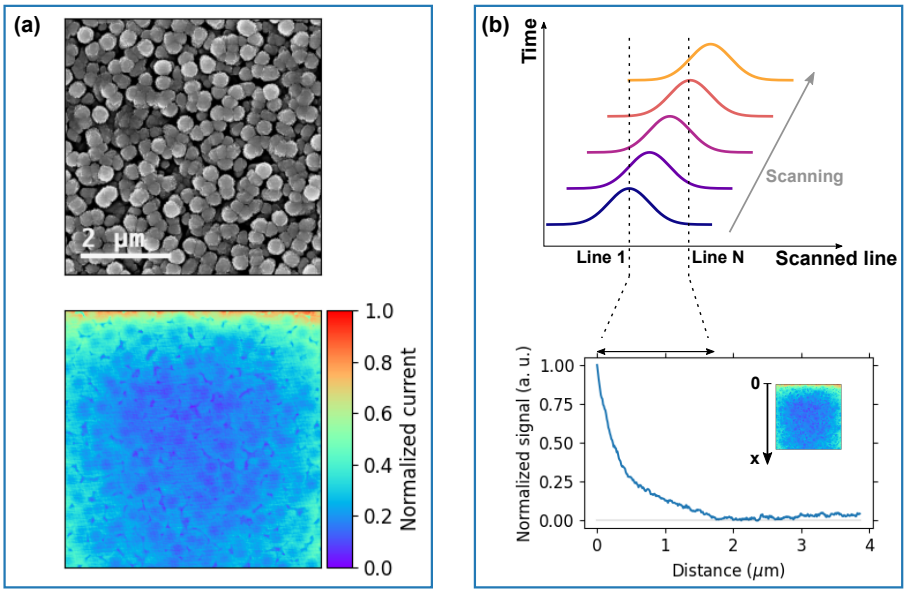

Figure A.4: **(a)** Top-view SEM image and EBIC map of the normalized current in a Si NW/a-Si:H solar cell. The scanning is from top to bottom and from left to right. **(b)** Schematics of the scanning process with e-beam (top) explaining the profile of current (bottom). The inset shows the orientation of the profile. $V_{acc} = 20\,kV$.

The degradation under e-beam is very fast and makes the high-resolution EBIC observation of Si NW/a-Si:H difficult. Figure A.4 **(a)** displays a high-magnification SEM image and the corresponding EBIC map of Si NW/a-Si:H. The scanning is from top to bottom and from left to right. A high signal can be observed at the top of the map, but it quickly vanishes. This degradation is strongly detrimental for the observation of a-Si:H with EBIC. Low electron doses and large probe volumes (with high acceleration voltages) are a possible solution. In addition, in the same way that a reverse bias prevents the recombination of e^-/h^+ pairs and the creation of SWE-related defects, a

reverse bias during EBIC observation could help. Yet, it is possible only for solar cells with a high R_{shunt}.

The signal decrease can be used to determine the size of the probe volume. Scanning is made line by line, but the probe volume is larger than the pixel size and affects the neighboring pixels, as drawn in Figure A.4 **(b)**. The cross-section of the probe volume is represented as a gaussian distribution. *Line 1* is the first line scanned for the map, which corresponds to the highest EBIC. Because of the dispersion of the beam, the generation is not limited to the scanned line. After the complete scanning, *line 1* has been exposed to half of the probe, while *line N* is the first line which has been exposed to the whole probe. The following lines are as much exposed as *line N*, the signal is steady. The distance required for the stabilization of the signal corresponds to half the probe cross-section. We determine this distance from the profile in **(b)** and estimate the total diameter of the probe cross-section to ∼3 µm for V_{acc}= 20 kV (full width at half maximum $FWHM \simeq 1.8\,\mu m$[1]). Simulations of a flat sample (detailed in Section A.3) show that, in the a-Si:H film, 95 % of the energy of electrons is lost in a cross-section of less than 2 µm diameter, which is similar to the FWHM we expect.

A.3 Effect of the acceleration voltage V_{acc}

In Si NW/a-Si:H solar cells, two junctions can be probed with EBIC. They are displayed in Figure A.5 **(a)**. Given the polarity of the connection, the p-i-n junction should result in a negative current. There may also be a Schottky barrier at the interface between the amorphous silicon and the ITO. The generated current at the Schottky junction should be positive. I studied a Si NW/a-Si:H solar cell with plane-view EBIC, using different acceleration voltages V_{acc}, i. e. different energies of the incoming electrons. The sample studied in this section has a thick ITO layer (nominally 240 nm) as top contact. Figure A.5 **(b-c)** shows the change in the EBIC map of Si NW/a-Si:H for an acceleration voltage ranging from 5 kV to 25 kV. We can see a circular area, which corresponds to the ITO area, on which a dot of Ag paste has been made to connect it with a probe. The same cell is observed with different V_{acc}. We started the observation with the lowest V_{acc}, increasing it by 5 kV steps.

With the lowest V_{acc} (5 kV), we can see a higher current generated on the edge of the ITO pad. In the center, the current is almost null. Increasing V_{acc} to 10 kV results in a higher current everywhere in the cell. At 15 kV, the current generated and collected is almost uniform. At 20 kV and 25 kV, the contrast differs: the current on the edge is lower than in the center. In addition, the maximal current at 20 kV is lower than at 15 kV.

When the acceleration voltage is increased, incoming electrons can penetrate deeper in the sample. It does not significantly affect the SEM image, because the secondary electrons used for detection come from a thin layer below the surface due to their low energy. However, it can strongly change the EBIC signal. It has to be taken into account for a good understanding of the observed signal. It is used in plane-view observation to probe the different layers of a planar sample. To understand better the probe volume in

[1] If we consider that the lateral distribution of the generation volume is gaussian (see Section A.1), we can estimate the full width at half maximum ($FWHM$). We consider the total diameter d_0 to be $\simeq 2 \times 2\sigma$, with σ the gaussian deviation. Hence $FWHM = \sqrt{2 \ln 2}\frac{d_0}{2} = 1.8\,\mu m$.

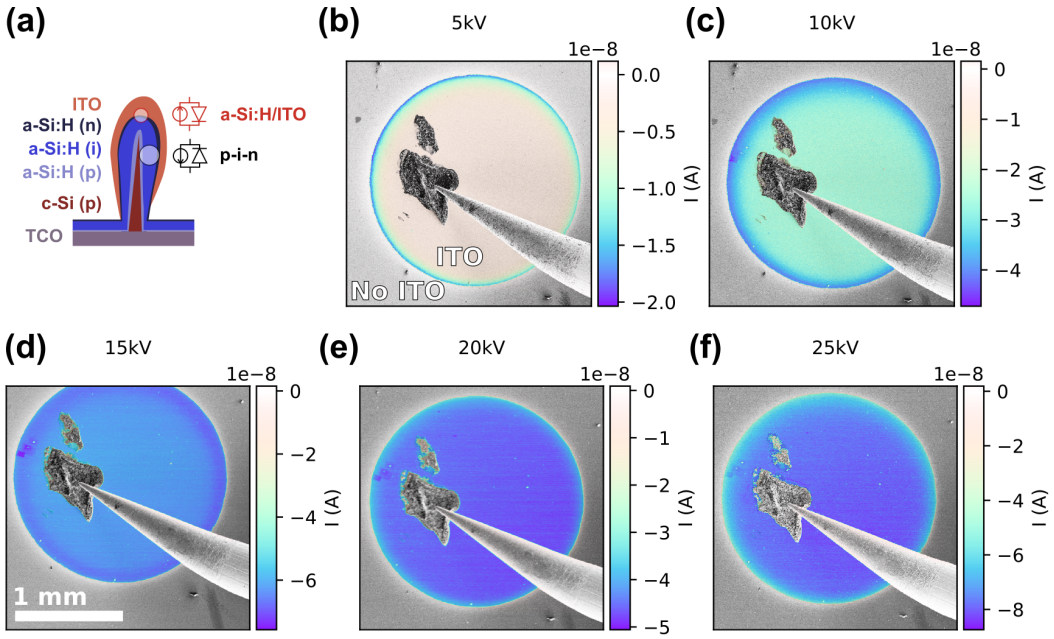

Figure A.5: **(a)** Schematics of a single Si NW/a-Si:H. The two junctions that can be observed in EBIC are shown with a diode and a current source. **(b-e)** EBIC map superimposed on a SEM image of a Si NW/a-Si:H solar cell for an acceleration voltage of **(b)** 5 kV, **(c)** 10 kV, **(d)** 15 kV, **(e)** 20 kV, **(f)** 25 kV.

the Si NW/a-Si:H, I modeled the solar cell by a stack of thin films and ran Monte-Carlo simulations using Casino[2]. Figure A.6 shows the trajectories of electrons for different acceleration voltages, as well as the maximal depth they reach. It is clear that with 5 kV, electrons cannot go through the ITO film and excite e^-/h^+ pairs in a-Si:H in the flat structure, which accounts for the absence of current in the center of the cell. On the edge of the cell however, the ITO film is likely thinner and e^-/h^+ pairs can still be generated by the electron beam. Increasing the acceleration voltage results in a deeper probe. In particular, the maximum of generation in a-Si:H likely occurs for V_{acc} between 15 kV and 20 kV. Indeed, both show an almost uniform current and there is a change in contrast in the current value between the center and the edge of the cell between the two V_{acc}. In the Casino simulation, the acceleration voltage that results in the maximal generation in the a-Si:H layer is between 10 kV and 15 kV. We would rather expect the NW geometry to diminish the acceleration voltage needed to reach a-Si:H compared to a planar structure, and the difference between the measurements and the simulation is not yet fully understood.

Finally, at high acceleration voltage, the edge of the cell presents a lower current than the center. It may be related to a difficult collection of current in the thin ITO on the edge. However, it is more likely due to the degradation of a-Si:H under the electron beam, which results in the absence of EBIC (see Section A.2). Because the ITO is thinner on the edge, e^-/h^+ pairs were generated in the a-Si:H close to the edge from lower V_{acc}. Since the observation is on the same cell and with increasing V_{acc}, the a-Si:H

[2]Program based on Monte-Carlo simulations of the trajectory of electrons in solids. It has been developed at Université de Sherbrooke (Canada), https://www.gegi.usherbrooke.ca/casino/.

on the edge started degrading before the a-Si:H in the center. This degradation also accounts for the lower current observed with 20 kV compared to 15 kV. After this row of measurements, we made a second observation with $V_{acc} = 15$ kV. It shows a similar distribution of current compared to the first map at 15 kV, but the maximal value is reduced to -5.8×10^{-8} A.

To observe the current induced in the p-i-n junction for Si NW/a-Si:H solar cells covered with a thick layer of ITO, an acceleration voltage of 15-20 kV is needed. It could be reduced with thinner contacts. Bias could be used to flatten one of the junction and prove its presence or absence at different V_{acc}. However, we observed large cells, with many shunt paths, and an applied bias results in a strong current that saturates the amplifier and prevents the reading of EBIC. Nonetheless, to map the current and its transport over the cell, probing the Si NW/a-Si:H/ITO interface with lower voltages can be sufficient, even though the current does not come from the junction. In addition, if there was a Schottky contact between ITO and a-Si:H, a positive current would be recorded, especially at low V_{acc}, which is not the case. Although the ITO/a-Si:H interface is difficult to probe in this geometry, it suggests that there is no significant Schottky barrier between ITO and n-doped a-Si:H. It would be interesting to compare between different TCOs.

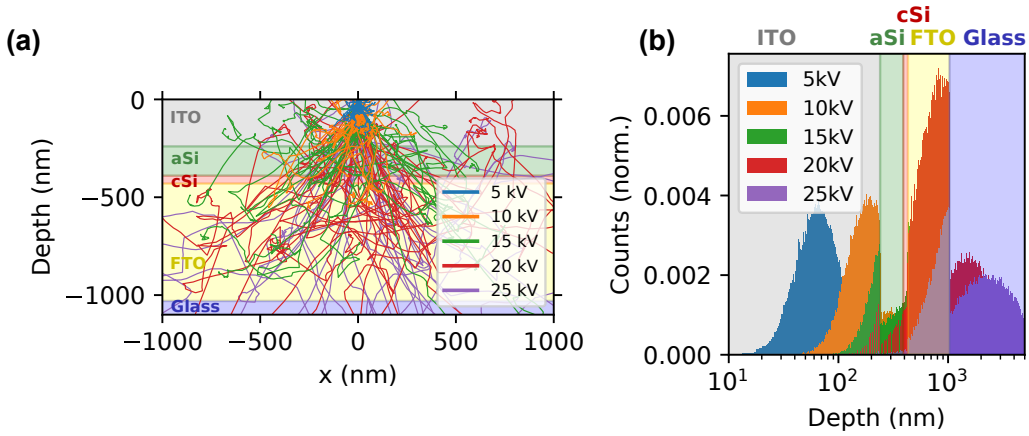

Figure A.6: **(a)** Trajectories of electrons in a FTO/c-Si/a-Si:H/ITO model of our Si NW/a-Si:H cells. **(b)** Distribution of the maximal depth reached by incoming electrons. The simulations were run over 200k electrons. Because of the much lower density of a-Si:H compared to TCOs, incoming electrons are not slowed down much in the a-Si:H layer, which leads to a discontinuity in the distribution of the maximal depth. In both figures, the layers are indicated by a background color.

A.4 III-V NW on Si tandem solar cells

A.4.1 Why III-V NWs for tandem cells?

The highest conversion of the solar light with a tandem cell made on c-Si requires a 1.7 eV band gap energy. Thanks to the tunability of their band gap energy with the alloy composition, III-V materials are a possible absorber for the top cell. However, they cannot be grown directly on c-Si because of lattice mismatch and antiphase domains.

A thick buffer layer made of defective III-V could be used for the growth directly on the c-Si cell, but raises optical and electrical issues for a solar cell. Instead, the III-V cell needs to be transferred to the c-Si one. Thanks to their surface relaxation of stress, NWs are thus a possible route to efficient monolithic III-V/Si tandem solar cells. For a 2-terminal device, an electrical connection is needed between the two cells. A tunnel junction is one possibility. This structure, first described in 1958 by Esaki [Esaki 1958], consists in very thin and highly doped p- and n- regions, that enable a tunneling of charge carriers from one cell to the other, hence a current, with no loss in the energy of carriers. Due to the control of the doping and thickness, a working tunnel diode is not so easy to make and EBIC can be used to characterize it as well as the full tandem device.

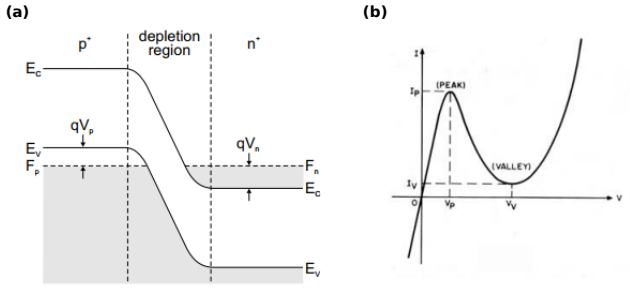

Figure A.7: **(a)** Band diagram at thermal equilibrium and **(b)** I-V curve of a tunnel junction. The transition between the tunneling and the diffusion currents results in a decrease of current with an increase in voltage, called the *negative differential resistance (NDR)* and is typical of a tunnel junction. Extracted from [Grundmann 2006].

A.4.2 Top-down

A top-down approach through etching is also possible. It enables a better control of the material parameters and can confirm that a structure is relevant.

An InGaP axial junction with a tunnel diode has been grown and transferred to a c-Si substrate (no junction) at Fraunhofer. NWs have been etched down at IBM Zürich, with the resulting structure shown in Figure A.8 **(a)**. The InGaP axial junction is a p-i-n junction. Between the p-doped region and the c-Si cell, a tunnel junction made of highly doped n and p layers makes the electrical connection. I added the expected junctions and their orientation in the Figure as diodes and current sources. The diode current cannot be directly assessed with EBIC.

Figure A.8 **(b)** shows the signal corresponding to the p-i-n junction under a 0.5 V bias, while **(c)** displays the EBIC of diodes opposite to the junction. At the NW bottom, we see the tunnel diode. At the top of the NW, we also observe a current. It corresponds to a Schottky barrier between the tip and the NW. Opposite biases are needed to observe the diodes of opposite polarity. For a better observation of a junction, we can apply a reverse bias to it. This improves the collection of carriers at the junction and ensures that the opposite junctions in the device are not preventing the collection of the current (opposite diodes are then forward-biased). EBIC observation confirms the presence of

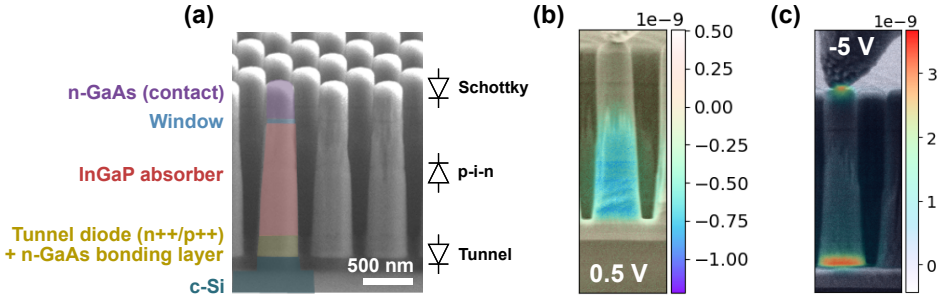

Figure A.8: **(a)** Colored SEM image of the Si/InGaP NW solar cell, **(b)** EBIC map (superimposed on SEM image) corresponding to the p-i-n junction ($V_{bias} = 0.5\,V$), **(c)** EBIC map (superimposed on SEM image) corresponding to the tunnel diode and showing a Schottky barrier ($V_{bias} = -5\,V$). $V_{acc} = 3\,kV$.

the p-i-n junction and the tunnel diode and their position. Their signals are detailed below.

Tunnel diode From the EBIC map, we can draw a profile of the tunnel diode current, as shown in Figure A.9. A very narrow depletion layer is needed in tunnel junctions, to ensure the current tunneling. Typically, it corresponds to a few tens of nanometers. It is below the EBIC map resolution and the width of the depletion region of high-quality tunnel junctions cannot be precisely determined from the EBIC profile. Still, the use of EBIC confirms that a working junction has been made at the interface between the c-Si substrate and the III-V NW.

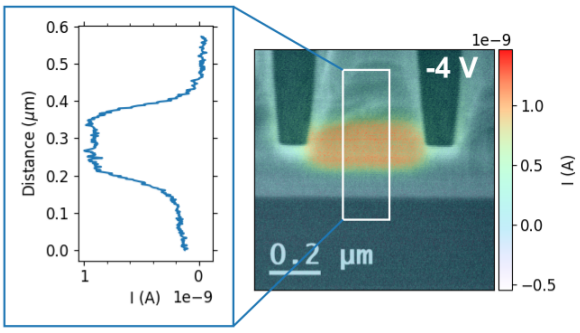

Figure A.9: EBIC map superimposed on SEM image of the n^{++}/p^{++} tunnel junction for $V_{bias} = -4\,V$ and profile of the current. $V_{acc} = 3\,kV$.

p-i-n junction First, a reverse bias is needed to collect the generated current. It is required because of the Schottky contact between the tip of the probe and the NW. Although the tunnel junction also has an opposite polarity, it works as an ohmic contact and should not play a significant role. In an ideal p-i-n structure, there is a constant electric field in the intrinsic region and we expect a flat profile of current over the intrinsic part in EBIC. We indeed observe a wide signal in the p-i-n region, but it does not correspond to the whole intrinsic layer (Figure A.8 **(b)**). It is limited on the n-side.

In addition, the current is slightly higher at the bottom of the NW (Figure A.10). It is likely related to the lower mobility of holes in InGaP. In a p-i-n junction, the span of the profile and the position of maximal current are actually dependent on the mobility of charge carriers through the drift length L_{drift} [Abou-Ras 2019]. If the mobilities of electrons and holes differ, a maximum in current is observed closer to the contact of lower mobility carriers. It can also account for the lack of signal in the intrinsic part closer to the n contact. This effect can be more important in EBIC, since the high generation rate results in screening and reduces the electric field.

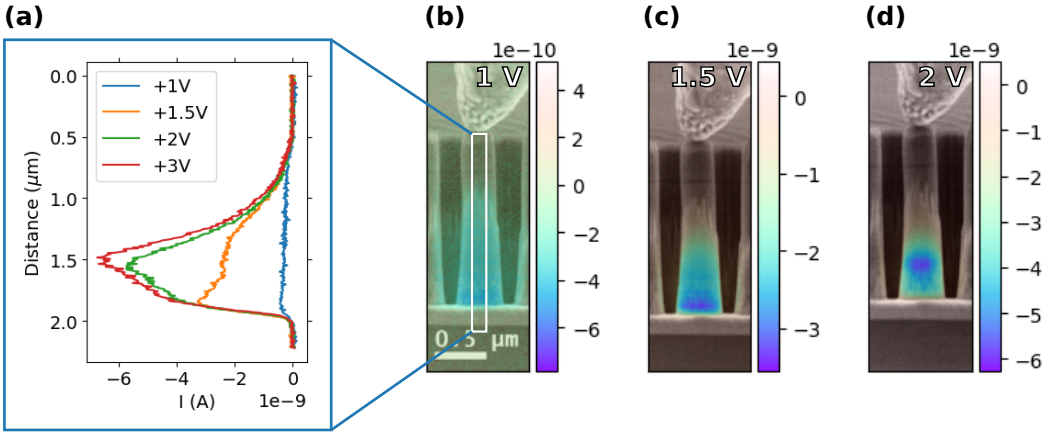

Figure A.10: **(b-d)** EBIC maps superimposed on SEM of a p-i-n InGaP NW under reverse bias. Due to the electrical connections, the junction current is negative. **(a)** shows the profiles of the current under reverse bias. The region over which the profile is plotted is shown in **(b)**.

We also noticed that the profile of the generated and collected current is strongly altered by the (reverse) bias (Figure A.10). Under stronger bias, the current level increases, the region of maximal signal becomes narrower and the maximum shifts from the p^{++}/p interface to a position inside the intrinsic layer. We confirmed that this effect does not come from charging of traps under exposure to the e-beam (it is reversible when the bias is reduced again).

Nominal bias vs. actual bias In addition, the bias applied to the whole cell may differ from the one obtained at the junction. It depends on the structure of the solar cell and the resistances inside, but also on the contact with the probe. Due to mechanical vibrations, the probe can (partially to totally) lose the contact to the NW. The same nominal bias can thus result in very different observations. This is illustrated in Figure A.11. Although **(b, c)** have the same nominal bias, the current level and distribution differ.

A.4.3 Bottom-up

Structure and growth Tandem solar cells made of III-V NWs on c-Si have been made at INL (Institut des Nanotechnologies de Lyon) by M. Gendry and A. Fave in the framework of the ANR project *Hetonan*. Their structure is shown in Figure A.12 **(a)**.

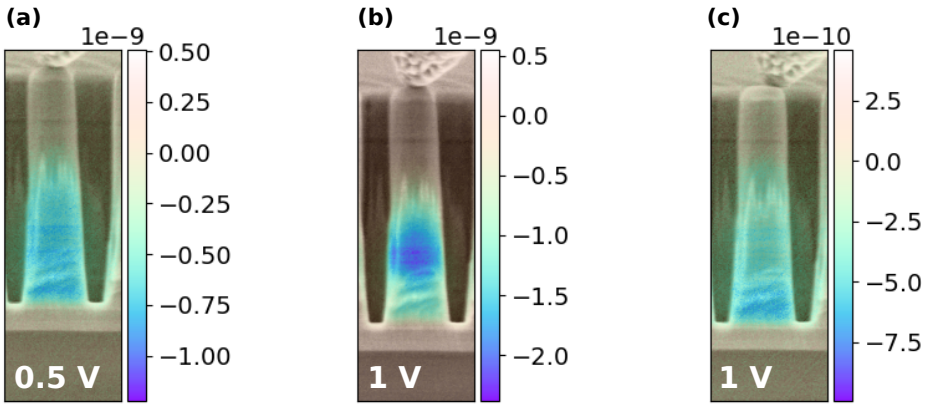

Figure A.11: EBIC maps superimposed on SEM image of a p-i-n InGaP NW under reverse bias. **(a, b)** were recorded in a row. **(c)** was recorded later, after a new contact was made (see the different position of the tip). It is different from the first map at $V_{bias} = 1\,V$, but is similar to the map at $V_{bias} = 0.5\,V$. $V_{acc} = 3\,kV$.

A c-Si cell with a tunnel diode is used as substrate for the NW growth. A GaAs core, p-doped with Be, is first grown by MBE with a Ga catalyst. Although GaAs does not have the optimal bandgap for the tandem solar cell, the growth of AlGaAs NWs is challenging. Therefore, a GaAs core was formed to enable the radial growth of a AlGaAs shell. The consumption of the catalyst at the end of the growth of the GaAs core results in an intrinsic part on top of the GaAs NW. The shell is made of a p-i-n junction of $Al_{0.2}Ga_{0.8}As$, with Be and Si for the p- and n- dopings respectively. Details on the growth can be found in [Piazza 2018]. This AlGaAs composition corresponds to a band gap energy of 1.7 eV, optimal for a tandem on c-Si. A passivation layer (InAlAs) is added to reduce recombinations at the NW surface. NWs are then embedded in BCB. After RIE and ITO sputtering, a device is obtained. For EBIC observations, the electrical connection is always made between the top of NWs (+) and the back contact of the c-Si cell. The current corresponding to the p-i-n junction is then negative.

p-i-n radial junction Because the junction is radial, we expect a collection from the whole NW. As displayed in Figure A.12 **(b)**, the current is indeed collected over a large region (>1 um), with a flat profile over 500 nm. The decrease in the bottom part of the NW may be related to a thinner shell, which we observe in the SEM images. It is particularly an issue regarding the n-doped layer. If it is too thin, it may be poorly conductive, even though the depletion effect due to surface states is limited thanks to passivation.

Homogeneity EBIC observations also enable to assess the homogeneity from NW to NW. Figure A.13 **(a)** displays the SEM image and the corresponding map of the p-i-n EBIC in NWs. Thanks to the ITO contact, induced current from several NWs can be collected. The three central nanowires show a good homogeneity (intensity of current and spreading of the signal). Other NWs in the EBIC map, such as the right NW in the white frame, display a shorter (apparent) active region. The absence of current in the bottom part compared to other NWs is due to a lower generation of e^-/h^+ pairs.

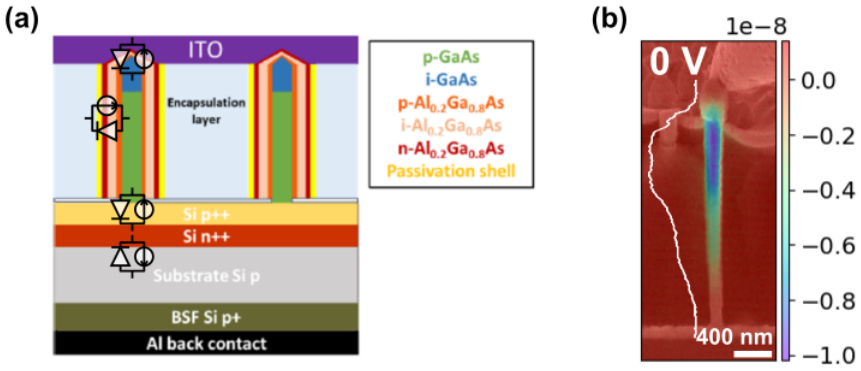

Figure A.12: **(a)** Structure of a tandem cell made of radial p-i-n AlGaAs NWs on c-Si. The expected junctions and their orientation are schematically represented as diodes and current sources. **(b)** EBIC map superimposed on a SEM image of a single NW. The current profile is drawn in white. $V_{bias} = 0\,V$, $V_{acc} = 5\,kV$.

These NWs are partly embedded in BCB (see SEM in Figure A.13 **(a)**), which absorbs electrons. Because of the low acceleration voltage, the probe depth is not sufficient to reach the NWs. In addition, we observe some dead NWs (white frame, left NW). They correspond to NWs disconnected, either from the ITO or from the substrate. We indeed observed that some NW feet broke under e-beam exposure (no manipulation with the probe). It may be due to mechanical stress induced by the BCB under exposure to the electron beam.

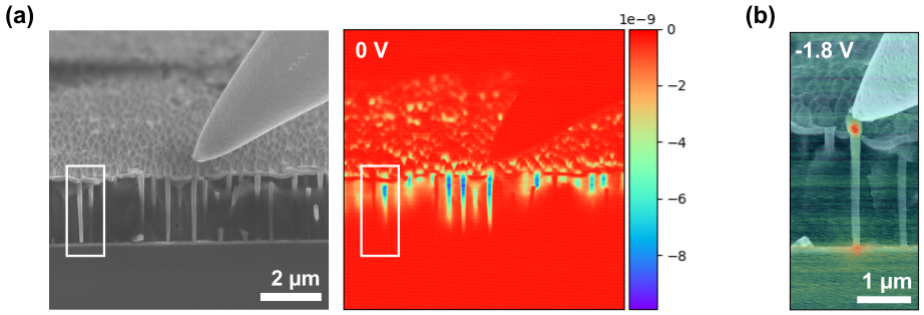

Figure A.13: Cross-sectional **(a)** SEM image and corresponding EBIC map of GaAs/AlGaAs NWs on c-Si with no bias. The p-i-n signal can be seen. **(b)** EBIC superimposed on SEM image under forward bias (with respect to the p-i-n junction). $V_{acc} = 5\,kV$.

Tandem cell I observed only one junction during EBIC observations: NWs were active while no signal was observed in the Si sub-cell, despite different biases (from $-2.5\,V$ to $1\,V$). To discard the surface effects that can be detrimental in the EBIC measurement of a cleaved planar cell, I also used higher acceleration voltages, up to $V_{acc} = 25\,kV$.

Still, I recorded no signal from the c-Si cell.[3] This behavior actually comes from the local excitation in EBIC. During scanning, the electron beam generates carriers in a small region, i.e. only in one cell. Because the top and bottom cells are connected in series through the tunnel diode, current matching is required. It is not fulfilled under e-beam scanning, since the non-illuminated cell does not generate an equal current. This explains why we do not observe the c-Si cell. Yet, we are still able to see the signal coming from the NWs. If there are shunts in the bottom cell, they may enable the current to go through. The I-V curve shows a low R_{shunt} which would confirm this idea. In addition, this could also explain why we observe the NW signal and not the c-Si one. The silicon cell is much larger than one NW and it is thus more likely to have shunt paths. Still, a shunt current would require a small reverse bias and we observe the NW illumination current even at zero bias. The actual bias at the bottom cell likely differs from the globally applied bias, because of voltage drops due to resistance effects (see Figure A.11).

We should still be able to see the tunnel diode. When a reverse bias is applied to the tunnel junction (negative bias here), both cells are forward-biased and they do not hinder the flow of current. However, we observed no clear signal that we could attribute to the tunnel diode with certainty: some signal was present at the foot of the NW (Figure A.13 **(b)**), in the white planar layer. However, it me be related to artifacts due to the parasitic growth.

Figure A.14 shows a high-magnification EBIC map of one NW under different biases. **(a)** shows that the intrinsic GaAs top due to the growth partly prevents the collection of current at the top contact, due to a Schottky barrier with ITO. In **(b)**, the EBIC signal from the junction shows a lateral variation, with a change in the decrease slope. The SEM signal also shows variations at the same positions, that stem from the facets of the NW. The EBIC profile is modified by the shape of the NW, because it affects the generation profile. With a tilted illumination, the active region appears deeper and results in a lower generation. In addition, a lateral shift of the beam (i.e. scanning) corresponds to less and less probed active region. This accounts for the change in the slope.

A.5 GaN/InGaN NW LEDs

In Section 1.2, we detailed the benefits of nanowires in solar cells. Their mechanical properties are also an asset for the integration of GaN LEDs on Si, due to the absence of lattice-matched substrate. Gallium nitride (GaN) with InGaN is mostly used for blue light LEDs. With quantum wells, injected electrons and holes are confined in the well. It increases the overlap of their wavefunctions and leads to an enhanced emission. GaN/InGaN NWs LEDs have been made at C2N (axial junction) and at CRHEA (radial junction) and characterized with EBIC.

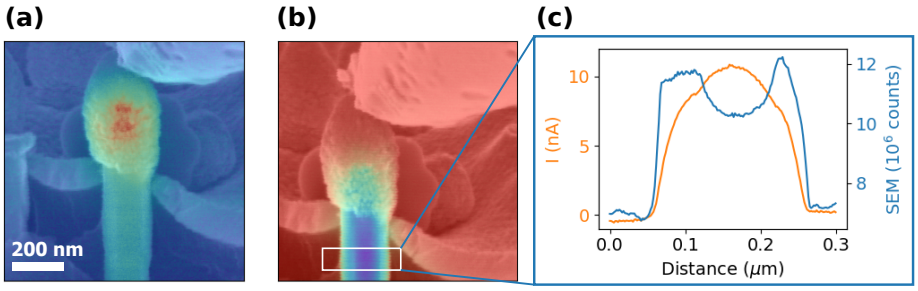

Figure A.14: EBIC map superimposed on SEM image for different biases. **(a)** $V_{bias} = -0.8\,V$ shows the barrier at the contact between the intrinsic GaAs part and the ITO, **(b)** $V_{bias} = 0\,V$ shows the signal of the p-i-n junction. **(c)** Lateral current (orange) and SE signal (blue) profiles in the NW. A positive signal is plotted for an easier comparison with the SEM signal. $V_{acc} = 5\,kV$.

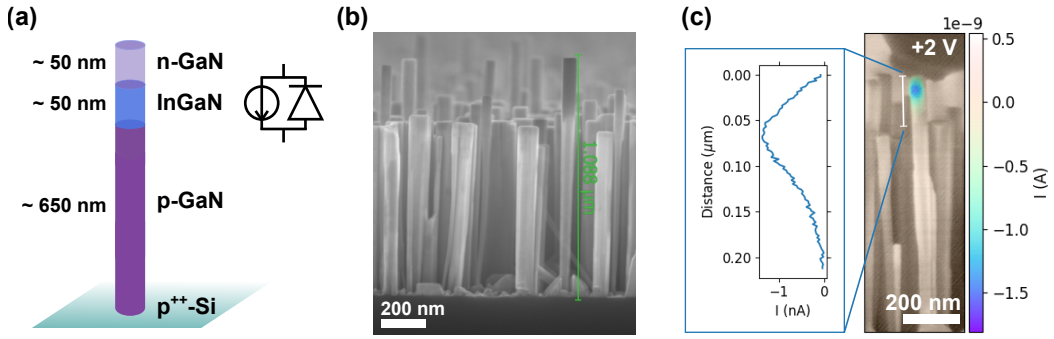

Figure A.15: **(a)** Nominal structure of GaN/InGaN NWs. The expected junction is schematically represented as a diode and current source, **(b)** SEM image of the NWs, showing the dispersion in length and diameter, **(c)** EBIC map superimposed on SEM image of a long NW. $V_{acc} = 5\,kV$.

A.5.1 Axial junction GaN/InGaN NWs

GaN/InGaN NWs were grown at C2N by A. Kunti and N. Gogneau using MBE. Their structure is presented in Figure A.15 **(a)**. They consist in an axial p-i-n heterojunction, with an intrinsic InGaN region between two doped GaN regions. The In content is around 20-22 %. The NWs are self-catalyzed and Mg and Si are respectively used for doping of the p and n parts. The n-part is on top, which is expected to limit the radial growth [Saket 2021]. Figure A.15 **(b)** displays the morphology of the NWs. There seems to be two types of NWs: most are ∼750 nm high, but some are ∼1.1 µm high and appear thinner. The origin of this bimodal distribution is not fully understood. I have observed 16 NWs, among them 13 presented an EBIC signal. The position and distribution of the current differed between NWs. Figure A.15 **(c)** displays the EBIC map and profile of a long NW that corresponds to the expected structure. The current is maximal 50-70 nm from the top of the NW, which would be close to the n-GaN/InGaN junction and spans over 150-200 nm. 7/13 NWs presented the same type of signal. 5/13 NWs presented a signal over the whole NW[4]. It is likely related to a radial growth. These NWs are thicker than the ones with the signal on top. They may also lack the top n-doped GaN, which would account for the absence of signal from the axial junction.

After EBIC observation, the NW array was processed (encapsulation, etching of the encapsulant and electrical contact) and characterized by N. Amador-Mendez. Since the p-i-n junction was observed only for thin and long NWs, the etching time was chosen so that only the longer NWs emerged. Atomic-Force Microscopy measurements showed that only 1 % of the grown NWs were connected. The emission of light with the processed LED was demonstrated (Figure A.16). We can see the peak corresponding to the InGaN segment around 430 nm. A lower peak is observed at 380 nm, which is likely related to a defect in one of the GaN segments.

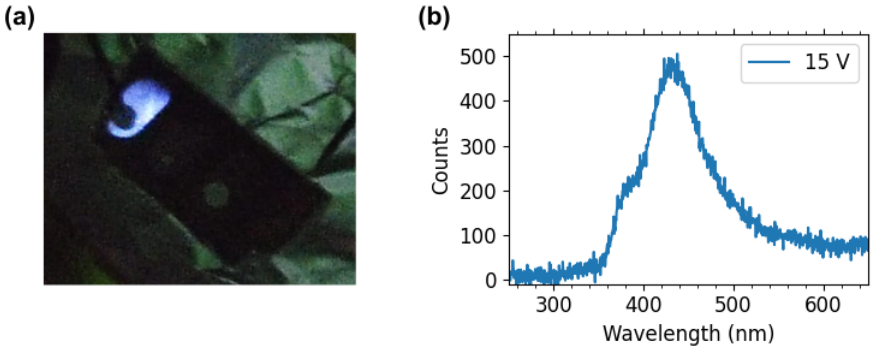

Figure A.16: **(a)** Picture of the GaN/InGaN NW LED. The luminescent area is a few mm^2, **(b)** electroluminescence spectrum at 15 V. Process and characterization carried out by Nuño Amador-Mendez.

[3]Because the cell was processed and due to the (insulating) mask used for the NW growth, I could not contact the c-Si cell alone.

[4]The last nanowire displayed a signal at the interface with the substrate.

A.5.2 Radial junction GaN/InGaN NWs

I have also worked on GaN/InGaN NWs grown at CRHEA. While both C2N and CRHEA nanowires are bottom-up NWs made of GaN and InGaN for LEDs, the growth method, the structure (radial vs. axial junction) and the resulting morphology are very different.

Structure GaN NWs with InGaN quantum wells were grown with MOCVD at CRHEA by J. Bosch and B. Alloing. As displayed in Figure A.17 **(a)**, they consist in a GaN core with radial InGaN quantum wells (QWs) and a p-doped GaN shell. Mg and Si are used respectively as p- and n-dopants. The growth starts with a high silane flux, which promotes the axial growth and also induces a high n-doping. In addition, during the growth of the heavily n-doped core, the silicon dopants segregate at the surface and make an alloy with the nitrogen and gallium atoms [Kapoor 2020]. A SiN or SiGaN layer is obtained around the core which prevents radial growth. For this reason, a non-intentionally doped (*nid*) part is added. In addition, an *underlayer*, here made of undoped GaN, is added around the core to improve the quality of the InGaN/GaN layers. The SEM images indeed show NWs with a shell ∼4 µm long (half the NW).

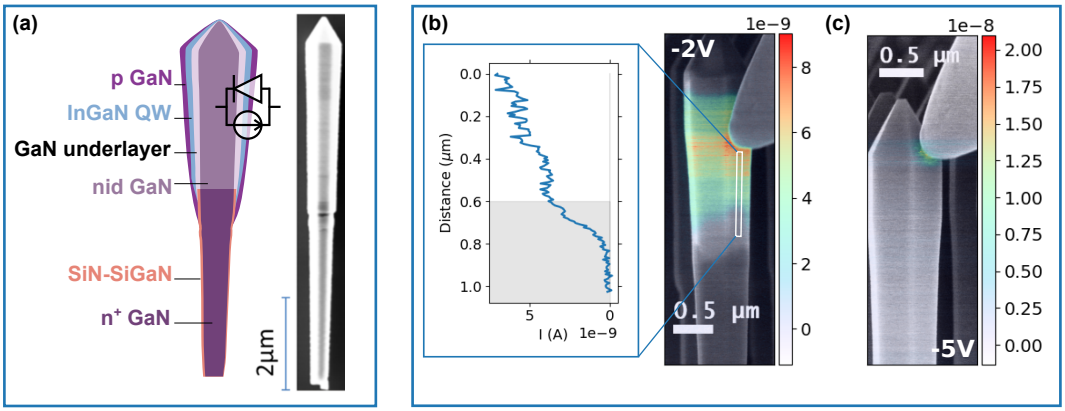

Figure A.17: **(a)** Structure of GaN/InGaN nanowires and SEM image of a NW. The expected junction is schematically represented as a diode and current source. **(b, c)** EBIC map superimposed on SEM image of a GaN/InGaN NW for **(b)** $V_{bias} = -2\,V$ and the tip on the m-planes and **(c)** $V_{bias} = -5\,V$ and the tip on the semi-polar planes on top of the NW. The current profile is also drawn for **(b)**. The horizontal lines are due to the instability of the electron beam, whose intensity could vary between linescans. $V_{acc} = 5\,kV$.

Limited conductivity of the shell Figure A.17 **(b)** presents the EBIC map of a NW together with the current profile. The junction is clearly observed under reverse bias, with a generated and collected current over most of the shell. However, it does not correspond to the whole shell, the top and bottom parts do not show any induced current. The maximum in current is obtained close to the tip of the probe and decreases away from it, as can be seen in the upper part of the profile. In a radial junction, it means that the conductivity of the outer layer is limiting the collected current. The shell

is thus more resistive than the core and the performance of the LED could be hindered by the conductivity of the GaN shell. An all-around ITO contact can be used to improve the injection of carriers in the LED. Nonetheless, there seems to be a different reason for the steep decrease of the signal down to 0 nA. As highlighted in the shaded part of the profile, there is an abrupt change in the slope ∼0.6 µm away from the probe. It likely stems from the insulating SiN layer which covers the n-doped core. The radial layers grow only on the undoped core, but because of overgrowth, part of the doped core is also covered.

The absence of signal from the top part of the NW is due to a very low conductivity of the shell. Figure A.17 **(c)** shows that a current can be collected if the probe is positioned on the top surface. It is strongly localized, under the probe. The low conductivity of the shell on the semi-polar planes can be related to its thickness, since the GaN growth is slower along this direction.

Appendix B

Ag NW process

Contents

B.1 Effect of dimensions on the opto-electrical properties

B.1.1 NW length

As explained in Section 2.4.1, with longer nanowires, lower densities of NWs are needed for percolation (eq. (2.24)). However, no conclusion is yet possible on the benefit of longer NWs for TCEs. For a given density, the NW length alters the total amount of Ag, hence the optical performance of the network. In order to assess the optical properties of the network, the surface coverage should be considered.

If we dismiss the overlap between NWs (i.e. low densities) and the interactions with light due to their dimensions, the surface coverage corresponds to the extinction due to Ag NWs and should be as low as possible. With d the diameter and L the length of Ag NWs, the coverage needed for percolation $f_{S,th}$ is

$$f_{S,th} = 5.637 \, \frac{d}{L}. \tag{B.1}$$

A lower percolation threshold is indeed obtained for longer NWs. However, compared to the previous formula, the dependence is now proportional to the inverse of L.

B.1.2 NW diameter

To a first approximation, the conductance of a nanowire of diameter d scales with d^2, while its extinction cross-section scales with d. Thicker NWs should thus perform better.

However, because of their small diameter, both optical and electrical scalings do not always hold. The resistivity of thin NWs shows a d^{-1} dependence ($d^{-2/3}$ for very thin NWs) [Sambles 1982]. In particular, for diameters below or close to the mean free path of electrons (∼35 nm in silver), a substantial increase in resistivity is observed [Bid 2006]. Likewise, the extinction cross-section is not linear with the diameter. Simulations show that the ratio between the extinction and geometrical cross-sections of NWs increases with the NW diameter (Figure B.1 **(a)**). Thin NWs ($d < 70$ nm) even have an extinction cross-section smaller than the geometrical one [Bergin 2012].

To take both effects into account for single NWs, the conductance and the extinction cross-section can be compared for different diameters. The dependence on the diameter is not monotonous anymore, as can be seen in Figure B.1 **(b)**: either very thin NWs ($d < 30$ nm) may be beneficial thanks to their optical properties, or thicker nanowires, thanks to their conductivity. Around 50-100 nm, a lower opto-electrical performance is expected.

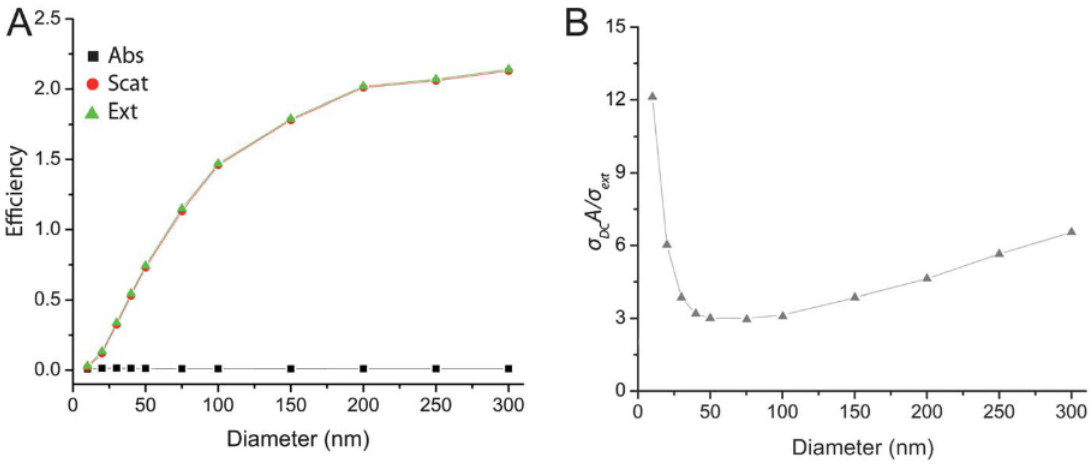

Figure B.1: **(a)** Ratio of the absorption, scattering or extinction cross-section and the geometrical cross-section depending on the diameter of Ag NWs, averaged over 400-800 nm. **(b)** Ratio of the conductance and the extinction cross-section depending on the diameter of Ag NWs. Results come from finite-difference time-domain calculations in [Bergin 2012].

In a network, the density of NWs is a supplementary parameter. For instance, the high contact resistance between NWs limits the conductivity of a sparse network. Because thinner NWs result in more possible connections, they may lead to lower $R_\square$ for a given transparency. For dense networks, the area between nanowires can become too small for the light to go through. Besides, the overlap between nanowires has to be considered.

Finally the diameter strongly affects the stability of NWs as detailed in Section B.3.1.

Briefly, thicker nanowires should display better opto-electrical performance thanks to a strong improvement of the electrical properties and a better stability, except for sparse networks (high transmittance), due to the junction resistance.

B.1.3 NW dimensions in this work

Despite these principles, we chose diameters with dimensions (10±5) µm × (60±10) nm. We dismissed very thin nanowires because of stability and cost, but we kept small diameters to achieve a finer meshing of the Si NW/a-Si:H array.

In addition, we compared the sheet resistance of drop-cast NWs with different lengths, (10±5) µm or (40±5) µm (same nominal diameter (60±10) nm). We intended to deposit the same mass of material in both cases, but the mass of deposited 10 µm NWs was lower (∼20 % lower). Although the ratio of the expected density to the percolation threshold was greater for the longer NWs, they resulted in higher sheet resistances. It is likely related to process issues. Ag NWs in suspension are prone to aggregation, especially for longer nanowires. Prior to deposition, dispersion techniques, as an ultrasonic bath, can be used. However, during deposition, aggregates can form again. For instance, thicker coffee rings were observed with longer NWs.

B.2 Deposition

Solution processing is one of the assets of Ag NW electrodes, with various deposition methods, including Mayer rod coating [Hu 2010], spin-coating [Lee 2013] and drop-casting [Lee 2008] or vacuum filtration on a membrane [De 2009]. Transferable networks can also be made [Jang 2016].

For the chosen design of the Si NW/a-Si:H solar cells, the reference size is 4 mm in diameter, with typically 21 cells on one sample (6×4 mm + 15×2 mm). To assess the effect of the density of Ag NWs, we chose to keep the same sample for different densities. Common methods for the deposition of Ag NWs are not suited to the dimensions of a single cell. Consequently, we dismissed these methods in a first approach.

B.2.1 Drop casting

Substrate temperature A small drop of Ag NW suspension is cast on the ITO cell. The substrate temperature is expected to play a role in the drying process of the suspension, which would affect the uniformity of the deposition. Several substrate temperatures, from 35 °C to 110 °C, have been tested on a glass substrate with ITO. Figure B.2 displays pictures of the resulting networks. Three main regimes are observed: at room temperature, Ag NWs constitute a uniform and low-density area with a thick outline (*coffee ring*). For medium temperatures (below 70 °C) a central dot made of Ag NW agglomerates is observed, which dies out when the deposition temperature is increased. For higher temperatures, there are several drying rings, which become clearer with an increasing deposition temperature. These effects are typical from the drop-casting of a suspension and are related to the surface tensions inside the droplet and the subsequent flows.

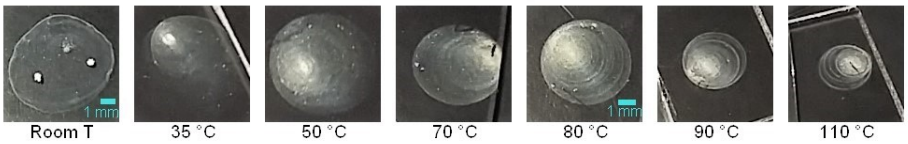

Figure B.2: Pictures of Ag NWs deposited on glass/ITO at different temperatures. The scale slightly varies from one picture to another. On the sample at room temperature (RT) only, dots of Ag paste for electrical contact can be seen.

As could be expected the evaporation time is shorter for higher temperatures, from 60 s at 35 °C to 20 s at 90 °C. Since the size results from a competition between the drying and spreading of the suspension, the area also decreases with an increase of temperature, from 7 mm at room temperature to 4 mm at 80 °C. Hence, higher average densities are obtained for higher temperatures.

A small droplet is characterized by the surface tensions at the interface of the surrounding gas and the liquid (γ_{LG}), of the gas and the solid (γ_{SG}) and of the liquid and the solid (γ_{SL}). If gravity is neglected, they determine the equilibrium contact angle θ at the triple line, following Young equation

$$\gamma_{SG} = \gamma_{SL} + \gamma_{LG} \cos\theta. \tag{B.2}$$

Origin of a pinned line Because of the heterogeneities in the substrate (geometrical or chemical), the contact angle during the liquid recession can vary. The triple line can therefore be pinned on the substrate (no change in radius, but change in contact angle), until its energy increase is enough to overcome the potential barrier. If pinning originally occurs because of substrate inhomogeneities, it is increased by the deposition of particles at the edge [Orejon 2011]. Indeed, particles alter the substrate morphology and lead to new interfaces.

Capillary and Marangoni flows inside the droplet In addition, during drying, evaporation is faster at the triple line. Because of line pinning, a flow towards the edge appears (capillary or edgeward flow). This flow brings particles at the outline of the droplet and is responsible for the coffee ring effect [Deegan 1997]. However, substrate heating also leads to a difference in temperature inside the droplet (higher close to the edge). Surface tension decreases at higher temperatures, hence a surface tension gradient is observed. Surface tension gradients in liquids (due to temperature or composition) result in the Marangoni effect, where the lower surface tension liquid is pulled towards the higher surface tension one. A flow from the edge to the apex appears [Girard 2006], which brings the particles back to the center of the droplet. A temperature increase should increase both phenomena, especially the capillary flow [Kim 2011a]. Kinetics may also alter the drying process. For instance if the droplet is drying very quickly, the evaporation will be done before the outward flow takes place.

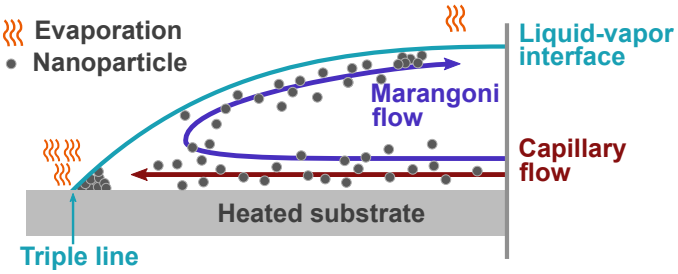

Figure B.3: Schematics of the capillary and Marangoni flows in a heated drying droplet.

Room temperature When the substrate is not heated, the droplet cannot overcome the energy barrier required for depinning and the contact line remains pinned on the substrate. During the long drying time, Ag NWs are brought to the edge by the capillary flow, where they deposit, resulting in a thick coffee ring.

Medium temperatures When the substrate is heated, depinning is easier. At medium temperatures, the coffee ring vanishes and a dot-like deposition is observed. The contact line can still be pinned, but it does not remain pinned for long. Since the outward flow is low, few particles will be deposited along the contact line, thus not observed with the eye. The Marangoni flow brings nanowires back to the center of the droplet. Because of poor interactions with the substrate, they do not adhere to it until the last part of the drying process.

High temperatures At higher temperatures, stick and-slip rings are observed. They stem from successive pinnings and depinnings of the droplet on the substrate. Combined to the outward flow, it leads to rings, formed by Ag NWs deposited along the pinned contact line. Although the effect of pinning is expected to fade when the temperature increases, the deposition of Ag NWs on the edge intensifies (increase of the outward flow compared to the Marangoni one). In addition, the pinned lines become more visible.

Leidenfrost effect At 110 °C the droplet moves on the substrate, which is due to Leidenfrost effect. When a liquid is on a substrate with a temperature sufficiently higher than its boiling point, a significant part evaporates but remains between the liquid and the substrate. This gas thermally insulates the liquid from the hot substrate, which slows the drying process down, and acts as a lubricant. Because of IPA weak surface tension, its Leidenfrost temperature is rather low, ca. 115 °C [Luo 2017]. At 90 °C and below, it was not observed.

Ag NWs alignment The assumption of a random network when drop-casting Ag nanowires is not completely valid. During spreading and receding of the droplet on the substrate, radial flows take place. The fluid motion against nanowires leads to a shear force, which radially aligns Ag NWs. This is mostly observed when spreading or drying are fast, because of stronger induced flows. Alignment along the contact line comes from the decrease in overall surface tension enabled by this new interface. It can remind of Pickering emulsions, where particles are used to stabilize the liquid droplets. Both alignments can be used to control the organization of the network [Dai 2015, Wang 2017].

Higher temperature depositions could be preferred, since it leads to a grid with nanowires aligned radially and along the rings. Nonetheless, we chose a room temperature deposition, because it resulted in a uniform central part.

Over large substrates, spin-coating, Mayer-rod coating or blade coating are used.

B.2.2 Mayer-rod coating

Mayer-rod coating is frequently used for the deposition of Ag NWs. It consists in a steel rod coiled with a wire, which is pulled over the substrate. The wire diameter controls the thickness of the wet coating. The concentration of the suspension and the number of coatings also determine the density of the final network. In addition, NWs are slightly aligned along the pulling direction: with successive depositions in orthogonal directions, well connected networks can be obtained [Zhu 2013]. This method results in low loss of suspension and is scalable to substrates a few meters wide.

Nonetheless, attempts of Mayer rod coating (close-wound, 0.30 mm-diameter wire, for wet coatings of 24 µm) on Si NW/a-Si:H samples showed that this method is not suited to NW arrays. Although as gentle as possible, the pressure needed for deposition was damaging the NWs.

B.2.3 Spin-coating

With spin-coating, uniform and reproducible depositions are achievable. However, most of the suspension is lost in the process and the method cannot be upscaled. In addition, the radial alignment might be an issue for electrical connection.

Still, because of its high uniformity and repeatability, we used spin-coating for the largest samples (chapter 3 on Ag NWs aging). Samples were spinned at 1000 rpm for 30 s with Ag NW suspension in IPA. For a uniform film, spinning had to be carried out directly after deposition, as the IPA quickly evaporates.

B.2.4 Deposition methods in this work

The deposition of Ag NWs on small ITO cells required drop-casting. We chose a room temperature deposition, because it resulted in a uniform central part. For large substrates, spin-coating was preferred because of its uniformity and repeatability.

B.3 Annealing

The network resistance arises from the inner resistance of nanowires and the contact resistance at junctions between nanowires. The latter is quite significant, due to organic residues from the synthesis (polyvinylpyrrolidone, PVP) acting as an insulating layer, and poor geometrical contact between nanowires. Values around MΩ have been measured on single (non-treated) junctions, compared to a few 10 Ω or 100 Ω for the resistance of the nanowire, depending on dimensions [Garnett 2012, Nian 2015, Bellew 2015]. For low-density networks of Ag NWs, the junction resistance strongly limits the electrical performance of the electrode. Thus, silver nanowires require a post treatment, in order to remove PVP and to sinter nanowires. Thermal annealing is commonly used

[Lee 2008], but acid or plasma treatment, electroforming, applied pressure or a conductive coating are also possible solutions [Hu 2010, Zhu 2013, Lee 2020].

Although bulk Ag melting point is much higher than the temperatures used in thermal annealing (962 °C), the dimensions of NWs enable partial melting at a lower temperature (typically 100-250 °C) [Lagrange 2015]. In nanostructures, more atoms are close to the surface compared to bulk and their higher free energy requires less thermal energy to achieve melting. With this partial melting, a reduction of surface is possible and the NWs can be sinterered at lower temperatures than bulk.

B.3.1 Thermal annealing in air

We chose the most simple and easy way to upscale annealing method, an oven with ambient atmosphere. The annealing effect was assessed through the sheet resistance value, $R_{\square}$.

Annealing of Ag NWs does not require an inert atmosphere NWs are known to possibly degrade in ambient atmosphere (details in Section 3.2.1). Thus we wanted to assess whether annealing in air was detrimental to the Ag NWs. Our monitoring of the electrical and morphological properties does not give evidence of such behavior. Under the right conditions of temperature and time, electrical properties of Ag NWs on glass are improved and no change in morphology except at junctions is observed in SEM. Nevertheless, such annealing could prompt a degradation mechanism [Deignan 2017].

Optimal temperature dependence on diameter Different annealing temperatures for Ag nanowires on ITO were tested. The effect on the sheet resistance of 20 min in air at 200 °C or 240 °C for nanowires with 60 nm and 40 nm diameter is summarized in Table B.1. Whereas 240 °C is necessary to strongly decrease the value of $R_{\square}$ for the thicker NWs, it leads to an increase in $R_{\square}$ for the thinner ones. The decrease in $R_{\square}$ stems from welded junctions, as can be seen in several regions in Figure B.4 **(a)**. Welded junctions are also observed for thinner NWs at 200 °C. The origin of the $R_{\square}$ increase is obvious from Figure B.4 **(b)**. Many particles instead of NWs are seen.

Both effects are expected and have the same origin. With heating, the mobility of atoms is increased. For low heating, rearrangement occurs only on a limited scale. At higher temperatures however, the energy may be sufficient for a full reformation of NWs into spheres [Lagrange 2015]. The energy required for rearrangement depends on the free energy of atoms. In thinner NWs, more atoms are at the surface and have a higher energy. Hence, the optimal temperature for annealing and the spheroidization temperatures are lower for thinner NWs.

Optimal annealing is a trade-off between sintering and broken NWs An annealed network of Ag NWs displays at the same time welded junctions and broken nanowires in SEM, as shown in Figure B.5. This mix has been observed for networks which showed either a decrease in $R_{\square}$ or an increase in $R_{\square}$. Both phenomena are related to heating, but are expected to occur at different temperatures [Lagrange 2015]. Yet, because these temperatures strongly depend on the diameter of the wires, both melted and broken NWs can be observed in one sample. There is indeed a dispersion in the diameters of the wires in suspension. This dispersion is clear from SEM, with nanowires

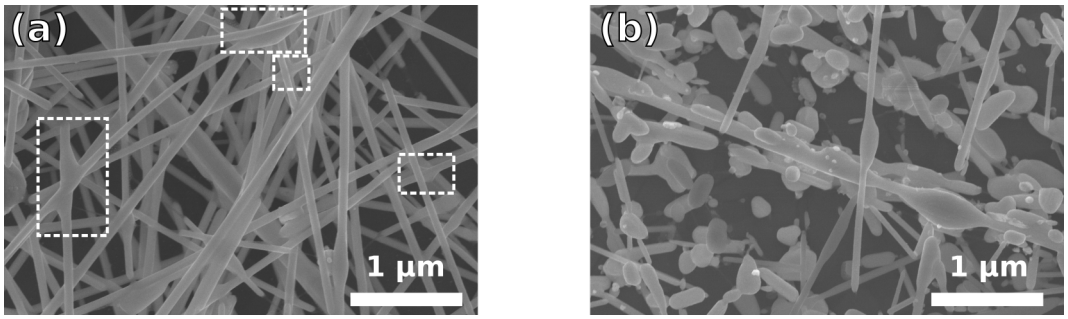

Figure B.4: SEM images of **(a)** 60 nm×10 µm and **(b)** 40 nm×35 µm Ag NWs annealed at 240 °C. Some melted junctions are highlighted with a white frame.

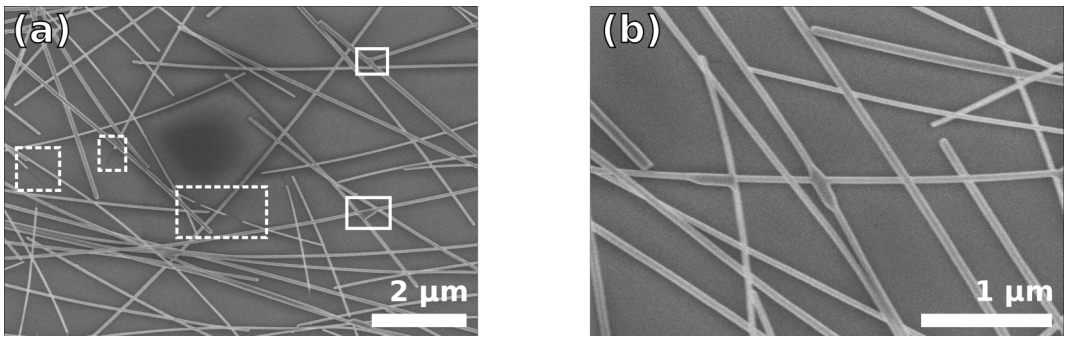

Figure B.5: **(a, b)** SEM images of 60 nm×10 µm Ag NWs annealed at 180 °C. In the lower magnification image **(a)**, melted junctions are highlighted with a frame made of a solid line, while broken nanowires are highlighted with a frame made of a dashed line.

Table B.1: Sheet resistance for different Ag NWs on ITO annealed at 200 °C and 240 °C. The measurement error on $R_{\square}$ is a few Ω/□. The averaged density of Ag NWs is also given as a function of the percolation threshold N_{th}

Ag NWs dimensions	R_{sheet} Before annealing	R_{sheet} After annealing	Ag NWs density
	Annealing at 200 °C		
60 nm×10 µm	42 Ω/□	31 Ω/□	11 N_{th}
40 nm×35 µm	34 Ω/□	22 Ω/□	108 N_{th}
Bare ITO	39 Ω/□	36 Ω/□	
	Annealing at 240 °C		
60 nm×10 µm	41 Ω/□	10 Ω/□	11 N_{th}
40 nm×35 µm	27 Ω/□	30 Ω/□	108 N_{th}
Bare ITO	42 Ω/□	32 Ω/□	

ranging at least from 30 nm to 90 nm, when the nominal diameter is (60±10) nm. In a disperse suspension, thinner NWs can thus be broken before the welding of others and the optimal annealing conditions are a balance between the amounts of melted and of broken nanowires.

B.3.2 N_2 annealing for TZO substrates

TZO annealing in air Annealing of doped ZnO (both TZO and AZO) following the same conditions as for ITO substrates led to a strong increase in $R_{\square}$. For TZO alone (80 nm), $R_{\square}$ rose from 150 Ω/□ to 7700 Ω/□ . NIR direct transmittance of AZO showed an increase beyond 1.5 µm after annealing, pointing towards a lower density of free carriers.[1] This increase is attributed to the presence of oxygen. A higher resistivity after annealing in air has been reported for AZO, although beyond 400 °C. It is related to a decrease in the carrier density, probably through increased compensation of dopants, either with higher densities of oxygen interstitials [Noh 2008] or Zn vacancies [Koida 2017]. The difference with ITO could stem from the nature and the density of compensating defects [Lany 2007].

N_2 vs. Ar:H_2 atmospheres Consequently, we considered atmospheres without oxygen, N_2 and Ar:H_2 (Ar + 5 % H_2). For a T_0 setpoint, with either N_2 or Ar:H_2, the sample was first heated up to $T_0 - 40$ °C with a 10 °C/s ramp. After stabilization for 30 s, the sample was heated up to T_0 with a 4 °C/s ramp. After 20 min, it was cooled down with N_2 and removed from the oven when the temperature reached 70 °C (∼40 min later).

Annealing of TZO in both atmospheres led to no change in the NIR direct transmittance. A small increase of the sheet resistance was observed for both gases (∼ 10 % of 80 Ω/□ for 100 nm TZO). It may be related to residual O_2.

[1] However, NIR transmittance of TZO presented no change.

New temperature conditions for Ag NWs annealing in N_2 atmosphere These conditions were deemed good enough for TZO as the substrate of Ag NWs[2]. For simplicity, N_2 atmosphere was preferred. Yet, because the heating system is different (chamber size, heating ramp, gas flows, etc), a new optimization of the annealing conditions of Ag NWs was required. An annealing temperature 30 °C lower was chosen. As displayed in Figure B.6, the same trend in $R_\square$ with annealing is observed for Ag NWs on glass or on TZO.

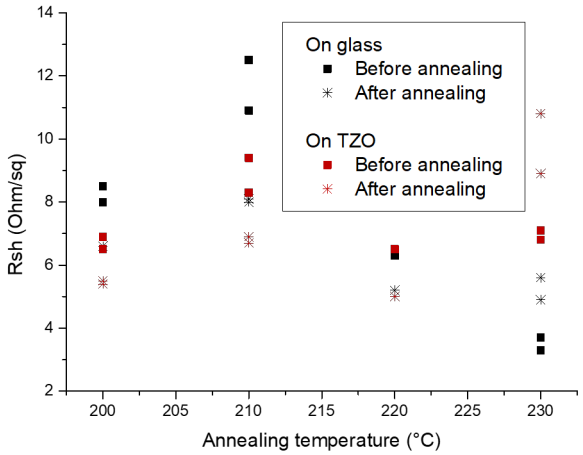

Figure B.6: Sheet resistance before and after annealing for Ag NWs on glass or on glass/TZO. Annealing was carried out in N_2 for 20 min. In the air oven, the optimal temperature for these Ag NWs was 240 °C.

Nonetheless, the oven under ambient atmosphere at 240 °C still resulted in a better annealing of Ag NWs (without TZO). This is likely related to the heating mode and the temperature profile during heating and cooling.

[2]The $R_\square$ increase is likely related to the temperature, as annealing of 80 nm TZO at 170 °C under N_2 showed a small decrease in $R_\square$ from 177 Ω/□ to 168 Ω/□.

Appendix C

Measurements under strong illumination

C.1 Laser profile

We determined the size of the laser beam after the pinhole with the knife-edge method. As a gaussian beam, the total power can be fitted with the error function. The gaussian profiles for the three pinholes are displayed in C.1. The diameter chosen for the power density is the $1/e^2$ diameter, that corresponds to a power $P = P_{\max}/e^2 \simeq 0.135\, P_{\max}$. We chose diameters large enough to avoid diffraction effects. They are still observed on the edge of the smaller pinhole (400 µm).

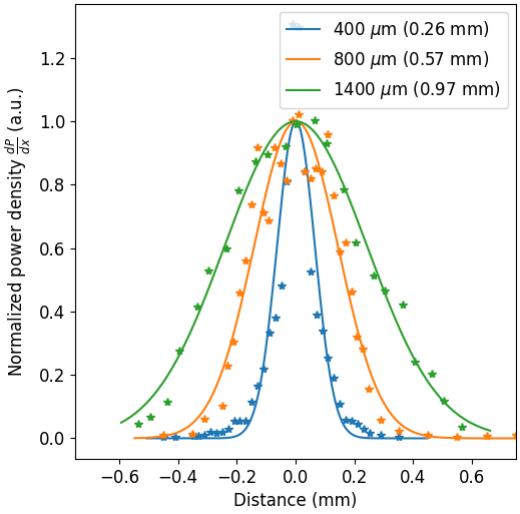

Figure C.1: Normalized power density distribution of the laser beam through pinholes of 400 µm, 800 µm and 1400 µm diameter. For each pinhole, the $1/e^2$ diameter is given in brackets. The gaussian profiles for the measurements are displayed with $\star$, the profiles for the fits with a solid line.

C.2 Performance of the measured cells under 1 Sun

Figure C.2 shows the J-V curves under 1 Sun illumination of the Si NW/a-Si:H, planar a-Si:H and c-Si solar cells used for measurements under strong illumination. The planar cell with a-Si:H displays a so-called *S-shaped* I-V curve. There is an inflection point, close to the open-circuit conditions. S-shaped I-V curves are related to potential barriers that limit the charge transport [Saive 2019]. In our cell, we believe a barrier exists at the interface between the p-doped amorphous silicon and the AZO due to a poor band alignment. It is likely related to the work function of the AZO film, which may be affected by the crystallinity and the doping of AZO, both dependent on the substrate temperature during sputtering. Interestingly, the same back-contact is used for Si NW/a-Si:H cells but does not result in an S-shaped I-V, except for a very low density of NWs. The carriers are indeed collected by the c-Si cores and the alignment between a-Si:H and AZO is not relevant for the NWs. It is however significant for the parasitic flat cell and accounts for the change at low NW densities.

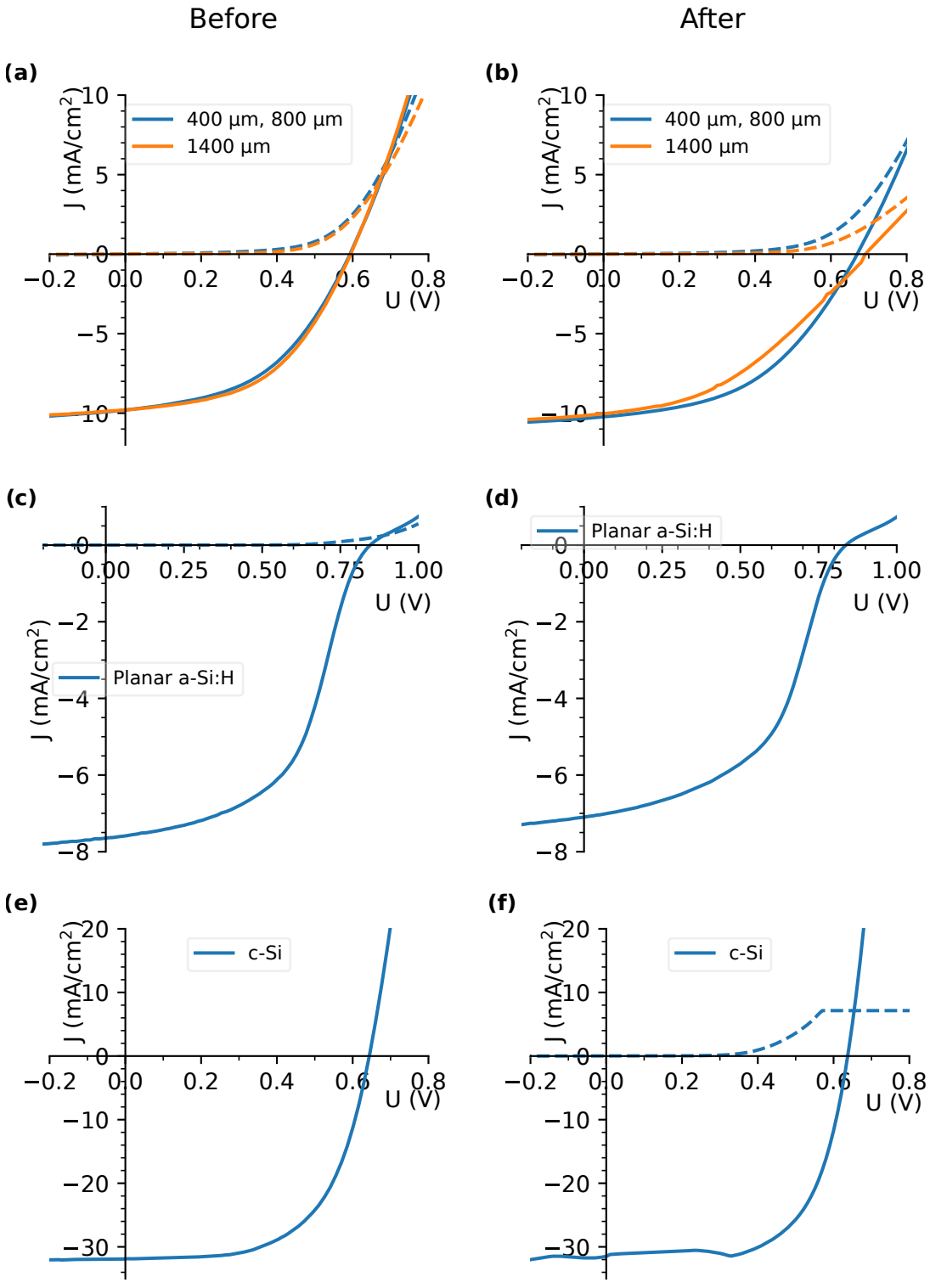

Figure C.2: J-V curve of **(a, b)** Si NW/a-Si:H, **(c, d)** planar a-Si:H and **(e, f)** c-Si solar cells under 1 Sun illumination before (left) and after (right) the strong illumination measurements. The dark c-Si current was limited by the setup.

Bibliography

[Aberg 2016] Ingvar Aberg, Giuliano Vescovi, Damir Asoli, Umear Naseem, James P. Gilboy, Christian Sundvall, Andreas Dahlgren, K. Erik Svensson, Nicklas Anttu, Mikael T. Bjork and Lars Samuelson. *A GaAs Nanowire Array Solar Cell With 15.3% Efficiency at 1 Sun.* IEEE Journal of Photovoltaics, vol. 6, no. 1, pages 185–190, 10.1109/JPHOTOV.2015.2484967. (Cited on pages 14, 18 and 19.)

[Abou-Ras 2016] Abou-Ras, Kirchartz and Rau. Advanced Characterization Techniques for Thin Film Solar Cells. Wiley-VCH, 2nd édition, 2016. (Cited on page 128.)

[Abou-Ras 2019] Daniel Abou-Ras and Thomas Kirchartz. *Electron-Beam-Induced Current Measurements of Thin-Film Solar Cells.* ACS Applied Energy Materials, vol. 2, no. 9, pages 6127–6139, 10.1021/acsaem.9b01172. (Cited on page 162.)

[Adachi 2010] M. M. Adachi, M. P. Anantram and K. S. Karim. *Optical Properties of Crystalline-Amorphous Core-Shell Silicon Nanowires.* Nano Letters, vol. 10, no. 10, pages 4093–4098, 10.1021/nl102183x. (Cited on page 21.)

[Adachi 2013] M. M. Adachi, M. P. Anantram and K. S. Karim. *Core-shell silicon nanowire solar cells.* Scientific Reports, vol. 3, no. 1, page 1546, 10.1038/srep01546. (Cited on page 21.)

[Ahmed 2020] Nafis Ahmed, P. Ramasamy, P. Balaji Bhargav, Arokiyadoss Rayerfrancis and Balaji Chandra. *Development of silicon nanowires with optimized characteristics and fabrication of radial junction solar cells with $<$ 100 nm amorphous silicon absorber layer.* Materials Science in Semiconductor Processing, vol. 106, page 104778, 10.1016/j.mssp.2019.104778. (Cited on page 21.)

[Akbarnejad 2018] Elaheh Akbarnejad, Fatemeh Dehghan Nayeri and Mahmood Ghoranneviss. *Core–shell solar cell fabrication using heterostructure of ZnO-nanowires arrays decorated with sputtered CdTe-nanoparticles.* Journal of Physics D: Applied Physics, vol. 51, no. 9, page 095105, 10.1088/1361-6463/aaa9ff. (Cited on page 17.)

[Al-Ghzaiwat 2018] Mutaz Al-Ghzaiwat, Martin Foldyna, Takashi Fuyuki, Wanghua Chen, Erik V. Johnson, Jacques Meot and Pere Roca i Cabarrocas. *Large Area Radial Junction Silicon Nanowire Solar Mini-Modules.* Scientific Reports, vol. 8, no. 1, page 1651, 10.1038/s41598-018-20126-5. (Cited on page 44.)

[Al-Ghzaiwat 2019a] Mutaz Al-Ghzaiwat. *Fabrication and study of solar cell modules based on silicon nanowire based radial junction solar cells.* PhD thesis, Ecole polytechnique, 2019. (Cited on page 21.)

[Al-Ghzaiwat 2019b] Mutaz Al-Ghzaiwat, Antonino Foti, André Nuesslein, Lukas Halagacka, Jacques Meot, Anne Labouret, Razvigor Ossikovski, Pere Roca i Cabarrocas and Martin Foldyna. *Toward Efficient Radial Junction Silicon Nanowire-Based Solar Mini-Modules.* physica status solidi (RRL) - Rapid Research Letters, vol. 13, no. 2, page 1800402, 10.1002/pssr.201800402. (Cited on page 22.)

[Al Tarabsheh 2015] A. Al Tarabsheh. *Description of the ideality factor of a-Si:H photovoltaic cells under different illumination intensity levels.* Journal of Renewable and Sustainable Energy, vol. 7, no. 2, page 023119, 10.1063/1.4918286. (Cited on page 107.)

[Alekseev 2015] Prokhor A. Alekseev, Mikhail S. Dunaevskiy, Vladimir P. Ulin, Tatiana V. Lvova, Dmitriy O. Filatov, Alexey V. Nezhdanov, Aleksander I. Mashin and Vladimir L. Berkovits. *Nitride Surface Passivation of GaAs Nanowires: Impact on Surface State Density.* Nano Letters, vol. 15, no. 1, pages 63–68, 10.1021/nl502909k. (Cited on page 18.)

[Alpuim 1999] P. Alpuim, V. Chu and J. P. Conde. *Amorphous and microcrystalline silicon films grown at low temperatures by radio-frequency and hot-wire chemical vapor deposition.* Journal of Applied Physics, vol. 86, no. 7, pages 3812–3821, 10.1063/1.371292. (Cited on page 102.)

[Anand 2021] Aman Anand, Md Moidul Islam, Rico Meitzner, Ulrich S. Schubert and Harald Hoppe. *Introduction of a Novel Figure of Merit for the Assessment of Transparent Conductive Electrodes in Photovoltaics: Exact and Approximate Form.* Advanced Energy Materials, vol. 11, no. 26, page 2100875, 10.1002/aenm.202100875. (Cited on page 40.)

[Austin 1979] I. G. Austin, T. S. Nashashibi, T. M. Searle, P. G. Le Comber and W. E. Spear. *Photoluminescence and lifetime studies on plasma discharge a-Si.* Journal of Non-Crystalline Solids, vol. 32, pages 373–391, 1979. (Cited on page 128.)

[Azizur-Rahman 2015] K M Azizur-Rahman and R R LaPierre. *Wavelength-selective absorptance in GaAs, InP and InAs nanowire arrays.* Nanotechnology, vol. 26, no. 29, page 295202, 10.1088/0957-4484/26/29/295202. (Cited on page 15.)

[Babras 1990] Suvarna Babras, V. G. Bhide, N. R. Rajopadhye and S. V. Bhoraskar. *Defect creation by 10-keV electron irradiation in phosphorous-doped a -Si:H.* Journal of Applied Physics, vol. 67, no. 6, pages 2800–2805, 10.1063/1.345446. (Cited on page 156.)

[Bae 2010] Sukang Bae, Hyeongkeun Kim, Youngbin Lee, Xiangfan Xu, Jae-Sung Park, Yi Zheng, Jayakumar Balakrishnan, Tian Lei, Hye Ri Kim, Young Il Song, Young-Jin Kim, Kwang S. Kim, Barbaros Özyilmaz, Jong-Hyun Ahn, Byung Hee Hong and Sumio Iijima. *Roll-to-roll production of 30-inch graphene films for transparent electrodes.* Nature Nanotechnology, vol. 5, no. 8, pages 574–578, 10.1038/nnano.2010.132. (Cited on page 38.)

[Bardet 2021] Laetitia Bardet, Dorina T. Papanastasiou, Chiara Crivello, Masoud Akbari, João Resende, Abderrahime Sekkat, Camilo Sanchez-Velasquez, Laetitia Rapenne, Carmen Jiménez, David Muñoz-Rojas, Aurore Denneulin and Daniel Bellet. *Silver Nanowire Networks: Ways to Enhance Their Physical Properties and Stability.* Nanomaterials, vol. 11, no. 11, page 2785, 10.3390/nano11112785. (Cited on page 67.)

[Bellew 2015] Allen T. Bellew, Hugh G. Manning, Claudia Gomes da Rocha, Mauro S. Ferreira and John J. Boland. *Resistance of Single Ag Nanowire Junctions and*

Their Role in the Conductivity of Nanowire Networks. ACS Nano, vol. 9, no. 11, pages 11422–11429, 10.1021/acsnano.5b05469. (Cited on page 176.)

[Bennett 1969] H. E. Bennett, R. L. Peck, D. K. Burge and J. M. Bennett. *Formation and Growth of Tarnish on Evaporated Silver Films.* Journal of Applied Physics, vol. 40, no. 8, pages 3351–3360, 10.1063/1.1658187. (Cited on page 66.)

[Bergin 2012] Stephen M. Bergin, Yu-Hui Chen, Aaron R. Rathmell, Patrick Charbonneau, Zhi-Yuan Li and Benjamin J. Wiley. *The effect of nanowire length and diameter on the properties of transparent, conducting nanowire films.* Nanoscale, vol. 4, no. 6, page 1996, 10.1039/c2nr30126a. (Cited on page 172.)

[Beyer 2003] W Beyer. *Diffusion and evolution of hydrogen in hydrogenated amorphous and microcrystalline silicon.* Solar Energy Materials and Solar Cells, vol. 78, no. 1-4, pages 235–267, 10.1016/S0927-0248(02)00438-5. (Cited on page 140.)

[Bid 2006] Aveek Bid, Achyut Bora and A. K. Raychaudhuri. *Temperature dependence of the resistance of metallic nanowires of diameter ? 15 nm : Applicability of Bloch-Grüneisen theorem.* Physical Review B, vol. 74, no. 3, page 035426, 10.1103/PhysRevB.74.035426. (Cited on pages 38 and 172.)

[Black 2017] L. E. Black, A. Cavalli, M. A. Verheijen, J. E. M. Haverkort, E. P. A. M. Bakkers and W. M. M. Kessels. *Effective Surface Passivation of InP Nanowires by Atomic-Layer-Deposited Al $_2$ O $_3$ with PO $_x$ Interlayer.* Nano Letters, vol. 17, no. 10, pages 6287–6294, 10.1021/acs.nanolett.7b02972. (Cited on page 18.)

[Breitenstein 2004] O. Breitenstein, J. P. Rakotoniaina, M. H. Al Rifai and M. Werner. *Shunt types in crystalline silicon solar cells.* Progress in Photovoltaics: Research and Applications, vol. 12, no. 7, pages 529–538, 10.1002/pip.544. (Cited on page 88.)

[Breitenstein 2007] O. Breitenstein, J. Bauer and J. P. Rakotoniaina. *Material-induced shunts in multicrystalline silicon solar cells.* Semiconductors, vol. 41, no. 4, pages 440–443, 10.1134/S106378260704015X. (Cited on page 88.)

[Breitenstein 2008] Otwin Breitenstein, Jan Bauer, Thorsten Trupke and Robert A. Bardos. *On the detection of shunts in silicon solar cells by photo- and electroluminescence imaging.* Progress in Photovoltaics: Research and Applications, vol. 16, no. 4, pages 325–330, 10.1002/pip.803. (Cited on page 87.)

[Breitenstein 2009] O. Breitenstein, J. Bauer, A. Lotnyk and J.-M. Wagner. *Defect induced non-ideal dark – characteristics of solar cells.* Superlattices and Microstructures, vol. 45, no. 4-5, pages 182–189, 10.1016/j.spmi.2008.10.025. (Cited on page 152.)

[Breitenstein 2013] O. Breitenstein and S. Rißland. *A two-diode model regarding the distributed series resistance.* Solar Energy Materials and Solar Cells, vol. 110, pages 77–86, 10.1016/j.solmat.2012.11.021. (Cited on page 24.)

[Brown 2010] Gregory Brown, Alex Pudov, Ben Cardozo, Vladimir Faifer, Eugene Bykov and Miguel Contreras. *Quantitative imaging of electronic nonuniformities*

in Cu(In,Ga)Se2 solar cells. Journal of Applied Physics, vol. 108, no. 7, page 074516, 10.1063/1.3485814. (Cited on page 88.)

[Cai 2009] Weiwei Cai, Yanwu Zhu, Xuesong Li, Richard D. Piner and Rodney S. Ruoff. *Large area few-layer graphene/graphite films as transparent thin conducting electrodes.* Applied Physics Letters, vol. 95, no. 12, page 123115, 10.1063/1.3220807. (Cited on page 38.)

[Cairns 2000] Darran R. Cairns, Richard P. Witte, Daniel K. Sparacin, Suzanne M. Sachsman, David C. Paine, Gregory P. Crawford and R. R. Newton. *Strain-dependent electrical resistance of tin-doped indium oxide on polymer substrates.* Applied Physics Letters, vol. 76, no. 11, pages 1425–1427, 10.1063/1.126052. (Cited on page 42.)

[Carlson 1976] D. E. Carlson and C. R. Wronski. *Amorphous silicon solar cell.* Applied Physics Letters, vol. 28, no. 11, pages 671–673, 10.1063/1.88617. (Cited on page 103.)

[Carlson 1998] D. E. Carlson and K. Rajan. *Evidence for proton motion in the recovery of light-induced degradation in amorphous silicon solar cells.* Journal of Applied Physics, vol. 83, no. 3, pages 1726–1729, 10.1063/1.366902. (Cited on page 118.)

[Carlson 2000] D.E. Carlson, G. Lin and G. Ganguly. *Temperature dependence of amorphous silicon solar cell PV parameters.* In Conference Record of the Twenty-Eighth IEEE Photovoltaic Specialists Conference - 2000 (Cat. No.00CH37036), pages 707–712, Anchorage, AK, USA, 2000. IEEE. (Cited on pages 131 and 133.)

[Chen 2015] Dustin Chen, Jiajie Liang, Chao Liu, Gillian Saldanha, Fangchao Zhao, Kwing Tong, Jiang Liu and Qibing Pei. *Thermally Stable Silver Nanowire-Polyimide Transparent Electrode Based on Atomic Layer Deposition of Zinc Oxide on Silver Nanowires.* Advanced Functional Materials, vol. 25, no. 48, pages 7512–7520, 10.1002/adfm.201503236. (Cited on page 70.)

[Chen 2019] Zhongtao Chen, Yuanyuan Liu, Weijie Zhang, Xinli Guo, Liangliang Yin, Yixuan Wang, Long Li, Yao Zhang, Zengmei Wang and Tong Zhang. *Growth of graphene/Ag nanowire/graphene sandwich films for transparent touch-sensitive electrodes.* Materials Chemistry and Physics, vol. 221, pages 78–88, 10.1016/j.matchemphys.2018.09.039. (Cited on page 37.)

[Chen 2021a] Hung-Ling Chen, Romaric De Lépinau, Andrea Scaccabarozzi, Fabrice Oehler, Jean-Christophe Harmand, Andrea Cattoni and Stéphane Collin. *Quantitative Assessment of Carrier Density by Cathodoluminescence. II. Ga As Nanowires.* Physical Review Applied, vol. 15, no. 2, page 024007, 10.1103/PhysRevApplied.15.024007. (Cited on page 18.)

[Chen 2021b] Hung-Ling Chen, Andrea Scaccabarozzi, Romaric De Lépinau, Fabrice Oehler, Aristide Lemaître, Jean-Christophe Harmand, Andrea Cattoni and Stéphane Collin. *Quantitative Assessment of Carrier Density by Cathodoluminescence. I. Ga As Thin Films and Modeling.* Physical Review Applied, vol. 15, no. 2, page 024006, 10.1103/PhysRevApplied.15.024006. (Cited on page 128.)

[Chia 2011] A C E Chia and R R LaPierre. *Contact planarization of ensemble nanowires.* Nanotechnology, vol. 22, no. 24, page 245304, 10.1088/0957-4484/22/24/245304. (Cited on page 42.)

[Chia 2012] Andrew C. E. Chia and Ray R. LaPierre. *Analytical model of surface depletion in GaAs nanowires.* Journal of Applied Physics, vol. 112, no. 6, page 063705, 10.1063/1.4752873. (Cited on page 18.)

[Chibbaro 2011] C. Chibbaro, M. Zimbone, G. Litrico, P. Baeri, M. L. Lo Trovato and F. Aleo. *A general and precise method to evaluate the series resistance of photovoltaic cells from I-V characteristics.* Journal of Applied Physics, vol. 110, no. 4, page 044505, 10.1063/1.3622617. (Cited on page 26.)

[Chittick 1969] R. C. Chittick, J. H. Alexander and H. F. Sterling. *The Preparation and Properties of Amorphous Silicon.* Journal of The Electrochemical Society, vol. 116, no. 1, page 77, 10.1149/1.2411779. (Cited on page 98.)

[Chung 2020] Jaehoon Chung, Seong Sik Shin, Kyeongil Hwang, Geunjin Kim, Ki Woong Kim, Da Seul Lee, Wansun Kim, Boo Soo Ma, Young-Ki Kim, Taek-Soo Kim and Jangwon Seo. *Record-efficiency flexible perovskite solar cell and module enabled by a porous-planar structure as an electron transport layer.* Energy & Environmental Science, vol. 13, no. 12, pages 4854–4861, 10.1039/D0EE02164D. (Cited on page 82.)

[Cirlin 2009] G. E. Cirlin, V. G. Dubrovskii, I. P. Soshnikov, N. V. Sibirev, Yu. B. Samsonenko, A. D. Bouravleuv, J. C. Harmand and F. Glas. *Critical diameters and temperature domains for MBE growth of III-V nanowires on lattice mismatched substrates: Critical diameters and temperature domains for MBE growth of III-V nanowires.* physica status solidi (RRL) - Rapid Research Letters, vol. 3, no. 4, pages 112–114, 10.1002/pssr.200903057. (Cited on page 15.)

[Clarke 2022] L Clarke, Y.-M. Wei, A De La Vega Navarro, A Garg, A. N. Hahmann, Smail Khennas, Inês M L Azevedo, Andreas Löschel, Ajay Kumar Singh, Linda Steg, G Strbac and K Wada. *Energy Systems.* In IPCC, 2022: Climate Change 2022: Mitigation of Climate Change. Contribution of Working Group III to the Sixth Assessment Report of the Intergovernmental Panel on Climate Change. 2022. (Cited on pages 1 and 2.)

[Coutancier 2020] Damien Coutancier, Shan-Ting Zhang, Simone Bernardini, Olivier Fournier, Tiphaine Mathieu-Pennober, Frédérique Donsanti, Maria Tchernycheva, Martin Foldyna and Nathanaelle Schneider. *ALD of ZnO:Ti: Growth Mechanism and Application as an Efficient Transparent Conductive Oxide in Silicon Nanowire Solar Cells.* ACS Applied Materials & Interfaces, vol. 12, no. 18, pages 21036–21044, 10.1021/acsami.9b22973. (Cited on pages 44, 45 and 46.)

[Dai 2015] Han Dai, Ruiqiang Ding, Meicheng Li, Jinjer Huang, Yingfeng Li and Mwenya Trevor. *Ordering Ag nanowire arrays by spontaneous spreading of volatile droplet on solid surface.* Scientific Reports, vol. 4, no. 1, page 6742, 10.1038/srep06742. (Cited on page 175.)

[Dauzon 2022] Emilie Dauzon, Xavier Sallenave, Cedric Plesse, Fabrice Goubard, Aram Amassian and Thomas D. Anthopoulos. *Versatile methods for improving the mechanical properties of fullerene and non-fullerene bulk heterojunction layers to enable stretchable organic solar cells.* Journal of Materials Chemistry C, page 10.1039.D1TC05263B, 10.1039/D1TC05263B. (Cited on page 83.)

[De Lépinau 2020] Romaric De Lépinau. *GaAs-on-Si solar cells based on nanowire arrays grown by molecular beam epitaxy.* PhD thesis, Université Paris-Saclay, 2020. (Cited on page 9.)

[De 2009] Sukanta De, Thomas M. Higgins, Philip E. Lyons, Evelyn M. Doherty, Peter N. Nirmalraj, Werner J. Blau, John J. Boland and Jonathan N. Coleman. *Silver Nanowire Networks as Flexible, Transparent, Conducting Films: Extremely High DC to Optical Conductivity Ratios.* ACS Nano, vol. 3, no. 7, pages 1767–1774, 10.1021/nn900348c. (Cited on pages 38, 49, 61 and 173.)

[De 2010] Sukanta De, Paul J. King, Philip E. Lyons, Umar Khan and Jonathan N. Coleman. *Size Effects and the Problem with Percolation in Nanostructured Transparent Conductors.* ACS Nano, vol. 4, no. 12, pages 7064–7072, 10.1021/nn1025803. (Cited on pages 40, 41 and 61.)

[Deegan 1997] Robert D. Deegan, Olgica Bakajin, Todd F. Dupont, Greb Huber, Sidney R. Nagel and Thomas A. Witten. *Capillary flow as the cause of ring stains from dried liquid drops.* Nature, vol. 389, no. 6653, pages 827–829, 10.1038/39827. (Cited on page 174.)

[Deignan 2017] Geoffrey Deignan and Irene A. Goldthorpe. *The dependence of silver nanowire stability on network composition and processing parameters.* RSC Advances, vol. 7, no. 57, pages 35590–35597, 10.1039/C7RA06524H. (Cited on pages 66, 67 and 177.)

[Diedenhofen 2011] Silke L. Diedenhofen, Olaf T. A. Janssen, Grzegorz Grzela, Erik P. A. M. Bakkers and Jaime Gómez Rivas. *Strong Geometrical Dependence of the Absorption of Light in Arrays of Semiconductor Nanowires.* ACS Nano, vol. 5, no. 3, pages 2316–2323, 10.1021/nn103596n. (Cited on page 15.)

[Dong 2017] Gangqiang Dong, Yurong Zhou, Hailong Zhang, Fengzhen Liu, Guangyi Li and Meifang Zhu. *Passivation of high aspect ratio silicon nanowires by using catalytic chemical vapor deposition for radial heterojunction solar cell application.* RSC Advances, vol. 7, no. 71, pages 45101–45106, 10.1039/C7RA08343B. (Cited on page 18.)

[Dong 2019] Bin Dong, Jing Hu, Xinyu Xiao, Sheng Tang, Xue Gao, Zongyang Peng and Dechun Zou. *High-Efficiency Fiber-Shaped Perovskite Solar Cell by Vapor-Assisted Deposition with a Record Efficiency of 10.79%.* Advanced Materials Technologies, vol. 4, no. 7, page 1900131, 10.1002/admt.201900131. (Cited on page 83.)

[Donolato 1981] C. Donolato. *An analytical model of SEM and STEM charge collection images of dislocations in thin semiconductor layers: I. Minority carrier gener-*

ation, diffusion, and collection. Physica Status Solidi (a), vol. 65, no. 2, pages 649–658, 10.1002/pssa.2210650231. (Cited on page 153.)

[Donovan 1983] E. P. Donovan, F. Spaepen, D. Turnbull, J. M. Poate and D. C. Jacobson. *Heat of crystallization and melting point of amorphous silicon.* Applied Physics Letters, vol. 42, no. 8, pages 698–700, 10.1063/1.94077. (Cited on page 141.)

[Dressel 2002] Martin Dressel and George Grüner. Electrodynamics of solids: optical properties of electrons in matter. Cambridge University Press, Cambridge ; New York, 2002. (Cited on pages 29, 34, 35 and 40.)

[Drude 1900] P. Drude. *Zur Elektronentheorie der Metalle.* Annalen der Physik, vol. 306, no. 3, pages 566–613, 10.1002/andp.19003060312. (Cited on page 30.)

[Dupont 2020] Elise Dupont, Rembrandt Koppelaar and Hervé Jeanmart. *Global available solar energy under physical and energy return on investment constraints.* Applied Energy, vol. 257, page 113968, 10.1016/j.apenergy.2019.113968. (Cited on page 1.)

[Dupré 2015] O. Dupré, R. Vaillon and M.A. Green. *Physics of the temperature coefficients of solar cells.* Solar Energy Materials and Solar Cells, vol. 140, pages 92–100, 10.1016/j.solmat.2015.03.025. (Cited on page 131.)

[Dürkop 2004] T. Dürkop, S. A. Getty, Enrique Cobas and M. S. Fuhrer. *Extraordinary Mobility in Semiconducting Carbon Nanotubes.* Nano Letters, vol. 4, no. 1, pages 35–39, 10.1021/nl034841q. (Cited on page 38.)

[El Mhamdi 2014] El Mahdi El Mhamdi, Jakub Holovsky, Bénédicte Demaurex, Christophe Ballif and Stefaan De Wolf. *Is light-induced degradation of a-Si:H/c-Si interfaces reversible?* Applied Physics Letters, vol. 104, no. 25, page 252108, 10.1063/1.4885501. (Cited on page 118.)

[Elechiguerra 2005] Jose Luis Elechiguerra, Leticia Larios-Lopez, Cui Liu, Domingo Garcia-Gutierrez, Alejandra Camacho-Bragado and Miguel Jose Yacaman. *Corrosion at the Nanoscale: The Case of Silver Nanowires and Nanoparticles.* Chemistry of Materials, vol. 17, no. 24, pages 6042–6052, 10.1021/cm051532n. (Cited on pages 66 and 68.)

[Ellmer 2012] Klaus Ellmer. *Past achievements and future challenges in the development of optically transparent electrodes.* Nature Photonics, vol. 6, no. 12, pages 809–817, 10.1038/nphoton.2012.282. (Cited on pages 35, 36, 37, 41 and 44.)

[Engemann 1976] D. Engemann and R. Fischer. *Radiative and non-radiative recombination in amorphous silicon.* In AIP Conference Proceedings, volume 31, pages 37–43. AIP, 1976. ISSN: 0094243X. (Cited on page 128.)

[Esaki 1958] Leo Esaki. *New Phenomenon in Narrow Germanium p - n Junctions.* Physical Review, vol. 109, no. 2, pages 603–604, 10.1103/PhysRev.109.603. (Cited on page 160.)

[Esser 1990] A. Esser, K. Seibert, H. Kurz, G. N. Parsons, C. Wang, B. N. Davidson, G. Lucovsky and R. J. Nemanich. *Ultrafast recombination and trapping in amorphous silicon.* Physical Review B, vol. 41, no. 5, pages 2879–2884, 10.1103/PhysRevB.41.2879. (Cited on page 122.)

[Everhart 1971] T. E. Everhart and P. H. Hoff. *Determination of Kilovolt Electron Energy Dissipation vs Penetration Distance in Solid Materials.* Journal of Applied Physics, vol. 42, no. 13, pages 5837–5846, 10.1063/1.1660019. (Cited on page 153.)

[Fan 2010] Qi Hua Fan, Changyong Chen, Xianbo Liao, Xianbi Xiang, Xinmin Cao, William Ingler, Nirupama Adiga and Xunming Deng. *Spectroscopic aspects of front transparent conductive films for a-Si thin film solar cells.* Journal of Applied Physics, vol. 107, no. 3, page 034505, 10.1063/1.3298932. (Cited on page 53.)

[Feng 2018] Jiangshan Feng, Xuejie Zhu, Zhou Yang, Xiaorong Zhang, Jinzhi Niu, Ziyu Wang, Shengnan Zuo, Shashank Priya, Shengzhong (Frank) Liu and Dong Yang. *Record Efficiency Stable Flexible Perovskite Solar Cell Using Effective Additive Assistant Strategy.* Advanced Materials, vol. 30, no. 35, page 1801418, 10.1002/adma.201801418. (Cited on page 83.)

[Fernandes 2015] M. Fernandes, Y. Vygranenko, M. Vieira, A. Sazonov, R. Yang and A. Khosropour. *Characterization of a-Si:H Solar Cell Modules on Plastic Substrates by High Resolution LBIC Technique.* Energy Procedia, vol. 84, pages 93–98, 10.1016/j.egypro.2015.12.300. (Cited on page 88.)

[Fortner 1989] J. Fortner and J. S. Lannin. *Radial distribution functions of amorphous silicon.* Physical Review B, vol. 39, no. 8, pages 5527–5530, 10.1103/PhysRevB.39.5527. (Cited on page 99.)

[Fountaine 2014] Katherine T. Fountaine, William S. Whitney and Harry A. Atwater. *Resonant absorption in semiconductor nanowires and nanowire arrays: Relating leaky waveguide modes to Bloch photonic crystal modes.* Journal of Applied Physics, vol. 116, no. 15, page 153106, 10.1063/1.4898758. (Cited on pages 13 and 15.)

[Franey 1985] J.P. Franey, G.W. Kammlott and T.E. Graedel. *The corrosion of silver by atmospheric sulfurous gases.* Corrosion Science, vol. 25, no. 2, pages 133–143, 10.1016/0010-938X(85)90104-0. (Cited on page 66.)

[Fraser 1972] D. B. Fraser and H. D. Cook. *Highly Conductive, Transparent Films of Sputtered In[sub 2-x]Sn[sub x]O[sub 3-y].* Journal of The Electrochemical Society, vol. 119, no. 10, page 1368, 10.1149/1.2403999. (Cited on pages 39 and 40.)

[Fraunhofer ISE 2022] Fraunhofer ISE. *Photovoltaics Report.* Technical report, 2022. (Cited on pages 1, 12 and 36.)

[Frederiksen 2017] Rune Frederiksen, Gozde Tutuncuoglu, Federico Matteini, Karen L. Martinez, Anna Fontcuberta i Morral and Esther Alarcon-Llado. *Visual Understanding of Light Absorption and Waveguiding in Standing Nanowires with 3D*

Fluorescence Confocal Microscopy. ACS Photonics, vol. 4, no. 9, pages 2235–2241, 10.1021/acsphotonics.7b00434. (Cited on page 15.)

[Frischknecht 2020] Rolf Frischknecht, Rene Itten, Parikhit Sinha, Mariska de Wild-Scholten, Jia Zhang, Garvin A Heath and Carol Olson. *Life Cycle Inventories and Life Cycle Assessments of Photovoltaic Systems.* Technical report NREL/TP-6A20-73853, 1561526, 2020. (Cited on pages 2 and 13.)

[Fritzsche 2001] Hellmut Fritzsche. *Development in Understanding and Controlling the Staebler-Wronski Effect in a-Si:H.* Annual Review of Materials Research, vol. 31, no. 1, pages 47–79, 10.1146/annurev.matsci.31.1.47. (Cited on page 100.)

[Gao 2019] Zhengning Gao and Parag Banerjee. *Review Article: Atomic layer deposition of doped ZnO films.* Journal of Vacuum Science & Technology A, vol. 37, no. 5, page 050802, 10.1116/1.5112777. (Cited on page 46.)

[Garnett 2010] Erik Garnett and Peidong Yang. *Light Trapping in Silicon Nanowire Solar Cells.* Nano Letters, vol. 10, no. 3, pages 1082–1087, 10.1021/nl100161z. (Cited on page 73.)

[Garnett 2012] Erik C. Garnett, Wenshan Cai, Judy J. Cha, Fakhruddin Mahmood, Stephen T. Connor, M. Greyson Christoforo, Yi Cui, Michael D. McGehee and Mark L. Brongersma. *Self-limited plasmonic welding of silver nanowire junctions.* Nature Materials, vol. 11, no. 3, pages 241–249, 10.1038/nmat3238. (Cited on pages 49 and 176.)

[Gaspar 2008] Joao Gaspar, Oliver Paul, Virginia Chu and Joao Pedro Conde. *Mechanical Properties and Reliability of Amorphous vs. Polycrystalline Silicon Thin Films.* MRS Proceedings, vol. 1066, pages 1066–A15–04, 10.1557/PROC-1066-A15-04. (Cited on page 83.)

[Geisz 2020] John F. Geisz, Ryan M. France, Kevin L. Schulte, Myles A. Steiner, Andrew G. Norman, Harvey L. Guthrey, Matthew R. Young, Tao Song and Thomas Moriarty. *Six-junction III–V solar cells with 47.1% conversion efficiency under 143 Suns concentration.* Nature Energy, vol. 5, no. 4, pages 326–335, 10.1038/s41560-020-0598-5. (Cited on page 6.)

[Gerber 2015] A. Gerber, V. Huhn, T.M.H. Tran, M. Siegloch, Y. Augarten, B.E. Pieters and U. Rau. *Advanced large area characterization of thin-film solar modules by electroluminescence and thermography imaging techniques.* Solar Energy Materials and Solar Cells, vol. 135, pages 35–42, 10.1016/j.solmat.2014.09.020. (Cited on page 87.)

[Ginley 2011] David S. Ginley, editor. Handbook of Transparent Conductors. Springer US, Boston, MA, 2011. (Cited on pages 35 and 45.)

[Girard 2006] Fabien Girard, Mickaël Antoni, Sylvain Faure and Annie Steinchen. *Evaporation and Marangoni Driven Convection in Small Heated Water Droplets.* Langmuir, vol. 22, no. 26, pages 11085–11091, 10.1021/la061572l. (Cited on page 174.)

[Gleskova 1993] H. Gleskova, P. A. Morin and S. Wagner. *Kinetics of recovery of the light-induced defects in hydrogenated amorphous silicon under illumination.* Applied Physics Letters, vol. 62, no. 17, pages 2063–2065, 10.1063/1.109480. (Cited on pages 106 and 118.)

[Gordon 2000] Gordon. *Criteria for Choosing Transparent Conductors.* MRS bulletin, 2000. (Cited on pages 35, 40 and 44.)

[Graedel 1992] T. E. Graedel. *Corrosion Mechanisms for Silver Exposed to the Atmosphere.* Journal of The Electrochemical Society, vol. 139, no. 7, pages 1963–1970, 10.1149/1.2221162. (Cited on page 66.)

[Green 2003] Martin A. Green. *General temperature dependence of solar cell performance and implications for device modelling.* Progress in Photovoltaics: Research and Applications, vol. 11, no. 5, pages 333–340, 10.1002/pip.496. (Cited on page 131.)

[Green 2015] Martin A. Green. *The Passivated Emitter and Rear Cell (PERC): From conception to mass production.* Solar Energy Materials and Solar Cells, vol. 143, pages 190–197, 10.1016/j.solmat.2015.06.055. (Cited on page 37.)

[Green 2021] Martin Green, Ewan Dunlop, Jochen Hohl-Ebinger, Masahiro Yoshita, Nikos Kopidakis and Xiaojing Hao. *Solar cell efficiency tables (version 57).* Progress in Photovoltaics: Research and Applications, vol. 29, no. 1, pages 3–15, 10.1002/pip.3371. (Cited on page 82.)

[Green 2022] Martin A. Green, Ewan D. Dunlop, Jochen Hohl-Ebinger, Masahiro Yoshita, Nikos Kopidakis and Xiaojing Hao. *Solar cell efficiency tables (version 59).* Progress in Photovoltaics: Research and Applications, vol. 30, no. 1, pages 3–12, 10.1002/pip.3506. (Cited on page 13.)

[Griffiths 2013] David J. Griffiths. Introduction to electrodynamics. Pearson, Boston, fourth edition édition, 2013. (Cited on page 31.)

[Grimbergen 1993] M Grimbergen, R McConville, D Redfield and R. H. Bube. *Relaxation of electron beam induced metastable defects in a-Si:H.* In Materials Research Society Symposium Proceedings, volume 297, page 6, 1993. (Cited on page 156.)

[Grundmann 2006] Marius Grundmann. The physics of semiconductors: an introduction including devices and nanophysics. Springer, Berlin ; New York, 2006. OCLC: ocm70201027. (Cited on pages 120 and 160.)

[Grzela 2014] Grzegorz Grzela, Ramón Paniagua-Domínguez, Tommy Barten, Dick van Dam, José A. Sánchez-Gil and Jaime Gómez Rivas. *Nanowire Antenna Absorption Probed with Time-Reversed Fourier Microscopy.* Nano Letters, vol. 14, no. 6, pages 3227–3234, 10.1021/nl5005948. (Cited on page 14.)

[Guha 1981] S. Guha, K. L. Narasimhan and S. M. Pietruszko. *On light-induced effect in amorphous hydrogenated silicon.* Journal of Applied Physics, vol. 52, no. 2, pages 859–860, 10.1063/1.328849. (Cited on page 118.)

[Guha 2000] S. Guha. *Multijunction Solar Cells and Modules.* In Robert A. Street, editor, Technology and Applications of Amorphous Silicon, volume 37 of *Springer Series in Materials Science*. Springer Berlin Heidelberg, Berlin, Heidelberg, 2000. (Cited on pages 102 and 103.)

[Guha 2013] Subhendu Guha, Jeffrey Yang and Baojie Yan. *High efficiency multi-junction thin film silicon cells incorporating nanocrystalline silicon.* Solar Energy Materials and Solar Cells, vol. 119, pages 1–11, 10.1016/j.solmat.2013.03.036. (Cited on pages 82 and 105.)

[Guillemoles 2019] Jean-Francois Guillemoles, Thomas Kirchartz, David Cahen and Uwe Rau. *Guide for the perplexed to the Shockley–Queisser model for solar cells.* Nature Photonics, vol. 13, no. 8, pages 501–505, 10.1038/s41566-019-0479-2. (Cited on page 6.)

[Haacke 1976] G. Haacke. *New figure of merit for transparent conductors.* Journal of Applied Physics, vol. 47, no. 9, pages 4086–4089, 10.1063/1.323240. (Cited on pages 39 and 40.)

[Haney 2015] Paul M Haney, Heayoung P Yoon, Prakash Koirala, Robert W Collins and Nikolai B Zhitenev. *Electron beam induced current in the high injection regime.* Nanotechnology, vol. 26, no. 29, page 295401, 10.1088/0957-4484/26/29/295401. (Cited on page 153.)

[Hashemi 2020] Seyyed Alireza Hashemi, Seeram Ramakrishna and Armin Gerhard Aberle. *Recent progress in flexible–wearable solar cells for self-powered electronic devices.* Energy & Environmental Science, vol. 13, no. 3, pages 685–743, 10.1039/C9EE03046H. (Cited on page 81.)

[Hatalis 1998] Miltiadis K Hatalis and David W Greve. *Large grain polycrystalline silicon by low-temperature annealing of low-pressure chemical vapor deposited amorphous silicon films.* Journal of Applied Physics, vol. 63, no. 7, pages 2260–2266, 1998. (Cited on page 141.)

[Haug 2015] F.-J. Haug and C. Ballif. *Light management in thin film silicon solar cells.* Energy & Environmental Science, vol. 8, no. 3, pages 824–837, 10.1039/C4EE03346A. (Cited on page 106.)

[Hecht 2011] David S. Hecht, Liangbing Hu and Glen Irvin. *Emerging Transparent Electrodes Based on Thin Films of Carbon Nanotubes, Graphene, and Metallic Nanostructures.* Advanced Materials, vol. 23, no. 13, pages 1482–1513, 10.1002/adma.201003188. (Cited on page 37.)

[Heinrich 2020] Martin Heinrich. *A comparison of different solar cell technologies for integrated photovoltaics*, 2020. (Cited on page 81.)

[Hertwich 2015] Edgar G. Hertwich, Thomas Gibon, Evert A. Bouman, Anders Arvesen, Sangwon Suh, Garvin A. Heath, Joseph D. Bergesen, Andrea Ramirez, Mabel I. Vega and Lei Shi. *Integrated life-cycle assessment of electricity-supply scenarios confirms global environmental benefit of low-carbon technologies.* Proceedings of the National Academy of Sciences, vol. 112, no. 20, pages 6277–6282, 10.1073/pnas.1312753111. (Cited on page 2.)

[Hinken 2007] David Hinken, Klaus Ramspeck, Karsten Bothe, Bernhard Fischer and Rolf Brendel. *Series resistance imaging of solar cells by voltage dependent electroluminescence.* Applied Physics Letters, vol. 91, no. 18, page 182104, 10.1063/1.2804562. (Cited on page 26.)

[Ho 2013] Xinning Ho, Ju Nie Tey, Wenjun Liu, Chek Kweng Cheng and Jun Wei. *Biaxially stretchable silver nanowire transparent conductors.* Journal of Applied Physics, vol. 113, no. 4, page 044311, 10.1063/1.4789795. (Cited on page 50.)

[Hofmann 2003] S. Hofmann, C. Ducati, R. J. Neill, S. Piscanec, A. C. Ferrari, J. Geng, R. E. Dunin-Borkowski and J. Robertson. *Gold catalyzed growth of silicon nanowires by plasma enhanced chemical vapor deposition.* Journal of Applied Physics, vol. 94, no. 9, pages 6005–6012, 10.1063/1.1614432. (Cited on page 21.)

[Hopcroft 2010] Matthew A. Hopcroft, William D. Nix and Thomas W. Kenny. *What is the Young's Modulus of Silicon?* Journal of Microelectromechanical Systems, vol. 19, no. 2, pages 229–238, 10.1109/JMEMS.2009.2039697. (Cited on page 83.)

[Hosono 1996] Hideo Hosono, Naoto Kikuchi, Naoyuki Ueda and Hiroshi Kawazoe. *Working hypothesis to explore novel wide band gap electrically conducting amorphous oxides and examples.* Journal of Non-Crystalline Solids, vol. 198-200, pages 165–169, 10.1016/0022-3093(96)80019-6. (Cited on page 37.)

[Hsiao 2014] Sheng-Tsung Hsiao, Hsi-Wen Tien, Wei-Hao Liao, Yu-Sheng Wang, Shin-Ming Li, Chen-Chi MMa, Yi-Hsiuan Yu and Wen-Pin Chuang. *A highly electrically conductive graphene–silver nanowire hybrid nanomaterial for transparent conductive films.* Journal of Materials Chemistry C, vol. 2, no. 35, page 7284, 10.1039/C4TC01217H. (Cited on page 38.)

[Hsu 2008] Ching-Mei Hsu, Stephen T. Connor, Mary X. Tang and Yi Cui. *Wafer-scale silicon nanopillars and nanocones by Langmuir–Blodgett assembly and etching.* Applied Physics Letters, vol. 93, no. 13, page 133109, 10.1063/1.2988893. (Cited on page 17.)

[Hu 2010] Liangbing Hu, Han Sun Kim, Jung-Yong Lee, Peter Peumans and Yi Cui. *Scalable Coating and Properties of Transparent, Flexible, Silver Nanowire Electrodes.* ACS Nano, vol. 4, no. 5, pages 2955–2963, 10.1021/nn1005232. (Cited on pages 38, 173 and 177.)

[Hu 2014] Ya Hu, Kui-Qing Peng, Zhen Qiao, Xing Huang, Fu-Qiang Zhang, Rui-Nan Sun, Xiang-Min Meng and Shuit-Tong Lee. *Metal-Catalyzed Electroless Etching of Silicon in Aerated HF/H $_2$ O Vapor for Facile Fabrication of Silicon Nanostructures.* Nano Letters, vol. 14, no. 8, pages 4212–4219, 10.1021/nl500361u. (Cited on page 17.)

[Hu 2017] Nan Hu, Hongkun Cai, Xiaowan Dai, Guifeng Chen, Yong Wang and Dexian Zhang. *Figure of merit for front electrodes of solar cells.* Solar Energy Materials and Solar Cells, vol. 161, pages 382–387, 10.1016/j.solmat.2016.12.014. (Cited on page 40.)

[Hwang 2016] B. Hwang, M. Park, T. Kim and S. M. Han. *Effect of RGO deposition on chemical and mechanical reliability of Ag nanowire flexible transparent electrode.* RSC Advances, vol. 6, no. 71, pages 67389–67395, 10.1039/C6RA10338C. (Cited on page 67.)

[Hwang 2017] Byungil Hwang, Youngseo An, Hyangsook Lee, Eunha Lee, Stefan Becker, Yong-Hoon Kim and Hyoungsub Kim. *Highly Flexible and Transparent Ag Nanowire Electrode Encapsulated with Ultra-Thin Al2O3: Thermal, Ambient, and Mechanical Stabilities.* Scientific Reports, vol. 7, no. 1, page 41336, 10.1038/srep41336. (Cited on pages 67, 70 and 74.)

[Hwang 2018] Inchan Hwang, Han-Don Um, Byeong-Su Kim, Munib Wober and Kwanyong Seo. *Flexible crystalline silicon radial junction photovoltaics with vertically aligned tapered microwires.* Energy & Environmental Science, vol. 11, no. 3, pages 641–647, 10.1039/C7EE03340K. (Cited on page 84.)

[Isomura 1991] M Isomura, N Hata and S Wagner. *The saturation of light-induced defects in hydrogenated amorphous silicon.* Journal of Non-Crystalline Solids, no. 137-138, pages 223–226, 1991. (Cited on page 105.)

[Jacobs 2016] Daniel A. Jacobs, Kylie R. Catchpole, Fiona J. Beck and Thomas P. White. *A re-evaluation of transparent conductor requirements for thin-film solar cells.* Journal of Materials Chemistry A, vol. 4, no. 12, pages 4490–4496, 10.1039/C6TA01670G. (Cited on pages 40 and 43.)

[Jang 2016] Hyejin Jang, Dongjae Kim, Hyowon Tak, Jaewook Nam and Tae-il Kim. *Ultra-mechanically stable and transparent conductive electrodes using transferred grid of Ag nanowires on flexible substrate.* Current Applied Physics, vol. 16, no. 1, pages 24–30, 10.1016/j.cap.2015.10.005. (Cited on pages 38 and 173.)

[Jinno 2017] Hiroaki Jinno, Kenjiro Fukuda, Xiaomin Xu, Sungjun Park, Yasuhito Suzuki, Mari Koizumi, Tomoyuki Yokota, Itaru Osaka, Kazuo Takimiya and Takao Someya. *Stretchable and waterproof elastomer-coated organic photovoltaics for washable electronic textile applications.* Nature Energy, vol. 2, no. 10, pages 780–785, 10.1038/s41560-017-0001-3. (Cited on page 82.)

[Jiu 2015] Jinting Jiu, Jun Wang, Tohru Sugahara, Shijio Nagao, Masaya Nogi, Hirotaka Koga, Katsuaki Suganuma, Masanao Hara, Eri Nakazawa and Hiroshi Uchida. *The effect of light and humidity on the stability of silver nanowire transparent electrodes.* RSC Advances, vol. 5, no. 35, pages 27657–27664, 10.1039/C5RA02722E. (Cited on pages 66, 67 and 77.)

[Johnson 1972] P. B. Johnson and R. W. Christy. *Optical Constants of the Noble Metals.* Physical Review B, vol. 6, no. 12, pages 4370–4379, 10.1103/PhysRevB.6.4370. (Cited on page 33.)

[Kaminski 2004] A Kaminski, O Breitenstein, J P Boyeaux, P Rakotoniaina and A Laugier. *Light beam induced current and infrared thermography studies of multicrystalline silicon solar cells.* Journal of Physics: Condensed Matter, vol. 16, no. 2, pages S9–S18, 10.1088/0953-8984/16/2/002. (Cited on page 88.)

[Kapoor 2020] Akanksha Kapoor, Sylvain Finot, Vincent Grenier, Eric Robin, Catherine Bougerol, Joel Bleuse, Gwénolé Jacopin, Joël Eymery and Christophe Durand. *Role of Underlayer for Efficient Core–Shell InGaN QWs Grown on m -plane GaN Wire Sidewalls.* ACS Applied Materials & Interfaces, vol. 12, no. 16, pages 19092–19101, 10.1021/acsami.9b19314. (Cited on page 168.)

[Kasemann 2006] Martin Kasemann, Martin C. Schubert, Manuel The, Mariana Köber, Martin Hermle and Wilhelm Warta. *Comparison of luminescence imaging and illuminated lock-in thermography on silicon solar cells.* Applied Physics Letters, vol. 89, no. 22, page 224102, 10.1063/1.2399346. (Cited on page 87.)

[Kavanagh 2010] Karen L Kavanagh. *Misfit dislocations in nanowire heterostructures.* Semiconductor Science and Technology, vol. 25, no. 2, page 024006, 10.1088/0268-1242/25/2/024006. (Cited on page 15.)

[Kawazoe 1997] Hiroshi Kawazoe, Masahiro Yasukawa, Hiroyuki Hyodo, Masaaki Kurita, Hiroshi Yanagi and Hideo Hosono. *P-type electrical conduction in transparent thin films of CuAlO2.* Nature, vol. 389, no. 6654, pages 939–942, 10.1038/40087. (Cited on page 37.)

[Kayes 2005] Brendan M. Kayes, Harry A. Atwater and Nathan S. Lewis. *Comparison of the device physics principles of planar and radial p-n junction nanorod solar cells.* Journal of Applied Physics, vol. 97, no. 11, page 114302, 10.1063/1.1901835. (Cited on page 16.)

[Khaligh 2017] H H Khaligh, L Xu, A Khosropour, A Madeira, M Romano, C Pradére, M Tréguer-Delapierre, L Servant, M A Pope and I A Goldthorpe. *The Joule heating problem in silver nanowire transparent electrodes.* Nanotechnology, vol. 28, no. 42, page 425703, 10.1088/1361-6528/aa7f34. (Cited on pages 66, 67 and 77.)

[Khanarian 2013] G. Khanarian, J. Joo, X.-Q. Liu, P. Eastman, D. Werner, K. O'Connell and P. Trefonas. *The optical and electrical properties of silver nanowire mesh films.* Journal of Applied Physics, vol. 114, no. 2, page 024302, 10.1063/1.4812390. (Cited on page 49.)

[Kim 2011a] Jung-Hoon Kim, Sang-Byung Park, Jae Hyun Kim and Wang-Cheol Zin. *Polymer Transports Inside Evaporating Water Droplets at Various Substrate Temperatures.* The Journal of Physical Chemistry C, vol. 115, no. 31, pages 15375–15383, 10.1021/jp202429p. (Cited on page 174.)

[Kim 2011b] Yong Hyun Kim, Christoph Sachse, Michael L. Machala, Christian May, Lars Müller-Meskamp and Karl Leo. *Highly Conductive PEDOT:PSS Electrode with Optimized Solvent and Thermal Post-Treatment for ITO-Free Organic Solar Cells.* Advanced Functional Materials, vol. 21, no. 6, pages 1076–1081, 10.1002/adfm.201002290. (Cited on page 37.)

[Kim 2013] Areum Kim, Yulim Won, Kyoohee Woo, Chul-Hong Kim and Jooho Moon. *Highly Transparent Low Resistance ZnO/Ag Nanowire/ZnO Composite Electrode for Thin Film Solar Cells.* ACS Nano, vol. 7, no. 2, pages 1081–1091, 10.1021/nn305491x. (Cited on page 67.)

[Kind 2011] R. Kind, R. A. C. M. M. van Swaaij, F. A. Rubinelli, S. Solntsev and M. Zeman. *Thermal ideality factor of hydrogenated amorphous silicon p-i-n solar cells.* Journal of Applied Physics, vol. 110, no. 10, page 104512, 10.1063/1.3662924. (Cited on page 123.)

[King 1997] D.L. King, J.A. Kratochvil and W.E. Boyson. *Temperature coefficients for PV modules and arrays: measurement methods, difficulties, and results.* In Conference Record of the Twenty Sixth IEEE Photovoltaic Specialists Conference - 1997, pages 1183–1186, Anaheim, CA, USA, 1997. IEEE. (Cited on page 133.)

[Klein 1968] Claude A. Klein. *Bandgap Dependence and Related Features of Radiation Ionization Energies in Semiconductors.* Journal of Applied Physics, vol. 39, no. 4, pages 2029–2038, 10.1063/1.1656484. (Cited on page 153.)

[Koida 2017] Takashi Koida, Tetsuya Kaneko and Hajime Shibata. *Carrier Compensation Induced by Thermal Annealing in Al-Doped ZnO Films.* Materials, vol. 10, no. 2, page 141, 10.3390/ma10020141. (Cited on page 179.)

[Kottmann 2001] Jörg P. Kottmann, Olivier J. F. Martin, David R. Smith and Sheldon Schultz. *Plasmon resonances of silver nanowires with a nonregular cross section.* Physical Review B, vol. 64, no. 23, page 235402, 10.1103/PhysRevB.64.235402. (Cited on pages 49 and 73.)

[Krogstrup 2013] Peter Krogstrup, Henrik Ingerslev Jørgensen, Martin Heiss, Olivier Demichel, Jeppe V. Holm, Martin Aagesen, Jesper Nygard and Anna Fontcuberta i Morral. *Single-nanowire solar cells beyond the Shockley–Queisser limit.* Nature Photonics, vol. 7, no. 4, pages 306–310, 10.1038/nphoton.2013.32. (Cited on page 15.)

[Kuschnereit 1995] R Kuschnereit, H Fath, A A Kolomenskii, M Szabadi and P Hess. *Mechanical and elastic properties of amorphous hydrogenated silicon films studied by broadband surface acoustic wave spectroscopy.* Applied Physics A, page 8, 1995. (Cited on page 83.)

[Laaziri 1999] Khalid Laaziri, S. Kycia, S. Roorda, M. Chicoine, J. L. Robertson, J. Wang and S. C. Moss. *High-energy x-ray diffraction study of pure amorphous silicon.* Physical Review B, vol. 60, no. 19, pages 13520–13533, 10.1103/PhysRevB.60.13520. (Cited on page 99.)

[Lagrange 2015] M. Lagrange, D. P. Langley, G. Giusti, C. Jiménez, Y. Bréchet and D. Bellet. *Optimization of silver nanowire-based transparent electrodes: effects of density, size and thermal annealing.* Nanoscale, vol. 7, no. 41, pages 17410–17423, 10.1039/C5NR04084A. (Cited on pages 38, 48, 49 and 177.)

[Lany 2007] Stephan Lany and Alex Zunger. *Dopability, Intrinsic Conductivity, and Nonstoichiometry of Transparent Conducting Oxides.* Physical Review Letters, vol. 98, no. 4, page 045501, 10.1103/PhysRevLett.98.045501. (Cited on pages 37 and 179.)

[LaPierre 2013] R. R. LaPierre, A. C. E. Chia, S. J. Gibson, C. M. Haapamaki, J. Boulanger, R. Yee, P. Kuyanov, J. Zhang, N. Tajik, N. Jewell and K. M. A.

Rahman. *III-V nanowire photovoltaics: Review of design for high efficiency: III-V nanowire photovoltaics: Review of design for high efficiency.* physica status solidi (RRL) - Rapid Research Letters, vol. 7, no. 10, pages 815–830, 10.1002/pssr.201307109. (Cited on page 17.)

[Latu-Romain 2008] E Latu-Romain, P Gilet, P Noel, J Garcia, P Ferret, M Rosina, G Feuillet, F Lévy and A Chelnokov. *A generic approach for vertical integration of nanowires.* Nanotechnology, vol. 19, no. 34, page 345304, 10.1088/0957-4484/19/34/345304. (Cited on page 42.)

[Lee 2008] Jung-Yong Lee, Stephen T. Connor, Yi Cui and Peter Peumans. *Solution-Processed Metal Nanowire Mesh Transparent Electrodes.* Nano Letters, vol. 8, no. 2, pages 689–692, 10.1021/nl073296g. (Cited on pages 38, 173 and 177.)

[Lee 2012] Phillip Lee, Jinhwan Lee, Hyungman Lee, Junyeob Yeo, Sukjoon Hong, Koo Hyun Nam, Dongjin Lee, Seung Seob Lee and Seung Hwan Ko. *Highly Stretchable and Highly Conductive Metal Electrode by Very Long Metal Nanowire Percolation Network.* Advanced Materials, vol. 24, no. 25, pages 3326–3332, 10.1002/adma.201200359. (Cited on page 50.)

[Lee 2013] Mi-Sun Lee, Kyongsoo Lee, So-Yun Kim, Heejoo Lee, Jihun Park, Kwang-Hyuk Choi, Han-Ki Kim, Dae-Gon Kim, Dae-Young Lee, SungWoo Nam and Jang-Ung Park. *High-Performance, Transparent, and Stretchable Electrodes Using Graphene–Metal Nanowire Hybrid Structures.* Nano Letters, vol. 13, no. 6, pages 2814–2821, 10.1021/nl401070p. (Cited on page 173.)

[Lee 2020] Sangyeob Lee, Jiseong Jang, Taejun Park, Young Min Park, Joon Sik Park, Yoon-Kee Kim, Hyoung-Keun Lee, Eun-Chae Jeon, Doh-Kwon Lee, Byungmin Ahn and Choong-Heui Chung. *Electrodeposited Silver Nanowire Transparent Conducting Electrodes for Thin-Film Solar Cells.* ACS Applied Materials & Interfaces, vol. 12, no. 5, pages 6169–6175, 10.1021/acsami.9b17168. (Cited on page 177.)

[Lee 2021] Jin-Woo Lee, Cheng Sun, Boo Soo Ma, Hyeong Jun Kim, Cheng Wang, Jong Min Ryu, Chulhee Lim, Taek-Soo Kim, Yun-Hi Kim, Soon-Ki Kwon and Bumjoon J. Kim. *Efficient, Thermally Stable, and Mechanically Robust All-Polymer Solar Cells Consisting of the Same Benzodithiophene Unit-Based Polymer Acceptor and Donor with High Molecular Compatibility.* Advanced Energy Materials, vol. 11, no. 5, page 2003367, 10.1002/aenm.202003367. (Cited on page 83.)

[Leterrier 2004] Y. Leterrier, L. Médico, F. Demarco, J.-A.E. Månson, U. Betz, M.F. Escolà, M. Kharrazi Olsson and F. Atamny. *Mechanical integrity of transparent conductive oxide films for flexible polymer-based displays.* Thin Solid Films, vol. 460, no. 1-2, pages 156–166, 10.1016/j.tsf.2004.01.052. (Cited on page 42.)

[Levtchenko 2018] Alexandra Levtchenko, Sylvain Le Gall, Raphaël Lachaume, Jérôme Michallon, Stéphane Collin, José Alvarez, Zakaria Djebbour and Jean-Paul Kleider. *Optoelectrical modeling of solar cells based on c-Si/a-Si:H nanowire array: focus on the electrical transport in between the nanowires.* Nanotechnology,

vol. 29, no. 25, page 255401, 10.1088/1361-6528/aab7e8. (Cited on pages 21 and 120.)

[Li 2009] Jiantong Li and Shi-Li Zhang. *Finite-size scaling in stick percolation*. Physical Review E, vol. 80, no. 4, page 040104, 10.1103/PhysRevE.80.040104. (Cited on page 48.)

[Lin 2013] X X Lin, X Hua, Z G Huang and W Z Shen. *Realization of high performance silicon nanowire based solar cells with large size*. Nanotechnology, vol. 24, no. 23, page 235402, 10.1088/0957-4484/24/23/235402. (Cited on page 18.)

[Liu 2020] Feng Liu and Jeroen C.J.M. van den Bergh. *Differences in CO2 emissions of solar PV production among technologies and regions: Application to China, EU and USA*. Energy Policy, vol. 138, page 111234, 10.1016/j.enpol.2019.111234. (Cited on page 2.)

[Louwen 2017] Atse Louwen, Ruud E.I. Schropp, Wilfried G.J.H.M. van Sark and André P.C. Faaij. *Geospatial analysis of the energy yield and environmental footprint of different photovoltaic module technologies*. Solar Energy, vol. 155, pages 1339–1353, 10.1016/j.solener.2017.07.056. (Cited on page 2.)

[Luo 2017] Cheng Luo, Manjarik Mrinal and Xiang Wang. *Self-propulsion of Leidenfrost Drops between Non-Parallel Structures*. Scientific Reports, vol. 7, no. 1, page 12018, 10.1038/s41598-017-12279-6. (Cited on page 175.)

[Luque 2003] A. Luque and Steven Hegedus, editors. Handbook of photovoltaic science and engineering. Wiley, Hoboken, NJ, 2003. (Cited on pages 11, 101 and 102.)

[Mahabaduge 2015] H. P. Mahabaduge, W. L. Rance, J. M. Burst, M. O. Reese, D. M. Meysing, C. A. Wolden, J. Li, J. D. Beach, T. A. Gessert, W. K. Metzger, S. Garner and T. M. Barnes. *High-efficiency, flexible CdTe solar cells on ultra-thin glass substrates*. Applied Physics Letters, vol. 106, no. 13, page 133501, 10.1063/1.4916634. (Cited on page 82.)

[Mahan 2006] A. H. Mahan, B. Roy, R. C. Reedy, D. W. Readey and D. S. Ginley. *Rapid thermal annealing of hot wire chemical-vapor-deposited a-Si:H films: The effect of the film hydrogen content on the crystallization kinetics, surface morphology, and grain growth*. Journal of Applied Physics, vol. 99, no. 2, page 023507, 10.1063/1.2159550. (Cited on page 141.)

[Maier 2007] Stefan A. Maier. Plasmonics: Fundamentals and Applications. Springer US, New York, NY, 2007. (Cited on pages 33 and 35.)

[Mariani 2013] Giacomo Mariani, Zhengliu Zhou, Adam Scofield and Diana L. Huffaker. *Direct-Bandgap Epitaxial Core–Multishell Nanopillar Photovoltaics Featuring Subwavelength Optical Concentrators*. Nano Letters, vol. 13, no. 4, pages 1632–1637, 10.1021/nl400083g. (Cited on page 18.)

[Matsui 2014] Takuya Matsui, Adrien Bidiville, Hitoshi Sai, Takashi Suezaki, Mitsuhiro Matsumoto, Kimihiko Saito, Isao Yoshida and Michio Kondo. *Improved metastability and performance of amorphous silicon solar cells*. MRS Proceedings, vol. 1666, pages mrss14–1666–a01–01, 10.1557/opl.2014.918. (Cited on page 106.)

[Matsui 2015a] Takuya Matsui, Adrien Bidiville, Keigou Maejima, Hitoshi Sai, Takashi Koida, Takashi Suezaki, Mitsuhiro Matsumoto, Kimihiko Saito, Isao Yoshida and Michio Kondo. *High-efficiency amorphous silicon solar cells: Impact of deposition rate on metastability.* Applied Physics Letters, vol. 106, no. 5, page 053901, 10.1063/1.4907001. (Cited on page 20.)

[Matsui 2015b] Takuya Matsui, Keigou Maejima, Adrien Bidiville, Hitoshi Sai, Takashi Koida, Takashi Suezaki, Mitsuhiro Matsumoto, Kimihiko Saito, Isao Yoshida and Michio Kondo. *High-efficiency thin-film silicon solar cells realized by integrating stable a-Si:H absorbers into improved device design.* Japanese Journal of Applied Physics, vol. 54, no. 8S1, page 08KB10, 10.7567/JJAP.54.08KB10. (Cited on pages 103 and 105.)

[Mayousse 2015] Céline Mayousse, Caroline Celle, Alexandra Fraczkiewicz and Jean-Pierre Simonato. *Stability of silver nanowire based electrodes under environmental and electrical stresses.* Nanoscale, vol. 7, no. 5, pages 2107–2115, 10.1039/C4NR06783E. (Cited on pages 66 and 68.)

[McIntyre 2019] P.C. McIntyre and A. Fontcuberta i Morral. *Semiconductor nanowires: to grow or not to grow?* Materials Today Nano, vol. 9, no. 100058, 10.1016/j.mtnano.2019.100058. (Cited on page 17.)

[Meaudre 1992] R. Meaudre and M. Meaudre. *Influence of illumination during annealing of quenched defects in undoped amorphous silicon.* Physical Review B, vol. 45, no. 20, pages 12134–12136, 10.1103/PhysRevB.45.12134. (Cited on page 106.)

[Mecklenburg 2019] Matthew Mecklenburg, William A. Hubbard, Jared J. Lodico and B.C. Regan. *Electron beam-induced current imaging with two-angstrom resolution.* Ultramicroscopy, vol. 207, page 112852, 10.1016/j.ultramic.2019.112852. (Cited on page 152.)

[Mendez-Gamboa 2016] J.A. Mendez-Gamboa, R. Castro-Rodriguez, I.V. Perez-Quintana, R.A. Medina-Esquivel and A. Martel-Arbelo. *A figure of merit to evaluate transparent conductor oxides for solar cells using photonic flux density.* Thin Solid Films, vol. 599, pages 14–18, 10.1016/j.tsf.2015.12.038. (Cited on pages 39 and 40.)

[Meng 2015] L. Meng, A.G. Street, J.C.H. Phang and C.S. Bhatia. *Application and modeling of single contact electron beam induced current technique on multicrystalline silicon solar cells.* Solar Energy Materials and Solar Cells, vol. 133, pages 143–147, 10.1016/j.solmat.2014.11.003. (Cited on page 152.)

[Merten 1998] J. Merten, J.M. Asensi, C. Voz, A.V. Shah, R. Platz and J. Andreu. *Improved equivalent circuit and analytical model for amorphous silicon solar cells and modules.* IEEE Transactions on Electron Devices, vol. 45, no. 2, pages 423–429, 10.1109/16.658676. (Cited on page 25.)

[Misiakos 1988] K. Misiakos and F. A. Lindholm. *Analytical and numerical modeling of amorphous silicon p - i - n solar cells.* Journal of Applied Physics, vol. 64, no. 1, pages 383–393, 10.1063/1.341439. (Cited on page 120.)

[Misra 2013] Soumyadeep Misra, Linwei Yu, Martin Foldyna and Pere Roca i Cabarrocas. *High efficiency and stable hydrogenated amorphous silicon radial junction solar cells built on VLS-grown silicon nanowires.* Solar Energy Materials and Solar Cells, vol. 118, pages 90–95, 10.1016/j.solmat.2013.07.036. (Cited on page 106.)

[Misra 2015a] Soumyadeep Misra. *Single and tandem radial junction silicon thin film solar cells based on PECVD grown crystalline silicon nanowire arrays.* PhD thesis, Ecole polytechnique, 2015. (Cited on pages 21, 42 and 106.)

[Misra 2015b] Soumyadeep Misra, Linwei Yu, Martin Foldyna and Pere Roca i Cabarrocas. *New Approaches to Improve the Performance of Thin-Film Radial Junction Solar Cells Built Over Silicon Nanowire Arrays.* IEEE Journal of Photovoltaics, vol. 5, no. 1, pages 40–45, 10.1109/JPHOTOV.2014.2366688. (Cited on pages ix, 18, 19, 20 and 22.)

[Mokkapati 2012] S. Mokkapati and K. R. Catchpole. *Nanophotonic light trapping in solar cells.* Journal of Applied Physics, vol. 112, no. 10, page 101101, 10.1063/1.4747795. (Cited on page 15.)

[Morales 2014] M Morales, D Munoz-Martin, Y Chen, O García, J J García-Ballesteros, J Cárabe, J J Gandía, C Molpeceres and Av Complutense. *Study of a-Si crystallization dependence on power and irradiation time using a CW green laser.* page 10, 2014. (Cited on page 141.)

[Mott 1969] N. F. Mott. *Conduction in non-crystalline materials: III. Localized states in a pseudogap and near extremities of conduction and valence bands.* Philosophical Magazine, vol. 19, no. 160, pages 835–852, 10.1080/14786436908216338. (Cited on page 97.)

[Mott 2012] N. F. Mott and E. A. Davis. Electronic processes in non-crystalline materials. International series of monographs on physics. Clarendon Press, Oxford, 2nd ed édition, 2012. (Cited on page 122.)

[Muskens 2008] Otto L. Muskens, Jaime Gómez Rivas, Rienk E. Algra, Erik P. A. M. Bakkers and Ad Lagendijk. *Design of Light Scattering in Nanowire Materials for Photovoltaic Applications.* Nano Letters, vol. 8, no. 9, pages 2638–2642, 10.1021/nl0808076. (Cited on pages 14 and 15.)

[Nair 2008] R. R. Nair, P. Blake, A. N. Grigorenko, K. S. Novoselov, T. J. Booth, T. Stauber, N. M. R. Peres and A. K. Geim. *Fine Structure Constant Defines Visual Transparency of Graphene.* Science, vol. 320, no. 5881, pages 1308–1308, 10.1126/science.1156965. (Cited on page 38.)

[Naumann 2014] Volker Naumann, Dominik Lausch, Angelika Hähnel, Jan Bauer, Otwin Breitenstein, Andreas Graff, Martina Werner, Sina Swatek, Stephan Großer, Jörg Bagdahn and Christian Hagendorf. *Explanation of potential-induced degradation of the shunting type by Na decoration of stacking faults in Si solar cells.* Solar Energy Materials and Solar Cells, vol. 120, pages 383–389, 10.1016/j.solmat.2013.06.015. (Cited on page 88.)

[Nian 2015] Qiong Nian, Mojib Saei, Yang Xu, Ganguli Sabyasachi, Biwei Deng, Yong P. Chen and Gary J. Cheng. *Crystalline Nanojoining Silver Nanowire Percolated Networks on Flexible Substrate.* ACS Nano, vol. 9, no. 10, pages 10018–10031, 10.1021/acsnano.5b03601. (Cited on page 176.)

[Nichterwitz 2013] Melanie Nichterwitz and Thomas Unold. *Numerical simulation of cross section electron-beam induced current in thin-film solar-cells for low and high injection conditions.* Journal of Applied Physics, vol. 114, no. 13, page 134504, 10.1063/1.4823519. (Cited on page 153.)

[Nielsen 1982] L.D. Nielsen. *Distributed series resistance effects in solar cells.* IEEE Transactions on Electron Devices, vol. 29, no. 5, pages 821–827, 10.1109/T-ED.1982.20784. (Cited on page 24.)

[Noh 2008] Jun Hong Noh, Hyun Suk Jung, Jung-Kun Lee, Jin Young Kim, Chin Moo Cho, Jae-sul An and Kug Sun Hong. *Reversible change in electrical and optical properties in epitaxially grown Al-doped ZnO thin films.* Journal of Applied Physics, vol. 104, no. 7, page 073706, 10.1063/1.2987472. (Cited on page 179.)

[Nomura 2004] Kenji Nomura, Hiromichi Ohta, Akihiro Takagi, Toshio Kamiya, Masahiro Hirano and Hideo Hosono. *Room-temperature fabrication of transparent flexible thin-film transistors using amorphous oxide semiconductors.* Nature, vol. 432, no. 7016, pages 488–492, 10.1038/nature03090. (Cited on page 37.)

[Norton 2018] E. Norton, L. Farrell, A. Zhussupbekova, D. Mullarkey, D. Caffrey, D. T. Papanastasiou, D. Oser, D. Bellet, I. V. Shvets and K. Fleischer. *Bending stability of $Cu_{0.4}CrO_2$ —A transparent p-type conducting oxide for large area flexible electronics.* AIP Advances, vol. 8, no. 8, page 085013, 10.1063/1.5027038. (Cited on page 37.)

[Novoselov 2004] K. S. Novoselov, A. K. Geim, S. V. Morozov, D. Jiang, Y. Zhang, S. V. Dubonos, I. V. Grigorieva and A. A. Firsov. *Electric Field Effect in Atomically Thin Carbon Films.* Science, vol. 306, no. 5696, pages 666–669, 10.1126/science.1102896. (Cited on page 38.)

[Ohshita 2019] Yoshio Ohshita, Yukio Miyashita, Atsushi Ogura, Kohei Onishi, Ryo Yokogawa, Tappei Nishihara, Takefumi Kamioka, Kyotaro Nakamura, Tomoyuki Kawatsu, Toshiki Nagai and Noboru Yamada. *Ultra-Thin Lightweight Bendable Crystalline Si Solar Cells for Solar Vehicles.* In 2019 IEEE 46th Photovoltaic Specialists Conference (PVSC), pages 1131–1134, Chicago, IL, USA, June 2019. IEEE. (Cited on page 83.)

[Ohta 2000] Hiromichi Ohta, Masahiro Orita, Masahiro Hirano, Hiroaki Tanji, Hiroshi Kawazoe and Hideo Hosono. *Highly electrically conductive indium–tin–oxide thin films epitaxially grown on yttria-stabilized zirconia (100) by pulsed-laser deposition.* Applied Physics Letters, vol. 76, no. 19, pages 2740–2742, 10.1063/1.126461. (Cited on page 44.)

[Orejon 2011] Daniel Orejon, Khellil Sefiane and Martin E. R. Shanahan. *Stick–Slip of Evaporating Droplets: Substrate Hydrophobicity and Nanoparticle Concentration.*

Langmuir, vol. 27, no. 21, pages 12834–12843, 10.1021/la2026736. (Cited on page 174.)

[Otnes 2017] Gaute Otnes and Magnus T. Borgström. *Towards high efficiency nanowire solar cells.* Nano Today, vol. 12, pages 31–45, 10.1016/j.nantod.2016.10.007. (Cited on page 17.)

[Paire 2011] Myriam Paire, Artabaze Shams, Laurent Lombez, Nicolas Péré-Laperne, Stéphane Collin, Jean-Luc Pelouard, Jean-François Guillemoles and Daniel Lincot. *Resistive and thermal scale effects for Cu(In, Ga)Se2 polycrystalline thin film microcells under concentration.* Energy & Environmental Science, vol. 4, no. 12, page 4972, 10.1039/c1ee01661j. (Cited on page 128.)

[Paire 2012] Myriam Paire. *Highly efficient solar cells in low dimensionality based on Cu(In,Ga)Se2 chalcopyrite materials.* PhD thesis, 2012. (Cited on page 111.)

[Pathirane 2017] Minoli K. Pathirane, Hadi Hosseinzadeh Khaligh, Irene A. Goldthorpe and William S. Wong. *Al-doped ZnO/Ag-nanowire Composite Electrodes for Flexible 3-Dimensional Nanowire Solar Cells.* Scientific Reports, vol. 7, no. 1, page 8916, 10.1038/s41598-017-07180-1. (Cited on pages 43, 51, 61 and 84.)

[Pekker 2010] Á. Pekker and K. Kamarás. *A general figure of merit for thick and thin transparent conductive carbon nanotube coatings.* Journal of Applied Physics, vol. 108, no. 5, page 054318, 10.1063/1.3476278. (Cited on page 40.)

[Peng 2011] Cheng Peng, Zheng Jia, Dan Bianculli, Teng Li and Jun Lou. *In situ electro-mechanical experiments and mechanics modeling of tensile cracking in indium tin oxide thin films on polyimide substrates.* Journal of Applied Physics, vol. 109, no. 10, page 103530, 10.1063/1.3592341. (Cited on page 84.)

[Peng 2021] Jun Peng, Daniel Walter, Yuhao Ren, Mike Tebyetekerwa, Yiliang Wu, The Duong, Qiaoling Lin, Juntao Li, Teng Lu, Md Arafat Mahmud, Olivier Lee Cheong Lem, Shenyou Zhao, Wenzhu Liu, Yun Liu, Heping Shen, Li Li, Felipe Kremer, Hieu T. Nguyen, Duk-Yong Choi, Klaus J. Weber, Kylie R. Catchpole and Thomas P. White. *Nanoscale localized contacts for high fill factors in polymer-passivated perovskite solar cells.* Science, vol. 371, no. 6527, pages 390–395, 10.1126/science.abb8687. (Cited on page 7.)

[Pham 2016] Anh-Tuan Pham, Xuan-Quang Nguyen, Duc-Huy Tran, Vu Ngoc Phan, Thanh-Tung Duong and Duy-Cuong Nguyen. *Enhancement of the electrical properties of silver nanowire transparent conductive electrodes by atomic layer deposition coating with zinc oxide.* Nanotechnology, vol. 27, no. 33, page 335202, 10.1088/0957-4484/27/33/335202. (Cited on page 70.)

[Piazza 2018] Valerio Piazza. *Electron Beam Based Techniques for the Characterization of Nanowire Solar Cell.* PhD thesis, Université Paris-Saclay, 2018. (Cited on page 163.)

[Piscanec 2003] S. Piscanec, M. Cantoro, A. C. Ferrari, J. A. Zapien, Y. Lifshitz, S. T. Lee, S. Hofmann and J. Robertson. *Raman spectroscopy of silicon nanowires.*

Physical Review B, vol. 68, no. 24, page 241312, 10.1103/PhysRevB.68.241312. (Cited on page 130.)

[Reddy 2007] J N Reddy. Theory and Analysis of Elastic Plates and Shells, Second Edition. CRC Press, 2nd edition édition, 2007. (Cited on page 81.)

[Richey 2020] Nathaniel E. Richey, Camila de Paula and Stacey F. Bent. *Understanding chemical and physical mechanisms in atomic layer deposition.* The Journal of Chemical Physics, vol. 152, no. 4, page 040902, 10.1063/1.5133390. (Cited on pages 46 and 72.)

[Riesen 2016] Y. Riesen, M. Stuckelberger, F.-J. Haug, C. Ballif and N. Wyrsch. *Temperature dependence of hydrogenated amorphous silicon solar cell performances.* Journal of Applied Physics, vol. 119, no. 4, page 044505, 10.1063/1.4940392. (Cited on page 133.)

[Sai 2016] Hitochi Sai, Takuya Matsui and Koji Matsubara. *Stabilized 14.0%-efficient triple-junction thin-film silicon solar cell.* Applied Physics Letters, vol. 109, no. 18, page 183506, 10.1063/1.4966996. (Cited on pages 20 and 103.)

[Saive 2019] Rebecca Saive. *S-Shaped Current–Voltage Characteristics in Solar Cells: A Review.* IEEE Journal of Photovoltaics, vol. 9, no. 6, pages 1477–1484, 10.1109/JPHOTOV.2019.2930409. (Cited on page 182.)

[Saket 2020] Omar Saket, Chalermchai Himwas, Valerio Piazza, Fabien Bayle, Andrea Cattoni, Fabrice Oehler, Gilles Patriarche, Laurent Travers, Stephane Collin, François H Julien, Jean-Christophe Harmand and Maria Tchernycheva. *Nanoscale electrical analyses of axial-junction GaAsP nanowires for solar cell applications.* Nanotechnology, vol. 31, no. 14, page 145708, 10.1088/1361-6528/ab62c9. (Cited on page 152.)

[Saket 2021] Omar Saket, Junkang Wang, Nuño Amador-Mendez, Martina Morassi, Arup Kunti, Fabien Bayle, Stéphane Collin, Arnaud Jollivet, Andrey Babichev, Tanbir Sodhi, Jean-Christophe Harmand, François H Julien, Noelle Gogneau and Maria Tchernycheva. *Investigation of the effect of the doping order in GaN nanowire p–n junctions grown by molecular-beam epitaxy.* Nanotechnology, vol. 32, no. 8, page 085705, 10.1088/1361-6528/abc91a. (Cited on page 167.)

[Sambles 1982] J R Sambles, K C Elsom and T W Preist. *The resistivity of thin wires.* Journal of Physics F: Metal Physics, vol. 12, no. 6, pages 1169–1183, 10.1088/0305-4608/12/6/017. (Cited on page 172.)

[Sannicolo 2018] Thomas Sannicolo. *Transparent electrodes based on silver nanowire networks: electrical percolation, physical properties, and applications.* PhD thesis, Université Grenoble Alpes, 2018. (Cited on page 48.)

[Schneider 1987] Ulrich Schneider, Bernd Schröder and Friedhelm Finger. *The creation of metastable defects in a-Si: H films by high dose irradiation with keV-electrons.* Journal of Non-Crystalline Solids, vol. 97-98, pages 795–798, 1987. (Cited on pages 105 and 156.)

[Schrenker 2021] Nadine J. Schrenker, Zhuocheng Xie, Peter Schweizer, Marco Moninger, Felix Werner, Nicolas Karpstein, Mirza Mačković, George D. Spyropoulos, Manuela Göbelt, Silke Christiansen, Christoph J. Brabec, Erik Bitzek and Erdmann Spiecker. *Microscopic Deformation Modes and Impact of Network Anisotropy on the Mechanical and Electrical Performance of Five-fold Twinned Silver Nanowire Electrodes.* ACS Nano, vol. 15, no. 1, pages 362–376, 10.1021/acsnano.0c06480. (Cited on page 50.)

[Shim 2010] Bong Sup Shim, Jian Zhu, Edward Jan, Kevin Critchley and Nicholas A. Kotov. *Transparent Conductors from Layer-by-Layer Assembled SWNT Films: Importance of Mechanical Properties and a New Figure of Merit.* ACS Nano, vol. 4, no. 7, pages 3725–3734, 10.1021/nn100026n. (Cited on page 39.)

[Shin 2009] Dong-Wook Shin, Jong Hak Lee, Yu-Hee Kim, Seong Man Yu, Seong-Yong Park and Ji-Beom Yoo. *A role of HNO_3 on transparent conducting film with single-walled carbon nanotubes.* Nanotechnology, vol. 20, no. 47, page 475703, 10.1088/0957-4484/20/47/475703. (Cited on page 38.)

[Shkrob 1998] Ilya A. Shkrob and Robert A. Crowell. *Ultrafast charge recombination in undoped amorphous hydrogenated silicon.* Physical Review B, vol. 57, no. 19, pages 12207–12218, 10.1103/PhysRevB.57.12207. (Cited on page 122.)

[Shockley 1949] W Shockley. *The Theory of p-n Junctions in Semiconductors and p-n Junction Transistors.* Bell System Technical Journal, page 55, 1949. (Cited on page 12.)

[Shockley 1961] William Shockley and Hans J Queisser. *Detailed Balance Limit of Efficiency of p-n Junction Solar Cells.* Journal of Applied Physics, vol. 32, no. 510, page 11, 1961. (Cited on page 6.)

[Sinton 1987] Ronald Sinton and Richard Swanson. *Recombination in Highly Injected Silicon.* IEEE Transactions on Electron Devices, vol. 34, no. 6, pages 1380–1389, 1987. (Cited on page 122.)

[Smith 1985] Z E. Smith, S. Wagner and B. W. Faughnan. *Carrier lifetime model for the optical degradation of amorphous silicon solar cells.* Applied Physics Letters, vol. 46, no. 11, pages 1078–1080, 10.1063/1.95767. (Cited on pages 116 and 118.)

[Snow 2005] E. S. Snow, P. M. Campbell, M. G. Ancona and J. P. Novak. *High-mobility carbon-nanotube thin-film transistors on a polymeric substrate.* Applied Physics Letters, vol. 86, no. 3, page 033105, 10.1063/1.1854721. (Cited on page 38.)

[Sobkowicz 2014] Igor Paul Sobkowicz. *Study and optimization of the growth of a-Si:H on wet-chemically textured c-Si substrates for the enhancement of a-Si:H/c-Si heterojunction solar cells.* PhD thesis, 2014. (Cited on page 109.)

[Söderström 2008] T. Söderström, F.-J. Haug, V. Terrazzoni-Daudrix and C. Ballif. *Optimization of amorphous silicon thin film solar cells for flexible photovoltaics.* Journal of Applied Physics, vol. 103, no. 11, page 114509, 10.1063/1.2938839. (Cited on page 82.)

[Söderström 2009] T. Söderström, F.-J. Haug, X. Niquille and C. Ballif. *TCOs for nip thin film silicon solar cells: TCOs FOR NIP THIN FILM SILICON SOLAR CELLS*. Progress in Photovoltaics: Research and Applications, vol. 17, no. 3, pages 165–176, 10.1002/pip.869. (Cited on page 56.)

[Song 2013] Myungkwan Song, Dae Sung You, Kyounga Lim, Sujin Park, Sunghoon Jung, Chang Su Kim, Dong-Ho Kim, Do-Geun Kim, Jongk-Kuk Kim, Juyun Park, Yong-Cheol Kang, Jinhee Heo, Sung-Ho Jin, Jong Hyun Park and Jae-Wook Kang. *Highly Efficient and Bendable Organic Solar Cells with Solution-Processed Silver Nanowire Electrodes*. Advanced Functional Materials, vol. 23, no. 34, pages 4177–4184, 10.1002/adfm.201202646. (Cited on page 50.)

[Song 2015] Tze-Bin Song, You Seung Rim, Fengmin Liu, Brion Bob, Shenglin Ye, Yao-Tsung Hsieh and Yang Yang. *Highly Robust Silver Nanowire Network for Transparent Electrode*. ACS Applied Materials & Interfaces, vol. 7, no. 44, pages 24601–24607, 10.1021/acsami.5b06540. (Cited on page 67.)

[Spear 1975] W E Spear and P G Le Comber. *Substitutional Doping of Amorphous Silicon*. Solid State Communications, vol. 17, no. 9, pages 1193–1196, 1975. (Cited on page 99.)

[Spear 1976] W. E. Spear and P. G. Le Comber. *Electronic properties of substitutionally doped amorphous Si and Ge*. Philosophical Magazine, vol. 33, no. 6, pages 935–949, 10.1080/14786437608221926. (Cited on page 102.)

[Staebler 1977] D. L. Staebler and C. R. Wronski. *Reversible conductivity changes in discharge-produced amorphous Si*. Applied Physics Letters, vol. 31, no. 4, pages 292–294, 10.1063/1.89674. (Cited on page 105.)

[Stiebig 1996] H Stiebig, Th Eickhoff, J Zimmer, C Beneking and H Wagner. *Measured and simulated temperature dependence of a-Si:H solar cell parameters*. In Materials Research Society Symposium Proceedings, volume 420, page 6, 1996. (Cited on page 133.)

[str 1991] *Saturation and recovery kinetics of current-induced effects in a-Si:H*. Journal of Non-Crystalline Solids, vol. 137-138, pages 263–266, 1991. (Cited on pages 106 and 118.)

[Street 1981] R. A. Street. *Recombination in a-Si:H: Auger effects and nongeminate recombination*. Physical Review B, vol. 23, no. 2, pages 861–868, 10.1103/PhysRevB.23.861. (Cited on page 122.)

[Street 1991] Robert A. Street. Hydrogenated Amorphous Silicon. Cambridge solid state édition, 1991. (Cited on pages 97, 98, 99, 100, 101, 102, 105 and 128.)

[Street 2000] Robert A. Street, Robert Hull, R. M. Osgood, H. Sakaki and Alex Zunger, editors. Technology and Applications of Amorphous Silicon, volume 37 of *Springer Series in Materials Science*. Springer Berlin Heidelberg, Berlin, Heidelberg, 2000. (Cited on page 134.)

[Stutzmann 1985] M. Stutzmann, W. B. Jackson and C. C. Tsai. *Light-induced metastable defects in hydrogenated amorphous silicon: A systematic study.* Physical Review B, vol. 32, no. 1, pages 23–47, 10.1103/PhysRevB.32.23. (Cited on pages 106, 116 and 117.)

[Stutzmann 2000] Martin Stutzmann, Martin S Brandt and Martin W Bayerl. *Spin-dependent processes in amorphous and microcrystalline silicon: a survey.* Journal of Non-Crystalline Solids, vol. 266-269, pages 1–22, 2000. (Cited on page 105.)

[Sugimura 2012] Emi Sugimura, Sohichiroh Takamoto, Shinichiro Tsujii, Kenji Hirata, Ayumi Tani and Takashi Fuyuki. *Spatially Resolved Electroluminescence Imaging of Shunt Sources in Crystalline Silicon Solar Cells.* Japanese Journal of Applied Physics, vol. 51, page 10NA02, 10.1143/JJAP.51.10NA02. (Cited on page 87.)

[Sugnaux 2015] Caroline Sugnaux, Anna Dalmau Mallorquí, Jane Herriman, Harm-Anton Klok and Anna Fontcuberta i Morral. *Polymer Brush Guided Formation of Conformal, Plasmonic Nanoparticle-Based Electrodes for Microwire Solar Cells.* Advanced Functional Materials, vol. 25, no. 25, pages 3958–3965, 10.1002/adfm.201404235. (Cited on page 38.)

[Sun 2002] Yugang Sun, Byron Gates, Brian Mayers and Younan Xia. *Crystalline Silver Nanowires by Soft Solution Processing.* Nano Letters, vol. 2, no. 2, pages 165–168, 10.1021/nl010093y. (Cited on page 50.)

[Sun 2018] Xiaolin Sun, Ting Zhang, Junzhuan Wang, Fan Yang, Ling Xu, Jun Xu, Yi Shi, Kunji Chen, Pere Roca i Cabarrocas and Linwei Yu. *Firmly standing three-dimensional radial junctions on soft aluminum foils enable extremely low cost flexible thin film solar cells with very high power-to-weight performance.* Nano Energy, vol. 53, pages 83–90, 10.1016/j.nanoen.2018.08.038. (Cited on pages 15, 22, 84 and 85.)

[Suo 1999] Z. Suo, E. Y. Ma, H. Gleskova and S. Wagner. *Mechanics of rollable and foldable film-on-foil electronics.* Applied Physics Letters, vol. 74, no. 8, pages 1177–1179, 10.1063/1.123478. (Cited on page 90.)

[Swanepoel 1983] R Swanepoel. *Determination of the thickness and optical constants of amorphous silicon.* Journal of Physics E: Scientific Instruments, vol. 16, no. 12, pages 1214–1222, 10.1088/0022-3735/16/12/023. (Cited on page 53.)

[Tammenmaa 1985] M. Tammenmaa, T. Koskinen, L. Hiltunen, L. Niinistö and M. Leskelä. *Zinc chalcogenide thin films grown by the atomic layer epitaxy technique using zinc acetate as source material.* Thin Solid Films, vol. 124, no. 2, pages 125–128, 10.1016/0040-6090(85)90254-8. (Cited on page 46.)

[Tang 2011] Jinyao Tang, Ziyang Huo, Sarah Brittman, Hanwei Gao and Peidong Yang. *Solution-processed core–shell nanowires for efficient photovoltaic cells.* Nature Nanotechnology, vol. 6, no. 9, pages 568–572, 10.1038/nnano.2011.139. (Cited on page 17.)

[Terrón 1994] M. J. Terrón and A. Luque. *Reduction of the apparent shunt resistance effect in silicon concentrator solar cells.* Progress in Photovoltaics: Research and

Applications, vol. 2, no. 3, pages 187–202, 10.1002/pip.4670020302. (Cited on page 111.)

[Tian 2016] Lin Tian, Lorenzo Di Mario, Antonio Minotti, Giorgio Tiburzi, Budhika G Mendis, Dagou A Zeze and Faustino Martelli. *Direct growth of Si nanowires on flexible organic substrates.* Nanotechnology, vol. 27, no. 22, page 225601, 10.1088/0957-4484/27/22/225601. (Cited on pages 16 and 84.)

[Togonal 2016] Aliénor Svietlana Togonal, Martin Foldyna, Wanghua Chen, Jian Xiong Wang, Vladimir Neplokh, Maria Tchernycheva, Joaquim Nassar, Pere Roca i Cabarrocas and Rusli. *Core–Shell Heterojunction Solar Cells Based on Disordered Silicon Nanowire Arrays.* The Journal of Physical Chemistry C, vol. 120, no. 5, pages 2962–2972, 10.1021/acs.jpcc.5b09618. (Cited on page 14.)

[Tsakalakos 2007] L Tsakalakos, J Balch, J Fronheiser, B A Korevaar, O Sulima and J Rand. *Silicon nanowire solar cells.* Appl. Phys. Lett., vol. 91, no. 233117, page 4, 2007. (Cited on page 14.)

[Tseng 2011] Zong-Liang Tseng, Po-Ching Kao, Chi-Shin Yang, Yung-Der Juang, Yu-Mei Kuo and Sheng-Yuan Chu. *Transparent Conducting Ti-Doped ZnO Thin Films Applied to Organic Light-Emitting Diodes.* Journal of The Electrochemical Society, vol. 158, no. 5, page J133, 10.1149/1.3554730. (Cited on page 45.)

[Turek 2014] Marko Turek. *Current and illumination dependent series resistance of solar cells.* Journal of Applied Physics, vol. 115, no. 14, page 144503, 10.1063/1.4871017. (Cited on page 24.)

[van Dam 2016] Dick van Dam, Niels J. J. van Hoof, Yingchao Cui, Peter J. van Veldhoven, Erik P. A. M. Bakkers, Jaime Gómez Rivas and Jos E. M. Haverkort. *High-Efficiency Nanowire Solar Cells with Omnidirectionally Enhanced Absorption Due to Self-Aligned Indium–Tin–Oxide Mie Scatterers.* ACS Nano, vol. 10, no. 12, pages 11414–11419, 10.1021/acsnano.6b06874. (Cited on pages 18 and 42.)

[van de Groep 2012] Jorik van de Groep, Pierpaolo Spinelli and Albert Polman. *Transparent Conducting Silver Nanowire Networks.* Nano Letters, vol. 12, no. 6, pages 3138–3144, 10.1021/nl301045a. (Cited on page 73.)

[van der Pauw 1958] L.J. van der Pauw. *A method of measuring specific resistivity and Hall effect of discs of arbitrary shape.* Philips Research Reports, vol. 13, no. 1, pages 1–9, 1958. (Cited on pages 22 and 23.)

[Vaněček 1998] M. Vaněček, A. Poruba, Z. Remeš, N. Beck and M. Nesládek. *Optical properties of microcrystalline materials.* Journal of Non-Crystalline Solids, vol. 227-230, pages 967–972, 10.1016/S0022-3093(98)00202-6. (Cited on page 101.)

[Viera 2001] G Viera, S Huet and L Boufendi. *Crystal size and temperature measurements in nanostructured silicon using Raman spectroscopy.* Journal of Applied Physics, vol. 90, no. 8, pages 4175–4183, 2001. (Cited on pages 129 and 130.)

[Virtuani 2010] A Virtuani, D Pavanello and G Friesen. *Overview of temperature coefficients of different thin film photovoltaic technologies.* page 5, 2010. (Cited on page 133.)

[Vollmar 1993] Hans-Peter Vollmar and Roland Bindemann. *Enhanced non-radiative recombination in hydrogenated amorphous silicon at low carrier densities and low temperatures.* Philosophical Magazine Letters, vol. 67, no. 4, pages 231–237, 10.1080/09500839308240934. (Cited on page 122.)

[Vorasayan 2011] P. Vorasayan, T.R. Betts and R. Gottschalg. *Spatially distributed model for the analysis of laser beam induced current (LBIC) measurements of thin film silicon solar modules.* Solar Energy Materials and Solar Cells, vol. 95, no. 1, pages 111–114, 10.1016/j.solmat.2010.02.020. (Cited on page 88.)

[Vossier 2010] Alexis Vossier, Baruch Hirsch and Jeffrey M. Gordon. *Is Auger recombination the ultimate performance limiter in concentrator solar cells?* Applied Physics Letters, vol. 97, no. 19, page 193509, 10.1063/1.3510474. (Cited on page 122.)

[Voutsas 2003] A T Voutsas. *A new era of crystallization: advances in polysilicon crystallization and crystal engineering.* Applied Surface Science, page 13, 2003. (Cited on page 141.)

[Wagner 1964] R. S. Wagner and W. C. Ellis. *Vapor-liquid-solid mechanism of single crystal growth.* Applied Physics Letters, vol. 4, no. 5, pages 89–90, 10.1063/1.1753975. (Cited on pages 17 and 21.)

[Walsh 2008] Aron Walsh, Juarez L. F. Da Silva, Su-Huai Wei, C. Körber, A. Klein, L. F. J. Piper, Alex DeMasi, Kevin E. Smith, G. Panaccione, P. Torelli, D. J. Payne, A. Bourlange and R. G. Egdell. *Nature of the Band Gap of In 2 O 3 Revealed by First-Principles Calculations and X-Ray Spectroscopy.* Physical Review Letters, vol. 100, no. 16, page 167402, 10.1103/PhysRevLett.100.167402. (Cited on page 45.)

[Wan 2021] Juanyong Wan, Yonggao Xia, Junfeng Fang, Zhiguo Zhang, Bingang Xu, Jinzhao Wang, Ling Ai, Weijie Song, Kwun Nam Hui, Xi Fan and Yongfang Li. *Solution-Processed Transparent Conducting Electrodes for Flexible Organic Solar Cells with 16.61% Efficiency.* Nano-Micro Letters, vol. 13, no. 1, page 44, 10.1007/s40820-020-00566-3. (Cited on page 82.)

[Wang 2017] Xiaofeng Wang, Giho Kang, Baekhoon Seong, Illkyeong Chae, Hadi Teguh Yudistira, Hyungdong Lee, Hyunggun Kim and Doyoung Byun. *Transparent arrays of silver nanowire rings driven by evaporation of sessile droplets.* Journal of Physics D: Applied Physics, vol. 50, no. 45, page 455302, 10.1088/1361-6463/aa8c23. (Cited on page 175.)

[Weaire 1971] D. Weaire and M. F. Thorpe. *Electronic Properties of an Amorphous Solid. I. A Simple Tight-Binding Theory.* Physical Review B, vol. 4, no. 8, pages 2508–2520, 10.1103/PhysRevB.4.2508. (Cited on page 97.)

[Weber 2003] Marvin J. Weber. Handbook of optical materials. The CRC Press laser and optical science and technology series. CRC Press, Boca Raton, 2003. (Cited on page 134.)

[Werner 1988] U Werner, F Koch and G Oelgart. *Kilovolt electron energy loss distribution in Si.* Journal of Physics D: Applied Physics, vol. 21, no. 1, pages 116–124, 10.1088/0022-3727/21/1/017. (Cited on page 153.)

[Wolf 1963] Martin Wolf and Hans Rauschenbach. *Series resistance effects on solar cell measurements.* Advanced Energy Conversion, vol. 3, no. 2, pages 455–479, 10.1016/0365-1789(63)90063-8. (Cited on page 25.)

[Wong 2021] Joeson Wong, Stefan T. Omelchenko and Harry A. Atwater. *Impact of Semiconductor Band Tails and Band Filling on Photovoltaic Efficiency Limits.* ACS Energy Letters, vol. 6, no. 1, pages 52–57, 10.1021/acsenergylett.0c02362. (Cited on page 129.)

[Wu 2004] Zhuangchun Wu, Zhihong Chen, Xu Du, Jonathan M. Logan, Jennifer Sippel, Maria Nikolou, Katalin Kamaras, John R. Reynolds, David B. Tanner, Arthur F. Hebard and Andrew G. Rinzler. *Transparent, Conductive Carbon Nanotube Films.* Science, vol. 305, no. 5688, pages 1273–1276, 10.1126/science.1101243. (Cited on page 38.)

[Wu 2010] Junbo Wu, Mukul Agrawal, Héctor A. Becerril, Zhenan Bao, Zunfeng Liu, Yongsheng Chen and Peter Peumans. *Organic Light-Emitting Diodes on Solution-Processed Graphene Transparent Electrodes.* ACS Nano, vol. 4, no. 1, pages 43–48, 10.1021/nn900728d. (Cited on page 38.)

[Xiao 2019] Chuanxiao Xiao, Chun-Sheng Jiang, Steve P. Harvey, Dana Sulas, Xihan Chen, Jun Liu, Jie Pan, Helio Moutinho, Andrew Norman, Peter Hacke, Steve Johnston and Mowafak Al-Jassim. *Large-Area Material and Junction Damage in c–Si Solar Cells by Potential-Induced Degradation.* Solar RRL, vol. 3, no. 4, page 1800303, 10.1002/solr.201800303. (Cited on page 88.)

[Xie 2012] Xiaobing Xie, Xiangbo Zeng, Ping Yang, Hao Li, Jingyan Li, Xiaodong Zhang and Qiming Wang. *Radial n-i-p structure SiNW-based microcrystalline silicon thin-film solar cells on flexible stainless steel.* Nanoscale Research Letters, vol. 7, no. 1, page 621, 10.1186/1556-276X-7-621. (Cited on page 21.)

[Xu 2011] Jun Xu, Xia Yang, Hongkang Wang, Xue Chen, Chunyan Luan, Zongxiang Xu, Zhenzhen Lu, V. A. L. Roy, Wenjun Zhang and Chun-Sing Lee. *Arrays of ZnO/Zn $_x$ Cd $_{1-x}$ Se Nanocables: Band Gap Engineering and Photovoltaic Applications.* Nano Letters, vol. 11, no. 10, pages 4138–4143, 10.1021/nl201934k. (Cited on page 17.)

[Yamamoto 2018] Kenji Yamamoto, Kunta Yoshikawa, Hisashi Uzu and Daisuke Adachi. *High-efficiency heterojunction crystalline Si solar cells.* Japanese Journal of Applied Physics, vol. 57, no. 8S3, page 08RB20, 10.7567/JJAP.57.08RB20. (Cited on page 104.)

[Yan 2006] Baojie Yan, Guozhen Yue, Jessica Owens, Jeffrey Yang and Subhendu Guha. *Over 15% Efficient Hydrogenated Amorphous Silicon Based Triple-Junction Solar Cells Incorporating Nanocrystalline Silicon.* In 2006 IEEE 4th World Conference on Photovoltaic Energy Conference, pages 1477–1480, Waikoloa, HI, 2006. IEEE. (Cited on page 82.)

[Yan 2009] Ruoxue Yan, Daniel Gargas and Peidong Yang. *Nanowire photonics.* Nature Photonics, vol. 3, no. 10, pages 569–576, 10.1038/nphoton.2009.184. (Cited on page 13.)

[Yang 1991] L. Yang, L. Chen and A. Catalano. *Intensity and temperature dependence of photodegradation of amorphous silicon solar cells under intense illumination.* Applied Physics Letters, vol. 59, no. 7, pages 840–842, 10.1063/1.105253. (Cited on page 107.)

[Yang 2006] Y. Yang, X.W. Sun, B.J. Chen, C.X. Xu, T.P. Chen, C.Q. Sun, B.K. Tay and Z. Sun. *Refractive indices of textured indium tin oxide and zinc oxide thin films.* Thin Solid Films, vol. 510, no. 1-2, pages 95–101, 10.1016/j.tsf.2005.12.265. (Cited on pages 45 and 53.)

[Yao 2015] Maoqing Yao, Sen Cong, Shermin Arab, Ningfeng Huang, Michelle L. Povinelli, Stephen B. Cronin, P. Daniel Dapkus and Chongwu Zhou. *Tandem Solar Cells Using GaAs Nanowires on Si: Design, Fabrication, and Observation of Voltage Addition.* Nano Letters, vol. 15, no. 11, pages 7217–7224, 10.1021/acs.nanolett.5b03890. (Cited on page 18.)

[Yelon 2000] Arthur Yelon, Hellmut Fritzsche and Howard M Branz. *Electron beam creation of metastable defects in hydrogenated amorphous silicon: hydrogen collision model.* Journal of Non-Crystalline Solids, vol. 266-269, pages 437–443, 10.1016/S0022-3093(99)00772-3. (Cited on page 156.)

[Yoshihiro 1994] Hishikawa Yoshihiro and Okamoto Shingo. *Dependence of the I–V characteristics of amorphous silicon solar cells on illumination intensity and temperature.* Solar Energy Materials and Solar Cells, vol. 33, no. 2, pages 157–168, 10.1016/0927-0248(94)90204-6. (Cited on page 107.)

[Yoshikawa 2017] Kunta Yoshikawa, Hayato Kawasaki, Wataru Yoshida, Toru Irie, Katsunori Konishi, Kunihiro Nakano, Toshihiko Uto, Daisuke Adachi, Masanori Kanematsu, Hisashi Uzu and Kenji Yamamoto. *Silicon heterojunction solar cell with interdigitated back contacts for a photoconversion efficiency over 26%.* Nature Energy, vol. 2, no. 5, page 17032, 10.1038/nenergy.2017.32. (Cited on pages 7, 12 and 25.)

[Yu 2009] Linwei Yu, Benedict O'Donnell, Pierre-Jean Alet, S Conesa-Boj, F Peiró, J Arbiol and Pere Roca i Cabarrocas. *Plasma-enhanced low temperature growth of silicon nanowires and hierarchical structures by using tin and indium catalysts.* Nanotechnology, vol. 20, no. 22, page 225604, 10.1088/0957-4484/20/22/225604. (Cited on page 84.)

[Yu 2010] Linwei Yu, Benedict O'Donnell, Pierre-Jean Alet and Pere Roca i Cabarrocas. *All-in-situ fabrication and characterization of silicon nanowires on TCO/glass*

substrates for photovoltaic application. Solar Energy Materials and Solar Cells, vol. 94, no. 11, pages 1855–1859, 10.1016/j.solmat.2010.06.021. (Cited on page 21.)

[Yu 2012] Rui Yu, Qingfeng Lin, Siu-Fung Leung and Zhiyong Fan. *Nanomaterials and nanostructures for efficient light absorption and photovoltaics.* Nano Energy, vol. 1, no. 1, pages 57–72, 10.1016/j.nanoen.2011.10.002. (Cited on page 18.)

[Yu 2016] Peng Yu, Jiang Wu, Shenting Liu, Jie Xiong, Chennupati Jagadish and Zhiming M. Wang. *Design and fabrication of silicon nanowires towards efficient solar cells.* Nano Today, vol. 11, no. 6, pages 704–737, 10.1016/j.nantod.2016.10.001. (Cited on page 17.)

[Yuan 2009] Zhijun Yuan, Qihong Lou, Jun Zhou, Jingxing Dong, Yunrong Wei, Zhijiang Wang, Hongming Zhao and Guohua Wu. *Numerical and experimental analysis on green laser crystallization of amorphous silicon thin films.* Optics & Laser Technology, vol. 41, no. 4, pages 380–383, 10.1016/j.optlastec.2008.09.003. (Cited on page 126.)

[Zardetto 2011] Valerio Zardetto, Thomas M. Brown, Andrea Reale and Aldo Di Carlo. *Substrates for flexible electronics: A practical investigation on the electrical, film flexibility, optical, temperature, and solvent resistance properties.* Journal of Polymer Science Part B: Polymer Physics, vol. 49, no. 9, pages 638–648, 10.1002/polb.22227. (Cited on page 42.)

[Zeman 2000] M. Zeman, R. A. C. M. M. van Swaaij, J. W. Metselaar and R. E. I. Schropp. *Optical modeling of a-Si:H solar cells with rough interfaces: Effect of back contact and interface roughness.* Journal of Applied Physics, vol. 88, no. 11, pages 6436–6443, 10.1063/1.1324690. (Cited on page 49.)

[Zhai 2015] Xiongfei Zhai, Guoyang Cao, Shaolong Wu, Aixue Shang and Xiaofeng Li. *Study on limiting efficiencies of a-Si:H/ μ c-Si:H-based single-nanowire solar cells under single and tandem junction configurations.* Applied Physics Letters, vol. 107, no. 18, page 181106, 10.1063/1.4935077. (Cited on page 122.)

[Zhang 2006] Daihua Zhang, Koungmin Ryu, Xiaolei Liu, Evgueni Polikarpov, James Ly, Mark E. Tompson and Chongwu Zhou. *Transparent, Conductive, and Flexible Carbon Nanotube Films and Their Application in Organic Light-Emitting Diodes.* Nano Letters, vol. 6, no. 9, pages 1880–1886, 10.1021/nl0608543. (Cited on page 38.)

[Zhang 2011] Chunfu Zhang, Jincheng Zhang, Yue Hao, Zhenhua Lin and Chunxiang Zhu. *A simple and efficient solar cell parameter extraction method from a single current-voltage curve.* Journal of Applied Physics, vol. 110, no. 6, page 064504, 10.1063/1.3632971. (Cited on page 26.)

[Zhang 2019] Ting Zhang, Junzhuan Wang, Linwei Yu, Jun Xu and Pere Roca i Cabarrocas. *Advanced radial junction thin film photovoltaics and detectors built on standing silicon nanowires.* Nanotechnology, vol. 30, no. 30, page 302001, 10.1088/1361-6528/ab0e57. (Cited on page 17.)

[Zhang 2021] Shaobo Zhang, Ting Zhang, Zongguang Liu, Junzhuan Wang, Linwei Yu, Jun Xu, Kunji Chen and Pere Roca i Cabarrocas. *Highly flexible radial tandem junction thin film solar cells with excellent power-to-weight ratio.* Nano Energy, vol. 86, page 106121, 10.1016/j.nanoen.2021.106121. (Cited on pages 22 and 44.)

[Zhigunov 2018] D M Zhigunov, G N Kamaev, P K Kashkarov and V A Volodin. *On Raman scattering cross section ratio of crystalline and microcrystalline to amorphous silicon.* Appl. Phys. Lett., page 5, 2018. (Cited on page 129.)

[Zhou 2008] Yinhua Zhou, Fengling Zhang, Kristofer Tvingstedt, Sophie Barrau, Fenghong Li, Wenjing Tian and Olle Inganäs. *Investigation on polymer anode design for flexible polymer solar cells.* Applied Physics Letters, vol. 92, no. 23, page 233308, 10.1063/1.2945796. (Cited on page 37.)

[Zhou 2020] Ruinan Zhou, Mingzhe Yu, David Tweddle, Phillip Hamer, Daniel Chen, Brett Hallam, Alison Ciesla, Pietro P. Altermatt, Peter R. Wilshaw and Ruy S. Bonilla. *Understanding and optimizing EBIC pn-junction characterization from modeling insights.* Journal of Applied Physics, vol. 127, no. 2, page 024502, 10.1063/1.5139894. (Cited on pages 152 and 153.)

[Zhu 2009] Jia Zhu, Zongfu Yu, George F. Burkhard, Ching-Mei Hsu, Stephen T. Connor, Yueqin Xu, Qi Wang, Michael McGehee, Shanhui Fan and Yi Cui. *Optical Absorption Enhancement in Amorphous Silicon Nanowire and Nanocone Arrays.* Nano Letters, vol. 9, no. 1, pages 279–282, 10.1021/nl802886y. (Cited on pages 14 and 53.)

[Zhu 2013] Siwei Zhu, Yuan Gao, Bin Hu, Jia Li, Jun Su, Zhiyong Fan and Jun Zhou. *Transferable self-welding silver nanowire network as high performance transparent flexible electrode.* Nanotechnology, vol. 24, no. 33, page 335202, 10.1088/0957-4484/24/33/335202. (Cited on pages 176 and 177.)

[Zink 2006] B. L. Zink, R. Pietri and F. Hellman. *Thermal Conductivity and Specific Heat of Thin-Film Amorphous Silicon.* Physical Review Letters, vol. 96, no. 5, page 055902, 10.1103/PhysRevLett.96.055902. (Cited on page 134.)

[Zuo 2018] Chuantian Zuo, Doojin Vak, Dechan Angmo, Liming Ding and Mei Gao. *One-step roll-to-roll air processed high efficiency perovskite solar cells.* Nano Energy, vol. 46, pages 185–192, 10.1016/j.nanoen.2018.01.037. (Cited on page 81.)